UNIVERSITY OF THE BASQUE COUNTRY

DOCTORAL THESIS

Spin- and Valley-Dependent Transport in Hybrid Systems and 2D Dirac Materials

Author:
Xianpeng ZHANG

Supervisors:
Dr. F. Sebastian BERGERET
Dr. Miguel A. CAZALILLA

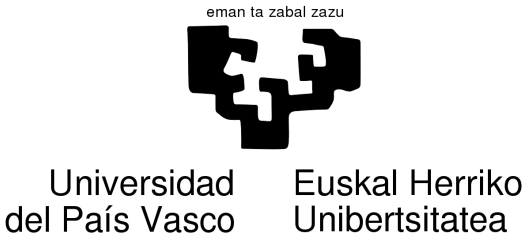

Mesoscopic Physics Group
Faculty of Physics, Chemistry and Materials Science
Polymers and Advanced Materials: Physics, Chemistry and Technology

October 30, 2020

Resumen

En la era de la información y las redes, no hay duda de que la vida diaria no puede separarse de los dispositivos electrónicos, como televisores, teléfonos inteligentes u ordenadores. En las últimas décadas hay una demanda creciente de la tecnología de la información, en particular para resolver los inevitables problemas del alto consumo de energía y los aquellos asociados con la miniaturización.

Para superar estos problemas técnicos, cada vez más científicos y técnicos se han dedicado a buscar nuevas funcionalidades a la electrónica convencional. Teniendo en cuenta que, además de la carga, el electrón posee otro grado de libertad conocido como espín. Este último está asociado al momento angular intrínseco del electrón, cuyo momento magnético puede tomar dos valores: $+\hbar/2$ y $-\hbar/2$, denotados como spin up y spin down, respectivamente, donde hbar es la constante de Planck reducida. El espín como portador de información es el ingrediente básico de la espintrónica, cuyo objetivo es aprovechar el grado de libertad del espín en las corrientes eléctricas para transmitir y manipular información. La espintrónica, como tecnología muy prometedora en la electrónica, tiene muchas ventajas destacadas, como gran capacidad de almacenamiento, equipos ultrarrápidos y bajo consumo de energía. Sin embargo, tiene otros problemas. Por ejemplo, es bien sabido que el grado interno de libertad de giro se aprovecha para almacenar, manipular y leer. Por lo tanto, merece la pena buscar una alternativa a la espintrónica. Además de los grados de libertad de carga y espín, los electrones están dotados de un grado de libertad de valle en muchos materiales bidimensionales, cuyas estructuras de bandas electrónicas ofrecen dos mínimos locales distintos (valles), K y K' dentro de la primera zona de Brillouin. Por lo tanto, naturalmente se puede esperar la existencia de valleytronics, que apunta a la manipulación del grado de libertad del valle para la nueva electrónica. En contraste con la espintrónica, las notables superioridades de la valleytronics son la insensibilidad al campo magnético, la larga vida útil del valle y la facilidad de manipulación eléctrica y óptica.

En esta tesis, nuestro objetivo es estudiar el transporte dependiente del espín y valle en sistemas híbridos y materiales bidimensionales. Por este motivo, dividimos la tesis en dos partes.

Parte I. Transporte de espín en heteroestructuras metal no magnético/material magnético aislante

En la Parte I (Capítulos 2-5), nos concentramos en el estudio del transporte de espín en heteroestructuras de aislante magnético/metal no magnético. Presentamos una teoría microscópica completa de la magnetorresistencia de spin Hall en tales estructuras. La teoría es general y se aplica a cualquier tipo de fase magnética (paramagnética, ferromagnética, antiferromagnética, etc.). Como ejemplos, lo aplicamos para describir la magnetorresistencia Hall de espín (SMR, por sus siglas en inglés, spin Hall magnetoresistance) en un aislante paramagnético y un aislante ferromagnético, específicamente platino/$Gd_3Ga_5O_{12}$ (Pt/GGG) y platino/sulfuro de europio (Pt / EuS), respectivamente. Podemos extraer los parámetros en la intercara, por ejemplo, la densidad de los momentos magnéticos y el acoplamiento de intercambio

de espín entre los electrones itinerantes en metales no magnéticos y los momentos magnéticos en el aislante magnético, así como cuantificar la conductancia dependiente del espín, parámetros clave en la SMR. La conductancia dependiente del espín tiene distintas componentes, y se clasifica como conductancia de absorción de espín (G_s) y conductancia de mezcla de giro $G_{\uparrow\downarrow} = G_r + iG_i$ con G_r y G_i en relación con el torque de transferencia de espín y el torque de tipo campo, respectivamente. Particularmente G_i, parametriza el campo de intercambio efectivo en la interfaz magnética, y es muy relevante en el área de superconductores con división de espín en las proximidades del aislante magnético. Además, si el metal no magnético se reemplaza por un metal normal en la proximidad del superconductor por debajo de la temperatura crítica, podemos investigar la interacción de los efectos de proximidad magnéticos y superconductores. Los nanocables semiconductores en las proximidades de aislantes ferromagnéticos y superconductores son fundamentales para la creación de un estado superconductor topológicamente no trivial.

- En el Capítulo 2, presentamos una teoría microscópica de la SMR de metales normales en contacto con aislantes magnéticos. Nuestra teoría proporciona una herramienta útil para comprender los experimentos sobre metales pesados en contacto con aislantes magnéticos de diferentes tipos, y permite utilizar el efecto de SMR como técnica para estudiar el magnetismo en las interfaces. Los principales resultados de este capítulo son: Primero, expresamos la conductancia de mezcla de espín, que gobierna la fenomenología del efecto, en términos de los parámetros microscópicos de la intercara y las funciones de correlación espín-espín de los momentos locales en la superficie del aislante magnético. En segundo lugar, la dependencia del campo magnético y la temperatura de la conductancia de mezcla de espín dando lugar un comportamiento de la resistencia debido a una interacción entre el efecto Hanle y la mezcla de espín en la intercara. En tercer lugar, describimos una magnetorresistencia negativa inusual originada por un efecto Hanle no local.

- En el Capítulo 3, analizamos teóricamente la primera observación de SMR en una película de Pt sobre un aislante paramagnético $Gd_3Ga_5O_{12}$ (GGG). Hay tres hallazgos clave para la comunidad de la espintrónica: primero, la señal SMR exhibe un claro comportamiento de saturación al aplicar grandes campos magnéticos a baja temperatura, lo cual es consistente con su curva de magnetización similar a un material paramagnético. En segundo lugar, hacemos uso de la teoría microscópica de SMR para relacionar la señal observada con la conductancia de mezcla de espín en la interfaz, donde encontramos que la contribución deltorque de tipo campo (G_i) es tan importante como la contribución de torque transferencia de espín (G_r) en la interfcara Pt/GGG. En tercer lugar, podemos cuantificar la interacción de intercambio entre los electrones de conducción en el Pt y los espines localizados 4f en Gd $^{3+}$. Nuestro análisis experimental de SMR utilizando la teoría microscópica nos permite cuantificar los parámetros clave en la intercara del metal no magnético y el aislante magnético, demostrando el poder de dicha técnica.

- En el Capítulo 4, presentamos la primera medición y descripción teórica SMR en Pt sobre un aislante puramente ferromagnético, el sulfuro de europio (EuS). Al ajustar las medidas de SMR con nuestra teoría micrsocópica, extrajimos la dependencia de la temperatura de la conductancia dependiente del espín (G_s, G_r y G_i), obteniendola contribución del torque de tipo campo (G_i), el torque de transferencia de espín (G_r) y - la conductancia de absorción de espín (G_s).

El valor obtenido de G_i es al menos tres veces mayor que G_r por debajo de la temperatura de Curie del EuS. A partir de G_i, encontramos que el campo de intercambio interfacial que actúa sobre los electrones de conducción de Pt del orden de 1 meV. Nuestro trabajo proporciona un método fácil para cuantificar este campo de división de espín interfacial, que juega un papel clave en campos emergentes como la espintrónica superconductora y la caloritrónica (Linder and Robinson, 2015; Giazotto, Heikkilä, and Bergeret, 2015) y la superconductividad topológica (Virtanen et al., 2018; Liu et al., 2019a).

- En el Capítulo 5, se estudian los de proximidad magnética y superconductividad en un nanohilo (NW por sus siglas en inglés, nanowire) semiconductor desordenado en contacto a un superconductor y un aislante ferromagnético (FI por sus siglas en inglés, ferromagnetic insulator). Mostramos que surge una polarización de espín de equilibrio considerable en el NW debido a la interacción entre las correlaciones superconductoras y el campo de intercambio en el FI. La magnetización resultante tiene una contribución no local que se extiende en el NW durante la longitud de coherencia superconductora y es de signo opuesto a la polarización de espín local inducida por el efecto de proximidad magnética en el estado normal. Para la configuración de unión de Josephson, mostramos que la magnetización no local puede ser controlada por la polarización de fase superconductora a través de la unión. Nuestros hallazgos son relevantes para la implementación de estados ligados de Majorana en estructuras híbridas de última generación.

Parte II. Transporte de espín y valle en materiales Dirac bidimensionales

En la Parte II (Capítulos 6-7), trabajamos sobre los efectos Hall de espín y valle y la resistencia no local en materiales de Dirac bidimensionales. Investigamos los posibles mecanismos responsables de las versiones clásicas de los efectos Hall de espín y valle, y proponemos los esquemas para la detección experimental de estos efectos mediante medidas de resistencia no local. La comprensión de las propiedades magnéticas de la resistencia no local es significativa para la reciente controversia sobre el origen físico de la resistencia no local medida en dispositivos de barra Hall de grafeno con absorbentes, donde la presencia de gran resistencia no local y la ausencia de oscilación de Hanle, es decir , una oscilación de la resistencia no local con campo magnético en el plano, sugieren la posibilidad del nuevo origen de la resistencia no local insensible al campo magnético.

- En el Capítulo 6, estudiamos el efecto Hall de valle clásico de la deformación no uniforme. El grafeno sujeto a altos niveles de deformación por cizallamiento conduce a fuertes campos pseudo-magnéticos que dan como resultado la aparición de niveles de pseudo-Landau. Aquí mostramos que, con niveles modestos de tensión, el grafeno también puede sostener un efecto Hall de valle clásico (VHE por sus siglas en inglés, valley Hall effect) que se puede detectar en mediciones de transporte no local. Proporcionamos una teoría del VHE inducido por deformación a partir de la ecuación cuántica de Boltzmann. Esto nos permite mostrar que promediar configuraciones de impurezas de corto alcance destruye la coherencia cuántica entre valles, dejando el tiempo de dispersión elástica y la tasa de dispersión entre valles como los únicos parámetros que caracterizan la teoría del transporte. Usando esta teoría, calculamos la resistencia no local de un dispositivo de barra Hall en el régimen de difusión.

Nuestra teoría también es relevante para el estudio de los efectos de deformación moderada en las propiedades de transporte (no locales) de otros materiales bidimensionales y heteroestructuras de van der Waals.

- En el Capítulo 7, estudiamos la interacción del efecto Hall de espín y valle en materiales 2D de Dirac. Eliminaré esta oración: además del espín, los electrones en muchos materiales poseen un grado de libertad de pseudo-espín adicional conocido como 'valle'. En materiales donde los grados de libertad de espín y valle están débilmente acoplados, ambos pueden excitarse y controlado de forma independiente. En este capítulo, estudiamos un modelo que describe la interacción de los efectos Hall de espín y valle en estos materiales bidimensionales. Demostramos la aparición de una corriente longitudinal neutra adicional que está polarizada tanto en espín como en valle. Esta corriente neutra se puede usar para controlar la densidad de espín ajustando la magnitud del efecto Hall del valle. Además, la interacción de los dos efectos puede suprimir el efecto Hanle. La última observación proporciona una posible explicación de la ausencia del efecto Hanle en varios experimentos recientes (Völkl et al., 2018; Kaverzin and Wees, 2015; Wang, Cai, and Reutt-Robey, 2015). Finalmente, enfatizamos que nuestro trabajo también abre la posibilidad de diseñar la conversión entre el valle y los grados de libertad de espín en materiales bidimensionales.

Abstract

Living in the era of information and networks, there is no doubt that our daily lives can not be separated from electronic devices, such as televisions, smartphones, or computers. In the last decades, there is an increasing demand for information technology, in particular, to solve the inevitable high-energy consumption and the issues associated with miniaturization.

To surmount these technical bottlenecks, more and more scientists and technicians have devoted themselves to searching for new functionalities to conventional electronics. Note that, in addition to the charge degree of freedom, electrons possess a spin degree of freedom. The latter is the intrinsic angular momentum, whose magnetic moment can take two values: $+\hbar/2$ and $-\hbar/2$, denoted as spin up and spin down, respectively, where $\hbar$ is the reduced Planck constant. Spin, as an information carrier, is the basic ingredient of spintronics, which aims at exploiting the spin degree of freedom in electronic currents to transmit and manipulate information. Spintronics, as an up-and-coming technology in electronics, has many preeminent advantages, such as super-large storage capacity, super-fast equipment, and low-energy consumption. However, it suffers from some other problems. For instance, it is well-known that the internal degree of freedom of spin is harnessed to store, manipulate, and readout. Hence, it is worth finding an alternative to spintronics. In addition to charge and spin degrees of freedom, electrons are endowed with a valley degree of freedom in many two-dimensional materials, whose electronic band structures offer two distinct local minima (valleys), K and K' within the first Brillouin zone. Thus, one can naturally expect the existence of valleytronics, which aims to manipulate the valley degree of freedom for new electronics. Contrasted with spintronics, the remarkable superiorities of valleytronics are insensitivity to a magnetic field, long valley lifetime, as well as easily electrical and optical manipulation.

This thesis aims to study the spin- and valley-dependent transport in the hybrid system and two-dimensional materials. For this sake, we divide the whole thesis into two parts. The structure of the thesis is as follows:

Part I. Spin transports in normal metal/magnetic insulator heterostructures

In **Part** I (Chapters 2-5), we concentrate on the study of the spin transport in non-magnetic metal/magnetic insulator heterostructure. We present a fully microscopic theory of the spin Hall magnetoresistance in such structures. The theory is rather general and applies to any magnetic phase (paramagnetic, ferromagnetic, antiferromagnetic, etc.). As examples, we apply it to describe the spin Hall magnetoresistance in paramagnetic and ferromagnetic spin Hall magnetoresistance, specifically Platinum/$Gd_3Ga_5O_{12}$ (Pt/GGG) and Platinum/Europium sulfide (Pt / EuS), respectively. We can extract the interfacial parameters, for instance, the density of magnetic moments and the spin exchange coupling between the itinerant electron in non-magnetic metal and magnetic moments in the magnetic insulator, and quantify the spin-dependent conductance, which is on the heart of spin Hall magnetoresistance, and is classified as spin-sink conductance (G_s) and spin-mixing conductance $G_{\uparrow\downarrow} = G_r + iG_i$ with G_r and G_i relative to spin-transfer torque and field-like torque,

respectively. Particularly G_i, it parameterizes the effective exchange field at a magnetic interface and is very relevant in the area of spin-split superconductors in proximity to a magnetic insulator. Furthermore, if the non-magnetic metal is replaced by normal metal in proximity to the superconductor below the critical temperature, we can investigate the interplay of magnetic and superconducting proximity effects. Semiconducting nanowires in proximity with ferromagnetic insulators and superconductors are central to creating a topologically non-trivial superconducting state.

- In Chapter 2, we present a microscopic theory of the spin Hall magnetoresistance of normal metals in contact with magnetic insulators. Our theory provides a useful tool for understanding the experiments on heavy metals in contact with magnetic insulators of different kinds, and it enables the spin Hall magnetoresistance effect to be used as a technique to study magnetism at interfaces. This chapter's main results are: First, we express the spin mixing conductance, which governs the phenomenology of the effect, in terms of the microscopic parameters of the interface and the spin-spin correlation functions of the local moments on the surface of the magnetic insulator. Second, the magnetic field and temperature dependence of the spin mixing conductance lead to a rich resistance behavior due to an interplay between the Hanle effect and the spin mixing at the interface. Third, we describe an unusual negative magnetoresistance originating from a non-local Hanle effect.

- In Chapter 3, we report and theoretically analyze the first observation of the spin Hall magneto-resistance (SMR) in a Pt film on top of a paramagnetic insulator $Gd_3Ga_5O_{12}$ (GGG). There are three key findings for the spintronics community: First, the SMR signal exhibits the clear saturation behavior with applying large magnetic fields at low temperature, which is consistent with its paramagnet-like magnetization curve. Second, we use the microscopic theory of SMR to relate the observed signal to the spin-mixing conductance at the interface, where we find that the field-like torque contribution (G_i) is as important as the spin-transfer torque contribution (G_r) in Pt/GGG interface. Third, we can quantify the exchange interaction between conduction electrons in Pt and $4f$ localized spins in Gd^{3+}. Our experimental analysis of SMR using the newly developed microscopic theory allows us to quantify key parameters at the interface of heavy metal/magnetic insulator, demonstrating the power of such a technique.

- In Chapter 4, we report the first measurement and theoretical description of the spin Hall magneto-resistance (SMR) of Pt on top of a purely ferromagnetic insulator, Europium sulfide (EuS). By fitting the SMR measurements with our microscopic theory, we extracted the temperature dependence of the spin-dependent conductance (G_s, G_r and G_i), disentangling the contribution of field-like torque (G_i), spin-transfer torque (G_r), and spin-sink conductance (G_s). The obtained value of G_i s at least three times larger than G_r below the Curie temperature of EuS. From G_i, We find an interfacial exchange field acting upon the conduction electrons of Pt of the order of 1 meV. Our work provides an easy method to quantify this interfacial spin-splitting field, which plays a key role in emerging fields such as superconducting spintronics and caloritronics (Linder and Robinson, 2015; Giazotto, Heikkilä, and Bergeret, 2015), and topological superconductivity (Virtanen et al., 2018; Liu et al., 2019a).

- In Chapter 5, we study the magnetic and superconducting proximity effects in a disordered or metallic semiconducting nanowire (NW) attached to superconducting leads and a ferromagnetic insulator (FI). We show that a sizable equilibrium spin polarization arises in the NW due to the interplay between the superconducting correlations and the exchange field in the FI. The resulting magnetization has a nonlocal contribution that spreads in the NW over the superconducting coherence length and is opposite in sign to the local spin polarization induced by the magnetic proximity effect in the normal state. For a Josephson-junction setup, we show that the nonlocal magnetization can be controlled by the superconducting phase bias across the junction. Our findings are relevant for the implementation of Majorana bound states in state-of-the-art hybrid structures.

Part II Spin and valley transport in two-dimensional Dirac materials

In **Part** II (Chapters 6-7), we work on the spin and valley Hall effects and nonlocal resistance in two dimensional Dirac materials. We investigated the possible mechanisms responsible for the classical versions of spin and valley Hall effects and proposed the schemes for experimental detection of these effects by nonlocal resistance measurements. The understanding of the magnetic properties of nonlocal resistance is significant for the recent controversy about the physical origin of nonlocal resistance measured in Hall bar devices made of graphene decorated with absorbates, where the presence of large nonlocal resistance and the absence of Hanle oscillation, that is, an oscillation of the nonlocal resistance with the in-plane magnetic field, suggest the possibility of the new origin of nonlocal resistance insensitive to the magnetic field.

- In Chapter 6, we study the classical valley Hall effect from the non-uniform strain. Graphene subject to high levels of shear strain leads to strong pseudomagnetic fields resulting in the emergence of pseudo-Landau levels. Here we show that, with modest levels of strain, graphene can also sustain a classical valley Hall effect (VHE) that can be detected in nonlocal transport measurements. We provide a theory of the strain-induced VHE starting from the quantum Boltzmann equation. This allows us to show that averaging over short-range impurity configurations destroys quantum coherence between valleys, leaving the elastic scattering time and inter-valley scattering rate as the only parameters characterizing the transport theory. Using the theory, we compute the nonlocal resistance of a Hall bar device in the diffusive regime. Our theory is also relevant for studying moderate strain effects in the (nonlocal) transport properties of other two-dimensional materials and van der Walls heterostructures.

- In chapter 7, we study the interplay of spin and valley Hall effect in 2D Dirac materials. I will remove this sentence: In addition to spin, electrons in many materials possess an additional pseudo-spin degree of freedom known as 'valley.' In materials where the spin and valley degrees of freedom are weakly coupled, they can be both excited and controlled independently. In this chapter, we study a model describing the interplay of the spin and valley Hall effects in such two-dimensional materials. We demonstrate the emergence of an additional longitudinal neutral current that is both spin and valley polarized. This additional neutral current can control the spin density by tuning the magnitude of the valley Hall effect. Besides, the interplay of the two effects can suppress the Hanle effect. The latter observation provides a possible explanation

for the absence of the Hanle effect in several recent experiments (Völkl et al., 2018; Kaverzin and Wees, 2015; Wang, Cai, and Reutt-Robey, 2015). Finally, we emphasize that our work also opens the possibility to engineer the conversion between the valley and spin degrees of freedom in two-dimensional materials.

Acknowledgements

Time flies. I still clearly remember the first day I arrived and walked along Donostia's attractive beach three years ago. It is an amazing three-year experience of my life, and there is no doubt that I will keep in mind forever. As a Ph.D. student, the ship of my scientific career set sail here. I enjoyed it, I laughed, I suffered, and most importantly, I gained a lot. Because of all this, I want to acknowledge all people that contribute to this.

First of all, I would like to express my sincere gratitude to my advisors, Prof. Sebastian Bergeret and Prof. Miguel Angel Cazalilla, to provide me such a wonderful opportunity to join the mesoscopic physics group, for patient guidance of scientific research, and the continuous support of my Ph.D. study. Your great enthusiasm and immense knowledge always impress and encourage me a lot. I enjoy discussing our results, learning how to do science, how to think, how to improve, and so on. Without both of you, I could not have had this enriching experience both personally and professionally. Besides, I also thank my third "supervisor", Dr. Vitaly N. Golovach. Your rigorous amplitudes and invaluable inspirations always remind me to be a theoretician.

Besides my advisors, I would like to thank the experimental collaborators, Prof. Felix Casanova, Prof. Eiji Saitoh, Prof Teruo Ono, and Prof. Francesco Giazotto and their students Dr. Juan M. Gomez-Perez, Dr. Koichi Oyanag, and Dr. Kento Oda. You taught me how to think physics from the view of experimental points, how to work together with experimental groups, how to converge between experimentalists and theoreticians. It is really a fruitful collaboration, and I hope we will have more in the future.

I also want to thank Dr. Chunli Huang for teaching me so many analytical techniques. We have so much unforgettable memory from Taiwan to Spain, such as the Kinmen Kaoliang on the night of FamilyMart, the beers, beach, and dinner in Spain. I absolutely enjoyed working with you!

I am also very grateful to all our groups, Dr. Dario Bercioux, Dr. Stefan Ilic, Dr. Tineke van den Berg, Dr. Alba Pascual, Dr. Julie Baumard, Dr. Bogusz Bujnowski, Cristina Sanz, and Mikel Rouco, for personal or scientific supports. It is really an impressive experience of my life to work together with you.

Finally, I would like to thank my family: my parents and sisters to support me spiritually throughout writing this thesis and my life in general.

Contents

List of Abbreviations

2D	**T**wo-**D**imensional
3D	**T**hree-**D**imensional
AHE	**A**nomalous **H**all **E**ffect
Al	**Al**uminium
EuS	**Eu**ropium **S**ulfide
FLT	**F**ield-**L**ike **T**orque
FM	**F**erro-**M**agnet
FI	**F**erromagnetic **I**nsulator
HE	**H**anle **E**ffect
HM	**H**eavy **M**etal
HMR	**H**anle **M**agneto-**R**esistance
GF	**G**reen **F**unction
GGG	**G**adolinium **G**allium **G**arnet
GMR	**G**iant **M**agneto-**R**esistance
MI	**M**agnetic **I**nsulator
MR	**M**agneto-**R**esistance
MZM	**M**ajorana-**Z**ero-**M**odes
NLM	**N**on-**L**ocal-**M**agnetization
NLR	**N**on-**L**ocal-**R**esistance
NM	**N**ormal **M**etal
NW	**N**ano-**W**ire
OHE	**O**rdinary **H**all **E**ffect
PM	**P**ara-**M**agnet
Pt	**Pt**inum
SC	**S**uper-**C**onductor
SHE	**S**pin **H**all **E**ffect
SMC	**S**pin-**M**ixing **C**onductance
SMR	**S**pin-Hall **M**agneto-**R**esistance
SOC	**S**pin **O**rbit **C**oupling
SSC	**S**pin-**S**ink **C**onductance
STT	**S**pin-**T**ransfer **T**orque
SR	**S**pin **R**elaxation
SVHE	**S**pin-**V**alley **H**all **E**ffect
TMD	**T**ransition-**M**etal **D**ichalcogenides
VHE	**V**alley **H**all **E**ffect
VOC	**V**alley **O**rbit **C**oupling

Physical Constants

Speed of Light	$c_0 = 2.998 \times 10^8\,\mathrm{m\,s^{-1}}$
Plank Constant	$\hbar = 1.054 \times 10^{-34}\,\mathrm{m^2 kg/s}$
Charge of Electron	$e = 1.602 \times 10^{-19}\,\mathrm{C}$
Bohr Magneton	$\mu_B = 9.274 \times 10^{-24}\,\mathrm{J\,T^{-1}}$
Boltzmann Constant	$k_B = 1.380 \times 10^{-23}\,\mathrm{J/K}$
Electronvolt	$\mathrm{eV} = 1.602 \times 10^{-19}\,\mathrm{J}$
Mass of electron	$\mathrm{m} = 9.109 \times 10^{-31}\,\mathrm{kg}$
G-factor of electron	$\mathrm{g} = 2$

List of Symbols

$\hat{S}^a$	spin operator of local moment
$\vec{E}$	Electric field
$\vec{B}$	Magnetic field
$\vec{v}$	Velocity
v_F	Fermi velocity
E_F	Fermi energy
q	Charge of carrier
T	Temperature
$G_{\uparrow\downarrow}$	Spin-mixing conductance
G_s	Spin-sink conductance
$\vec{k}$	Kinetic momentum
$\vec{p}$	Momentum
$\vec{L}$	Angular momentum
$\vec{J}_c$	charge current density
$\vec{J}_s$	spin current density
$\vec{J}_v$	valley current density
$\vec{J}_{sv}$	spin-valley current density
N_c	charge density
N_s	spin density
N_v	valley density
N_{sv}	spin-valley density
$\mathcal{D}$	diffusion coefficient
μ_c	charge basis
μ_s	spin basis
μ_v	valley basis
$\hat{\sigma}^a$	Pauli matrix for sublattice space
ν_F	Density of state
$\hat{s}^a$	Pauli matrix for spin space
$\hat{\tau}^a$	Pauli matrix for valley space
$\hat{\kappa}^a$	Pauli matrix in Nambu space
ω	angular frequency
ω_B	Larmor frequency
ω_L	Rebormalized Larmor frequency
ρ	Drude resistivity
τ	Drude relaxation time
σ	Drude conductivity

Chapter 1

Introduction

This chapter is divided into six sections, which introduce the basic concepts related to this thesis topic. I begin with general motivations for spintronics and valleytronics. Sections 1.2 (1.3) review spin (valley) Hall effects and spin (valley) relaxation, with special emphasis on the microscopic origins of spin-(valley-)orbit coupling, respectively. Next, I discuss the spin-dependent transport in normal metal/magnetic insulator heterostructures in section 1.4 and the spin- and valley-dependent transport in two-dimensional (2D) Dirac materials in section 1.5. The chapter ends with an outline of the thesis.

1.1 Motivations

Many people may have asked themselves what will happen if all the electronic devices stopped working? Indeed, all aspects of our lives nowadays are greatly influenced by electronic technology. In the last decades, significant progress in electronic industries benefits from the development of electronics, which exploits the charge degree of freedom of the electron for reading, writing, transporting, and storing information. However, with the increasing demand for information technology, traditional electronic industries are suffering from many difficulties. They are i) more and more expensive manufacturing costs, ii) inevitable high-energy consumption, as well as iii) smaller and smaller units in integrated circuits so that the Moore's Law fails.

To overcome these difficulties, scientists and technicians have been paying attention to the spin degree of freedom of electron. Note that the spin of the electron can be an alternative to usual electronics, and hence logical levels 0 and 1 can be encoded by different values of magnetic moments. We then reach the spintronics area, which relies upon the spin degree of freedom of electronic currents to realize the manipulation, transmission, storing, and read-out of information. Indeed, some spintronic devices are nowadays widely used in electronics, due to many remarkable advantages, for instance, super-large storage capacity, super-fast equipment, and low-energy consumption.

The birth of spintronics stems from the pioneering works of the groups led by Albert Fert [Baibich et al., 1988] and Peter Grünberg [Binasch et al., 1989]. In two almost simultaneous but independent experiments on ferromagnet/normal-metal multilayers, revealed simultaneously, they found a new and revolutionary effect: the giant magnetoresistance (GMR). It is a sizable change of resistance when the magnetic moments of adjacent ferromagnetic layers are changed from a parallel to an antiparallel alignment in a configuration denoted as a spin valve. Both were awarded the Nobel prize in Physics in 2007 because of this discovery (Fert, 2008; Fullerton and Schuller, 2007). In spintronics, the logical levels 0 and 1 can be respectively encoded by high and low magnetoresistance states, which correspond to the

antiparallel and parallel orientation of magnetic layers in a spin valve. Thus, it can be used for the reading process in hard disk drives (Berg et al., 2013). Moreover, the GMR effect can be applied in information storage technologies, such as magnetoresistive random-access memory (Zhu, 2008; Apalkov, Dieny, and Slaughter, 2016; Bhatti et al., 2017). It supports a non-volatile memory with near-zero leakage power consumption (Umesh and Mittal, 2019). In addition to GMR, another ingredient of spintronics is spin-transfer torque (STT). It describes the phenomenon by which the orientation of a magnetic layer embedded in a magnetic tunnel junction or spin valve can be control by injecting a spin-polarized current. This effect can be utilized to switch between logic 0 and 1 in magnetic random-access memory (Brataas, Kent, and Ohno, 2012), and hence it is also essential for the writing process (Kawahara et al., 2012).

Though spintronics has obvious advantages mentioned above, as the internal degree of freedom of electron, it is harnessed to manipulate spin. It is generally linked to strong magnetic fields, which introduces additional technical limitations on the application of spintronics. The spin is also electrically insensitive to gate voltage and hence makes it hard to interface conventional electronics. Moreover, due to magnetic impurities and spin-orbit disorder, the spin lifetime is short (0.1-1ns), and hence in some cases, electrons lose their spin states before one can perform the operation that one intends. To avoid these problems, further alternatives are needed.

In two-dimensional (2D) materials, such as silicon inversion layers (Sham et al., 1978; Bloss, Sham, and Vinter, 1979), graphene (Rycerz, Tworzydło, and Beenakker, 2007), and transition metal dichalcogenide (TMD) (Zeng et al., 2012), in which electronic band structures possess two distinct local minima, K and K' within the first Brillouin zone, (see Fig. 1.1), electrons are endowed with valley degree of freedom in addition to charge and spin. As a result, the logical levels 0 and 1 can be encoded by different discrete values of the crystal momentum. As a twin of spintronics, valleytronics aims to manipulate the valley degree of freedom for new electronics. Like spintronics, valleytronics also provides a tremendous advantage in storing and processing information (Schaibley et al., 2016). On the other hand, compared to spintronics, the remarkable advantages of valleytronics are i) valley degree of freedom is generally insensitive to a magnetic field (Zhang, Huang, and Cazalilla, 2017); ii) the intervalley scattering in 2D materials, in general, is weak in the material, which leads to a long valley lifetime.

There is increasing attention paid to valleytronics as an alternative or complement to electronics. The early studies of valley degree of freedom can stem from the works of Sham et al., 1978; Bloss, Sham, and Vinter, 1979, which focused on the valley degeneracy and inter-valley coupling in 2D electron gases in silicon inversion layers. Bloss, Sham, and Vinter, 1979 predicted that the intravalley exchange and correlation could generate spontaneous valley ferromagnetism, in analogy to spin ferromagnetism. Thus, Xu et al., 2014 suggested that the valley might also be exploited for non-volatile information storage. Besides, Isberg et al., 2013 proposed that the valley degree of freedom in diamond enables valleytronic information processing as a new route to quantum computing. On the other hand, valleytronics is currently under intensive research in graphene (Jiang et al., 2013; Gradinar et al., 2013; Cosma et al., 2014; Beconcini, Taddei, and Polini, 2016; Gorbachev et al., 2014) and other 2D materials (Xiao, Chang, and Niu, 2010; Shimazaki, Yamamoto, and Borzenets, 2015; Sie and McIver, 2015; Lee, Mak, and Shan, 2016).

In both spintronics and valleytronics, the generation of spin and valley currents

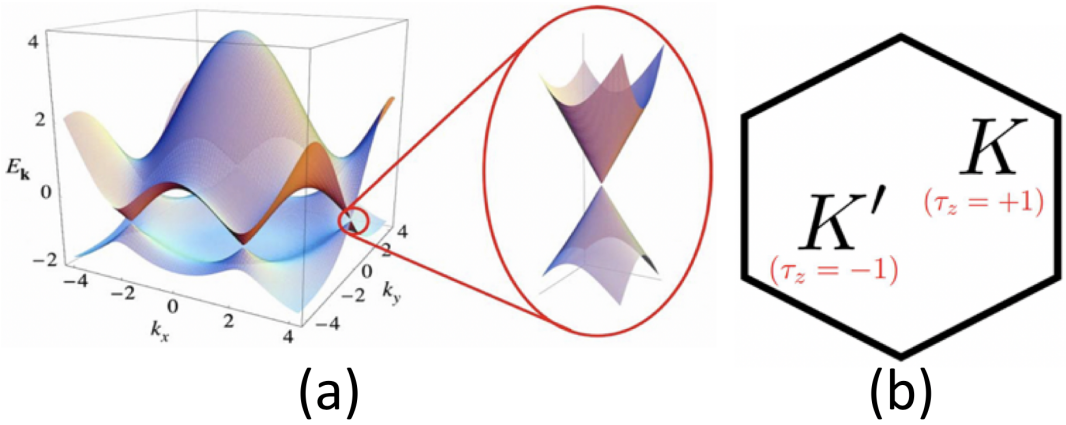

FIGURE 1.1: **Illustration of valley degree of freedom**. (a) Sketch of the energy spectrum of pristine graphene. (b) Indication of valley K and K′ in the first Brillouin zone. Panel (a) comes from Castro Neto et al., 2009

with high quality is pivotal in developing functional devices. One of the most efficient and convenient ways of generation, is by means of the spin (valley) Hall effect, *that is*, the conversion from *longitudinal* charge current to *transverse* spin (valley) current, respectively. The mechanism responsible for this conversion is spin-(valley-)orbit coupling, which will be introduced in subsections 1.2.1 (1.3.1), respectively.

1.2 Spin Hall effect and spin relaxation

In this section, I begin with the introduction of the origins of spin-orbit coupling (SOC) and discuss its contributions to spin Hall effect (SHE) and to spin relaxation in subsections 1.2.2 and 1.2.3, respectively.

1.2.1 Spin-orbit coupling

I first discuss the origin of SOC. The motion of electrons depends on the electric and magnetic fields that are applied to them. The magnetic field in the coordinate system which moves with the velocity of itinerant electrons, $\vec{v}$, reads

$$\vec{B}_{move} = \frac{\vec{B}_{static} - \frac{\vec{v}}{c_0^2} \times \vec{E}_{static}}{\sqrt{1 - \frac{v^2}{c_0^2}}}, \tag{1.2.1}$$

where c_0 is the velocity of light. $\vec{E}_{static}$, $\vec{B}_{static}$ are the electric and magnetic field in the static coordinate system. Eq. (1.2.1) reveals that a particle moving in an electrical field perceives an additional magnetic field directed perpendicularly to the electrical field and perpendicularly to the particle movement direction. As I will explain soon, this is the origin of SOC and the spin Hall effect introduced in subsection 1.2.2.

Read from Eq. (1.2.1), SOC is a relativistic effect arising from a spatially inhomogeneous potential, $V(\vec{r})$, which induces a static electric field, $\vec{E}_{static} = -(1/q)\nabla V(\vec{r})$ (see Winkler, 2003 and reference therein contained), where q is the charge of conduction particle. In the rest frame of the free electrons, they suffer from an effective magnetic field, which can be obtained from Eq. (1.2.1) in the non-relativistic limit

($v \ll c_0$)

$$\vec{B}_{SOC} = -\frac{1}{c_0^2}\vec{v} \times \vec{E}_{static} \,. \tag{1.2.2}$$

Consequently, an electron which moves in a static electrical field $\vec{E}_{static}$, perceives an effective magnetic field $\vec{B}_{SOC}$ in its own reference frame. It is well-known that electrons possess an intrinsic spin magnetic moment

$$\vec{\mu} = \frac{gq\hbar}{8m}\hat{\vec{s}}, \tag{1.2.3}$$

and its interaction with effective magnetic field (1.2.2) is described by

$$H_{SOC} = -\vec{\mu} \cdot \vec{B}_{SOC} = -\frac{g\hbar}{8m^2c_0^2}\vec{s} \cdot \vec{p} \times \vec{\nabla} V(\vec{r}), \tag{1.2.4}$$

where g is g-factor, m is the mass of conduction particle, and $\hat{\vec{s}}$ is Pauli matrix in spin space. In this subsection, I will introduce two different origins of this static electric field. They are i) nuclear potential, ii) conformal, and crystal potential in 2D materials.

In atoms, in which the static electric field is generated from nuclear potential $V_{AT}(\vec{r}) = -qZ/r$. Thus, one reaches $\vec{E}_{static}(\vec{r}) = Z\hat{\vec{r}}/r^2$, where q and Z are the charge of electron and nucleus, respectively. Note that electrons undergo cyclotron motion around nucleus with velocity $\vec{v}$, that is, the orbital rotation of an electron around nuclear. Its interaction with effective magnetic field (1.2.2) is described by

$$H_{SOC} = \frac{g\hbar}{8m^2c_0^2}\frac{\mathrm{d}V_{AT}(r)}{rdr}\hat{\vec{s}} \cdot \vec{L}. \tag{1.2.5}$$

Obviously, Eq. (1.2.5) depicts an interaction between spin magnetic moment $\hbar\hat{\vec{s}}/2$ and angular moment $\vec{L} = \vec{r} \times \vec{p}$. The effective magnetic field $\vec{B}_{SOC}$ affects the electron spin. Hence the spectrum of the electron become spin-dependent. This is the origin of the fine structure of energy levels of atoms.

Next, I discuss SOC in a 2D material contained in the $x-y$ plane. The remarkable properties are the spatial restriction in z direction. Bychkov and Rashba, 1984 have shown that there exists a SOC as a direct result of inversion symmetry breaking in the direction perpendicular to the two-dimensional (2D) plane. For instance, the conformal potential always induces a static electric field towards the bulk direction. This out-of-plane electric field breaks inversion symmetry and can be approximately described by a spatially inhomogeneous potential $V_{2D}(\vec{r}) = -qE_z z$. This is the origin of Rashba SOC

$$H_{SOC}^{\mathrm{R}} = -\alpha_{\mathrm{R}}(\hat{s}^x k^y - \hat{s}^y k^x), \tag{1.2.6}$$

where α_{R} is the constant of Rashba SOC. It can explain the anisotropic magnetoresistance (Schliemann and Loss, 2003) and provide the possibility of manipulating electron spins by electric fields (Datta and Das, 1990).

In addition to out-of-plane static electric field, there also exist in-plane one. Bernevig and Zhang, 2006 suggested a spatially inhomogeneous SOC in graphene

$$H_{SOC}^{\mathrm{BZ}} = -\alpha_{\mathrm{B}}(xk^y - yk^x)\hat{s}^z, \tag{1.2.7}$$

where α_B is the constant of Benevig-Zhang SOC. It can be treated as non-abelian spin gauge fields (Raimondi et al., 2012; Gorini et al., 2010). Linear to kinetic momentum $\vec{k}$, Benevig-Zhang SOC (1.2.7) can be combined with pristine Hamiltonian of 2D electron gas

$$H_0 = \frac{\hbar^2 k^2}{2m} + g\mu_B B\frac{\hat{s}^z}{2}, \tag{1.2.8}$$

where magnetic field $\vec{B}$ is assumed to be in z direction. Then, we reach the Hamiltonian of Benevig-Zhang model

$$\hat{H}_{\mathrm{BZ}} = H_0 + H_{SOC}^{\mathrm{BZ}} = \frac{\hbar^2}{2m}\left[\left(k_x - \frac{q}{\hbar}A_{SOC}^{x,z}\hat{s}^z\right)^2 + \left(k_y - \frac{q}{\hbar}A_{SOC}^{y,z}\hat{s}^z\right)^2\right] + g\mu_B B\frac{\hat{s}^z}{2}, \tag{1.2.9}$$

where the Benevig-Zhang SOC is described by spatially inhomogeneous spin gauge field

$$\hat{A}_{SOC}^{x,z}\hat{s}^z = +\hat{s}^z\frac{m\alpha_{\mathrm{B}}}{\hbar q}\alpha_{\mathrm{B}}y, \tag{1.2.10}$$

$$\hat{A}_{SOC}^{y,z}\hat{s}^z = -\hat{s}^z\frac{m\alpha_{\mathrm{B}}}{\hbar q}\alpha_{\mathrm{B}}x. \tag{1.2.11}$$

This spin gauge field $\vec{A}_{SOC}^{z}\hat{s}^z$ will induces a *spin magnetic field* defined by $\hat{s}^z\vec{\nabla}\times\vec{A}_{SOC}^{z}(x)$ and pointing in z direction

$$\hat{B}_{SOC}^{z} = B_{SOC}^{z}\hat{s}_z = \frac{m\alpha_{\mathrm{B}}}{\hbar q}\alpha_{\mathrm{B}}\hat{s}^z\ . \tag{1.2.12}$$

Finally, the Benevig-Zhang SOC is described by a *spin magnetic field* along the z-axis direction, which point in opposite direction for different spins.

I also briefly introduce here the Kane-Mele SOC, which will be used in Chapter 7. It is spatially homogeneous and is independent of kinetic momentum. To discuss this kind of SOC, I are required to briefly introduce graphene model, whose pristine Hamiltonian is given by

$$H_0(\vec{k}) = \hbar v_F\left(\hat{\tau}_z\hat{\sigma}_x k_x + \hat{\sigma}_y k_y\right), \tag{1.2.13}$$

where v_F is the Fermi velocity and σ_x, σ_y are the Pauli matrices in sublattice space. Kane and Mele, 2005 proposed a spatially homogeneous one, in monolayer graphene

$$H_{SOC}^{\mathrm{K}} = \alpha_{\mathrm{K}}\hat{s}_z\hat{\tau}_z\hat{\sigma}_z, \tag{1.2.14}$$

where α_{K} is the constant of Kane-Mele SOC. Compared to Rashba and Dresselhaus SOC, Kane-Mele one is independent of kinetic momentum. The physics of the spatially homogeneous SOC should be understood by ways of Berry curvature density. This is also the *spin magnetic field*, which has opposite sign for different spins.

In addition to SOC in 2D systems due to inversion symmetry breaking, 3D heavy metals exhibit large SOC, which is also addressed in this thesis. Its origin is material dependent, but extrinsic in several cases that is due to the presence of impurities.

The SOC has many interesting effects, such as the spin Hall effect, spin relaxation,

spin precession, spin-dependent scatterings, spin-transfer torque, and the enhancement of the applied magnetic field. Here I focus on the spin Hall effect and spin relaxation, which will be explained in subsections 1.2.2 and 1.2.3, respectively.

1.2.2 The Spin Hall effect

In spintronics, it is essential to generate spin currents. The SHE is one of the most important and convenient methods to generate them.

Before introducing the SHE, I discuss the ordinary Hall effect (OHE). It was first discovered by Hall, 1879 and explained using the Drude model, which was introduced by Drude, 1900 to explain the transport properties of electrons in normal metal with imperfections. It is well-known that the linear response of a normal metal to a weak electric field $\vec{E}$ is a charge current density in the electric field direction. In the presence of a weak magnetic field, $\vec{H}$ perpendicular to the electron velocity $\vec{v}$, the resulting Lorentz force $q\vec{v} \times \vec{H}$ is in the transverse direction and have an opposite direction for carriers with different signs of charge (such as negative for electrons and positive for holes). By weak, I here mean small enough magnetic fields so that the radius of the cyclotron motion R_c is much larger than mean-free path l, i.e., $R_c \gg l$. In this case, the system is in the diffusive regime, and the charge carriers are pushed towards the edges of the conductor and accumulate on the lateral boundaries, which results in the build-up of an electric field, $\vec{E}_b$ in the transverse direction. In the steady-state, the electronic motion ($\vec{v}$) is described by the equation of motion

$$\frac{\vec{v}}{\tau} = \frac{q}{m}\left(\vec{E} + \vec{v} \times \vec{z}B\right), \tag{1.2.15}$$

where $\vec{v}$, q and m, are *drift* velocity, charge, and mass of the carrier, respectively, and τ is the mean-free time between collisions with impurities. c_0 is the speed of light. Without losing generality, I set the magnetic field in the z-direction in this section. Note that, in the presence of a perpendicular magnetic field, carriers with a different sign of charge will be spatially separated and accumulate on opposite boundaries, as shown in FIGURE 1.2 (a).

In analogy to OHE, the spin degree of freedom of itinerant electrons indicates the existence of SHE. The mechanism responsible for SHE is the SOC mentioned above, which can be vividly described by a figure of merit, namely the *spin magnetic field* in z direction, $\hat{B}^z_{SOC} = \hat{s}^z B^z_{SOC}$, pointing upwards for spin-up electrons and downwards for spin-down electrons. It was first predicted by Dyakonov and Perel, 1971, and re-discovered by Hirsch, 1999, who introduced the name of "spin Hall effect". The spin-dependent extrinsic Mott scattering is at the heart of the emergence of SHE. As a result, a transverse spin current appears in response to passing a longitudinal electric current through the material. This leads to spin accumulation (i.e., magnetization) at the lateral boundaries and happens in the absence of any magnetic field.

One can describe the SHE in similar terms as the OHE. It is well-known that the SOC linear to kinetic momentum can be combined with kinetic energy and hence alternatively described by the spin gauge field as depicted in the work of Tokatly, 2008; Bernevig and Zhang, 2006; Berche et al., 2009. Hence, the spin transport associated with SOC, in general, can be vividly understood by a figure of merit, namely the *spin magnetic field*, which points in opposite directions for particles with different spins. Using this picture, in the steady-state, the SHE can be effectively described by the following extension to the Drude model:

$$\frac{\vec{v}_\pm}{\tau} = \frac{q}{m}\left[\vec{E} \pm \vec{v}_\pm \times \vec{z}B^z_{SOC}\right], \tag{1.2.16}$$

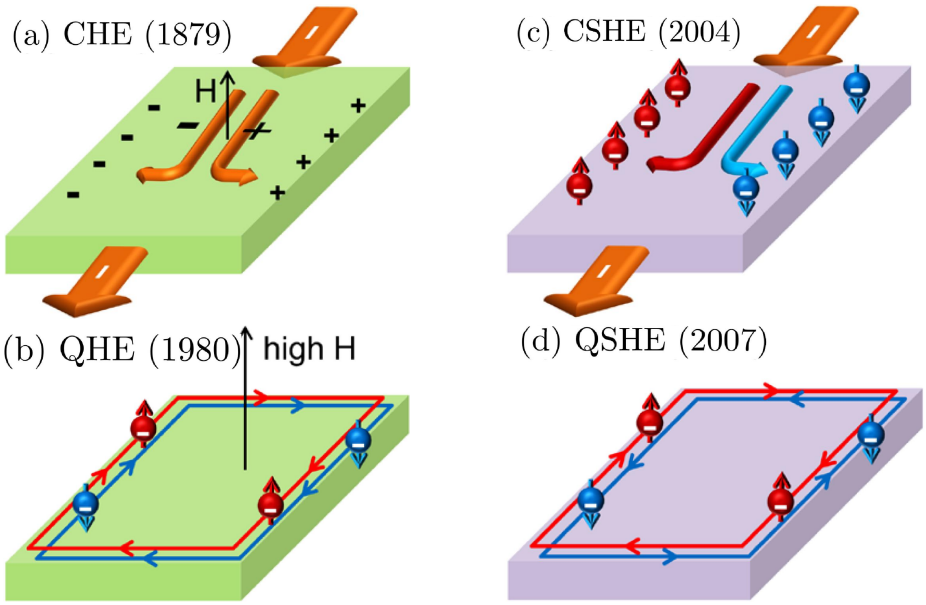

FIGURE 1.2: Members of the Hall effect family. (a) Classical Hall effect. (b) Quantum Hall effect. (c) Spin Hall effect. (d) Quantum Spin Hall effect. Numbers in parentheses indicate the years of each discovery. H is the external magnetic field. Figures come from Chang and Li, 2016.

where $\vec{v}_\pm$ is an drift velocity for the electrons with spin s ($s = 1$ for spin-up and $s = -1$ for spin-down electrons). The spin transport is described in FIGURE 1.2(c). Compared to the OHE, described by Eq. (1.2.15), the effective Lorentz force proportional to B_{SOC} in Eq. (1.2.16) has an opposite sign for carriers of different spins, which leads to the aforementioned spin accumulation at the lateral boundaries.

Phenomenologically, both OHE and SHE can be described by the time evolution of charge and spin current densities, J_c^j and J_s^{ja}, in steady state

$$\mathcal{D}\partial_j \mu_c + \theta_{OH}\epsilon^{jli} n^l J_c^i + \theta_{SH}^a \epsilon^{jai} J_s^{ia} = -J_c^j + \sigma E^j, \tag{1.2.17}$$

$$\mathcal{D}\partial_j \mu_s^a - \mathcal{D}\epsilon^{abc}\frac{e}{\hbar} A_j^b \mu_s^c + \theta_{OH}\epsilon^{jli} n^l J_s^{ia} + \theta_{SH}^a \epsilon^{jai} J_c^i = -J_s^{ja}, \tag{1.2.18}$$

where the conversion efficiency from longitudinal charge current to transverse charge and spin currents can be characterized by a figure of merit, namely the *ordinary and spin Hall angles*, respectively,

$$\theta_{OH} = \frac{e v_F B \tau}{\hbar k_F}, \tag{1.2.19}$$

$$\theta_{SH}^a = \frac{e v_F B_{SOC}^a \tau}{\hbar k_F}. \tag{1.2.20}$$

Here, the *spin magnetic field*, B^a_{SOC}, can be derived from both intrinsic and extrinsic SOC from a microscopic perspective (Tokatly, 2008; Zhang, Huang, and Cazalilla, 2019). τ is the Drude relaxation time. $\mathcal{D}$ is diffusion coefficient, σ is Drude conductivity, $\nu(\mu)$ is density of state at chemical potential μ. θ_C and θ^a_C are ordinary and spin Hall angles, respectively, which are induced by the real and spin magnetic field in $\vec{n}$ and $\vec{n}^a$ direction. For the sake of simplicity, I first switch off real magnetic field and begin with uniform case. Then Eqs. (1.2.17) and (1.2.18) reduce into

$$\vec{J}^j_c = \sum_a \theta^a_{SH} \vec{a} \times \vec{J}^a_s + \sigma \vec{E}, \tag{1.2.21}$$

$$\vec{J}^a_s = \theta^a_{SH} \vec{a} \times \vec{J}_c. \tag{1.2.22}$$

Eqs. (1.2.22) and (1.2.21) correspond to spin Hall effect and inverse spin Hall effect, respectively.

Being electrically neutral, direct detection of spin current is not easy, and their existence must be inferred in indirect ways. Averkiev and Dyakonov, 1983 proposed an indirect method to detect the SHE under optical spin orientation in semiconductors, which has been experimentally demonstrated by Bakun et al., 1984. The direct observation of SHE was realized more than 30 years later it was predicted. Electrically induced electron-spin polarization near the edges of a semiconductor channel was detected and imaged using Kerr rotation microscopy by Kato et al., 2004. Also, Wunderlich et al., 2005 reported the experimental observation of the spin-Hall effect in a 2D hole system, which allows an angle-resolved polarization detection at opposite edges. Moreover, Valenzuela and Tinkham, 2006 reported a direct and electrical measurement of the SHE in a diffusive metallic conductor, in which an induced voltage was observed, that results exclusively from the conversion of the injected spin current into charge imbalance through the inverse SHE. See more experimental demonstration in the review article of Sinova et al., 2015 and the references therein.

In addition to SHE, the SOC is also responsible for spin relaxation. In the next section, I discuss this issue.

1.2.3 Spin relaxation

Spintronics usage requires that the spin polarization of the electron ensemble in the device (such as a spin valve) can be retained sufficiently long. This is parameterized by the so-called spin-relaxation time characterizing the decay of spin polarization. At the end of this section, I discuss the origins of spin relaxation.

The time evolution of charge and spin densities, μ_c and μ^a_s, can be described by phenomenological equations

$$\partial_t \mu_c + \partial_j J^j_c = 0, \tag{1.2.23}$$

$$\partial_t \mu^a_s + \partial_j J^{ja}_s = -\frac{1}{\tau^a} \mu^a_s + \omega_L \epsilon^{abc} n^b \mu^c_s, \tag{1.2.24}$$

where τ^a is spin-relaxation time, and $\omega_L = g\mu_B B/\hbar$ is Larmor frequency describing the *Hanle precession*. The later is sketched in FIGURE 1.3, and describes a spin precession along the direction of magnetic field, as shown in the inset, when diffusing along the channel. It will induce a modulation of magnetoresistance and nonlocal resistance as I will explain in Sections 1.4 and 1.5, respectively.

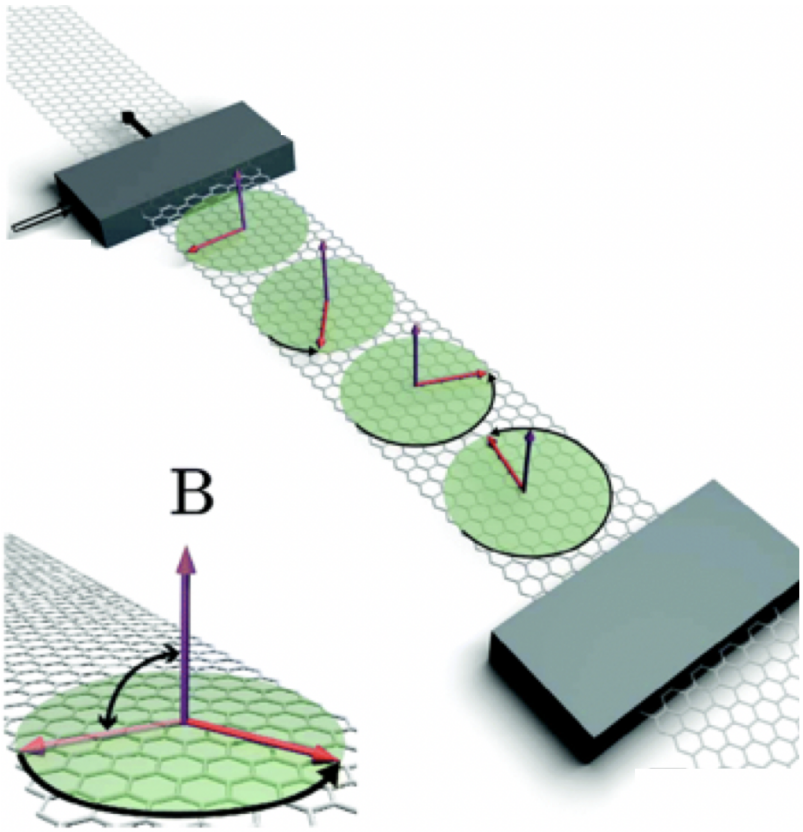

FIGURE 1.3: **Hanle effect**. Illustration of Hanle precession. Figure comes from Garcia et al., 2018.

The spin relaxation is caused by spin-flip processes and should be derived from a microscopic theory. Different mechanisms are responsible for spin relaxation (or spin-flip), as shown in FIGURE 1.4. Elliott, 1954; Yafet, 1963 revealed that itinerant electrons would undergo a spin-flip after many collisions with impurities inducing local SOC, as plotted in panel (a). In the materials without a center of symmetry, there exist sizable SOC, which, as I explained in subsection 1.2.1, is equivalent to a momentum-dependent *spin magnetic field*. In the presence of impurities inducing local scalar potential, the momentum is altered during the scattering, and hence the *spin magnetic field* changes as well. Consequently, the precession axis and frequency change randomly, as described by the panel (b). The contributions of the combination of SOC and scalar impurities to spin relaxations is referred to as the Dyakonov–Perel mechanism (D'yakonov and Perel, 1971; Dyakonov and Perel, 1972). Also, the mechanism proposed by Bir, Aronov, and Pikus, 1975 is sketched in panel (c). It origins from the efficient spin exchanges between electrons and holes in p-doped semiconductors. Note that the spin of a hole can relax very fast, and hence this exchange offers an indirect spin relaxation of conduction electrons. Furthermore, spin can also be flipped due to hyperfine interaction with the atomic nuclei, as shown in panel (d). Whereas SOC fundamentally causes the Elliott-Yafet, Dyakonov–Perel, and Bir-Aronov-Pikus spin relaxation. Another spin relaxation mechanism, which will be discussed in detail in Chapter 2, stems from the spin-exchange between itinerant electrons and local moments in magnetic insulators.

We now turn our focus on the valley degree of freedom. Specifically on the valley Hall effect.

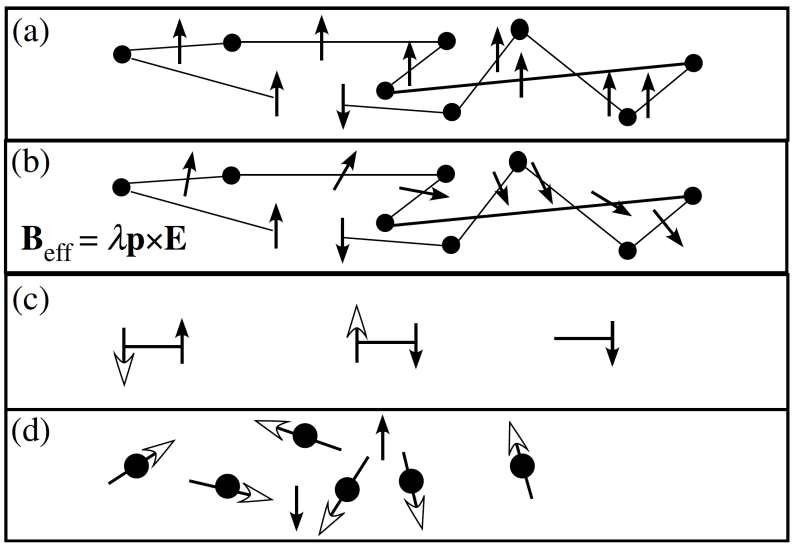

FIGURE 1.4: **Four mechanisms of electron spin relaxation in semiconductors resulting from spin-flip processes**. This figure was from Band and Avishai, 2013.

1.3 Valley Hall effect and valley relaxation

In this section, I introduce the origins of valley-orbit coupling (VOC) and discuss its contributions to the valley Hall effect (VHE) and valley relaxation in subsections 1.3.2 and 1.3.3, respectively.

1.3.1 Valley-orbit coupling

Xiao, Yao, and Niu, 2007; Yao, Xiao, and Niu, 2008 have theoretically predicted that the coupling between valley and orbit angular momentum can be realized in graphene when the sub-lattice inversion symmetry is broken. Experimentally, Gorbachev et al., 2014 first achieved this asymmetry by aligning graphene on top of hexagonal boron nitride. The presence of the substrate, breaking the sub-lattice inversion symmetry globally induces an energy difference between A and B sublattices

$$H_{\text{G}}^{2D} = \alpha_{\text{G}} \hat{\sigma}_z \, . \tag{1.3.25}$$

Consequently, an energy gap opens at the Dirac point, where the conduction and valence bands meet (Castro Neto et al., 2009; Katsnelson, 2012). We will see that the spatially homogeneous gap can be recognized as VOC, an analogy to the spatially homogeneous Kele Mele model to SOC introduced in subsection 1.2.1. Following the same way as the Kane-Mele SOC, we can obtain the Berry connection and Berry curvature density, which have an opposite sign for different valleys. The skewed motion induced by Berry curvature density is plotted in FIGURE 1.5 (a), where a finite Berry curvature density with an opposite sign at opposite valleys endows electrons with an anomalous velocity and leads to a valley-polarized current in bulk transverse to the applied electric field (Haldane, 2004; Xiao, Chang, and Niu, 2010).

Both SOC and VOC also have Berry curvature versions; the existence of spatially inhomogeneous Bernevig-Zhang SOC leads to the natural question if there is an inhomogeneous VOC. Here, I engineer this inhomogeneous VOC from shear strain in

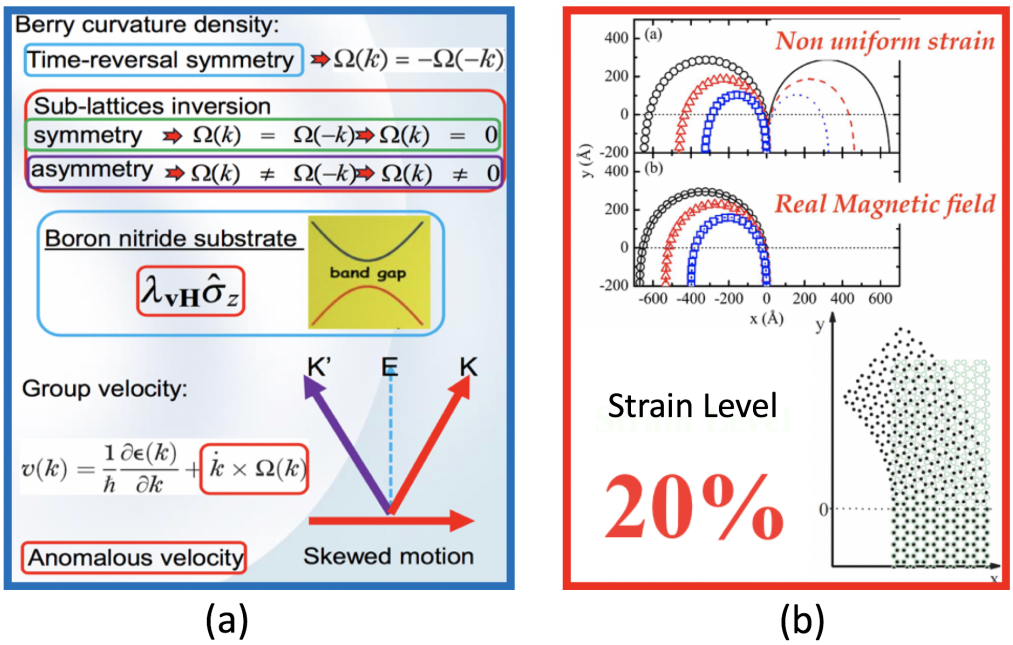

FIGURE 1.5: **The mechanisms responsible for valley-orbit coupling (VOC)**. (a) Berry curvature and anomalous velocity induced by substrate. (b) The SU(2) valley magnetic field generated by the non-uniform strain. Panels (a) and (b) are adapted from Gorbachev et al., 2014 and Chaves et al., 2010, respectively.

graphene. Within the $\vec{k}\cdot\vec{p}$ approximation to the band structure of graphene (see e.g. Katsnelson, 2012), the nonuniform (shear) strain can be described as a *valley gauge field* which takes opposite signs at opposite valleys (see e.g. Guinea, Katsnelson, and Geim, 2010; Vozmediano, Katsnelson, and Guinea, 2010; Katsnelson, 2012; Amorim et al., 2016):

$$H_0\left[\vec{k}-\frac{q}{\hbar}\vec{A}^z_{VOC}\hat{\tau}_z\right]=\hbar v_F\left[\hat{\tau}_z\hat{\sigma}_x(k_x-\frac{q}{\hbar}A^{x,z}_{VOC}\hat{\tau}^z)+\hat{\sigma}_y(k_y-\frac{q}{\hbar}A^{y,z}_{VOC}\hat{\tau}^z)\right]\,. \quad (1.3.26)$$

The valley-gauge field $\vec{A}^z_{VOC}(\vec{r})$ field which describes the (strain-induced) local displacement of the Dirac points at the two valleys, is given by the following expression:

$$\vec{A}^z_{VOC}(\vec{r})=(A^{x,z}_{VOC},A^{y,z}_{VOC})=\frac{\beta}{a}\left(u_{xx}-u_{yy},-2u_{xy}\right), \quad (1.3.27)$$

where $\beta=\frac{d\log t}{d\log a}\simeq 2$, t being the nearest neighbor hopping amplitude, a is the carbon-carbon distance, and

$$u_{ij}=\frac{1}{2}(\partial_i u_j+\partial_j u_i), \quad (1.3.28)$$

is the strain tensor. Note that, since u_{ij} is invariant (i.e. even) under time reversal and $\hat{\tau}_z\vec{A}^z_{VOC}$ is even under time reversal (recall that $\tau_z\to-\tau_z$ under time reversal). It can be combined with a linear energy spectrum and hence described by the valley gauge (magnetic) field. This is different from a real magnetic field, for which the gauge field is odd under time reversal. The pseudo-magnetic field that determines the valley Lorentz-like force, $\vec{F}^v_{\vec{k}}$ can be obtained from the standard expression:

$$\vec{B}^z_{VOC}\hat{\tau}_z=\nabla\times\vec{A}^z_{VOC}(\vec{r})\hat{\tau}_z=\hat{\tau}_z(\partial_x A^{y,z}_{VOC}-\partial_y A^{x,z}_{VOC})\,\vec{\hat{z}}\,. \quad (1.3.29)$$

Thus, as mentioned above, the pseudo-magnetic field $\hat{\tau}_z\vec{\mathcal{B}}_v$ induced by nonuniform strain has opposite signs at opposite valleys as required by the fact that strain does not break time-reversal invariance. In what follows, for the sake of simplicity, I shall assume that the pseudo-magnetic field $\hat{\tau}_z\vec{\mathcal{B}}_v$ is spatially uniform, which requires particular configurations of nonuniform strain (Guinea, Katsnelson, and Geim, 2010; Amorim et al., 2016; Zhang, Huang, and Cazalilla, 2017).

1.3.2 Valley Hall effect

In this subsection, I introduce the VHE in detail. As I discussed in subsection 1.3.1, there are two kinds of valley magnetic field, which results from spatially inhomogeneous and homogeneous VOC, respectively. The non-uniform strain causes the former. In contrast, the latter can be understood from the Berry curvature point of view.

In this subsection, I introduce the VHE in 2D materials. The mechanism responsible for VHE is the VOC mentioned above, which can be vividly described by a figure of merit, namely the *valley magnetic field* in z direction, $B^z_{VOC} = \tau^z B^z_{VOC}$, pointing upwards for valley-K electrons and downwards for valley-K' electrons in a two-dimensional electron gas (Mak et al., 2014; Zhang, Huang, and Cazalilla, 2017). In analogy to SHE, the VHE in graphene should also be captured by the following extension to the Drude model

$$\frac{\vec{v}_\pm}{\tau} = \frac{q}{m}\left[\vec{E} \pm \vec{v}_\pm \times \vec{z}(B^z_{VOC})\right], \tag{1.3.30}$$

where $\vec{v}_\pm$ is an drift velocity for the electrons with valley v ($v = 1$ for valley-K and $v = -1$ for valley-K' electrons). Here, the VOC is described by an effective valley magnetic field along the z-axis direction, which is described by τB^z_{VOC}. The corresponding physics are plotted in FIGURE 1.5 (b). For the real magnetic field, the cyclotron motion is merely happening on the left-hand side. For the valley magnetic field induced by the nonuniform strain, electrons with different valleys will undergo cyclotron motion on opposite sides. This is because in graphene and other 2D materials (Cazalilla, Ochoa, and Guinea, 2014; Pearce, Mariani, and Burkard, 2016) strain can be described as the valley gauge field, which induces an (Aharonov-Bohm-like) phase in real space. Thus, a direct consequence of the strain-induced gauge fields is the emergence of pseudo-Landau levels, whose experimental observation has been reported in both real (Levy et al., 2010; Shioya et al., 2015; Li et al., 2015) and artificial graphene systems (Gomes et al., 2012; Rechtsman et al., 2013). At the end of this subsection, I emphasize that the time evolutions of charge and valley current densities, J^j_c and J^{ja}_v, in steady-state are similar to Eqs. (1.2.17) and (1.2.18), respectively, where J^{ja}_s, μ^a_s and θ_{SH} are replaced by J^{ja}_v, μ^a_v and θ_{VH}. The latter is determined by the valley magnetic field B_{VOC}.

1.3.3 Valley relaxation

In this subsection, I briefly discuss the valley relaxation. As with spintronics, valleytronics' applications rely on the valley current and the decay of valley polarization, limited by valley relaxation. There are two main mechanisms responsible for valley relaxation. They are VOC and short-range disorders (Zhang, Huang, and Cazalilla, 2017). The mechanism associated with SOC is similar to spin relaxation induced by SOC. The latter can be understood from uncertainty principle in n dimensional system, $\Delta\vec{r}\cdot\Delta\vec{p} \geq \frac{\hbar^n}{2^n}$. The short-range disorder means small $\Delta\vec{r}$ and hence

large $\Delta\vec{p}$ to realized the valley-flip processes. Here, I emphasize that the time evolution of charge and valley densities, μ_c and μ_v^a, are described by similar equations as the spin ones, Eqs. (1.2.23) and (1.2.24), where μ_s^a and J_s^{ja} are replaced by μ_v^a and J_v^{ja}, respectively.

Being electrically neutral, direct detection of spin and valley Hall currents (effects) is impossible, and indirect methods must infer their existences. I discuss the experimental observations of Hall effects in heavy metal (HM)/magnetic insulator (MI) heterostructures and 2D Dirac materials in section 1.4 and section 1.5, respectively.

1.4 Spin-dependent transport in hybrid structures

In the first part of the thesis (Chapter 2-5), I will mainly study spin-dependent phenomena in hybrid HM/MI structures. A key effect in these systems is the spin Hall magnetoresistance (SMR) in HM/MI heterostructures, which I introduce in the next subsection 1.4.1, and which is addressed in detail in Chapters 2-4. In this introduction, I also discuss, subsection 1.4.2, the interplay between superconducting and magnetic proximity effects in hybrid nanowires (NWs) attached to superconductors. This will be the main focus of Chapter 5.

1.4.1 Spin Hall magnetoresistance in heavy metal/magnetic insulator heterostructures

This subsection aims to introduce the experimental detection of SHE using SMR. Because experiments are carried out in finite magnetic fields, it is unavoidable to address the interplay between SMR and other effects as the OHE and the Hanle precession.

Magnetoresistance (MR), just as its name implies, is the modulation of resistance by the magnetic field, $\vec{B}$. There are different mechanisms responsible for MR. The simplest origin of MR is the OH, explained in Section 1.2.2. The correction to the longitudinal charge current caused by the combination of OHE and inverse OHE reads

$$\delta\vec{J}_c = -\theta_{OH}^2\vec{J}_c^0. \tag{1.4.1}$$

The minus sign indicates that the OHE leads to an enhancement of the resistivity. The *ordinary Hall angle*, θ_{OH}, given by Eq. (1.2.19) is proportional to the magnetic field, and hence the correction is quadratic in the magnetic field.

The magnetic effect also couples to the spin of the electrons via the Zeeman effect. These effects may lead to a spin precession around the direction of the magnetic field; see FIGURE 1.3. However, the Zeeman term itself can not generate an MR effect because the charge current in a non-magnetic metal is not spin-polarized. Thus, to induce the MR effect from a magnetic field, the first and vital step is to create a spin current. There are two conventional ways to do that: i) by spin injection or ii) by spin Hall effect (SHE).

In this section, I focus on the SHE, whose physical picture was introduced in subsection 1.2.2. In a non-magnetic heavy metal (HM) with strong SOC, the spin

Hall current induced by the SHE, reads from (1.2.18)

$$\vec{J}_s^a(\vec{r}) = -\underbrace{\mathcal{D}\vec{\nabla}\mu_s^a(\vec{r})}_{diffusive\ current} + \underbrace{\theta_{SH}\vec{a}\times\vec{J}_c}_{drift\ current}. \tag{1.4.2}$$

The first term on the right-hand side is the diffusive spin current stemming from a spatially inhomogeneous spin density. The second term describes the spin Hall current from SOC. Need to say, the origin of SOC in heavy metal is rather complicated. There are so many possibilities of nonuniform potentials. For instance, the periodic crystal potential leads to intrinsic SOC, and the external potential from the imperfections induces extrinsic SOC (Sagasta et al., 2016). Independently of its origin, the SOC can be properly included by a single phenomenological parameter, the spin Hall angle, θ_{SH}, which enters the second term in the right-hand side of Eq. (1.4.2). The resulting spin Hall current, as shown in Eq. (1.2.17), can be converted back into charge current by the inverse SHE,

$$\vec{J}_c(\vec{r}) = \vec{J}_c + \theta_{SH}\vec{a}\times\vec{J}_s^a(\vec{r}) = \underbrace{(1-2\theta_{SH}^2)\vec{J}_c}_{drift\ current} - \underbrace{\theta_{SH}\mathcal{D}\vec{a}\times\vec{\nabla}\mu_s^a(\vec{r})]}_{diffusive\ current}. \tag{1.4.3}$$

Let us consider a HM which is homogeneous in the (x,y) plane and is assumed to be thin enough in z direction. We thus, can average expression (1.4.3) over the z direction

$$\vec{J}_c = \frac{1}{d_N}\int_0^{d_N} dz\vec{J}_c(z), \tag{1.4.4}$$

where d_N is the thickness of the HM. By substitution of Eq. (1.4.3), Eq. (1.4.4) becomes

$$J_c^x = (1-2\theta_{SH}^2)\sigma_D E - \theta_{SH}\frac{\mathcal{D}}{d_N}[\mu_s^y(d_N) - \mu_s^y(0)], \tag{1.4.5}$$

$$J_c^y = \theta_{SH}\frac{\mathcal{D}}{d_N}[\mu_s^x(d_N) - \mu_s^x(0)], \tag{1.4.6}$$

where the electric field is assumed to be in x direction. I find in this way that the MR can be expressed in terms of the edge spin accumulation (Dyakonov, 2007). Ultimately, we build the connection between longitudinal (transverse) charge currents and spin accumulation at both edges $\mu_s^y(0,d_N)$ and $\mu_s^x(0,d_N)$, respectively. Here I emphasize that Eqs. (1.4.5) and (1.4.6) are general and valid for any nanostructures with the above planar symmetry.

Thus, in order to obtain the resistivity, one needs to solve the diffusion equation for the non-equilibrium spin bias $\vec{\mu}_s$

$$\nabla_{\vec{r}}^2\mu_s^\upsilon(\vec{r}) = \ell_S^{-2}\delta_{\upsilon\nu}\mu_s^\nu(\vec{r}) - \ell_B^{-2}\epsilon_{\upsilon\kappa\nu}n_\kappa\mu_s^\nu(\vec{r}). \tag{1.4.7}$$

$\ell_S = \sqrt{\mathcal{D}\tau_S}$ and $\ell_B = \sqrt{\mathcal{D}/\omega_B}$ are the spin-diffusion and magnetic-field lengths, respectively, where τ_S is spin relaxation time and ω_B is Larmor frequency.

A simple way of modulating the edge-spin accumulation is by an external magnetic field by the Hanle precession. The corresponding MR effect is the so-called Hanle magnetoresistance (HMR). It was experimental demonstrated in Platinum (Pt) by Vélez et al., 2016b, and will be carefully explained in Chapter 2.

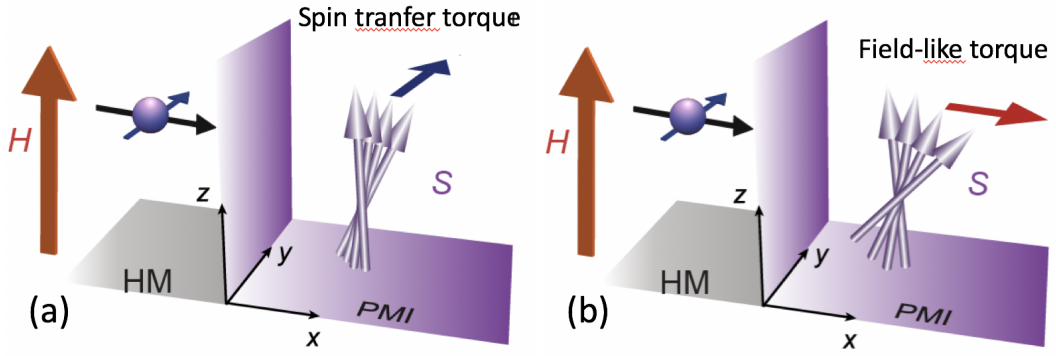

FIGURE 1.6: **Spin-transfer torque (STT) and field-like torque (FLT) at heavy metal/paramagnetic insulator (HM/PMI) interface**. The blue arrow in panel (a) and red arrow panel (b) represent the torque direction related to the STT and FLT, respectively. Obviously, STT keeps the spin polarization of itinerant electrons in NM, while FLT will changes similar to magnetic field. Here, H and S represent the applied magnetic field and the localized spin in PMI, respectively. Figures are adapted from Oyanagi et al., 2020.

The spin accumulation at edges can also be tuned by magnetic moments localized at an interface. I focus on the MR effect originated from the spin-dependent scattering of electrons at local magnetic moments from, for example, a MI. Such spin-dependent scattering is at the origin of many phenomena, from spin pumping (Burrowes et al., 2012; Heinrich et al., 2011; Mosendz et al., 2009) to spin Seebeck effect (Uchida et al., 2010a; Uchida et al., 2010b; Uchida et al., 2014) and spin Hall magnetoresistance (Isasa et al., 2016; Marmion et al., 2014; Vélez et al., 2016a; Nakayama et al., 2013; Kosub et al., 2018; Althammer et al., 2013; Vlietstra et al., 2013a; Ganzhorn et al., 2016; Hahn et al., 2013; Isasa et al., 2014; Hou et al., 2017). Theoretically, the spin transport at the HM/MI can be captured by the widely used boundary condition (Brataas, Nazarov, and Bauer, 2001):

$$-e\vec{J}_{s,z} = G_r\vec{M}\times(\vec{M}\times\vec{\mu}_s) + G_i\vec{M}\times\vec{\mu}_s. \tag{1.4.8}$$

where $\vec{\mu}_s$ is the electron spin of the HM, induced for example from SHE, and $\vec{M}$ is the magnetization of the MI. Here the spin current at magnetic interface is described by the phenological parameter, spin-mixing conductance $G_{\uparrow\downarrow} = G_r + iG_i$ (Brataas, Bauer, and Kelly, 2006a; Jia et al., 2011). The real and imaginary parts of the spin-mixing conductance originate from torques that the electron spins of the HM exert to the magnetization of the MI when both are noncollinear. On the one hand, G_r is determined by the spin-transfer torque (STT), which is collinear to the spin polarization of injected electrons as depicted in FIGURE 1.6 (a). It is an important quantity in STT magnetic random-access memory devices, currently ready for mass production (Liu and Yu, 2019). On the other hand, G_i describes the interfacial exchange field of the electron spins of the NM induced by the magnetic moments of the MI, which behaves as a field-like torque (FLT), as sketched FIGURE 1.6 (b). The interfacial exchange field (or magnetic proximity effect) is very relevant in different areas of spintronics. For instance, when the NM is a superconductor below its critical temperature, the exchange field leads to a spin-split density of states, as shown in FIGURE 1.9, even without an external magnetic field (Moodera et al., 1988; Li et al., 2013; Strambini et al., 2017; Rouco et al., 2019). Such spin splitting in superconductors are subjected to intense research (Bergeret et al., 2018; Heikkilä et al., 2019) because of their possible applications in cryogenic memories (De Simoni et

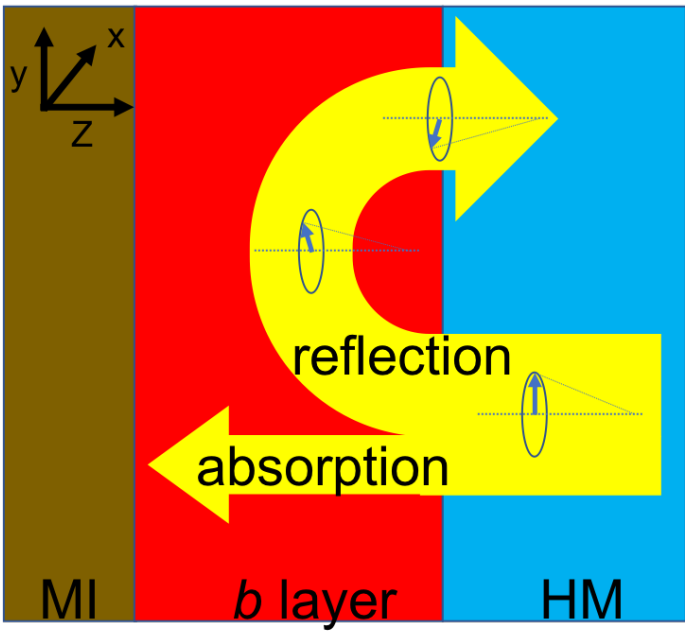

FIGURE 1.7: **Spin absorption and Hanle precession at HM/MI interface**. Illustration of spin reflection and absorption of spin currents, which are indicated by the straight and curved arrows, respectively. The later is due to the spin-dependent scattering from the local magnetic moments. In addition, the spins will process when they are propagating inside b layer.

al., 2018), thermoelectric detectors (Heikkilä et al., 2018), superconducting spintronics and caloritronics (Linder and Robinson, 2015; Giazotto, Heikkilä, and Bergeret, 2015). This interfacial exchange field has also been used to induce ferromagnetism in graphene (Wei et al., 2016; Leutenantsmeyer et al., 2016).

As discussed above, the spin-mixing conductance is of significance in many fields of spintronics. Then, a natural question that arises is how to quantify the interfacial spin-mixing conductance in a HM/MI heterostructure? For this sake, the spin Hall magnetoresistance (SMR) is a simple yet powerful technique. Adjacent to a MI, the HM with a sizable SOC can inject spin Hall current into HM/MI interface via the SHE. The SMR then manifests as a modulation of the HM resistivity with the relative orientation between the magnetization in the MI and the spin accumulation at the HM/MI interface (Nakayama et al., 2013; Chen et al., 2013). We can observe the typical oscillation of SMR, which is plotted in FIGURE 1.8 (b-c,e-f).

The SMR can be explained by the reflection and absorption of spin current at HM/MI interface. Though the itinerant electrons can not flow into the MI, they will experience a spin-dependent scattering caused by the local moments at NM/MI interface. To qualitatively understand these spin-dependent scattering, one can assume a thin enough b layer between HM and MI as plotted in FIGURE 1.7, in which itinerant electrons and magnetic moment of MI coexist (Zhang, Bergeret, and Golovach, 2019). The spin current at HM/MI interface is described by the spin-mixing conductance as shown in Eq. (1.4.8) and is equal to the reflected spin current plus injected spin current. The latter is induced by the SHE in the HM. When $\vec{\mu}_s \parallel \vec{M}$, as shown in Eq. (1.4.8), the spin current at HM/MI interface is zero, *i.e.*, $\vec{J}_{s,z} = 0$, which means spin current is fully reflected back into NM and converted back into longitudinal charge current. Thus, the SMR exhibits a minimum. On the contrary, when $\vec{\mu}_s \perp \vec{M}$, as shown in Eq. (1.4.8), the spin current at HM/MI interface is finite,

i.e., $\vec{J}_{s,z} \neq 0$, which means only part of the spin current is reflected into HM and hence partially converted into charge current. Thus, in this case, the SMR exhibits a maximum. As a result, the SMR appears as an oscillation of the HM resistivity, which follows the relative orientation between the magnetization in the MI and the spin-Hall induced spin accumulation in the HM, as shown in FIGURE 1.8. This modulation is a direct manifestation of the SHE in a NM in contact with a MI in NM/MI structures (Isasa et al., 2016; Althammer et al., 2013; Huang et al., 2012).

Although the theory of SMR is well established by Nakayama et al., 2013; Chen et al., 2013, and provides an accurate qualitative description of the effect, it does not describe the dependence of the resistivity on the strength of the applied magnetic field B, nor on the temperature T. The spin mixing conductance components, entering Eq. 1.4.8, are at the heart of the SMR effect and have been regarded as phenomenological parameters in each experiment. Recent experiments by Meyer et al., 2014; Vélez et al., 2019b; Das et al., 2019 show, however, that the SMR effect strongly depends both on B (Vélez et al., 2019b) and on T (Meyer et al., 2014; Vélez et al., 2019b; Das et al., 2019, see FIGURE 1.8), and that the magnetic state of the MI plays a crucial role. Furthermore, the magnetic field alone leads to the Hanle magnetoresistance (HMR) (Dyakonov, 2007; Vélez et al., 2016b), which has an identical angular dependence to SMR Vélez et al., 2016b, but does not require a MI. Even though SMR and HMR have different origins, they cannot always be easily separated in experiments, which adds to the uncertainties of interpreting the experimental data. In Chapter 2, I will present a fully microscopic theory of the SMR in HM/MI heterostructures, which provides a full description of MR experiments. I will apply this model to explore the SMR in different situations, including paramagnetic and ferromagnetic insulators attached to heavy metal. Specifically, I will present the results for Platinum/Gd3Ga5O12 (Pt/GGG) in Chapter 3 and Platinum/Europium sulfide (Pt/EuS) in Chapter 4.

Finally, it is important to emphasize that the sizable interfacial exchange field is responsible for the magnetic proximity effect in superconductor/magnetic insulator structures. This effect is very relevant in search of a topological non-trivial superconducting state in hybrid structures (Virtanen et al., 2018; Liu et al., 2019a; Vaitiekėnas et al., 2020), which should read to Majorana bound states. In the next section, I provide a brief introduction to the magnetic proximity effect in superconducting layers. A detailed discussion of this topic is presented in Chapter 5.

1.4.2 Superconducting and magnetic proximity effects in nanowires

Replacing the HM by the nanowire (NW) in proximity to a superconductor (SC), we reach the state-of-the-art hybrid structures for the implementation of Majorana zero modes (MZM). This subsection focuses on introducing the coexistence of superconducting and magnetic proximity effects in proximitized NWs and films.

Semiconducting NWs in proximity with SCs are crucial to the generation of topological superconductivity, which is demonstrated by the appearance of MZMs at the edges of the NWs (Lutchyn, Sau, and Sarma, 2010; Oreg, Refael, and Oppen, 2010; Mourik et al., 2012; Rokhinson, Liu, and Furdyna, 2012; Das et al., 2012; Finck et al., 2013; Albrecht et al., 2016; Deng et al., 2016; Suominen et al., 2017; Nichele et al., 2017; Takei et al., 2013; Chang et al., 2015; Lutchyn, Stanescu, and Sarma, 2011). The keys to the topologically non-trivial phase are the SOC, superconducting correlations, and Zeeman splitting (Qi and Zhang, 2011; Elliott and Franz, 2015; Beenakker, 2013; Alicea, 2012; Lutchyn et al., 2018; Sarma, Freedman, and Nayak, 2015; Stanescu and Tewari, 2013).. In contrast, SOC and superconductivity are intrinsic properties of

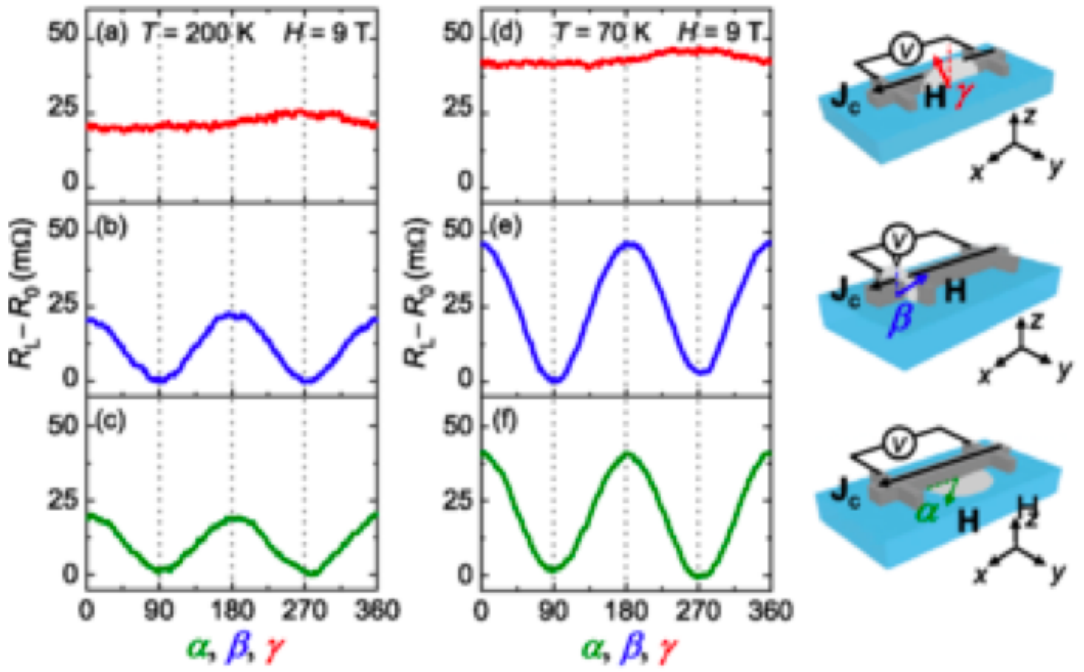

FIGURE 1.8: Spin Hall magnetoresistance. The modulation of SMR with the direction of magnetic fields rotating around (a,d) y, (b,e) x and (c,f) z directions. Panels (a-c) correspond to temperature T = 100K, while the panels (d-f) correspond to temperature T = 70K. Figure comes from Vélez et al., 2019b.

the materials, the Zeeman splitting is usually generated by applying a rather large magnetic field (Lutchyn, Sau, and Sarma, 2010; Oreg, Refael, and Oppen, 2010), which introduces technical limitations on the use of superconducting elements.

Alternatively, such a spin splitting can be generated without applying an external field by the magnetic proximity effect from a magnetic insulator (Bergeret et al., 2018; Giazotto and Taddei, 2008; Yang et al., 2013; Eremeev et al., 2013; Virtanen et al., 2018; Wei et al., 2016; Katmis et al., 2016). As shown in FIGURE 1.9, a Zeeman-like splitting at zero magnetic field has been observed in superconducting Al layers in contact with the ferromagnetic insulator (FI) EuS (Hao, Moodera, and Meservey, 1991; Meservey, Tedrow, and Fulde, 1970; Hao, Moodera, and Meservey, 1990; Strambini et al., 2017; Moodera et al., 1988; Rouco et al., 2019). Furthermore, Liu et al., 2019b reported the first hybrid epitaxial growth of InAs NWs in proximity with EuS and Al. Even though the experiment is inconclusive concerning Majorana physics, the NWs show the coexistence of the proximity-induced superconducting gap and spin splitting. Recently, Vaitiekėnas et al., 2020 have reported the experimental measurement of zero-field topological superconductivity in ferromagnetic hybrid NWs. These proximitized NWs are pivotal in the study of the topological superconductivity (Sau et al., 2010; Lee, Alicea, and Refael, 2012; Livanas, Sigrist, and Varelogiannis, 2019).

The emergence of MZMs at a certain critical value of a control parameter is necessarily accompanied by closing the bulk gap, which requires the demanding control of spin split induced by a magnetic field or the interfacial exchange field. In Chapter 5, I will explore NW and films in proximity to both SCs and MIs. I will study the

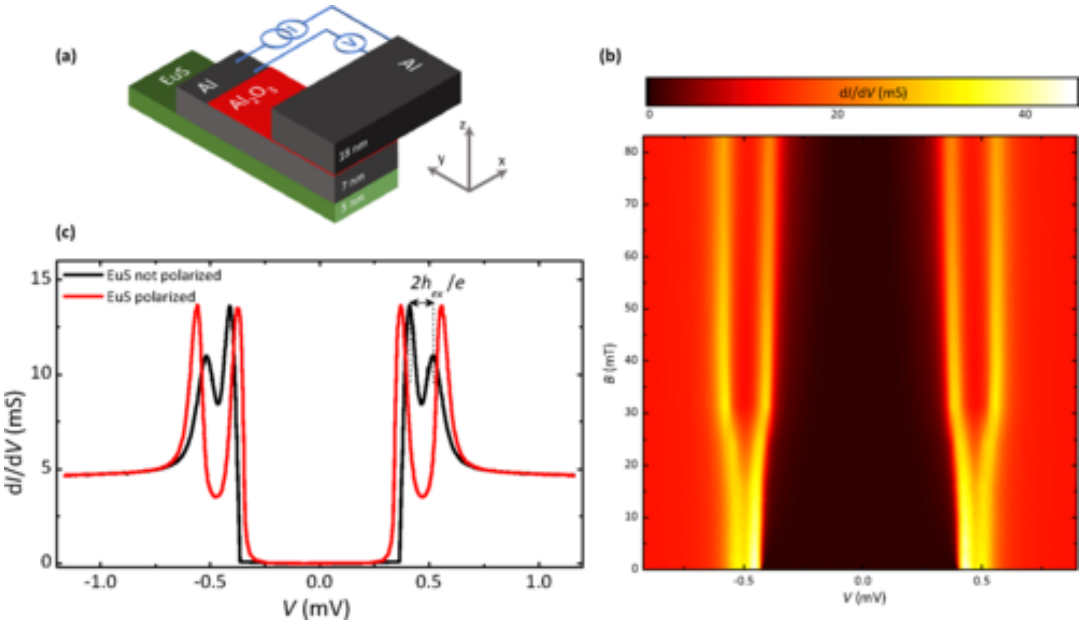

FIGURE 1.9: **Spin-splitting field in superconductor/ferromagnetic insulator heterostructure**. (a) Sketch of the cross bar forming the EuS/Al/Al_2O_3/Al vertical tunnel junction. (b) Evolution of the differential conductance, obtained from the numerical derivative of the curves, as a function of the voltage drop V and in-plane magnetic field B. (c) Comparison between the differential conductance of the tunnel junction measured at zero field before (black curve) and after (red curve) the magnetization of the EuS layer. All the measurements were taken at 25 mK. Adapted from Strambini et al., 2017.

nonlocal magnetization induced by the interplay of superconducting and magnetic proximity effects in terms of the interface parameters presented in chapter 2. I will also explore the possibility of controlling the exchange field in the NW by tuning the phase difference between two superconductors.

1.5 Spin- and valley-dependent transport in 2D Dirac materials

In the second part of the thesis (Chapter 6-7), I will concentrate on the spin- and valley-dependent transport in 2D Dirac materials, for instance, graphene, TMDs, and van der Wassls heterostructures. These materials provide a platform for the experimental observations of SHE and VHE using nonlocal transport measurements (Qian et al., 2014; Xu et al., 2014; Gorbachev et al., 2014).

Let us start with the definition of nonlocal resistance (NLR) in the 2D Hall bar device plotted in FIGURE 1.10. Driving an electric current between the two opposite right-hand side contacts of the device, transverse spin (valley) current is generated via SHE (VHE) (see detailed explanations of SHE and VHE in Subsections 1.2.2 and 1.3.2, respectively). The spin (valley) current diffuses in the direction perpendicular to the applied electric field, and they are converted back into electric current through inverse SHE (VHE), which leads to charge accumulation and a nonlocal voltage on the left-hand side of the device. The nonlocal resistance (NLR) is defined as the ratio of the nonlocal voltage, $V_{\rm nl}$ to the external current applied to the device, I (Abanin et al., 2009).

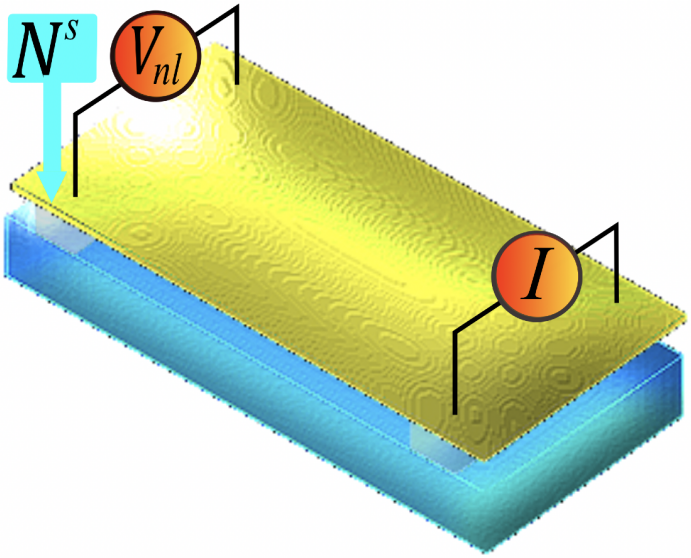

FIGURE 1.10: **Detection of nuetural currents**. The sketch of a Hall-bar device used for measuring nonlocal resistance, R_{nl}. It is defined as the ratio of the (non local) voltage V_{nl} detected in the right side and the injection current in the left side I, *i.e.*, $R_{\mathrm{nl}} \equiv V_{\mathrm{nl}}/I$.

NLR's earlier experiments on 2D Dirac materials concentrate on the phenomena associated with the spin degree of freedom (Balakrishnan et al., 2014; Balakrishnan et al., 2013). During the propagation in the channel, the spin of electrons undergoes a Hanle precession along the direction of the magnetic field, as plotted in FIGURE 1.3. A manifestation of the SHE in Hall-bar device is *Hanle oscillation*, that is, the oscillation of the NLR as a function of an in-plane magnetic field shown in FIGURE 1.11. It is considered to be the hallmark of the existence of spin currents (Balakrishnan et al., 2014; Balakrishnan et al., 2013; Huang, Chong, and Cazalilla, 2017; Abanin et al., 2009). Using this setup, the SHE has been experimentally observed in graphene decorated with absorbates (Balakrishnan et al., 2014; Balakrishnan et al., 2013; Weeks et al., 2011; Ma, Li, and Yang, 2012), TMD with sizable intrinsic SOC (Qian et al., 2014) and graphene-TMDs heterostructures (Avsar et al., 2014; Safeer et al., 2018; Benítez et al., 2018).

1.5.1 The controversy of the origin of nonlocal resistance

However, as indicated in FIGURE 1.12 (a), the absence of the Hanle effect in some experiments in which a large enhancement of the NLR was observed (Völkl et al., 2018; Kaverzin and Wees, 2015; Wang, Cai, and Reutt-Robey, 2015) hints at the existence of additional contributions to the NLR that are insensitive to the magnetic field. Furthermore, some recent simulations of Van Tuan et al., 2016 indicate the existence of a non-local signal in the absence of SOC, as shown in FIGURE 1.12 (b).

One candidate that can contribute to the NLR is a valley current. In Chapter 6, I will investigate the NLR induced by the VHE from the nonuniform strain present in the Hall bar device. Modest strain could generate huge VHE, as I explained in 1.3.1. Additionally, it is worth mentioning that the strain-induced valley Hall currents predicted here are neutral currents that do not couple to external magnetic fields. Therefore, unlike spin currents (Abanin et al., 2009; Balakrishnan et al., 2014), valley currents will not display Hanle precession. Indeed, a nonuniform strain may

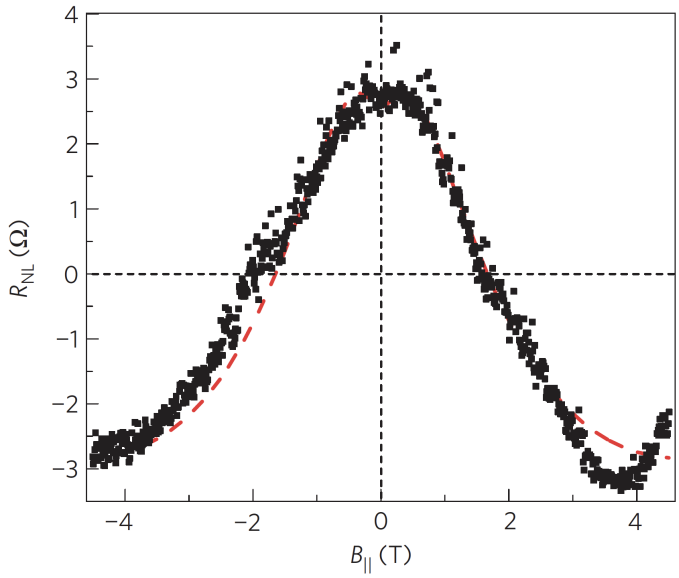

FIGURE 1.11: **Hanle oscillation**. Nonlocal resistance as a function of in-plane magnetic field. Figure comes from Balakrishnan et al., 2013.

have been introduced unintentionally during device preparation in the studies reported by Kaverzin and Wees, 2015; Wang, Cai, and Reutt-Robey, 2015.

1.5.2 The indivisibility of spin and valley transport

Previous theoretical studies of nonlocal transport have concentrated either on the VHE (Beconcini, Taddei, and Polini, 2016; Zhang, Huang, and Cazalilla, 2017; Song and Vignale, 2018) or on the SHE (Abanin et al., 2009; Huang, Chong, and Cazalilla, 2017). However, symmetry considerations imply that spin and valley are coupled in materials with broken spin-rotation and/or inversion symmetry (Xiao et al., 2012). For instance, in order to obtain the VHE, we are required to break inversion (or sublattice) symmetry, which also lifts the spin degeneracy of energy bands and hence results in the presence of both Rashbar and Dresselhaus SOC (Rashba and Sheka, 2015; Dresselhaus, 1955). On the other hand, with the knowledge of time-reversal symmetry, the spin splitting in different valleys must be the opposite. Hence, the valley carriers can also be distinguished by their spin moments (Feng et al., 2012). This is the basis of coupled spin and valley physics, and hence one is inevitably required to study the interplay between VHE and SHE.

Furthermore, the coexistence of SHE and VHE can be realized in an extrinsic way. To generate SHE by heavy adatoms inducing extrinsic SOC, the strain is unavoidable, which, as I discussed in the last subsection, is the ingredient of VHE. In Chapter 7, we will study the interplay of SHE and VHE in graphene with strain (VHE) and adatoms (SHE). It has emerged as one of the most promising platforms to integrate both spintronics and valleytronics.

1.6 Overview of this thesis

For the sake of consistency, I divided the thesis into two parts. The results presented in this thesis are divided into two parts. In Part I (Chapters 2-5), I work on the spin transports in a hybrid structure. While, in Part II (Chapters 6-7), I study the spin and valley transports in two dimensional materials.

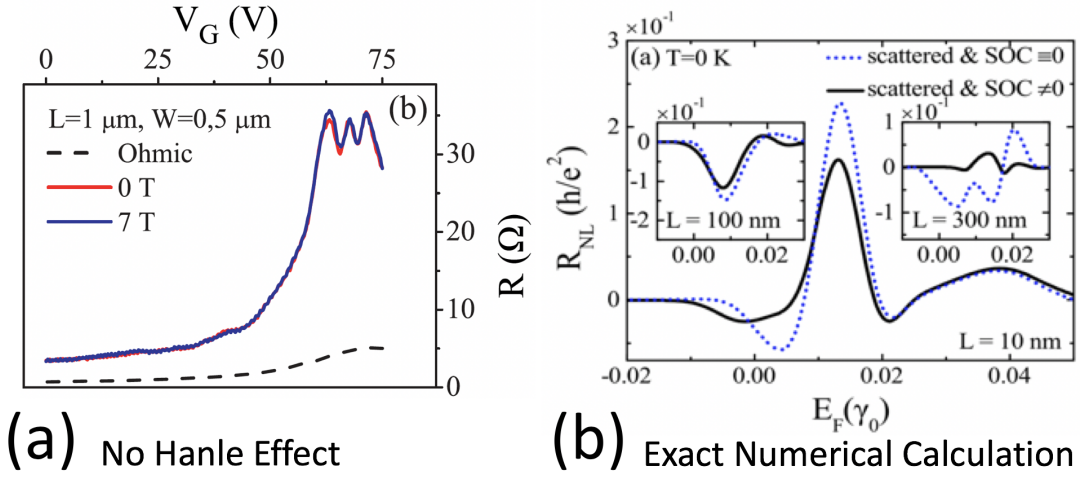

FIGURE 1.12: **The controversy about the origin of non-local resistance**. (a) NLR as a function of basis for different in-plane magnetic field. (b) Exact numerical calculation of NLR for SOC= 0 and SOC $\neq$ 0. Panels (a) and (b) are adapted from Kaverzin and Wees, 2015 and Van Tuan et al., 2016, respectively.

- In Chapter 1, I begin with a general introduction from electronics to spintronics and valleytronics. Next, I review a few significant Hall effects, for instance, the ordinary Hall effect (OH), the spin and valley Hall effects (SHE/VHE). Then, we introduce the background and motivations of spin Hall magnetoresistance (SMR) in heavy metal (HM) and nonlocal resistance (NLR) in 2D Dirac materials.

Part I. Spin transports in non-magnetic metal/magnetic insulator heterostructure

- In Chapter 2, I develop a microscopic theory of the SMR of metals in contact with magnetic insulators. First, I express the spin mixing conductance, which governs the phenomenology of the effect, in terms of the microscopic parameters of the interface and the spin-spin correlation functions of the local moments on the magnetic insulator's surface. Second, the magnetic field and temperature dependence of the spin mixing conductances leads to a rich resistance behavior due to an interplay between the Hanle effect and the spin mixing at the interface. Third, I describe an unusual negative magnetoresistance originating from a non-local Hanle effect.

- In Chapter 3, we report the first observation of the SMR in a Pt film on top of a paramagnetic insulator $Gd_3Ga_5O_{12}$ (GGG). First, the SMR signal exhibits clear saturation behavior by applying large magnetic fields at low temperatures, consistent with its paramagnet-like magnetization curve. Second, we use the microscopic theory of SMR to relate the observed signal to the spin-mixing conductance at the interface, where we find that the field-like torque contribution (G_i) is as important as the spin-transfer torque contribution (G_r) in Pt/GGG interface. Third, we can quantify the exchange interaction between conduction electrons in Pt and $4f$ localized spins in Gd^{3+}.

- In Chapter 4, we report the first measurement of the spin Hall magnetoresistance (SMR) of Pt on top of a purely ferromagnetic insulator Europium sulfide (EuS). First, we have demonstrated SMR measurements in a wide range of temperatures and fitted the results using a microscopic model. Second,

we extracted the temperature dependence of the spin-dependent conductance (G_s, G_r and G_i), disentangling the contribution of field-like torque (G_i), spin-transfer torque (G_r), and spin-sink conductance (G_s). Third, an interfacial exchange field of the order of 1 meV acting upon the conduction electrons of Pt can be estimated from G_i, which is at least three times larger than G_r below the Curie temperature.

- In Chapter 5, I study the magnetic and superconducting proximity effects in a nanowire (NW) and film attached to superconducting leads and a ferromagnetic insulator (FI). I show that a sizable equilibrium spin polarization arises in the NW and film due to the interplay between the superconducting correlations and the FI's exchange field. The resulting magnetization has a nonlocal contribution that spreads in the NW and film over the superconducting coherence length and is opposite in sign to the local spin polarization induced by the magnetic proximity effect in the normal state. For a Josephson-junction setup, I show that the nonlocal magnetization can be controlled by the superconducting phase bias across the junction.

Part II Spin and valley Hall effects in two dimensional Dirac materials

- n Chapter 6, I study the classical valley Hall effect from the non-uniform strain. First, I provide a theory of the strain-induced VHE starting from the quantum Boltzmann equation. This allows us to show that averaging over short-range impurity configurations destroys quantum coherence between valleys, leaving the elastic scattering time and inter-valley scattering rate as the only parameters characterizing the transport theory. Second, I show that, with modest levels of strain, graphene can also sustain a classical valley Hall effect (VHE) that can be detected in nonlocal transport measurements. Third, I compute the nonlocal resistance of a Hall bar device in the diffusive regime using our theory.

- In chapter 7, I study the interplay of spin and valley Hall effect in 2D Dirac materials. First, I demonstrate the emergence of an additional longitudinal neutral current that is both spin and valley polarized. Second, I prove that this additional neutral current allows the spin density control by tuning the magnitude of the valley Hall effect. Third, the interplay of the two effects can suppress the Hanle effect, that is, the oscillation of the nonlocal resistance in an in-plane magnetic field.

Part I

Spin transports in normal metal/magnetic insulator heterostructure

Chapter 2

Microscopic Theory of Spin Hall Magneto-resistance

2.1 Introduction

The spin-orbit coupling (SOC), as discussed in subsection 1.2.1, leads to a conversion between the charge and spin currents in metals and semiconductors, which results in the spin Hall effect (SHE) and its inverse effect (D'Yakonov and Perel, 1971; Dyakonov and Perel, 1971; Hirsch, 1999; Sinova et al., 2004; Valenzuela and Tinkham, 2006; Kimura et al., 2007; Kato et al., 2004; Sih et al., 2005; Wunderlich et al., 2005; Zhou et al., 2018; Maekawa and Kimura, 2017; Sinova et al., 2015; Nakayama et al., 2016). A manifestation of the SHE in a normal metal (NM) is a modulation of the magnetoresistance (MR) concerning the direction of the applied magnetic field when the metal is in contact with a magnetic insulator (MI) in NM/MI structures (Isasa et al., 2016; Althammer et al., 2013; Huang et al., 2012). This effect, called the spin Hall magnetoresistance (SMR), has been observed in several experiments (Weiler et al., 2012; Nakayama et al., 2013; Avci et al., 2015; Hahn et al., 2013; Dejene et al., 2015). As explained in subsection 1.4.1, the origin of the SMR is the absorption and reflection of spin current at the NM/MI interface, which depends on the angle between the polarization of spin Hall current and the magnetization of the MI (Nakayama et al., 2013; Chen et al., 2013). The latter can be controlled by an external magnetic field.

The previous theory of SMR, established by Nakayama et al., 2013; Chen et al., 2013 and discussed in subsection 1.4.1, merely offers a qualitative description of the effect, where spin-mixing conductance, which is at the heart of the SMR effect, have traditionally been regarded as phenomenological parameters. The microscopic mechanisms of the spin-mixing conductance are still not well understood, and their calculations were thought to be a formidable task, which could only be carried out by ab initio methods (Jia et al., 2011; Carva and Turek, 2007; Zhang, Hikino, and Yunoki, 2011; Xia et al., 2002; Dolui, Bajpai, and Nikolic, 2019). In addition, this theory can not describe the dependence of the resistivity on the strength of the applied magnetic field B, nor on the temperature T. However, recent experiments of Meyer et al., 2014; Vélez et al., 2019b; Das et al., 2019 show that the SMR effect strongly depends both on B (Vélez et al., 2019b) and on T (Meyer et al., 2014; Vélez et al., 2019b; Das et al., 2019), and that the magnetic state of the MI also plays an important role in SMR. Moreover, the magnetic field alone leads to the Hanle magnetoresistance (HMR) (Dyakonov, 2007; Vélez et al., 2016b), discussed in subsection **??**, which contributes further to the measured signal. Obviously, HMR has an identical angular dependence to SMR (Vélez et al., 2016b; Vélez et al., 2019b), but do not require an MI. Despite the fact that SMR and HMR have totally different origins, they cannot always be easily separated in experiments because they can only work on angular

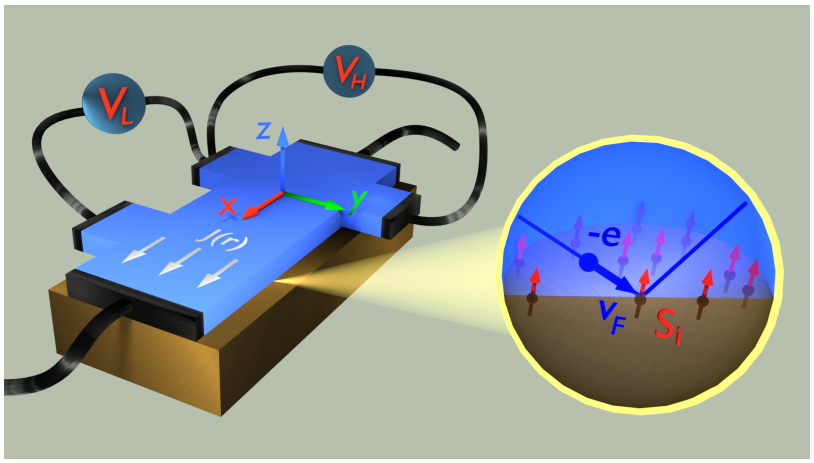

FIGURE 2.1: Sketch of a Hall bar fabricated from a thin metallic film (blue) deposited on the surface of a magnetic insulator (brown). The longitudinal (V_L) and Hall (V_H) voltages are sensitive to variations of the charge current occurring under the influence of the spin-dependent scattering at the interface. The inset shows the basic process responsible for SMR: an electron with charge $-e$ and Fermi velocity v_F moving randomly in the metal scatters off the surface of the magnetic insulator and interacts with a local moment $\vec{S}_i$. The SMR corrections are expressed in terms of the interfacial exchange field, the spin-flip rate, and the spin dephasing rate, which all depend on the magnetic state of the local moments, and thus, can be controlled by magnetic fields and temperature.

dependence. Consequently, the interplay of HMR and SMR adds to the uncertainties of interpreting the experimental data. Therefore, it is desirable to have a theory of SMR that has predictive power about the dependence of the spin mixing conductances on B and T and can cover a wide range of the magnetic system, from classical to quantum magnets.

In this chapter, we present a general theory of the electronic transport in NM/MI structures based on a microscopic model to describe the spin-dependent scattering at the NM/MI interface. Our model assumes a *sd*-coupling between local moments on the MI surface and itinerant electrons in the NM. The temperature and magnetic field dependence of the interfacial scattering coefficients are then obtained by expressing these coefficients in terms of spin-spin correlations. The latter are determined by the magnetic behavior of the MI layer and hence depend on temperature and magnetic field. We first apply our theory to study the MR of a metallic film adjacent to either a paramagnet (PM) or a Weiss ferromagnet (FM) in a large range of temperatures and applied fields. At low temperatures, we find a hitherto unknown non-monotonic behavior of the MR as a function of B, which we explain in terms of an interplay between the SMR and HMR effects. We apply our theory to describe experiments on NM/MI structures with different material combinations in subsequent chapters.

2.2 Model and Method

2.2.1 Model

We consider an NM in contact with an MI, as shown in FIGURE 2.1. For the sake of simplicity, we assume both layers to be homogeneous in the (x, y) plane and the NM/MI interface to be located at $z = 0$.

The general Hamiltonian of the NM/MI heterostructure can be divided into three parts

$$H = H_{\mathrm{NM}} + V_{sd} + H_{\mathrm{MI}} \,. \tag{2.2.1}$$

In the NM layer, the dynamic of itinerant electrons can be described by the Hamiltonian

$$H_{\mathrm{NM}} = \sum_{\vec{k},s} \frac{\hbar^2 k^2}{2m} c^{\dagger}_{\vec{k}s} c_{\vec{k}s} + g\mu_B B \sum_{\vec{k},s,s'} \vec{s}_{ss'} \cdot \vec{n} c^{\dagger}_{\vec{k}s} c_{\vec{k}s'} + V_{SO} \sum_{\vec{k},s,s'} (\vec{E} \times \vec{k}) \cdot \vec{s}_{ss'} c^{\dagger}_{\vec{k}s} c_{\vec{k}}, \tag{2.2.2}$$

where m is the mass of electron. g is the Landé g-factor and μ_B is the Bohr magneton. $c^{\dagger}_{\vec{k}s}$, and $c_{\vec{k}s}$ are, respectively, the creation and annihilation operators for the electron with kinetic momentum $\vec{k}$ and spin $s = (\uparrow, \downarrow)$, where spin is defined by choosing quantization axis along z direction. $\vec{s} = (s_x, s_y, s_z)$ is a set of matrices representing the spin $1/2$ of the itinerant electron, and $\vec{n}$ is the unit vector pointing in the direction of the magnetic field $\vec{B}$. The last term of the right-hand side of Eq. (2.2.2) is the SOC, whose strength is parameterized by V_{SO}. It is the ingredient of the SHE, which is used to generate spin Hall current injecting into MI. The spin dynamics of MI, takeing into account the interaction between the local moments, can be modeled by the Heisenberg Hamiltonian

$$H_{\mathrm{MI}} = g\mu_B \sum_j \vec{S}_j \cdot \vec{B} - \sum_{\langle ij \rangle} J_{ij} \vec{S}_i \cdot \vec{S}_j, \tag{2.2.3}$$

where $\vec{S}_j$ is the operator of the local moment at position $\vec{R}_j$ in the MI and the second sum in equation (2.2.3) is taken over pairs of interacting spins without repetition, and $\langle \dots \rangle$ means the nearest neighbor coupling J_{ij}. For example, a paramagnetic insulator (PMI) corresponds to $J_{ij} = 0$, whereas $J_{ij} > 0 / J_{ij} < 0$ describes a ferromagnet/antiferromagnet insulator. To assesses the spin transport in the FI/NW interface, we here assume a region of thickness b in which the local moments of FI and the itinerant electrons of NW interact via a spin-exchange coupling

$$V_{sd} = -J_{sd} \sum_{i^0} \vec{S}_{i^0} \cdot \vec{s}(\vec{R}_{i^0}), \tag{2.2.4}$$

where the superscript 0 of i indicates magnetic moments are localized at the NM/MI interface. The coupling constant J_{sd} arises from the s-d hybridization between the localized d-orbitals of the impurity and the extended s-orbitals of the metal host. $\vec{s}\left(\vec{R}_{i^0}\right)$ is the spin density of itinerant electrons at the site of the local moment

$$\vec{s}\left(\vec{R}_{i^0}\right) = \frac{1}{V} \sum_{\vec{k}\vec{k}'ss'} \vec{s}_{ss'} e^{i\left(\vec{k}'-\vec{k}\right)\cdot\vec{R}_{i^0}} c^{\dagger}_{\vec{k}s} c_{\vec{k}'s'}, \tag{2.2.5}$$

where V is the volume of the considered metal layer. For simplicity, the local moments of MI are treated as a quantum bath in an equilibrium situation that is weakly

coupled to the statistical environment, and hence we do not consider here the feedback effect of the itinerant electrons on the local moments. Furthermore, the thermal properties of interfacial moments $\vec{S}_{i0}$ are the same as those inside the MI layer.

2.2.2 Method

In this subsection, I systematically introduce the method used to obtain the field and temperature dependence of spin-dependent conductances and NM's resistivity.

To utilize the well-developed methods of quantum transport in a diffusive regime, we here assume that the metal is strongly disordered, such that the mean-free path l is much smaller than the thin-film thickness d_N and the spin-relaxation length λ_s. For such a *diffusive* motion of the electron in the thin film, the events of interaction with the local moments located on the surface of the MI appear as spikes of short duration, randomly distributed along the semiclassical trajectory of the electron. The precise positions of the spikes on the trajectory is clearly unimportant because the trajectory is sufficiently random. In this diffusive limit, we may allow ourselves to displace the local moments in a random fashion on the scale of l without any consequence for the disorder-averaged quantities, as long as we are interested in the dependence of those quantities on a larger scale, set by λ_s. Thus, we arrive at considering a fictitious layer of thickness b in which both the itinerant electrons and the local moments coexist, with the latter being randomly distributed but maintaining their spin-spin coupling plotted in FIGURE 2.2. We apply the Born-Markov approximation to H in this b-layer, with V_{sd} in Equation (2.2.4) as perturbation (see details in Appendix 2.5.1). Although the thickness b should be kept small ($b \sim l$), we obtain physically meaningful results by sending first $l \to 0$ in the diffusive limit, and only in a second step $b \to 0$, going thus through an intermediate stage of the calculation in which $l \ll b \ll \lambda_s$. This order of taking the limits represents a significant simplification in the derivation because powerful disorder-averaging techniques devised for homogeneously distributed impurities in the metal can be applied here to calculate the spin-relaxation tensor inside the b-layer in a local continuum approximation. It is important to remark that the coupling in Equation (2.2.4) acts more efficiently when the spin $\vec{S}_i$ is embedded in the metal as compared to the case when it is at the surface and interacts only with the tail of the electron wave function appearing in $\vec{s}(\vec{r}_i)$. We should, therefore, reduce J_{sd} in Equation (2.2.4) by a factor $n(z > \lambda_F)/n(z = 0)$, where $n(\vec{r})$ is the average charge density in the metal and λ_F is the Fermi wavelength. However, this suppression factor is expected to be on the order of unity in well-coupled systems, for which the local moments at the surface form bonds with the metal. We absorb this suppression factor into J_{sd} hereafter.

To simplify the magnetic problem, we further employ the Weiss mean-field theory for $H_{\rm MI}$. In this approximation, the state of the magnetic system is a product state of individual local moments, yielding

$$\langle S^i_\alpha(t) S^j_\gamma \rangle = \delta_{ij} \langle S^i_\alpha(t) S^i_\gamma \rangle + (1 - \delta_{ij}) \langle S^i_\alpha \rangle \langle S^j_\gamma \rangle \ . \tag{2.2.6}$$

The equilibrium properties of the local moments are determined by the spin expectations $\langle S_\alpha \rangle$ and $\langle S^2_\alpha \rangle$ ($\alpha = x, y, z$), which depend on T and B.

In this approach, we arrive at the usual continuity equation for the non-equilibrium spin bias $\vec{\mu}_s$ in the metal (including the b-layer) following a standard derivation of Dyakonov, 2017

$$\dot{\mu}^\alpha_s - \frac{1}{e\nu_F} \partial_i J^\alpha_{s,i} - \omega_L \epsilon_{\alpha\gamma\kappa} n_\gamma \mu^\kappa_s = -\Gamma_{\alpha\kappa} \mu^\kappa_s, \tag{2.2.7}$$

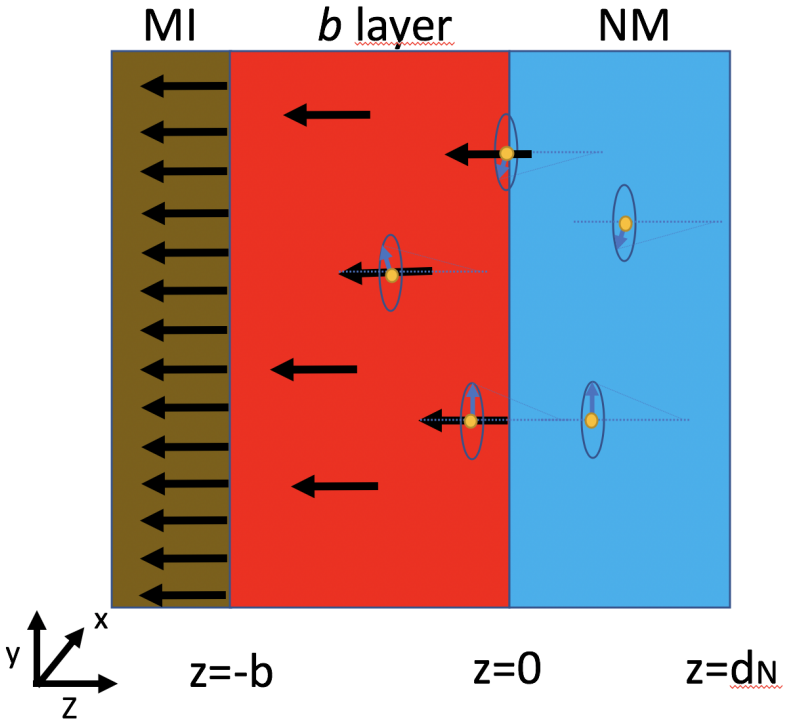

FIGURE 2.2: **The sketch of b layer**. We assume a fictitious layer of thickness b in which both the itinerant electrons (short blue arrows) and the local moments (long black arrows) coexist, with the latter being randomly distributed.

where superscript Greek indices denote spin projections ($\alpha = \{x, y, z\}$) and subscript Latin indices denote current directions ($i = \{x, y, z\}$), $\vec{n} = \vec{B}/B$ is the unit vector of the B-field, e is the elementary charge ($e > 0$), ν_F is the density of states per spin species at the Fermi level, $\epsilon_{\alpha\beta\gamma}$ is the antisymmetric tensor, and repeated indices are implicitly summed over. The spin current $J^{\alpha}_{s,i}$ has units of electrical current, with $-J^{\alpha}_{s,i}/2e$ giving the amount of spin with polarization α transported in direction i through a unit cross-section and per unit of time. Both the Larmor precession frequency, ω_L, and the spin relaxation tensor, $\Gamma_{\alpha\kappa}$ are inhomogeneous in space due to the b-layer insertion. Specifically, for the geometry in FIGURE 2.1, we have

$$\omega_L(z) = \omega_B - \frac{n^{2D}_{imp} J_{sd}}{\hbar} \langle \hat{S}_{\parallel} \rangle \delta_b(z), \tag{2.2.8}$$

where $\omega_B = g\mu_B B/\hbar$, with $g \approx 2$ being the electron g-factor and μ_B the Bohr magneton, n^{2D}_{imp} is the number of local moments per unit area at the MI/NM interface, $\hat{S}_{\parallel} = \hat{\vec{S}} \cdot \vec{n}$ is the longitudinal spin operator of a representative local moment, and $\delta_b(z)$ equals to $1/b$ in the b-region and zero elsewhere. In the limit $b \to 0$, $\delta_b(z)$ tends to the Dirac δ-function. The second term on the right-hand side in Equation (2.2.8) describes the interfacial exchange field. For instance, this field is particularly well pronounced in Al/EuS bilayers, leading to a directly measurable splitting of the density of states in the superconducting regime (Hao, Moodera, and Meservey, 1990; Strambini et al., 2017), which will be discussed in chapter 3.

The spin relaxation tensor in Equation (2.2.7) reads

$$\Gamma_{\alpha\kappa}(z) = \frac{\delta_{\alpha\kappa}}{\tau_s} + \left[\frac{\delta_{\alpha\kappa}}{\tau_\perp} + \left(\frac{1}{\tau_\parallel} - \frac{1}{\tau_\perp} \right) n_\alpha n_\kappa \right] \delta_b(z), \tag{2.2.9}$$

where τ_s is the spin relaxation time in the NM. We assume the spin relaxation in the NM to remain isotropic for the experimentally relevant magnetic fields, $B \lesssim 10$ T. Indeed, the Pauli paramagnetism has a weak effect on the SOC-induced spin relaxation at the Fermi level, because the density of states is almost spin-independent, $\nu_F^{\uparrow} \approx \nu_F^{\downarrow} \equiv \nu_F$, owing to the large Fermi energy of the NM. In Equation (2.2.9), $\tau_{\parallel}$ and $\tau_{\perp}$ denote, respectively, the longitudinal and transverse spin relaxation times per unit length for the itinerant electron in the b-region. In our notations, $T_1 = b\tau_{\parallel}$ is the relaxation time of the longitudinal spin component $\mu_{\parallel} = \vec{\mu}_s \cdot \vec{n}$, and $T_2 = b\tau_{\perp}$ is the decoherence time of the transverse spin components $\vec{\mu}_{\perp} = \vec{n} \times (\vec{\mu}_s \times \vec{n})$. Within the Born-Markov and Weiss-field approximations (see the detailed derivations in Appendix 2.5.1), we obtain

$$\frac{1}{\tau_{\parallel}} = \frac{2\pi}{T} n_{imp}^{2D} \nu_F J_{sd}^2 \omega_L^m n_B\left(\omega_L^m\right)\left[1 + n_B\left(\omega_L^m\right)\right] |\langle \hat{S}_{\parallel} \rangle|, \tag{2.2.10}$$

$$\frac{1}{\tau_{\perp}} = \frac{1}{2\tau_{\parallel}} + \frac{\pi}{\hbar} n_{imp}^{2D} \nu_F J_{sd}^2 \langle \hat{S}_{\parallel}^2 \rangle, \tag{2.2.11}$$

where $n_B(\omega) = 1/(e^{\hbar\omega/T} - 1)$ is the Bose-Einstein distribution function and $\omega_L^m = \omega_B - \langle \hat{S}_{\parallel} \rangle \sum_j J_{ij}/\hbar$, with J_{ij} being the coupling constant of the Heisenberg ferromagnet. In deriving Equations (2.2.10) and (2.2.11), we used the Weiss theory approximation in Equation (2.2.6) and have additionally assumed that the correlator $\langle \hat{S}_{\alpha} \hat{S}_{\beta} \rangle(\omega)$ for a spin on the MI surface can be approximated by the corresponding correlator for a spin deep in the bulk of the MI. We remark that $1/\tau_{\parallel}$ is due to spin-flip processes in which the itinerant electron is scattered, say, from a state $\vec{k} \uparrow$ to a state $\vec{k}' \downarrow$ and a spin excitation is created in the MI. This spin excitation is actually a magnon in general, although it is equivalent to a local moment excitation in the Weiss theory, because the magnon band is flat (Einstein model). The spin-flip correlators $\langle \hat{S}_{\pm} \hat{S}_{\mp} \rangle(\omega)$ have been expressed through the spin expectation value $\langle \hat{S}_{\parallel} \rangle$, see Supporting Information. Furthermore, we remark that $1/\tau_{\perp}$ contains two distinct terms. One term $(1/2\tau_{\parallel})$ is again due to spin-flip processes, whereas the other is due to spin dephasing. The dephasing contribution comes from scattering processes during which the electron spin, being in a superposition of spin-up and spin-down, acquires a precession phase about the $\vec{n}$-direction. Notably, it is the term $S_{\parallel}^i s_{\parallel}(\vec{r}_i)$ in the scalar product $\vec{S}^i \cdot \vec{s}(\vec{r}_i)$ in Equation 2.2.4 that is responsible for such random kicks of the spin precession phase, *i.e.* for dephasing. Therefore, the magnetic state of the MI is not changed in the Weiss-theory approximation since it is an eigenstate of $S_{\parallel}^i$. It is important to note also that the difference between $1/\tau_{\parallel}$ and $1/\tau_{\perp}$ is entirely due to the ordered magnetic state of the local moments at the interface. In the unordered state, we have

$$1/\tau_{\parallel} = 1/\tau_{\perp} = 2\pi n_{imp}^{2D} \nu_F J_{sd}^2 S(S+1)/3\hbar, \tag{2.2.12}$$

and no distinction between dephasing and spin-flip processes can be made.

To derive the boundary condition for the NM/MI interface, we integrate Equation (2.2.7) over z in the b-layer ($-b < z < 0$, see geometry in FIGURE 2.2), assuming

that $\vec{\mu}_s = (\mu_s^x, \mu_s^y, \mu_s^z)$ is almost constant and independent of time,

$$-\frac{1}{e\nu_F} J_{s,z}^{v}\Big|_{z=-b}^{z=0} = b\omega_L \epsilon_{v\gamma\kappa} n_\gamma \mu_s^\kappa - \left(\frac{b}{\tau_s} + \frac{1}{\tau_\perp}\right)\mu_s^v - \left(\frac{1}{\tau_\parallel} - \frac{1}{\tau_\perp}\right) n_v (\vec{n}\cdot\vec{\mu}_s). \tag{2.2.13}$$

Next we take the limit $b \to 0$ and write the boundary condition in a customary way (Brataas, Nazarov, and Bauer, 2001; Dejene et al., 2015)

$$-e\vec{J}_{s,z}(0) = G_s\vec{\mu}_s + G_r\vec{n}\times(\vec{n}\times\vec{\mu}_s) + G_i\vec{n}\times\vec{\mu}_s, \tag{2.2.14}$$

with $\vec{J}_{s,z} = (J_{s,z}^x, J_{s,z}^y, J_{s,z}^z)$, where we set $\vec{J}_{s,z} = 0$ at $z = -b$, because, by construction, the electron does not penetrate into the MI beyond the b-layer. The spin dependent conductance read

$$G_s = -e^2\nu_F\frac{1}{\tau_\parallel}, \tag{2.2.15}$$

$$G_r = e^2\nu_F\left(\frac{1}{\tau_\perp} - \frac{1}{\tau_\parallel}\right), \tag{2.2.16}$$

$$G_i = -\frac{e^2}{\hbar} n_{imp}^{2D}\nu_F J_{sd}\langle\hat{S}_\parallel\rangle. \tag{2.2.17}$$

It is customary to call the complex quantity $G_{\uparrow\downarrow} = G_r + iG_i$ spin-mixing conductance (Brataas, Nazarov, and Bauer, 2001), whereas G_s is sometimes called spin-sink conductance (SSC) (Dejene et al., 2015). We note that G_s originates entirely from spin-flip processes and can, therefore, be unambiguously associated with magnon emission and absorption. In contrast, G_r does not have a physical meaning on its own. However, the combination $G_r - G_s$ is proportional to the spin decoherence rate $(1/\tau_\perp)$ of the itinerant electron at the NM/MI interface. It follows from Equation (2.2.11) that a part of $G_r - G_s$ is due to spin-flip processes $(1/2\tau_\parallel)$, and hence is identical in nature to G_s, whereas the other part is due to spin dephasing. The purely dephasing contribution is $G_r - \frac{1}{2}G_s \propto \langle\hat{S}_\parallel^2\rangle$ and it originates from almost elastic spin-scattering processes, which do not involve any exchange of angular momentum with the MI. Thus, G_s and $G_r - \frac{1}{2}G_s$ correspond to different physical processes and have, therefore, distinct dependences on B and T. Finally, G_i is a measure of the interfacial exchange field, and it is proportional to the MI magnetization.

In addition, we can also understand the above three spin-dependent conductance from torques. The real and imaginary parts of the spin-mixing conductance, $G_{\uparrow\downarrow} = G_r + iG_i$ (Brataas, Bauer, and Kelly, 2006a; Jia et al., 2011), originate from torques that the electron spins of the NM exert to the magnetization of the MI when both are noncollinear. On the one hand, G_r is determined by the STT, which is collinear to the spin polarization of injected electrons as depicted in FIGURE 1.6 (a). On the other hand, G_i quantifies the interfacial exchange field between the electron spins of the NM and the magnetic moments of the MI, which induces a field-like torque (FLT), as described by FIGURE 1.6 (b). Furthermore, we find the negative SSC G_s also describes the STT just like the G_r as shown by the FIGURE 1.6 (a), which quantifies the interfacial spin current, when the electron spins of the NM are collinear with the magnetization of the MI (Flipse et al., 2014; Cornelissen et al., 2016; Das et al., 2019).

Having these pictures in mind, let us consider the real physics happening at

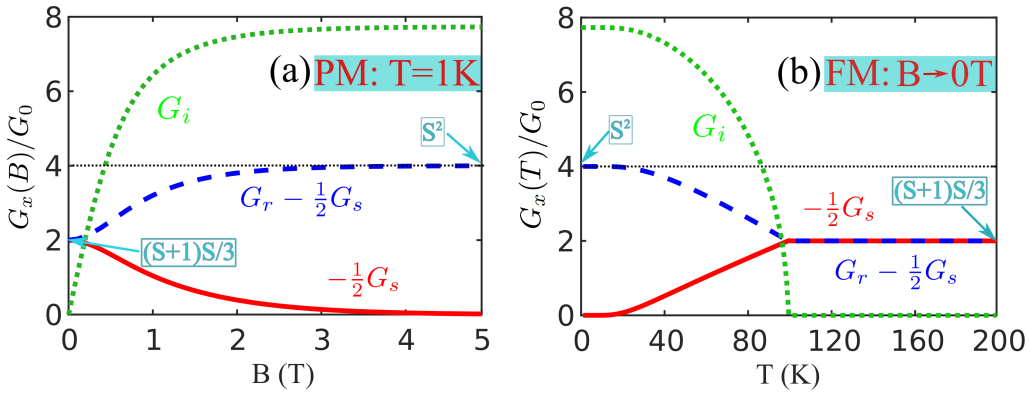

FIGURE 2.3: The spin dependent conductances G_x ($x = s, r, i$) arranged in combinations of $-\frac{1}{2}G_s$, $G_r - G_s$, and G_i to describe, respectively, the spin flips (magnon emission), the spin dephasing (no spin transfer to MI), and the interfacial exchange field. (a) The dependence on B for a PM insulator at $T = 1\,\mathrm{K}$. (b) The dependence on T for an FM insulator with a Curie temperature of $T_C = 100\,\mathrm{K}$. The conductances are measured in units of $G_0 = \frac{\pi}{\hbar} n_{imp}^{2D} (e\nu_F J_{sd})^2$. The sd-coupling constant is $J_{sd} a_c^{-3} = 0.2$ eV (Wahl et al., 2007), which is parameterized by the lattice constant of the NM, $a_c = 0.4\,\mathrm{nm}$. Other parameters: $S = 2$, $\nu_F J_{sd} \simeq 0.08$, and $n_{imp}^{2D} a_c^2 = 0.5$.

NM/MI interface. The interfacial spin current at NM/MI interface is described by three spin-dependent conductance, as shown in Eq. (2.2.14) and is equal to reflection spin current plus injection spin current. The later induced by the CSHE in NM is assumed to be constant. When $\vec{\mu}_s \parallel \vec{M}$, as shown in Eq. (2.2.14), the interfacial spin current at NM/MI interface $\vec{J}_{s,z} = (|G_s|/e)\vec{\mu}_s$ is small, which means the majority of the spin current is reflected into NM and converted back into longitudinal charge current. Thus, SMR exhibits a minimum. On the contrary, when $\vec{\mu}_s \perp \vec{M}$, as shown in Eq. (2.2.14), the interfacial spin current at NM/MI interface $\vec{J}_{s,z} = (|G_s|/e + G_r/e)\vec{\mu}_s$ is large, which means the minority of spin current is reflected into NM and converted back into charge current. Thus, SMR exhibits a maximum. As a result, the SMR appears as a modulation of the NM resistivity, governed by G_r and G_s, which follows the relative orientation between the magnetization in the MI and the spin-Hall induced spin accumulation in the NM, as shown in FIGURE 1.8.

2.3 Results and Discussion

2.3.1 Spin-dependent conductance

In this subsection, we sketch the field and temperature of spin-dependent conductances. As two typical examples, hereafter, we deal with paramagnetic and ferromagnetic insulators.

To highlight the physical picture of the spin-dependent conductance, we plot the quantities G_i, $G_r - \frac{1}{2}G_s$, and $-\frac{1}{2}G_s$ as functions of B for a PM in FIGURE 2.3 (a) and as functions of T for a FM in FIGURE 2.3 (b), respectively. If we consider the low-field limit of PM and high-temperature case of FM, we will reach the isotropic regime ($\tau_\parallel = \tau_\perp$), where $G_r = G_i = 0$, and $G_s = -\frac{2}{3}G_0 S(S+1)$, and hence the SMR is governed by the spin-flipping process. If we consider the high-field regime of PM and low temperature situation of PM, the spin of itinerant electrons are fully frozen

and hence spin flipping is forbidden. Ultimately, we arrive the strongly magnetized regime ($\tau_{\parallel} \gg \tau_{\perp}$), and we have $G_r = G_0 S^2$, $G_i = G_0 S/(\pi \nu_F J_{sd})$, and $G_s \approx 0$. Here, $G_0 = \frac{\pi}{\hbar} n_{imp}^{2D} (e\nu_F J_{sd})^2$ is a characteristic scale of the spin-dependent conductances. We estimate a value of $G_0 \approx 3.8 \times 10^{13} \Omega^{-1} \mathrm{m}^{-2}$ for a typical $n_{imp}^{2D} = 5 \times 10^{18} \mathrm{m}^{-2}$ and $\nu_F J_{sd} = 0.1$. This estimate is compatible with values of spin mixing conductances reported in experiments of Vlietstra et al., 2013a; Dejene et al., 2015; Das et al., 2019.

Next, we consider a ferrimagnet consisting of two species of local moments (S^a and S^b). In the mean-field approximation, no interference terms occur between different species and our results above are modified only by selectively weighting each species by its concentration on the surface (n_a^{2D} and n_b^{2D}) and taking into account its possibly different coupling strength (J_{sd}^a and J_{sd}^b). It is possible to obtain a situation in which the interfacial exchange fields of the two local-moment species closely compensate each other, resulting in $G_i \ll G_r$-a condition which is believed to hold for Pt thin films deposited on $Y_3Fe_5O_{12}$ (YIG) Vlietstra et al., 2013a and which would otherwise not be possible in a simple ferromagnet, because G_i is the largest spin mixing conductance for $\nu_F J_{sd} \ll 1$. The G_i-compensation condition for a ferrimagnet, thus, reads $n_a^{2D} J_{sd}^a S^a - n_b^{2D} J_{sd}^b S^b = 0$, which differs from the magnetization compensation condition, $n_a^{3D} S^a - n_b^{3D} S^b = 0$, and allows for the possibility of having a finite magnetization even when $G_i = 0$. And vice versa, the Néel order parameter of an antiferromagnet can manifest itself as an interfacial exchange field, provided the G_i-compensation condition is not fulfilled. We remark that, for YIG, we have $S^a = S^b = 5/2$ and $n_a^{3D}/n_b^{3D} = 3/2$. And for the Pt/YIG-[001] interface, we have $n_a^{2D} = n_b^{2D}$ and $J_{sd}^a \approx J_{sd}^b$. A small difference between J_{sd}^a and J_{sd}^b may originate from different crystal fields for the Fe^{3+} cation on the tetrahedral (a) and octahedral (b) sublattice of the garnet.

Even though YIG has been the material of choice in most experimental studies of SMR, recent experiments started also studying other MIs (Isasa et al., 2014; Isasa et al., 2016; Vélez et al., 2019b; Lammel et al., 2019; Fontcuberta et al., 2019). Here, we would like to draw attention to an effect due to G_i, which, to the best of our knowledge, has been overlooked theoretically. Moreover, it could appear rather puzzling when observed experimentally. This effect consists of a negative, linear-in-B magnetoresistance, which arises from an interplay between SMR and HMR, featuring a non-local Hanle effect. Furthermore, although the novel effect is primarily due to G_i, we keep G_r and G_s in the expressions below for completeness.

2.3.2 The interplay of HMR and SMR

In this subsection, we explore the interplay of HMR and SMR. As two typical examples, hereafter, we deal with paramagnetic and ferromagnetic insulators.

We make use of the boundary condition in Equation (2.2.14) and follow closely the derivation of the SMR and HMR effects (Nakayama et al., 2013; Chen et al., 2013; Vélez et al., 2016b; Vélez et al., 2019b), obtaining the corrections to the longitudinal (ρ_L) and transverse (ρ_T) resistivity of the Hall-bar setup in FIGURE 2.1

$$\rho_L \simeq \rho_D + \Delta\rho_0 + \Delta\rho_1 \left(1 - n_y^2\right), \tag{2.3.1}$$

$$\rho_T \simeq -\rho_D \omega_c \tau n_z + \Delta\rho_1 n_x n_y + \Delta\rho_2 n_z, \tag{2.3.2}$$

where ρ_D is the Drude resistivity and $\omega_c \tau$ is the Hall angle, with $\omega_c = eB/mc$ being the cyclotron frequency and τ being the momentum relaxation time. The combined

SMR+HMR resistivity corrections read (see detailed derivation in Appendix 2.5.4)

$$\Delta\rho_0 = \theta_{SH}^2\rho_D[2-\mathcal{R}(G_s,\lambda_s)], \tag{2.3.3}$$

$$\Delta\rho_1 = \theta_{SH}^2\rho_D\left\{\mathcal{R}(G_s,\lambda_s)-\mathrm{Re}\left[\mathcal{R}(G_s-G_{\uparrow\downarrow},\Lambda)\right]\right\}, \tag{2.3.4}$$

$$\Delta\rho_2 = \theta_{SH}^2\rho_D\mathrm{Im}\left[\mathcal{R}(G_s-G_{\uparrow\downarrow},\Lambda)\right], \tag{2.3.5}$$

where θ_{SH} is the spin Hall angle, $\lambda_s = \sqrt{\mathcal{D}\tau_s}$, with $\mathcal{D} = 1/2e^2\nu_F\rho_D$ being the diffusion constant, $G_{\uparrow\downarrow} = G_r + iG_i$ is the complex spin mixing conductance, $1/\Lambda = \sqrt{1/\lambda_s^2 + i\omega_B/\mathcal{D}}$, and the auxiliary function $\mathcal{R}(\mathcal{G},\ell)$ is defined as

$$\mathcal{R}(\mathcal{G},\ell) = \frac{2\ell}{d_N}\tanh\left(\frac{d_N}{2\ell}\right)\frac{1-\rho_D\mathcal{G}\ell\coth\left(\frac{d_N}{2\ell}\right)}{1-2\rho_D\mathcal{G}\ell\coth\left(\frac{d_N}{\ell}\right)}. \tag{2.3.6}$$

For $\Lambda = \lambda_s$, we recover the SMR corrections (Nakayama et al., 2013; Chen et al., 2013), whereas for $G_s = G_r = G_i = 0$, we recover the HMR corrections (Dyakonov, 2007; Vélez et al., 2016b). We remark that, in general, it is important to take into account G_s (Dejene et al., 2015; Vélez et al., 2019b), which is not negligible in the paramagnetic regime, see FIGURE 2.3. The corrections in Equation (2.3.5) were used in Ref. Vélez et al., 2019b to explain the unusual behavior of SMR in $Pt/LaCoO_3$ in the high-temperature limit.

For a PM or FM at sufficiently low temperatures, the scale to reach saturation represents only a relatively small portion of the experimentally accessible B-field range. The SMR effect develops quickly with increasing B and saturates as shown by the blue solid line in FIGURE 2.4a. The SMR effect is dominated by G_i for

$$G_r - G_s \ll G_i^2\lambda_s\rho_D\coth\left(d_N/\lambda_s\right), \tag{2.3.7}$$

which requires that

$$n_{imp}^{2D} \gg (\hbar/e^2\rho_D\lambda_s)\tanh\left(d_N/\lambda_s\right). \tag{2.3.8}$$

At the same time, the HMR effect develops gradually and becomes relevant only for large B as shown by the red solid line in Figure 2.4a. In the experiment, the HMR effect is well pronounced at relatively large magnetic fields, $B \lesssim 10\,\mathrm{T}$ (Vélez et al., 2016b). In the region of intermediate B, denoted as "interference region" in Figure 2.4a, the interplay between the SMR and HMR effects can lead to negative differential MR ($\partial\rho_L/\partial B < 0$). This behavior would not be so surprising if it occurred solely when G_i and ω_B had opposite signs. Indeed, G_i is a measure of the interfacial exchange field, which is a singular field created at the NM/MI interface by the *sd* coupling in Equation (2.2.4). The signs of G_i and ω_B are equal to each other for $J_{sd} > 0$ and opposite for $J_{sd} < 0$. For electrons diffusing over a characteristic length scale $\ell \sim \min(d_N,\lambda_s)$, the interfacial exchange field can be smeared near the interface over ℓ and superimposed onto ω_B, obtaining an average Larmor frequency $\omega_L = \omega_B + G_i/e^2\nu_F\ell$. One could naïvely expect that the HMR effect, which is proportional to ω_B^2 for all experimentally relevant B-field values, to become proportional to $\omega_L^2 = \left(\omega_B + G_i/e^2\nu_F\ell\right)^2$, generating, thus, after squaring a cross term proportional to $\omega_B G_i$. For $J_{sd} < 0$, this term would then naturally lead to a negative MR. Quite surprisingly, we find a negative MR even for $J_{sd} > 0$, provided G_i exceeds a certain critical value.

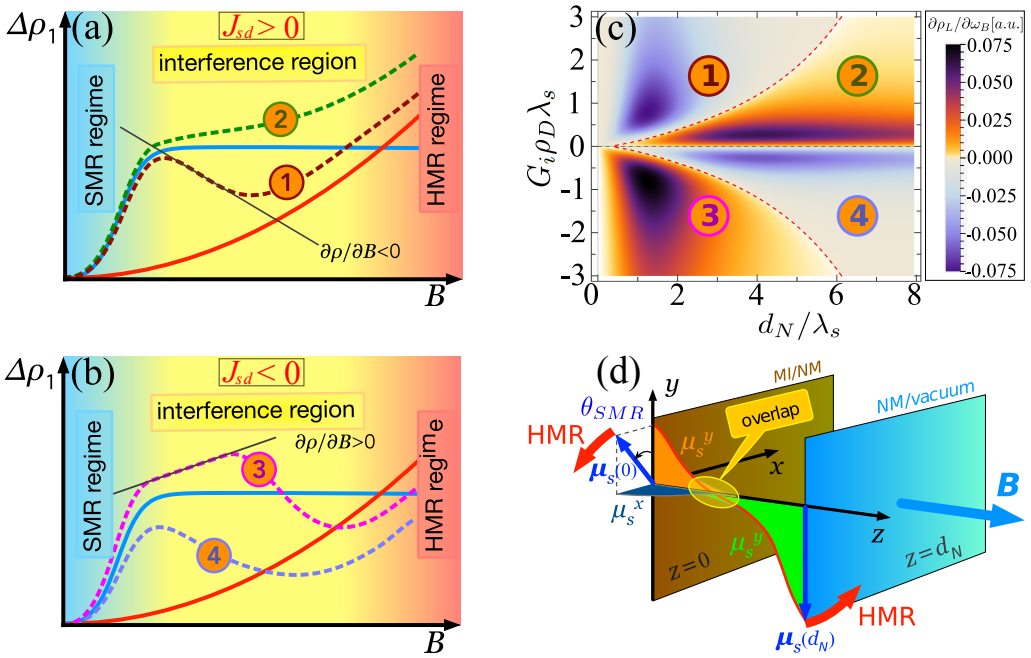

FIGURE 2.4: (a) Interplay between SMR and HMR effects for $J_{sd} > 0$ and MI in the paramagnetic regime. The blue and red solid lines show, respectively, the SMR and HMR effects in the absence of one another. Between the SMR regime (small B) and the HMR regime (large B) an intermediate "interference" region occurs, where anomalous behavior, marked by the straight black line, is possible due to a non-local Hanle effect and its interplay with SMR. The dashed line ① shows the qualitative behavior of $\Delta\rho_1(B)$ for the non-local interference, whereas line ② shows it for the local interference. (b) Same as in (a), but for $J_{sd} < 0$ and with lines ③ and ④ corresponding, respectively, to the non-local and local regimes of interference. (c) Separation of the parameter space (d_N, G_i) into different regimes of interference. The red dashed line shows the critical value of G_i in Equation (2.3.9) as a function of d_N. The regions ①-④ correspond to the four kinds of behavior shown in (a) and (b). The color code shows the sign of $\partial\rho_L/\partial\omega_B$ at constant G_i and $\omega_B \to 0$. (d) Sketch of the spin accumulation at the thin-film interfaces as created by the SHE and altered by the SMR effect. The SMR effect suppresses the spin density at NM/MI interface and rotates it by a finite angle, θ_{SMR}, about the magnetization direction. In the absence of overlap between the two spin accumulations (orange and green), the Hanle effect acts locally at each interface and alters the spin accumulation in an expected manner, quite similarly to the SMR effect, see text. The overlap between the two spin accumulations makes it possible for the Hanle effect from the NM/vacuum interface to affect significantly the spin accumulation at the NM/MI interface, especially when the latter is strongly suppressed due to SMR. With applying a B field, the component $\mu_s^y(z=0)$ can exhibit an increase instead of the decrease which one could naïvely expect from the local Hanle effect.

To investigate the origin of the anomalous behavior of the MR, we expand $\Delta\rho_1$ in Equation (2.3.5) in powers of ω_B at constant G_i and set, for simplicity, $G_r = G_s = 0$. The coefficient in front of the linear-in-ω_B term changes sign at the critical value of

G_i given by

$$G_{i,c}^2 = \frac{\sinh^2(d_N/2\lambda_s)}{2\lambda_s^2\rho_D^2\cosh(d_N/\lambda_s)}\left[\frac{\lambda_s}{d_N}\sinh\left(\frac{d_N}{\lambda_s}\right)-1\right]. \tag{2.3.9}$$

We find several qualitatively different behaviors of the MR, illustrated by the dashed lines in FIGURE 2.4a-b. The lines ①–④ correspond to the regions in the parameter space (d_N, G_i) shown in FIGURE 2.4c, obtained by plotting the magnitude of the linear-in-ω_B term. The critical value in Equation (2.3.9) as a function of d_N is shown in Figure 2.4c by the red dashed line. Thus, for $J_{sd} > 0$, the anomalous behavior manifests itself in a segment of negative MR on line ①, marked by the black straight line in FIGURE 2.4a. The dependence shown by line ② is consistent with the the physical picture, given above, in which the Zeeman and exchange fields can be superimposed locally with one another, giving rise to a shifted-to-the-left parabolic B-field dependence for $\Delta\rho_1(B)$, on top of the fully developed SMR gap. The dependence, shown by line ① cannot be understood in terms of a local interplay between the SMR and HMR effects occurring at the NM/MI interface. We remark that no anomalous behavior occurs in a semi-infinite space, at one interface. Therefore, it is essential to involve in the explanation of the NM/vacuum interface, which has a spin accumulation oriented predominantly opposite to, but not strictly anti-aligned with the spin accumulation at the NM/MI interface.

We illustrate the spin accumulations occurring in the SMR effect at both interfaces in Figure 2.4d. Since the SMR effect suppresses significantly the spin accumulation $\vec{\mu}_s(0)$ at the NM/MI interface, the Hanle effect occurring near that interface induces a rather small change of spin accumulation, which represents mainly a rotation about the B-field axis, such as $\delta\vec{\mu}_s(0) \propto \omega_B\,[\vec{n}\times\vec{\mu}_s(0)]$. In contrast, the Hanle effect occurring near the NM/vacuum interface induces, in the same fashion, a relatively larger change of spin accumulation, $\delta\vec{\mu}_s(d_N) \propto \omega_B\,[\vec{n}\times\vec{\mu}_s(d_N)]$. By means of diffusion or, in other words, when the film is so thin that the spin accumulations of both interfaces overlap with each other (see orange and green parts of μ_s^y in Figure 2.4d), a non-local interplay between SMR and HMR effects takes place. In particular, for a magnetic field along z as shown in Figure 2.4d, the Hanle effect at the NM/vacuum interface brings in a μ_s^x component generated from a μ_s^y component of opposite sign (green part of μ_s^y). After diffusing across the thin film thickness, the μ_s^x component is converted back into a μ_s^y component at the NM/MI interface due to the interfacial exchange field. The longitudinal resistivity correction is governed by the change in the y-component of the spin bias across the sample (Chen et al., 2013; Vélez et al., 2016b), $\Delta\rho_L \propto \mu_s^y(d_N) - \mu_s^y(0)$. A negative MR is obtained when the difference $\mu_s^y(0) - \mu_s^y(d_N)$ grows with applying a magnetic field, i.e. when the spin bias across the sample increases with B. This usual behavior is obtained also for the quantity $\mu_s^y(0)$ alone, although we find that the difference $\mu_s^y(0) - \mu_s^y(d_N)$ begins to increase with B at a smaller critical G_i than the value at which $\mu_s^y(0)$ begins to increase. Nevertheless, the physical picture leading to such a striking effect is common to both quantities: The μ_s^x component generated from a large negative spin accumulation at the NM/vacuum interface is converted into a μ_s^y component at the NM/MI interface due to G_i, obtaining a non-local contribution $\delta\mu_s^y(0) \propto -\omega_B G_i e^{-d_N/\lambda_s}\mu_s^y(d_N)$. This non-local contribution competes with the one generated locally by the Hanle effect at the NM/MI interface, $\delta\mu_s^y(0) \propto \omega_B\mu_s^x(0)$. Notably, $\mu_s^x(0)$ is suppressed for large G_i as $\propto 1/G_i$, which makes the correction generated locally small. From the balance of the local and non-local corrections to $\mu_s^y(0)$, we recover the exponential dependence of the critical G_i in Equation (2.3.9) for large $d_N \gg \lambda_s$, namely $G_{i,c} \propto e^{-d_N/2\lambda_s}$. Thus, we conclude that the transition from positive to negative MR for $J_{sd} > 0$ occurs when

the non-local interplay between HMR and SMR dominates over the local one.

In the case of $J_{sd} < 0$, see Figure 2.4b, a negative MR is not unusual since the Zeeman and exchange fields have opposite signs and can compensate each other to some extent. In this case, one would expect a shifted-to-the-right parabolic B-field dependence for $\Delta\rho_1(B)$, on top of the fully developed SMR gap. This expectation is, indeed, met when the magnitude of G_i is smaller than the critical value in Equation (2.3.9), see line ④ in Figure 2.4b. As for line ③, which corresponds to a large negative G_i ($G_i < G_{i,c} < 0$), its behavior resembles qualitatively that of line ④, and can not be reliably identified in the absence of the reference curves showing the pure SMR and pure HMR separately. Nevertheless, the anomalous behavior originating from the the non-local interplay between SMR and HMR consists herein having a positive slope at the beginning of the interference region, as marked by the straight black line in Figure 2.4b.

With the help of our theoretical model, we explore further several examples that illustrate the non-monotonic behavior of the MR in a realistic system and show how it evolves with temperature. Specifically, we assume that the MI can be described as a Weiss ferromagnetic insulator. It exhibits a spontaneous finite average magnetization, $\langle \hat{S}_\parallel \rangle$, at temperatures below the Curie-Weiss temperature T_c. The B- and T-dependence of $\langle \hat{S}_\parallel \rangle$ is obtained by solving the transcendental equation (see more discussion in Appendix 2.5.3),

$$\langle \hat{S}_\parallel \rangle = -S\mathcal{B}_S\left[\frac{S}{T}\left(\hbar\omega_B - \langle \hat{S}_\parallel \rangle \sum_j J_{ij}\right)\right], \tag{2.3.10}$$

where $\mathcal{B}_S(X)$ is Brillouin function. Equation (2.3.10) also describes a PM insulator after setting $J_{ij} = 0$. We remark that, for sufficiently small values of J_{ij} (including the case of a PM insulator), the Ruderman-Kittel-Kasuya-Yosida (RKKY) interaction Majlis, 2007 between local moments on the MI surface may dominate the surface magnetism. The RKKY coupling constant, $J_{ij}^{\mathrm{RKKY}} \sim \nu_F J_{sd}^2$, becomes on average exponentially suppressed over distances larger than the mean-free path De Gennes, 1962, although the fluctuations of this coupling constant remain long-ranged Zyuzin and Spivak, 1986; Bulaevskii and Panyukov, 1986. It is important to note, however, that this interaction leads to an effectively two-dimensional Heisenberg model on the surface of the MI and that the Weiss mean-field theory can then be applied only for sufficiently large temperatures, $T \gg \sum_j J_{ij}^{\mathrm{RKKY}}$, to avoid discrepancies with the Mermin-Wagner theorem of Mermin and Wagner, 1966.

We compute the longitudinal resistivity from Eqs. (2.3.2-2.3.6). The spin-dependent conductances, Equations (2.2.15-2.2.17), are determined from the relaxation times in Equations (2.2.10-2.2.11), which can be obtained after substitution of magnetization $\langle \hat{S}_\parallel \rangle$ from Equation (2.3.10) and spin-spin correlation function $\langle S_\parallel^2 \rangle$ from the relation (see detailed derivation in Appendix 2.5.3)

$$\langle S_\parallel^2 \rangle = S(S+1) + \coth[(\hbar\omega_B - \langle \hat{S}_\parallel \rangle \sum_j J_{ij})/2T] \langle S_\parallel \rangle . \tag{2.3.11}$$

Figure 2.5 summarizes our results for PM and FM insulators. The dashed lines in Figure 2.5a-d correspond to a field applied in y-direction, whereas the solid lines to a field in z-direction. It is in the latter situation that the predicted anomalous behavior becomes evident.

As one might anticipate, the non-monotonic behavior is best pronounced at low temperatures for which the spin-dependent conductances G_s, G_r, and G_i saturate

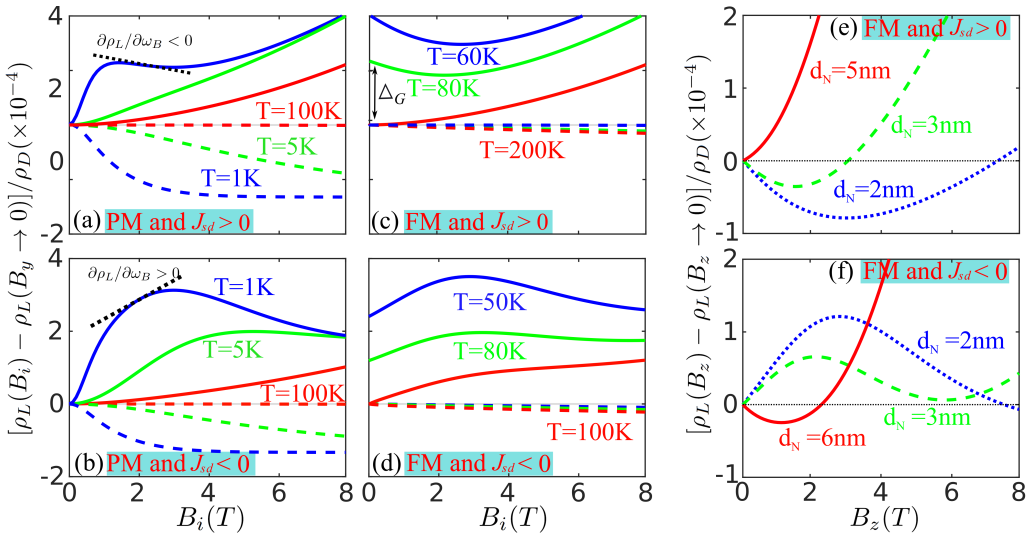

FIGURE 2.5: (a-d) Relative longitudinal resistivity, $[\rho_L(B_i)-\rho_L(B_y\to 0)]/\rho_D$, as a function of magnetic field B applied along main directions ($B\equiv B_i$ with $i=x,y,z$). Solid lines show the case $B\equiv B_z$ (or $B\equiv B_x$, which is equivalent), whereas dashed lines shows the case $B\equiv B_y$. Panels (a,b) correspond to a PM insulator, whereas panels (c,d) to a FM insulator with a Curie temperature of $T_C=100\,\mathrm{K}$. Panels (a,c) and (b,d) correspond, respectively, to positive and negative *sd*-coupling constant, $J_{sd}a_c^{-3}=\pm 0.1$ eV (Wahl et al., 2007; Myers et al., 2005), respectively. The NM thickness is chosen as $d_N=2\,\mathrm{nm}$ and the different curves correspond to different temperatures. (e-f) Different to above, relative longitudinal resistivity, $[\rho_L(B_z)-\rho_L(B_z\to 0)]/\rho_D$, as a function of magnetic field B applied in z-direction, for a FM insulator which couples to NM with a coupling constant: (e) $J_{sd}a_c^{-3}=+0.1$ eV and (f) $J_{sd}a_c^{-3}=-0.1$ eV. The temperature is chosen as $T=10\,\mathrm{K}$ and the different curves correspond to different thickness. In all panels we have chosen the following values of other parameters: $\theta_{SH}=0.1$, $\lambda_s=3.0\,\mathrm{nm}$, $\rho_D=1.0\times 10^{-6}\,\Omega\mathrm{m}$, $n_{imp}^{2D}a_c^2=0.5$, $S=2$, $|\nu_F J_{sd}|\simeq 0.04$, and $a_c=0.4\,\mathrm{nm}$.

after applying a relatively small magnetic field. We have chosen the parameters such that the solid curves in Figure 2.5a-d correspond to the predicted anomalous behaviors ① and ③ in Figure 2.4a-b. In the PM case, Figure 2.5a-b, the anomalous differential MR starts at finite fields when G_i is sufficiently large, *cf.* Figure 2.3a. In contrast, in the FM case, G_i is large enough even in small fields due to the spontaneous magnetization, and the anomalous behaviors are already seen for $B\to 0$ and over a larger range of temperatures below T_c, see Figure 2.5c-d. In the FM case, one also obtains the SMR gap, defined as

$$\Delta_G := \rho_L(B\equiv B_z\to 0)-\rho_L(B\equiv B_y\to 0). \tag{2.3.12}$$

In Figure 2.5e-f, we show $\rho_L(B)$ in the FM case for a field in z-direction and different values of the NM thickness, d_N. Following Equation 2.3.9, by changing d_N, one tunes the critical value of G_i and hence the behavior of the MR changes. For the chosen parameters in Figure 2.5e-f, the thickest film exhibits the normal behavior, see red solid lines in Figure 2.5e-f, whereas thinner films show the anomaly in the MR, blue and green dashed lines. Thus, our modeling shows that the anomalous

behavior is expected to be observed in MIs with sufficiently large values of G_i. This can be achieved, for example, in insulating FMs with large local moments, for example, in EuS or EuO (Müller, Miao, and Moodera, 2009; Strambini et al., 2017; Wei et al., 2016).

2.4 Conclusions

We have presented a theory of the SMR effect from a microscopic perspective, in which SMR relates to the microscopic processes of spin relaxation at the NM/MI interface. Our theory covers a wide range of MIs and can be used to investigate the effect of a magnetic field and temperature on MR in NM/MI Hall-bar setups and beyond. We found a non-local interplay between SMR and HMR, which gives rise to a negative linear-in-magnetic-field MR. Our theory provides a useful tool for understanding present and future experiments, and it has the potential to evolve into a full-fledged technique to measure the magnetic properties of the NM/MI interfaces, focusing exclusively on probing the very surface of the MI.

2.5 Appendix

2.5.1 Spin relaxation tensor in equations (2.2.10) and (2.2.11)

In this section, we show how to obtain the different terms of the spin relaxation tensor used in our kinetic equation. We define spin states at the Bloch sphere with arbitrary coordinates (θ, ϕ), where $\theta \in [0, \pi]$ and $\phi \in [0, 2\pi)$,

$$|\Uparrow\rangle = \cos(\frac{\theta}{2}) |\uparrow\rangle - e^{-i\phi} \sin(\frac{\theta}{2}) |\downarrow\rangle , \tag{B.5.1}$$

$$|\Downarrow\rangle = \cos(\frac{\theta}{2}) |\downarrow\rangle + e^{+i\phi} \sin(\frac{\theta}{2}) |\uparrow\rangle , \tag{B.5.2}$$

where $|\uparrow\rangle(|\downarrow\rangle)$ correspond to spin up(down) projections with respect to the quantization axis along the magnetic field. We set thw latter as the z direction. Noth that the sd coupling is $SU(3)$ invariant. We can rewrite it in any rotated spin basis defined by a rotation $R(\theta, \phi) : (A_x, A_y, A_z) \to (A_\mathbf{x}, A_\mathbf{y}, A_\mathbf{z})$ with $\vec{A} = \vec{s}, \vec{S^j}$:

$$R = \begin{bmatrix} \cos\theta\cos\phi & -\cos\theta\sin\phi & \sin\theta \\ \sin\phi & \cos\phi & 0 \\ -\sin\theta\cos\phi & \sin\theta\sin\phi & \cos\theta \end{bmatrix} . \tag{B.5.3}$$

Thus, $|\Uparrow\rangle(|\Downarrow\rangle)$ are the spin "up"("down") with quantization Pauli matrix $s_\mathbf{z}$. The sd coupling in the rotated spin basis reads

$$V_{sd} = -J_{sd} \sum_i \left\{ \frac{1}{2} \left[S^{i,\mathbf{z}}_+ s^\mathbf{z}_-(\vec{r}) + S^{i,\mathbf{z}}_- s^\mathbf{z}_+(\vec{r}) \right] + S^i_\mathbf{z} s_\mathbf{z}(\vec{r}) \right\} , \tag{B.5.4}$$

where

$$S^{i,\mathbf{z}}_+ = S^i_\mathbf{x} + iS^i_\mathbf{y}, s^\mathbf{z}_+(\vec{r}) = s_\mathbf{x}(\vec{r}) + is_\mathbf{y}(\vec{r}), \tag{B.5.5}$$

$$S^{i,\mathbf{z}}_- = S^i_\mathbf{x} - iS^i_\mathbf{y}, s^\mathbf{z}_-(\vec{r}) = s_\mathbf{x}(\vec{r}) - i\sigma_\mathbf{y}(\vec{r}). \tag{B.5.6}$$

The first term of the right hand side of equation (B.5.4) describes spin "exchange" ("split") for spin "up"("down"), i.e., $|\Uparrow\rangle(|\Downarrow\rangle)$ with quantization Pauli matrix $s_{\mathbf{z}}$. Here we emphasize that the pure spin exchange (flip) without double quotes describe the spin up (down), i.e., $|\uparrow\rangle(|\downarrow\rangle)$, with quantization Pauli Matrix s_z, i.e., along the magnetic field.

We turn now to calculating the spin relaxation times in the Born-Markov approximation Slichter, 2013. The rate for electron transition from $|\vec{k},\Uparrow\rangle$ into momentum $|\vec{k}',\Downarrow\rangle$ reads

$$W_{\Downarrow\Uparrow}(\vec{k}',\vec{k}) = \left(\frac{J_{sd}}{2\hbar V}\right)^2 \sum_{ij} e^{i\left(\vec{k}'-\vec{k}\right)\cdot\vec{R}_{j'j}} \int_{-\infty}^{\infty} dt e^{-i\left(\omega_{\vec{k}'\Downarrow}-\omega_{\vec{k}\Uparrow}\right)t} D^{\mathbf{z}}_{-+}(\vec{R}_{j'j},t), \tag{B.5.7}$$

where $D^{\mathbf{z}}_{-+}(\vec{R}_{j'j},t) = \langle S^{j',\mathbf{z}}_{-}(t) S^{j,\mathbf{z}}_{-}\rangle$ is spin-spin correlation function. The spin relaxation time induced by the spin "flip" described by the first term of the right hand side of equation (B.5.4) reads

$$\frac{1}{t_{\mathbf{z}}} = \frac{2}{k_B T V \nu_F} \sum_{\vec{k}\vec{k}'} W_{\Downarrow\Uparrow}\left(\vec{k}',\vec{k}\right) f\left(\hbar\omega_{\vec{k}\Uparrow}\right)\left[1-f\left(\hbar\omega_{\vec{k}'\Downarrow}\right)\right], \tag{B.5.8}$$

where k_B is Boltzman constant, T is the tempeature and ν_F is the density of state. $f(E) = 1/(e^{(E-\mu)/k_BT}+1)$ is Fermi-Dirac distribution function with chemical potential μ.

To calculate the above rate (B.5.7), we make two approximations. They are i) single scattering, which assumes the contributions of different local moments in an incoherent fashion,

$$D^{\mathbf{z}}_{-+}(\vec{R}_{j'j},t) = \delta_{jj'} D^{\mathbf{z}}_{-+}(t) + (1-\delta_{jj'})\langle S^{j',\mathbf{z}}_{-}(t)\rangle\langle S^{j,\mathbf{z}}_{-}\rangle. \tag{B.5.9}$$

ii) Weiss theory, which means the interaction between local moments amounts only to a renormalization of the Zeeman term. Hence, the scattering rate (B.5.7) reduces into compact form

$$W_{\Downarrow\Uparrow}(\vec{k}',\vec{k}) = 2\pi M \left(\frac{J_{sd}}{2\hbar V}\right)^2 D^{\mathbf{z}}_{-+}(\omega_{\vec{k}\uparrow}-\omega_{\vec{k}'\downarrow}), \tag{B.5.10}$$

where M is the number of magnetic moments within magnetic interface, and $D^{\mathbf{z}}_{-+}(\omega)$ is the Fourier transformation of $D^{\mathbf{z}}_{-+}(t)$.

With loss of generality, the longitudinal spin relaxation time corresponds to $\theta = 0, \phi = 0$ of equation (B.5.3). Hence we have

$$S^{\parallel}_{+} = S_x + iS_y, S^{\parallel}_{-} = S_x - iS_y. \tag{B.5.11}$$

And the correlation function becomes

$$D^{\parallel}_{-+}(\omega) = \delta(\omega-\omega_W)\left(\langle S^2_x\rangle + \langle S^2_y\rangle - \langle S_z\rangle\right), \tag{B.5.12}$$

where $\omega_W = \omega_B - \sum_j J_{ij}\langle S_{\parallel}\rangle/\hbar$ is the frequency of Weiss field. Then we obtain longitudinal spin relaxation time

$$\frac{1}{\tau_{\parallel}} = \frac{2\pi}{\hbar} n^{2D}_{imp} \nu_F J^2_{sd} \beta\hbar\omega^m_L n_B\left(\omega^m_L\right)\left[1+n_B\left(\omega^m_L\right)\right]|\langle\hat{S}_z\rangle|, \tag{B.5.13}$$

where we have written $t_{\parallel} = b\tau_{\parallel}$ by changing n_{imp}^{3D} to n_{imp}^{2D}. For the case of transverse spin relaxation time, we take $\theta = \pi/2$, $\phi = \pi$ of equation (B.5.3). Then we have

$$S_{+}^{\perp} = S_z - iS_y, S_{-}^{\perp} = S_z + iS_y. \tag{B.5.14}$$

And the correlation function becomes

$$D_{-+}^{\perp}(\omega) = +\frac{1}{4}\left[D_{+-}^{\parallel}(\omega) + D_{-+}^{\parallel}(\omega)\right] + \delta(\omega)\langle S_z^2\rangle. \tag{B.5.15}$$

Then we obtain transverse spin relaxation time

$$\frac{1}{\tau_{\perp}} = \frac{1}{2\tau_{\parallel}} + \frac{1}{\tau_{\phi}}, \tag{B.5.16}$$

with

$$\frac{1}{\tau_{\phi}} = \frac{\pi}{\hbar} n_{imp}^{2D} \nu_F J_{sd}^2 \langle \hat{S}_z^2\rangle. \tag{B.5.17}$$

2.5.2 Periodic Magnetic Moments

Strictly speaking, the expressions (B.5.8) are general and can be used for situations beyond the Weiss-field and single scattering approximations. Now let us show how to calculate the more exact expression for spin relaxation time. For periodic magnetic moments, the spin-spin correlation is a function of relative coordinate $\vec{R}_{j'j} = \vec{R}_{j'} - \vec{R}_j$: It can be represented as a Fourier series

$$D_{-+}^{\mathbf{z}}(\vec{R}_{j'j}, t) = \frac{1}{M}\sum_{\vec{q}} e^{i\vec{q}\cdot\vec{R}_{j'j}} \int_{-\infty}^{+\infty} d\omega e^{-i\omega t} D_{-+}^{\mathbf{z}}(\vec{q}, \omega). \tag{B.5.18}$$

Hence, we reach

$$W_{\Downarrow\Uparrow}(\vec{k}', \vec{k}) = \frac{\pi M J_{sd}^2}{2\hbar^2 V^2}\sum_{\vec{K}} D_{-+}^{\mathbf{z}}(\vec{k} - \vec{k}' + \vec{K}, \omega_{\vec{k}\uparrow} - \omega_{\vec{k}'\downarrow}). \tag{B.5.19}$$

where we have used the relation

$$\frac{1}{M}\sum_{j'} e^{i\left(\vec{k}' - \vec{k} + \vec{q}\right)\cdot\vec{R}_{j'j}} = \sum_{\vec{K}} \delta_{\vec{q},\vec{k}-\vec{k}'+\vec{K}}. \tag{B.5.20}$$

The sum over $\vec{K}$ describes umklapp processes and runs over the reciprocal (magnetic) lattice until one value is found for which $\vec{q} = \vec{k} - \vec{k}' + \vec{K}$ lies in the first Brillouin zone of the magnetic lattice. Hence, (B.5.8) becomes

$$\frac{1}{t_{\mathbf{z}}} = \frac{\pi n_{imp}^{3D} J_{sd}^2}{\hbar^2 k_B T V^2}\frac{1}{\nu_F}\sum_{\vec{k}\vec{k}'}\sum_{\vec{K}} D_{-+}^{\mathbf{z}}(\vec{k} - \vec{k}' + \vec{K}, \omega_{\vec{k}\uparrow} - \omega_{\vec{k}'\downarrow}) f\left(\hbar\omega_{\vec{k}\Uparrow}\right)\left[1 - f\left(\hbar\omega_{\vec{k}'\Downarrow}\right)\right]. \tag{B.5.21}$$

This is the general expression for all kinds of magnetic configuration for the periodic magnetic moments. However, it is too complicated. The calculation of spin-spin correlation functions $D_{-+}^{\mathbf{z}}(\vec{q}, \omega)$, itself, is an exciting challenge, which thousands of scientists devote themselves to after quantum mechanics was built.

2.5.3 Weiss theory

In Weiss theory, the interaction between local moments amounts only to a renormalization of the Zeeman term in equation (2.2.3),

$$g\mu_B \sum_j \vec{S}_j \cdot \vec{B} \to g\mu_B \sum_j \vec{S}_j \cdot \vec{H}_j. \tag{B.5.22}$$

The Weiss field $\vec{H}_j$ acting on the local moment becomes

$$\vec{H}_j = \vec{B} - \frac{1}{g\mu_B} \sum_i J_{ij} \langle \vec{S}_i \rangle, \tag{B.5.23}$$

where the sum is taken over the nearest neighbor. Since all spins have equal averages $\left\langle \vec{S}_j \right\rangle = \left\langle \vec{S} \right\rangle$ and equal Weiss fields $\vec{H}_j = \vec{H}$, all oriented co-linear with the magnetic field $\vec{B}$. It is convenient to introduce the following notation $S_\parallel = \vec{n} \cdot \vec{S}$. Hence,

$$H = B - \frac{J(\vec{0})}{g\mu_B} \langle S_\parallel \rangle, \tag{B.5.24}$$

with

$$J(\vec{q}) = \sum_j J_{ij} e^{+i\vec{q}\cdot\vec{R}_{ij}}. \tag{B.5.25}$$

By self-consistency, the average spin is determined by this Weiss field,

$$\langle S_\parallel \rangle = -SB_S \left[\beta S \left(\hbar\omega_B - J(\vec{0}) \langle S_\parallel \rangle \right) \right], \tag{B.5.26}$$

with $\omega_B = g\mu_B B/\hbar$, where $B_S(x)$ is the Brillouin function and $\beta = 1/k_B T$. This can be simply solved to obtain the magnetic field and temperature dependence of spin expactation.

Next, we show some important relations for spin-spin correlation function defined as $D_{\alpha\beta}(t) = \langle S_\alpha(t) S_\beta \rangle$, which can be expressed as a function of spin expectation, $\langle S_\parallel \rangle$ within Weiss theory. For longitudinal spin relaxation time induced by the spin-flip, we require correlators

$$D_{\mp\pm}(\omega) = \frac{1}{2\pi} \int_{-\infty}^{+\infty} dt e^{i\omega t} D_{\mp\pm}(t). \tag{B.5.27}$$

With Weiss theory, we reach

$$D_{\mp\pm}(\omega) = \langle S_\mp S_\pm \rangle \delta(\omega \mp \omega_W), \tag{B.5.28}$$

i.e.,

$$D_{-+}(\omega) = [S(S+1) - \langle S_\parallel^2 \rangle - \langle S_\parallel \rangle] \delta(\omega - \omega_W), \tag{B.5.29}$$

$$D_{+-}(\omega) = [S(S+1) - \langle S_\parallel^2 \rangle + \langle S_\parallel \rangle] \delta(\omega + \omega_W). \tag{B.5.30}$$

where $\omega_W = \omega_B - J(\vec{0}) \left\langle S_\parallel \right\rangle / \hbar$ is the frequency of Weiss field. By the virtue of the fluctuation-dissipation theorem (Giuliani and Vignale, 2005), we have

$$D_{-+}(\omega) = e^{\beta\hbar\omega} D_{+-}(-\omega). \tag{B.5.31}$$

Substituting equations (B.5.29) and (B.5.30) in to equation (B.5.31), we obtain

$$\langle S_{\parallel}^2 \rangle = S(S+1) + \coth(\beta\hbar\omega_W/2)\langle S_{\parallel}\rangle. \tag{B.5.32}$$

Substituting equation (B.5.32) into equations (B.5.29) and (B.5.30), we reach

$$D_{-+}(\omega) = [\coth(\beta\hbar\omega_W/2)+1]|\langle S_{\parallel}\rangle|\delta(\omega-\omega_W), \tag{B.5.33}$$
$$D_{+-}(\omega) = [\coth(\beta\hbar\omega_W/2)-1]|\langle S_{\parallel}\rangle|\delta(\omega+\omega_W). \tag{B.5.34}$$

2.5.4 Diffusion Equation

Let's start with the continuity equation and constitutive equation for the spin accumulation in NM

$$\dot{\mu}_s^v(z) + \frac{1}{e\nu_F}\partial_z J_s^v(z) - \omega_B \epsilon_{v\nu\kappa} n_\nu \mu_s^\kappa(z) = -\tau_S^{-1}\mu_s^v(z), \tag{B.5.35}$$

$$J_{s,i}^v(z) = -\frac{\sigma_D}{2e}\partial_i \mu_s^v(z) + \theta_{SH}\epsilon_{iv\kappa}\sigma_D E_\kappa\ . \tag{B.5.36}$$

For the simplicity, we have assume that both layers are translation invariant in the (x,y) plane. If the NM/MI interface is located at $z=0$, integrating continuity equation (B.5.35) over $[-b,0]$ leads to boundary condition at NM/MI interface

$$eJ_{s,z}^v\big|_{z=-b}^{z=0} = b\omega_L\epsilon_{v\nu\kappa}n_\nu\mu_s^\kappa - \left(\frac{b}{\tau_S}+\frac{1}{\tau_\perp}\right)\mu_s^v - \left(\frac{1}{\tau_\parallel}-\frac{1}{\tau_\perp}\right)n_v(\vec{n}\cdot\vec{\mu}_s). \tag{B.5.37}$$

The boundary conditions require that spin current $J_{s,i}^v(\vec{r})$ is continuous at both magnetic interface and vacuum interface. For vacuum interface $(z=d_N)$, the spin current should vanish, i.e., $J_{s,i}^v(d_N)=0$. It implies that no spin current can enter or exit the 2D conductive channel in $\hat{z}$-direction. Read from constitutive equation (B.5.36), we obtain first boundary condition:

$$0 = -\frac{\sigma_D}{2e}\,\partial_z\mu_s^v|_{z=d_N} - J_{SH}^0\delta_{vy}, \tag{B.5.38}$$

where $J_{SH}^0 = \theta_{SH}\sigma_D E_x$ is the uniform spin Hall current, i.e., the spin current generated directly by the SHE. At magnetic interface $(z=0)$, we have the second boundary condition

$$e\vec{J}_{s,z}(0) = G_s\vec{\mu}_s + G_r\vec{n}\times(\vec{n}\times\vec{\mu}_s) + G_i\vec{n}\times\vec{\mu}_s, \tag{B.5.39}$$

Substituting (B.5.35) into $\nabla\cdot$ (B.5.36), one obtains the spin-diffusion equation in the NM (Chen et al., 2013; Vélez et al., 2016b), which in the stationary case simply reads

$$\nabla_{\vec{r}}^2\mu_s^v(\vec{r}) = \mathcal{M}_{v\nu}\mu_s^\nu(\vec{r}), \tag{B.5.40}$$

with

$$\mathcal{M}_{v\nu} = \ell_S^{-2}\delta_{v\nu} - \ell_B^{-2}\epsilon_{v\kappa\nu}n_\kappa. \tag{B.5.41}$$

Here $\ell_S = \sqrt{\mathcal{D}\tau_S}$ and $\ell_B = \sqrt{\mathcal{D}/\omega_B}$, where $\mathcal{D} = \sigma_D/\left(2\nu_F e^2\right)$ is the diffusion coefficient. The electrons are diffused by eigen-modes of diffusion matrix $\mathcal{M}$. It is easy to get the eigenvalues and eigenvectors of diffusion matrix $\mathcal{M}$, i.e., $\ell_a^{-2}\mathcal{E}_{va} = \mathcal{M}_{v\nu}\mathcal{E}_{\nu a}$ with eigenvalues

$$\ell_a^{-2} = [\ell_S^{-2} + i\ell_B^{-2}, \ell_S^{-2} - i\ell_B^{-2}, \ell_S^{-2}], \tag{B.5.42}$$

and eigenvectors

$$\mathcal{E} = \begin{bmatrix} \frac{\hat{m}_1^2-1}{\sqrt{2}N_r} & \frac{\hat{m}_1^2-1}{\sqrt{2}N_r} & \hat{m}_1 \\ \frac{+i\hat{m}_3+\hat{m}_1\hat{m}_2}{\sqrt{2}N_r} & \frac{-i\hat{m}_3+\hat{m}_1\hat{m}_2}{\sqrt{2}N_r} & \hat{m}_2 \\ \frac{-i\hat{m}_2+\hat{m}_1\hat{m}_3}{\sqrt{2}N_r} & \frac{+i\hat{m}_2+\hat{m}_1\hat{m}_3}{\sqrt{2}N_r} & \hat{m}_3 \end{bmatrix}, \tag{B.5.43}$$

with $N_r = \sqrt{(1-\hat{m}_1^2)}$. Here we also present the inverse of eigenvectors

$$\mathcal{E}^{-1} = \begin{bmatrix} \frac{\hat{m}_1^2-1}{\sqrt{2}N_r} & \frac{-i\hat{m}_3+\hat{m}_1\hat{m}_2}{\sqrt{2}N_r} & \frac{+i\hat{m}_2+\hat{m}_1\hat{m}_3}{\sqrt{2}N_r} \\ \frac{\hat{m}_1^2-1}{\sqrt{2}N_r} & \frac{+i\hat{m}_3+\hat{m}_1\hat{m}_2}{\sqrt{2}N_r} & \frac{-i\hat{m}_2+\hat{m}_1\hat{m}_3}{\sqrt{2}N_r} \\ \hat{m}_1 & \hat{m}_2 & \hat{m}_3 \end{bmatrix}. \tag{B.5.44}$$

The solution of diffusion equation (B.5.40) can be assume that

$$\mu_s^v = \sum_\nu \mathcal{E}_{v\nu}[A_\nu e^{+z/\ell_\nu} + B_\nu e^{-z/\ell_\nu}]. \tag{B.5.45}$$

Substituting (B.5.45) into BCs (B.5.38), we obtain

$$\sum_\nu \frac{\sigma_D}{\ell_\nu}\left(A'_\nu - B'_\nu\right)\mathcal{E}_{v\nu} = -\delta_{vy} 2eJ^0_{SH}, \tag{B.5.46}$$

which leads into

$$\frac{A'_\nu}{2eJ^0_{SH}} - \frac{B'_\nu}{2eJ^0_{SH}} = -\mathcal{E}^{-1}_{\nu y}\frac{\ell_\nu}{\sigma_D}, \tag{B.5.47}$$

with

$$A'_\nu = A_\nu e^{+d_N/\ell_\nu}, B'_\nu = B_\nu e^{-d_N/\ell_\nu}. \tag{B.5.48}$$

So that we obtain $\mu_s^v = \mu_{\mathrm{CH}}^v + \mu_{\mathrm{SH}}^v$ with

$$\mu_{\mathrm{CH}}^v = \sum_\nu \mathcal{E}_{v\nu} A'_\nu 2\cosh\left(\frac{z-d_N}{\ell_\nu}\right), \tag{B.5.49}$$

$$\mu_{\mathrm{SH}}^v = 2eJ^0_{SH}\sum_\nu \mathcal{E}_{v\nu}\mathcal{E}^{-1}_{\nu 2}\frac{\ell_\nu}{\sigma_D}e^{-(z-d_N)/\ell_\nu}. \tag{B.5.50}$$

Substituting the above solutions (B.5.49) and (B.5.50) into BCs (B.5.39), we obtian

$$eJ_b^v = \sum_\nu \mathcal{E}_{v\nu} A'_\nu\left(g_\nu - \mathcal{G}_\nu\right)2\cosh\left(\frac{d_N}{\ell_\nu}\right), \tag{B.5.51}$$

with

$$g_\nu = \frac{\sigma_D}{2\ell_\nu}\tanh\left(\frac{d_N}{\ell_\nu}\right), \tag{B.5.52}$$

$$\mathcal{G}_\nu = \left[G_{\mathrm{s}}^+, G_{\mathrm{s}}^-, G_{\mathrm{s}}\right], G_{\mathrm{s}}^\pm = G_{\mathrm{s}} - \left(G_{\mathrm{r}} \pm iG_{\mathrm{i}}\right). \tag{B.5.53}$$

Here we used the relation

$$n^v = \mathcal{E}_{v3} = \mathcal{E}^{-1}_{3v}, \tag{B.5.54}$$

$$\eta_a \mathcal{E}_{va} = -\epsilon_{v\kappa\nu} n_\kappa \mathcal{E}_{va}, \tag{B.5.55}$$

with $\eta_a = [+i, -i, 0]$. The current J_b^v composes of two parts $eJ_b^v = \delta_{vy} eJ_{SH}^0 + eJ_{SH}^v$ with

$$\frac{J_{SH}^v}{J_{SH}^0} = \sum_\nu \mathcal{E}_{v\nu} \mathcal{E}_{\nu y}^{-1} \left(-1 + 2\mathcal{G}_\nu \frac{\ell_\nu}{\sigma_D} \right) e^{+d_N/\ell_\nu}. \tag{B.5.56}$$

Finally we obtain

$$A'_\nu \left(g_\nu - \mathcal{G}_\nu \right) 2\cosh\left(\frac{d_N}{\ell_\nu} \right) = \sum_v \mathcal{E}_{\nu v}^{-1} eJ_b^v, \tag{B.5.57}$$

which leads to

$$\frac{\mu_{\mathrm{CH}}^v}{eJ_{SH}^0} = \sum_\nu \mathcal{E}_{v\nu} \mathcal{E}_{\nu y}^{-1} \frac{\cosh\left[(z - d_N)/\ell_\nu \right]}{G_\nu \cosh\left(d_N/\ell_\nu \right)}, \tag{B.5.58}$$

with

$$G_\nu^{-1} = \frac{\frac{2\ell_\nu}{\sigma_D} \tanh\left(\frac{d_N}{2\ell_\nu} \right)}{1 - \mathcal{G}_\nu \frac{2\ell_\nu}{\sigma_D} \coth\left(\frac{d_N}{\ell_\nu} \right)} - 2\frac{\ell_\nu}{\sigma_D} e^{+d_N/\ell_\nu}. \tag{B.5.59}$$

Final we obtain the total solutions

$$\frac{\mu_s^v(z)}{eJ_{SH}^0} = 2\sum_\nu \mathcal{E}_{v\nu} \mathcal{E}_{\nu y}^{-1} \frac{\ell_\nu}{\sigma_D} \left[\frac{\cosh\left(\frac{z - d_N}{\ell_\nu} \right)}{\mathcal{X}_\nu \cosh\left(\frac{d_N}{\ell_\nu} \right)} - \frac{\sinh\left(\frac{z}{\ell_\nu} \right)}{\cosh\left(\frac{d_N}{\ell_\nu} \right)} \right]. \tag{B.5.60}$$

with

$$\mathcal{X}_\nu^{-1} = \frac{\tanh\left(\frac{d_N}{2\ell_\nu} \right)}{1 - \mathcal{G}_\nu \frac{2\ell_\nu}{\sigma_D} \coth\left(\frac{d_N}{\ell_\nu} \right)}. \tag{B.5.61}$$

For magnetic field in z-axis direction, we have

$$\mathcal{E} = \begin{bmatrix} \frac{-1}{\sqrt{2}} & \frac{-1}{\sqrt{2}} & 0 \\ \frac{+i}{\sqrt{2}} & \frac{-i}{\sqrt{2}} & 0 \\ 0 & 0 & 1 \end{bmatrix}, \mathcal{E}^{-1} = \begin{bmatrix} \frac{-1}{\sqrt{2}} & \frac{-i}{\sqrt{2}} & 0 \\ \frac{-1}{\sqrt{2}} & \frac{+i}{\sqrt{2}} & 0 \\ 0 & 0 & 1 \end{bmatrix}. \tag{B.5.62}$$

Hence, the spin densities reduce into

$$\frac{\mu_s^x(z)}{eJ_{SH}^0} = -2\mathrm{Im}\left\{ \frac{\Lambda}{\sigma_D} \left[\frac{\cosh\left(\frac{z - d_N}{\Lambda} \right)}{\mathcal{X} \cosh\left(\frac{d_N}{\Lambda} \right)} - \frac{\sinh\left(\frac{z}{\Lambda} \right)}{\cosh\left(\frac{d_N}{\Lambda} \right)} \right] \right\}, \tag{B.5.63}$$

$$\frac{\mu_s^y(z)}{eJ_{SH}^0} = +2\mathrm{Re}\left\{ \frac{\Lambda}{\sigma_D} \left[\frac{\cosh\left(\frac{z - d_N}{\Lambda} \right)}{\mathcal{X} \cosh\left(\frac{d_N}{\Lambda} \right)} - \frac{\sinh\left(\frac{z}{\Lambda} \right)}{\cosh\left(\frac{d_N}{\Lambda} \right)} \right] \right\}, \tag{B.5.64}$$

with

$$\mathcal{X}^{-1} = \frac{\tanh\left(\frac{d_N}{2\Lambda} \right)}{1 - \left[G_\mathrm{s} - (G_\mathrm{r} + iG_\mathrm{i}) \right] \frac{2\Lambda}{\sigma_D} \coth\left(\frac{d_N}{\Lambda} \right)}. \tag{B.5.65}$$

In the presence of SMR and HMR, we define the correction of charge current as

$$\Delta \vec{J}_c = -\frac{\theta_{SH} \sigma_D}{2ed_N} \int_0^{d_N} \left[\hat{\vec{x}} \times \hat{\vec{z}} \partial_z \mu_s^x(z) + \hat{\vec{y}} \times \hat{\vec{z}} \partial_z \mu_s^y(z) \right] dz. \tag{B.5.66}$$

For the electric field in x-axis direction, the total longitudinal (along $\hat{x}$) and transverse or Hall (along $\hat{y}$) charge currents become

$$\begin{aligned}\frac{\Delta J_c^L}{J_c^D} &= -\theta_{SH}^2 \frac{\sigma_D}{2d_N}\left[\frac{\mu_{s2}\left(d_N\right)}{eJ_{SH}^0} - \frac{\mu_{s2}\left(0\right)}{eJ_{SH}^0}\right] \\ &= +\theta_{SH}^2 \sum_\nu \mathcal{E}_{2\nu}\mathcal{E}_{\nu 2}^{-1}\mathcal{R}(\mathcal{G}_\nu, \ell_\nu),\end{aligned} \tag{B.5.67}$$

$$\begin{aligned}\frac{\Delta J_c^T}{j_c^0} &= +\theta_{SH}^2 \frac{\sigma_D}{2d_N}\left[\frac{\mu_{s1}\left(d_N\right)}{ej_{\rm sH}^0} - \frac{\mu_{s1}\left(0\right)}{ej_{SH}^0}\right] \\ &= -\theta_{\rm sH}^2 \sum_\nu \mathcal{E}_{1\nu}\mathcal{E}_{\nu 2}^{-1}\mathcal{R}(\mathcal{G}_\nu, \ell_\nu),\end{aligned} \tag{B.5.68}$$

with

$$\mathcal{R}(\mathcal{G}_\nu, \ell_\nu) = \mathcal{R}_{HMR}(\ell_\nu)\mathcal{R}_{SMR}(\mathcal{G}_\nu, \ell_\nu), \tag{B.5.69}$$

where

$$\mathcal{R}_{HMR}(\ell_\nu) = \frac{2\ell_\nu}{d_N}\tanh\left(\frac{d_N}{2\ell_\nu}\right), \tag{B.5.70}$$

$$\mathcal{R}_{SMR}(\mathcal{G}_\nu, \ell_\nu) = \frac{1 - \frac{\mathcal{G}_\nu \ell_\nu}{\sigma_D}\coth\left(\frac{d_N}{2\ell_\nu}\right)}{1 - \frac{\mathcal{G}_\nu \ell_\nu}{\sigma_D} 2\coth\left(\frac{d_N}{\ell_\nu}\right)}, \tag{B.5.71}$$

Substituting eigenvectors (B.5.43) and (B.5.44) into (B.5.67) and (B.5.68), we obtain

$$\frac{J_c^L}{j_c^0} = 1 + \theta_{\rm sH}^2\left\{\mathcal{R}(G_s, \ell_S) + \left[\mathrm{Re}\left(\mathcal{R}(G_s - G_{\uparrow\downarrow}, \ell_+)\right) - \mathcal{R}(G_s, \ell_S)\right]\left(1 - \hat{m}_1^2\right)\right\}, \tag{B.5.72}$$

$$\frac{J_c^T}{j_c^0} = -\theta_{\rm sH}^2\left\{\left[\mathcal{R}(G_s, \ell_S) - \mathrm{Re}\left(\mathcal{R}(G_s - G_{\uparrow\downarrow}, \ell_+)\right)\right]\hat{m}_1\hat{m}_2 - \mathrm{Im}\left(\mathcal{R}(G_s - G_{\uparrow\downarrow}, \ell_+)\right)\hat{m}_3\right\}, \tag{B.5.73}$$

which lead to

$$\rho_L \simeq \rho_D + \Delta\rho_0 + \Delta\rho_1\left(1 - \hat{n}_y^2\right), \tag{B.5.74}$$

$$\rho_T \simeq -\rho_D\omega_c\tau_D\hat{n}_z + \Delta\rho_1\hat{n}_x\hat{n}_y + \Delta\rho_2\hat{n}_z, \tag{B.5.75}$$

but now the different contributions are given by

$$\frac{\Delta\rho_0}{\rho_D} = \theta_{SH}^2[2 - \mathcal{R}(G_s, \ell_S)], \tag{B.5.76}$$

$$\frac{\Delta\rho_1}{\rho_D} = \theta_{SH}^2\{\mathcal{R}(G_s, \ell_S) - \mathrm{Re}\left[\mathcal{R}(G_s - G_{\uparrow\downarrow}, \ell_+)\right]\}, \tag{B.5.77}$$

$$\frac{\Delta\rho_2}{\rho_D} = \theta_{SH}^2 \mathrm{Im}\left[\mathcal{R}(G_s - G_{\uparrow\downarrow}, \ell_+)\right], \tag{B.5.78}$$

where we have included the correction of resistivity induced by SHE in $\Delta\rho_0$.

It is instructive to expand the HMR effect in powers of ω_L,

$$\frac{\ell_S}{\ell_+} = \sqrt{1 + i\omega_B\tau_S} \approx 1 + \frac{i}{2}\omega_B\tau_S + \frac{1}{8}(\omega_B\tau_S)^2. \tag{B.5.79}$$

The expansion parameter here is $\omega_B\tau_S \ll 1$. For most experimental needs, expansion

of HMR to the second-order in this small parameter is sufficient. Without any G's (more precisely for $G_i = 0$ and $\mathcal{R} = \mathcal{R}_{HMR}$), the linear in ω_B term drops out when expanding and taking the real part in Eq. (B.5.77). Then, only the quadratic term remains, and it leads to the characteristic quadratic dependence of the HMR effect, seen in the longitudinal resistivity as a function of the magnetic field applied along z or x. G_r and G_s are assumed to be constant here.

In the presence of G_i, the liner in ω_B term does not drop out when taking the real part in Eq. (B.5.77). Since the expansion coefficient is rather cumbersome, we further expand it for $d_N \ll \ell_S$ and $d_N \gg \ell_S$. However, before that, we write out the zeroth order in ω_B term by replacing $\ell_+ \to \ell_S$ in Eq. (B.5.77),

$$\frac{\Delta\rho_1(0)}{\rho_D} = \theta_{SH}^2\{\mathcal{R}(G_s, \ell_S) - \mathrm{Re}\left[\mathcal{R}(G_s - G_{\uparrow\downarrow}, \ell_S)\right]\}, \tag{B.5.80}$$

which represents SMR only without any HMR. The linear in ω_L term for $d_N \ll \ell_S$ reads

$$\Delta\rho_1 \approx \Delta\rho_1(0) - \frac{\theta_{SH}^2 d_N^3 G_i \omega_B}{4\mathcal{D}\ell_S^2\left[G_i^2 + (G_r - G_i)^2\right]}. \tag{B.5.81}$$

Interestingly, the parameter σ_D drops out from the absolute correction in this limit. In the limit $d_N \gg \ell_S$, we obtain

$$\Delta\rho_1 \approx \Delta\rho_1(0) + \frac{2\theta_{SH}^2\ell_S^4 G_i\omega_B\left(1 + 2\ell_S\frac{G_r - G_s}{\sigma_D}\right)}{\mathcal{D}d_N\sigma_0^2\left[\left(1 + 2\ell_S\frac{G_r - G_s}{\sigma_D}\right)^2 + \frac{4\ell_S^2 G_i^2}{\sigma_D^2}\right]^2}. \tag{B.5.82}$$

Interestingly, there is a change of sign of the linear in ω_B term, when going from the limit $d_N \ll \ell_S$ to the limit $d_N \gg \ell_S$. Also, in this limit, the correction depends on σ_D.

Chapter 3

Observation of paramagnetic spin Hall magnetoresistance in Pt/GGG

This work was performed in collaboration with Prof. Eiji Saitoh and Prof. Felix Casanova and their Ph.D. students Dr. Koichi Oyanagi and Dr. Juan M Gomez-Perez, respectively. My contribution to this work is the theoretical analysis and the numerical fitting to their experimental data.

3.1 Introduction

Spintronics (Maekawa and Kimura, 2017) aims to add new functionalities to the conventional electronics using interconversion of spin angular momentum between different carriers in solids (Otani et al., 2017). Especially, the spin exchange between conduction electron spins in a normal metal (NM), and magnetization, M, in a ferromagnet (FM) is a central topic (Tserkovnyak et al., 2005) to manipulate M for developing new types of magnetic memory devices (Liu and Yu, 2019). When spin angular momentum is transferred into a FM through a NM/FM interface, it modifies the transverse dynamics of M by exerting two types of torque, known as spin-transfer torque (Slonczewski, 1996) and field-like torque (Xia et al., 2002), while it hardly couples to the longitudinal component. This is because the magnetic susceptibility in spin order, such as FM, is anisotropic due to the broken rotational symmetry reflecting spontaneous M; the magnetic susceptibility is large (small) along the transverse (longitudinal) direction, resulting in anisotropy into the spin injection.

The spin-mixing conductance $G_{\uparrow\downarrow}$ has characterized the efficiency of the transverse spin injection (Tserkovnyak, Brataas, and Bauer, 2002). Its evaluation is of crucial importance in spintronics as $G_{\uparrow\downarrow}$ governs the device performance (Weiler et al., 2013). To this end, the spin Hall magnetoresistance (SMR) can be a powerful tool (Nakayama et al., 2013; Chen et al., 2013). As we explained in Subsection 1.4.1, SMR is a modulation of resistance to the relative orientation of the magnetization in the MI, which smoothly follows the direction of the external magnetic field and the spin polarization of spin Hall current generated by spin Hall effect (SHE) in HM. Prior experimental research of SMR has thoroughly investigated the interface between HM and ferrimagnetic insulators, such as $Tm_3Fe_5O_{12}$ (Vélez et al., 2019a; Avci et al., 2017) and $Y_3Fe_5O_{12}$ (YIG) (Isasa et al., 2016; Marmion et al., 2014; Nakayama et al., 2013; Kosub et al., 2018; Althammer et al., 2013; Vlietstra et al., 2013a; Hahn et al., 2013; Isasa et al., 2014; Meyer et al., 2014). However, little has been conducted to investigate other MIs, such as paramagnetic, ferromagnetic, and antiferromagnetic insulators, which are also attracting more and more attention due to the new physics and phenomena to be studied by SMR (Zhang, Bergeret, and Golovach, 2019). To be specific, a paramagnetic insulator (PMI) allows an efficient spin

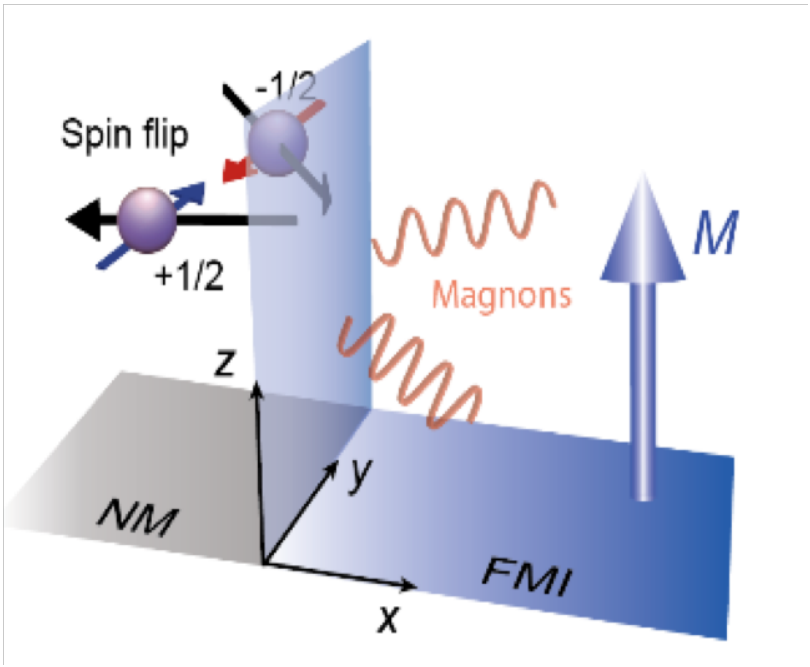

FIGURE 3.1: **The sketches of the transfer of angular momentum from the heavy metal (HM) to ferromagnetic insulator (FMI).** Figure comes from the PhD thesis of Dr. Koichi Oyanagi.

transport at the interface induced by spin-flip scattering in high-temperature and low field limit (Zhang, Bergeret, and Golovach, 2019), revealing that the spin-sink conductance G_s associated with STT as depicted in FIGURE 1.6 (a), can be pivotal in the HM/PMI interface, in addition to spin-mixing conductance G_r and G_i whose torques are plotted in FIGURE 1.6 (a) and (b), respectively. In contrast to a ferromagnetic insulator (FMI) as plotted in FIGURE 3.1, the magnetization of paramagnets is free from the exchange stiffness, and hence can be well controlled by the wide range of magnetic field. Moreover, in Chapter 2, we have expected the existence of an additional FLT, which is due to the interfacial Hanle precession induced by the local moments in the HM/PMI interface. It has the same role as the G_i in the SMR scenario, which stems from the interfacial SOC (Chen et al., 2013; Vlietstra et al., 2013b; Althammer et al., 2013; Meyer et al., 2015). In the case of YIG, G_i is at least one order of magnitude smaller than G_r, leading to a small contribution. Consequently, $\Delta\rho_2/\rho$ is 100 times smaller than $\Delta\rho_1/\rho$ (Althammer et al., 2013; Vlietstra et al., 2013b; Jia et al., 2011; Meyer et al., 2015). However, in the case of a PMI, this phenomenon could be different. In the high-field and low-temperature limits, the local moments at HM/PMI interface can acquire a sizable magnetization in the direction of the external magnetic field. Finally, the spin exchange coupling between the interfacial magnetic moment and the conduction electrons around HM/PMI interface might lead to a larger interfacial exchange field, *i.e.*, a larger G_i.

In this chapter, we demonstrate spin Hall magnetoresistance (SMR) in anisotropic paramagnetic insulator (PI) $Gd_3Ga_5O_{12}$ (GGG), with an NM (Pt) contact. Unlike FMs, a paramagnet has no spontaneous magnetization and shows huge longitudinal susceptibility. At the interface, conduction electron spins in NM couple to the transverse component (spin-transfer and field-like torque) and the longitudinal component of spins in PI through the interfacial spin-flip process, whose efficiency is characterized by the spin-sink conductance G_s. Both $G_{\uparrow\downarrow}$ and G_s can be crucial for the spin transport at NM/MI heterostructure. First, we show the evidence of

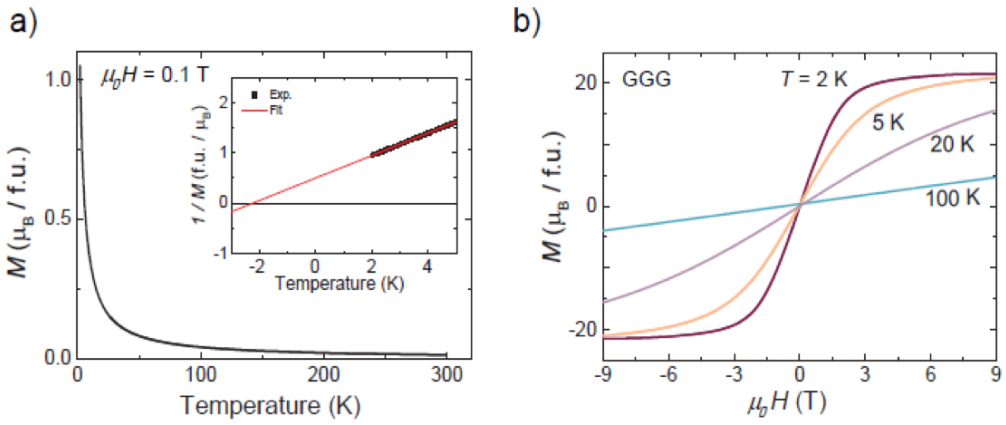

FIGURE 3.2: **The temperature and field dependence of the magnetization in GGG.** (a) The magnetization of GGG, M as a function of temperature T at field H = 0.1 T. The inset shows the temperature dependence of $1/M$, where the red line indicates the linear fit showing the Curie-Weiss temperature $T_{CW} = -2$ K. (b) M as a function of field H curves at different temperature T.

the paramagnetic SMR in Pt/GGG through transverse resistivity measurements. By combining experimental and theoretical results, we then evaluate $G_{\uparrow\downarrow}$ and G_s, and demonstrate that the conductance is controllable with external magnetic fields B, which is realized by changing B. Such controllability in paramagnets is distinct from SMR in FMs, highlighting the novelty of the paramagnetic SMR.

3.2 Experimental details

In this section, we briefly introduce the details of the SMR experiment in HM/PMI heterostructure, such as the thermal and magnetic properties of PMI and the device parameters.

Here, the paramagnetic insulator is chosen as $Gd_3Ga_5O_{12}$ (GGG). It has a lattice constant $a_{GGG} = 12.38$ A, an electric band gap of 6 eV (Ghimire et al., 2015), and a short-range magnetic order (Cornelissen et al., 2017). It is well known that GGG shows a textbook-like paramagnetic behavior down to low temperatures due to its small Curie-Weiss temperature $T_{CW} = -2$ K (Kinney and Wolf, 1979). FIGURE 3.2 (a) plots the temperature T dependence of the magnetization in GGG, M, which is measured by a vibrating sample magnetometer (Foner, 1959). M increases with decreasing T following the Curie-Weiss law. The inset of FIGURE 3.2 (a) plots the $1/M$ of GGG as a function of temperature, T, which clearly indicates the Curie-Weiss temperature T_{CW} of -2K. The field dependence of M is depicted in FIGURE 3.2 (b) for different temperatures. Obviously, we find that M increases linearly with the field at high-temperature case; whereas, at low-temperatures regime, M shows saturation behavior as a function of B. The magnetization of GGG arises from Gd^{3+} ions with spin 7/2, which couple with each other by the weak nearest-neighbor exchange interaction with strength $J_{ex} \sim 0.1$ K (Schiffer et al., 1995). Because of the half-filled $4f-$shell in Gd^{3+}, the orbital angular momentum is zero, and thus GGG shows a small magnetic anisotropy of 0.04 K (Schiffer et al., 1994; Overmeyer et al., 1963).

The devices consist of a 5-nm-thick Pt film deposited by magnetron sputtering in Ar atmosphere on top of the GGG (111) obtained from CRYSTAL GmbH. After

the Pt deposition, a Hall bar (width $w_N = 100\mu$m and length $l_N = 800\mu$m) was defined by photolithography and Ar-ion milling process. The strong SOC in Pt can be recognized as the spin magnetic field and generates spin Hall current via SHE, which is then injected into the Pt/GGG interface. For Pt with Drude resistivity of $\rho = 34\mu\Omega$·cm, the SHE can be parameterized by spin Hall angle $\theta_{SH} = 0.104$ and spin diffusion length $\lambda_s = 2$ nm (Sagasta et al., 2016). The latter is shorter than the thickness of HM, d_N, but is longer than the mean-field length $l = v_F\tau$, with v_F being Fermi velocity and τ being momentum relaxation time. If we further assume that the local moments at Pt/GGG interface are dilute and randomly distributed. Therefore, Pt is in a diffusive regime, with momentum scattering rate τ^{-1} is larger enough, $E_F\tau \ll 1$, and the quantities we are interested in are required to be much larger than the scale of mean-field length, l. Additionally, the g-factor is set to be $g = 2$, and the Fermi energy is tuned to be $E_F = 1.0$ eV, in Pt.

3.3 Results and discussions

We measured the Pt resistivity using direct current reversal method (Casanova et al., 2009) to exclude thermal effects, with a static magnetic field B up to 9 T in the temperature range from 2 K to 300 K. As discussed in Chapter 2, SMR appears in both longitudinal and transverse resistivity. The transverse resistivity is relative to the edge-spin-x accumulation, while the longitudinal resistivity is associated with the edge-spin-y accumulation. However, the longitudinal resistivity measurement, at low-temperature ($T < 50$ K) and high-field regime, posses an extra contribution due to the weak anti-localization in Pt, which is much larger than SMR (Gomez-Perez et al., 2020). To avoid it, we mainly focus on the transverse resistivity, which was derived in Chapter 2. Here, we show it again for the sake of convenience

$$\rho_T \simeq -\rho\omega_c\tau n_z + \Delta\rho_1 n_x n_y + \Delta\rho_2 n_z, \tag{3.3.1}$$

with

$$\Delta\rho_1 = \theta_{SH}^2\rho\left\{\mathcal{R}(G_s,\lambda_s) - \mathrm{Re}\left[\mathcal{R}(G_s - G_{\uparrow\downarrow},\Lambda)\right]\right\}, \tag{3.3.2}$$

$$\Delta\rho_2 = \theta_{SH}^2\rho_D\mathrm{Im}\left[\mathcal{R}(G_s - G_{\uparrow\downarrow},\Lambda)\right], \tag{3.3.3}$$

where weak anti-localization does not contribute to the magnetoresistance measurements. As shown in Eqs. (3.3.2) and (3.3.3), the feild and temperature dependence of spin-dependent conductance is hidden in SMR amplitudes $\Delta\rho_1$ and $\Delta\rho_2$.

3.3.1 Quantification of SMR amplitude $\Delta\rho_1/\rho$

Read from Eq. (3.3.1), the quantification of SMR amplitude $\Delta\rho_1/\rho$ can be easily obtained by measuring the transverse resistivity ρ_T with the external magnetic field applied in $xy-$plane, whose direction is described by angle α. First of all, we performed angle-dependent MR at $T = 2$ K and $\mu_0 H = 3.5$ T, which is plotted in FIGURE 3.3 (a). It exhibits a clear $\sin\alpha\cdot\cos\alpha$ dependence as expected from Eq. (3.3.1), with a maximum and minimum at $\alpha = 45^o$ and $\alpha = 135^o$, respectively. FIGURE 3.3 (b) presents the field-dependent MR curve of the normalized ρ_T at 2 K for different directions of fields. At $\alpha = 45^o$, ρ_T increases up to $\mu_0 H = 5$ T and saturates above this value. On the other hand, at $\alpha = 135^o$, ρ_T decreases with field, being consistent with the SMR symmetry in the work of Althammer et al., 2013; Vélez et al., 2016a.

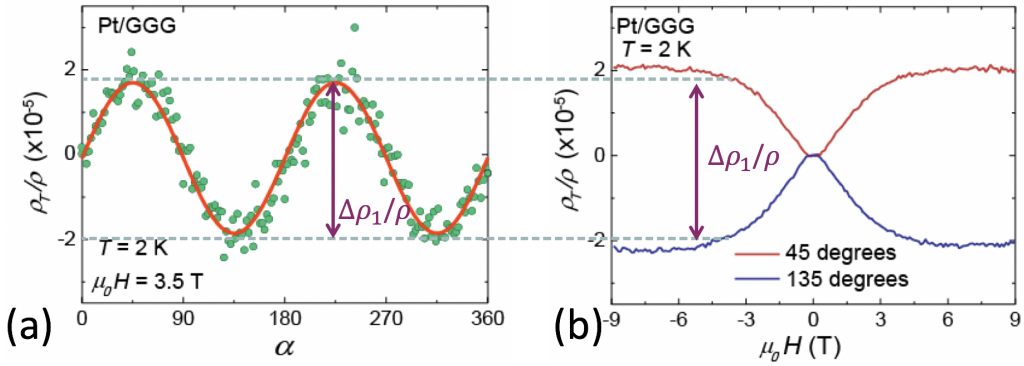

FIGURE 3.3: **Quantification of SMR amplitude $\Delta\rho_1/\rho$.** (a) Transverse angular-dependence MR at 2 K and 3.5 T. The solid line is the sinα·cosα fitting to extract the SMR amplitude $\Delta\rho_1/\rho$. (b) Transverse field-dependent MR at $\alpha = 45^o$ and $\alpha = 135^o$ at 2 K.

By fitting the transverse angle-dependent MR at different magnetic fields, we can obtain the SMR amplitude $\Delta\rho_1/\rho$ as a function of the magnetic field. We can see clearly that the SMR amplitude extracted from the transverse angle-dependent MR is the same as the difference between the transverse field-dependent MR at 45^o and 135^o at the same field, as shown by the dash lines in FIGURE 3.3. The saturation of the field-dependent MR above 5 T, as depicted in FIGURE 3.3 (a), cannot be explained by HMR (Vélez et al., 2016), which has the very same angle-dependent MR symmetry as the SMR but depends on the square of the field. Therefore, the observed trend can only be due to SMR because of the field-induced magnetization in GGG.

3.3.2 Quantification of SMR amplitude $\Delta\rho_2/\rho$

Read from Eq. (3.3.1), the quantification of SMR amplitude $\Delta\rho_2/\rho$ should be conducted by measuring the transverse resistivity ρ_T to the external magnetic field in z direction. It inevitably includes the contribution from OHE, i.e., the first term of the right-hand side of Eq. (3.3.1). The inset of FIGURE 3.4 plots the total transverse resistivity ρ_T/ρ at $T = 2$ K. In a large-field regime, one can observe a clear linear dependence with H, which is obviously related to the CHE in Pt. In a weak magnetic field, we find a non-linear dependence concerning H, which is exactly what we want. To study this signal, we are required to subtract the linear response of OHE from ρ_T/ρ.

FIGURE 3.4 plots the field dependence of ρ_T/ρ after excluding the background from the CHE, i.e., $\Delta\rho_2/\rho$ vs $\mu_0 H$. It is negative for positive H, changing the sign for positive H, which is consistent with the symmetry of the anomalous Hall effect (AHE)-like expected from SMR theory, see Eq. 3.3.1 (Chen et al., 2013). As depicted by the purple curve, $\Delta\rho_2/\rho$ saturates at $H \sim 3.5$ T for temperature $T = 2$ K. Notably, in contrast to YIG, the saturation value of $\Delta\rho_2/\rho \sim 3 \times 10^{-5}$ is in the same order of magnitude as that of $\Delta\rho_1/\rho \sim 5 \times 10^{-5}$. We can also observe this behavior at 5 K and 10 K, with a larger saturation field, which is the same behavior as that of the GGG magnetization presented in FIGURE 3.2(b). Therefore, we can infer that the observed AHE-like behavior corresponds to the component induced by the paramagnetic moments.

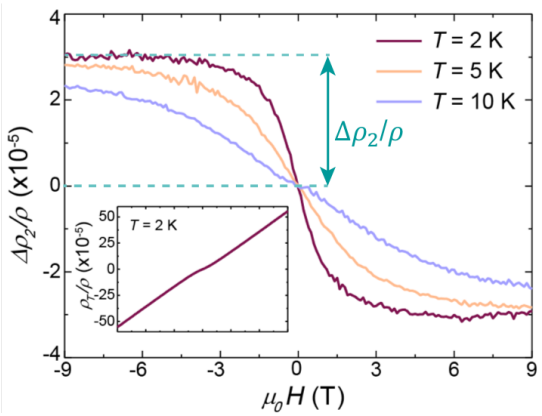

FIGURE 3.4: **Quantification of SMR amplitude $\Delta\rho_2/\rho$.** AHE-like term as a function of the magnetic field at 2.5 K, 5 K and 10 K, after subtracting the linear term related to the OHE (inset shows the raw data).

3.3.3 Calculation of the spin-dependent conductance

The spin transport at the Pt/GGG surface is sketched by the exchange interaction between the spin of itinerant electrons in the Pt, $\vec{s}(\vec{R}_i)$ and the spin of local moments in the GGG, $\vec{S}_j$, which is modeled by Hamiltonian (2.2.4) in chapter 2. The strength of spin-exchange coupling is parameterized by J_{sf}, which describes the hybridization of between 1s electrons in Pt and 4f electrons in GGG. In addition, there is another important parameter delimiting how many local moments participate in the spin transport of itinerant electrons, i.e., the density of magnetic moments in Pt/GGG surface n_{imp}^{2D}. Equipped with these two surface parameters and the expressions for spin-dependent conductance given by Eqs. (2.2.15)-(2.2.17) in chapter 2, we can perform the theoretical fitting of the experimental data $\Delta\rho_1/\rho$ and $\Delta\rho_2/\rho$, quantified in last two subsections with the help of Eqs. (3.3.2) and (3.3.3). For the sake of simplicity, we exclude the feedback effect of the itinerant electrons in Pt on local moments in GGG. The latter are treated as a quantum bath, and hence the magnetic and thermal properties of that are assumed to be independent of itinerant electrons. Based on this assumption, one can acquire the compact expressions for spin-dependent conductance within the Curie-Weiss theory approximation (Zhang, Bergeret, and Golovach, 2019). Furthermore, we will make the molecular field approximation for GGG magnetization, as explained in Appendix 3.5.1.

During the theoretical fitting, the Curie-Weiss temperature T_{CW}, and the surface parameters J_{sf} and n_{imp}^{2D} are treated as free parameters so that we can optimize the theoretical fitting of experimental data. This choice of free parameters is experimentally reasonable since the interfacial properties are complicated and are largely depended on the conditions of crystal growth, crystal face cutting, and so on. FIGURE 3.5 (a) plots the field dependence of theoretical fittings, where purple and blue lines, respectively, correspond to SMR amplitudes $\Delta\rho_1/\rho$ and $\Delta\rho_2/\rho$. The corresponding experimental data for $\Delta\rho_1/\rho$ and $\Delta\rho_2/\rho$ are indicated in the same panel by the purple circles and blue circles, respectively. The optimized theoretical fitting for both SMR amplitudes perfectly reproduces the field dependence of the signals, and the corresponding spin-dependent conductance is shown in FIGURE 3.5 (b). In the low-field limit, the spin orientation of local moments does not prefer any special direction, and hence spin relaxation of itinerant electrons is isotropic, and there is no interfacial exchange field induced by local moments. Consequently, both the real and imaginary parts of spin-mixing conductance G_r and G_i vanish. On the contrary,

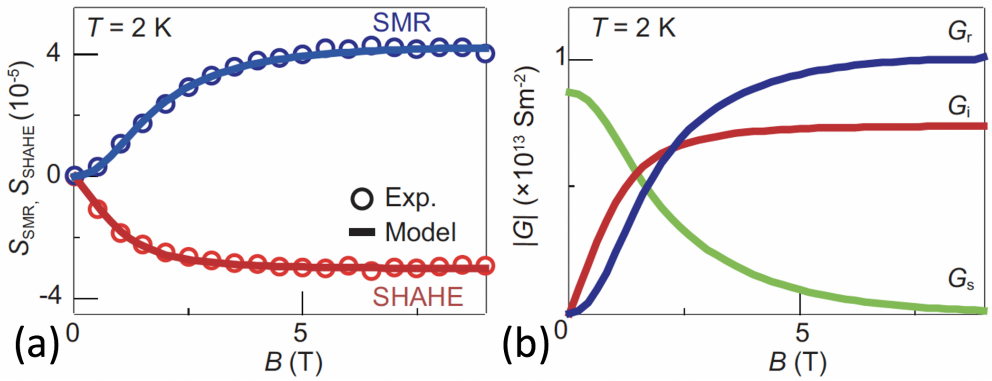

FIGURE 3.5: **Spin Hall magnetoresistance amplitudes and spin-dependent conductance.** (a) $\Delta\rho_1/\rho$ (purple circles) and $\Delta\rho_2/\rho$ (blue circles) as a function of H, with the corresponding fitting to Eqs. (3.3.2) and (3.3.3) using the Curie-Weiss model (purple lines and blue line, respectively) at 2 K for the $H > 0$ range. (b) Spin-dependent conductance obtained from the fittings in panel (a). The red, blue and green lines represent G_r, G_i and G_s, respectively.

a spin-flip happens so easily without any limit from the external magnetic field. As a result, spin-sink conductance G_s takes its maximum value $8 \times 10^{12}\ \Omega^{-1}\mathrm{m}^{-2}$. On the other hand, when H increases, the spins of magnetic moments prefer aligning in the direction of the external field. The itinerant electrons can feel the anisotropic spin relaxation and a sizable exchange field. Thus, spin-mixing conductance G_r and G_i increase and tend to saturate to $G_r \sim 1 \times 10^{13}\ \Omega^{-1}\mathrm{m}^{-2}$ and $G_i \sim 7 \times 10^{12}\ \Omega^{-1}\mathrm{m}^{-2}$, respectively. However, the spin-sink conductance G_s monotonically decreases to zero at large H, where the spin of the itinerant electron is fully frozen, and hence no spin-flip happens anymore.

Next we explore the detailed mechanisms behind SMR amplitudes $\Delta\rho_1/\rho$ and $\Delta\rho_2/\rho$. FIGURE 3.6 (b) shows the comparison between the real part of spin-mixing conductance G_r and the SMR amplitude $\Delta\rho_1/\rho$ as a function of field, H. We find that $\Delta\rho_1/\rho$ is directly proportional to G_r, which is responsible for the STT. This perfect agreement shown in FIGURE 3.6 (b) indicates that $\Delta\rho_1/\rho$ is definitely driven by the STT in Pt/GGG surface, , which is sketched in FIGURE 3.6 (a). On the other hand, FIGURE 3.6 (d) shows the comparison between the imaginary part of spin-mixing conductance G_i and SMR amplitude $|\Delta\rho_2|/\rho$ as a function of field, H. We observe that $|\Delta\rho_2|/\rho$ is also directly proportional to G_i, which is relative to the FLT. Again, the good agreement shown in FIGURE 3.6(b) reveals that $\Delta\rho_2/\rho$ is associated with FLT, which is depicted in FIGURE 3.6 (c). We can also notice that the saturation of $\Delta\rho_2/\rho$ occurs at lower field than that of $\Delta\rho_1/\rho$. This is because G_i is directly proportional to $\langle \widehat{S}_{\parallel} \rangle$ (see Eq. (2.2.17)), whereas G_r is associated with $\langle \widehat{S}_{\parallel}^2 \rangle$ as shown in Eqs. (2.2.16). Extracting the value of the spin-mixing conductance in Pt/GGG interface, we find that both spin-transfer and FLTs are equally important in the spin tranposrt at Pt/GGG heterostruncture. To be specific, we can compare the values extracted from Pt/GGG structrue with that of Pt/YIG in the work of Kosub et al., 2018: $G_r \sim 1 \times 10^{13}\ \Omega^{-1}\mathrm{m}^{-2}$ in Pt/GGG is about 7 times smaller than $G_r \sim 6.6 \times 10^{13}\ \Omega^{-1}\mathrm{m}^{-2}$ in Pt/YIG. However, the imaginary part of the spin-mixing conductance is dramatically opposite. $G_i \sim 7 \times 10^{12}\ \Omega^{-1}\mathrm{m}^{-2}$ in Pt/GGG is about 3 times larger than $G_i \sim 2.2 \times 10^{12}\ \Omega^{-1}\mathrm{m}^{-2}$ in Pt/YIG. In other words, whereas $G_r/G_i \approx 30$ in Pt/YIG, $G_r/G_i \approx 1$ in Pt/GGG.

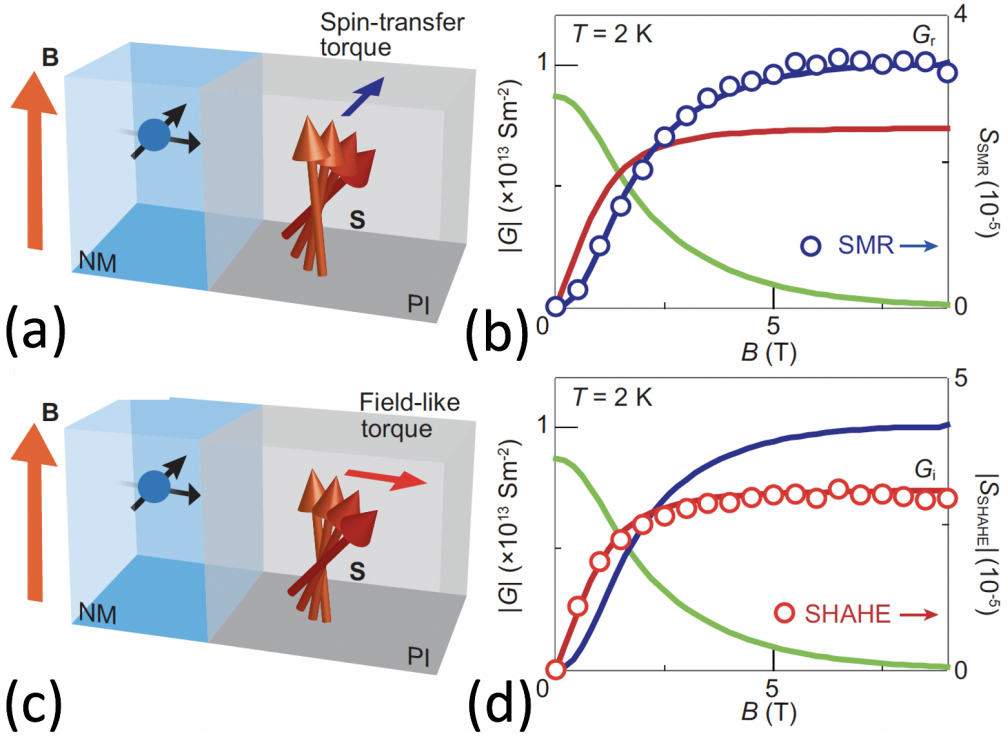

FIGURE 3.6: **The spin-transfer (field-like) torques, the real (imaginary) parts of spin-mixing conductance (spin-mixing conductance), and SMR amplitudes $\Delta\rho_1/\rho$ ($\Delta\rho_2/\rho$).** (a,b) Sketch of the mechanism of STT in panel (a), which is parameterized by real part of spin-mixing conductance G_r in panel (b), where the corresponding SMR amplitude $\Delta\rho_1/\rho$ is indicated by purple circles. (c,d) Sketch of the mechanism of FLT in panel (c), which is parameterized by the imaginary part of spin-mixing conductance G_i in panel (d), where the corresponding SMR amplitude $\Delta\rho_2/\rho$ is indicated by blue circles.

More importantly, from the fitting, we can also extract the Curie-Weiss temperature T_{CW}, and microscopic parameters n_{imp}^{2D} and J_{sf}, where the spin exchange coupling is parameterized by a dimensionless parameter $\nu_F J_{sf}$ with ν_F being density of state at Fermi energy. To obtain the great agreements shown in FIGURE 3.5 (a), the free parameters are chosen as $T_{CW} = -0.66$ K, $n_{imp}^{2D} = 6.7 \times 10^{16}$ atoms/m^2, and $\nu_F J_{sf} = 0.13$. Even though the bulk T_{CW} for GGG is -2 K, as shown in the inset of FIGURE 3.2 (a), we extracted a smaller values of -0.66 K. It is well known that SMR is only sensitive to the magnetic properties around the Pt/GGG surface. As a result, the estimated T_{CW} indicates that the effective exchange interaction between the Gd moments at the interface is smaller than that in the bulk. We also find that n_{imp}^{2D} is only 1% of the ideal value ($n_{Gd}^{2D} = 6.9 \times 10^{18}$ atom/m^2). The last parameter extracted is the *s-f* exchange interaction between the conduction electron of Pt and the localized spins in the 4*f* shell of Gd at the Pt/GGG interface, which is $J_{sf}/a_{Gd}^3 = 2$ meV, where $a_{Gd} = 0.38$ nm is the atomic distance between the Gd moments. Up to now, the interface exchange coupling between conduction electron and 4*f* electron has been assumed to be small. J_{sf} represents the overlap between the conduction electron and the localized spin, and it can be smaller for Pt/GGG than for Pt/YIG. This is expected because the strongly localized 4*f* electrons in Gd^{3+} (responsible for the GGG magnetic moments) overlap less with the conduction electrons in Pt in comparison to the 3*d* electrons in Fe^{3+} (responsible for the YIG magnetic moments).

However, the estimated J_{sf} is the same as that of Pt/YIG interface extracted in the work of Kajiwara et al., 2010. Kajiwara et al., 2010, assumed the ideal density Fe^{3+} at the interface, which could lead to an underestimation of J_{sf}. Another example is the work of Schlitz et al., 2018, where they already suggested the weak exchange coupling in Pt/GGG. The interfacial *s-f* exchange interaction is also assumed to be small in the experiments of spin Seebeck effect by Geprägs et al., 2016.

3.4 Conclusions

In summary, we demonstrate the presence of SMR in a Pt film on top of a paramagnetic insulator GGG. The observed SMR signal shows the clear saturation behavior by applying large magnetic fields at low temperatures, consistent with its paramagnet-like magnetization curve. Our microscopic theory reproduces the SMR signal as a B and T function and provides the spin mixing conductance at the Pt/GGG interface. The large imaginary part of spin mixing conductance indicates the FLT drives SMR using paramagnetic insulators. The smaller SMR signal in Pt/GGG than that in Pt/YIG is attributed to the small interface exchange interaction between 1s electrons in Pt and 4f electrons in GGG. Using a simple ferromagnet with strong interfacial exchange interaction is promising to enhance SMR by combining the spin-transfer and FLTs.

3.5 Appendix

3.5.1 Molecular field approximation for magnetization of GGG

GGG is an ideal Curie-paramagnet with a weak exchange interaction between spins of neighboring Gd ions. Using the molecular field approximation, the thermal average of spin m is calculated by the self-consistent equation

$$\langle m \rangle = -SB_S\left(SC_1 B_{\text{eff}}/T\right), \tag{C.5.1}$$

where S is the electron spin angular momentum of Gd ions, $B_S(x)$ is the Brillouin function of spin S as a function of X, $C_1 = g\mu_B/k_B$, g is the g-factor, μ_B is the Bohr magneton, $B_{\text{eff}} = B + N_{PI} m J_{ex}/g\mu_B$ is the effective field including the applied magnetic field B and the Weiss molecular fields, k_B is the Boltzmann constant, T is the temperature, N_{PI} is the number of the nearest neighbor of the interfacial magnetic moments, and J_{ex} is the strength of the antiferromagnetic exchange interaction among Gd ions. We used the effective (renormalized) Curie-Weiss temperature Θ_{CW}^{eff} for taking all the correlation effects on a Gd ion into account, which gives the effective field as $B_{\text{eff}} = BT(T - \Theta_{\text{CW}}^{\text{eff}})$. The Θ_{CW}^{eff} should recover the bare Curie-Weiss temperature Θ_{CW} in the limit $B \to 0$ and $3T\Theta_{CW}C_1(S+1)B$ in the limit $B \to \infty$, respectively. For practical purposes it is convenient to match these limiting cases into a crossover function for the effective Curie-Weiss temperature:

$$\Theta_{\text{CW}}^{\text{eff}}(B) = \frac{3\Theta_{\text{CW}}}{S+1}\frac{B_S(S\eta)}{\xi} \approx \begin{cases} \Theta_{\text{CW}} & (g\mu_{\text{B}}B/k_{\text{B}}T \ll 1) \\ \frac{3T}{C_1(S+1)B}\Theta_{\text{CW}} & (g\mu_{\text{B}}B/k_{\text{B}}T \gg 1) \end{cases}, \tag{C.5.2}$$

with the ansatz

$$\xi = -a_0 + a_1|B| + \sqrt{a_0^2 + (a_2 B)^2}, \tag{C.5.3}$$

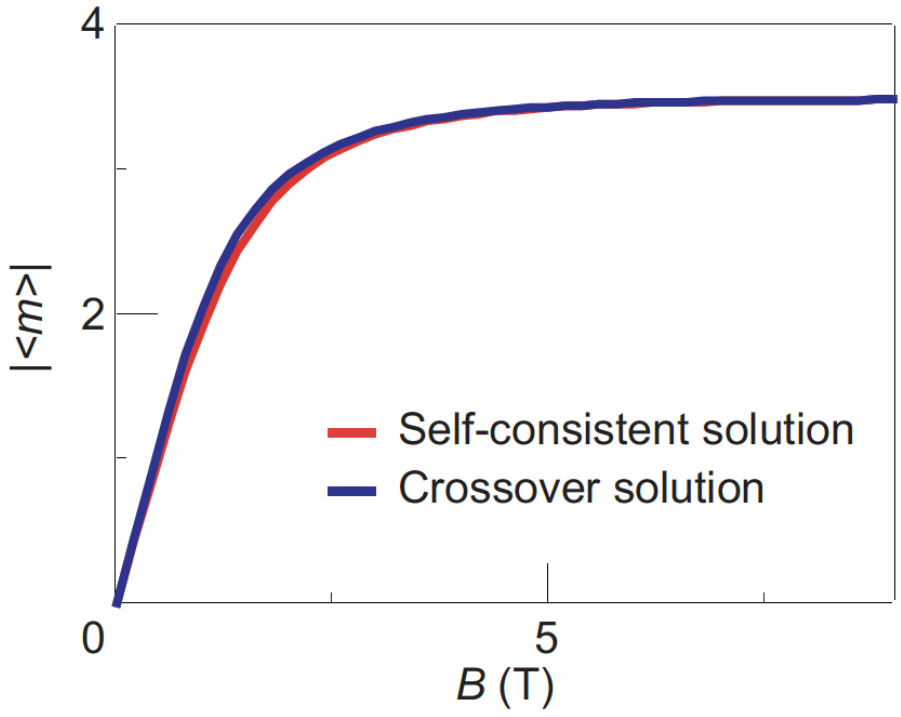

FIGURE 3.7: **The field dependence of the magnetization in GGG.** The red and blue lines represent the self-consistent solution and the approximation with the effective Curie-Weiss temperature solution for Eq. (C.5.2), respectively.

where

$$a_0 = -3\Theta_{CW}/(S+1)T, \tag{C.5.4}$$

$$a_1 = C_1/(T-\Theta_{CW}), \tag{C.5.5}$$

$$a_2 = C_1/T(1-T/\Theta_{\mathrm{CW}}). \tag{C.5.6}$$

FIGURE 3.7 shows the plots of Eq. (C.5.1) solved self-consistently (red line) and using with $\Theta_{CW}^{\mathrm{eff}}$ given as Eq. (C.5.2) (the blue line). We find a good agreement between both curves, justifying the use of $\Theta_{CW}^{\mathrm{eff}}$. In the following discussion and the main text, the approximate form of $B_{\mathrm{eff}} = BT(T-\Theta_{CW}^{\mathrm{eff}})$ is used to analyze the data.

In this case, the expressions for spin-mixing conductance reduce into

$$G_r = A_1\left\{S(S+1) - \left[\coth(\xi/2) + \frac{\xi}{4\sinh^2(\xi)}\right] SB_{\mathrm{S}}(S\xi)\right\}, \tag{C.5.7}$$

$$G_i = A_2 SB_S(S\xi), \tag{C.5.8}$$

$$G_s = -A_1\frac{\xi}{2\sinh^2(\xi/2)} SB_{\mathrm{S}}(S\xi), \tag{C.5.9}$$

where

$$A_1 = (\pi/\hbar) n_{\mathrm{PI}} (e J_{\mathrm{int}})^2 , \tag{C.5.10}$$

$$A_2 = (\pi/\hbar) n_{\mathrm{PI}} (e J_{\mathrm{int}}) . \tag{C.5.11}$$

Chapter 4

Observation of ferromagnetic spin Hall magnetoresistance in Pt/EuS

This work was performed in collaboration with Prof. Felix Casanova and his Ph.D. student Dr. Juan M Gomez-Perez. My contribution to this work is the theoretical analysis and the numerical fitting to their experimental data.

4.1 Introduction

Spin-dependent transport at the heavy metal (HM)/magnetic insulator (MI) heterostructure has been pushed to the forefront spintronics, due to its contributions to many novel phenomena, from spin pumping (Burrowes et al., 2012; Heinrich et al., 2011; Mosendz et al., 2009) to spin Seebeck effect (Uchida et al., 2010a; Uchida et al., 2010b; Uchida et al., 2014) and spin Hall magneto-resistance (Isasa et al., 2016; Marmion et al., 2014; Vélez et al., 2016a; Nakayama et al., 2013; Kosub et al., 2018; Althammer et al., 2013; Vlietstra et al., 2013a; Ganzhorn et al., 2016; Hahn et al., 2013; Isasa et al., 2014; Hou et al., 2017). The latter has been introduced in subsection 1.4.1. Thus, proper quantification of the spin-dependent conductance at different magnetic interfaces is vital for many future applications based on all these fancy phenomena. Spin Hall magneto-resistance (SMR) as a simple, but powerful tool, can give essential information about spin transport at the magnetic interface, in which spin-mixing conductance ($G_{\uparrow\downarrow}$), at the heart of the SMR effect, quantifies both STT and FLT at HM/MI interface, as explained in subsection 1.4.1.

Recently, SMR effects have been extensively studied in different MIs, for instance, ferrimagnetic insulators, basically YIG (Isasa et al., 2016; Marmion et al., 2014; Hahn et al., 2013; Isasa et al., 2014; Nakayama et al., 2013; Althammer et al., 2013; Vlietstra et al., 2013b; Meyer et al., 2014), antiferromagnetic insulators such as NiO, Cr_2O_3 and CoO (Hoogeboom et al., 2017; Baldrati et al., 2018; Ji et al., 2017; Wang et al., 2017; Fischer et al., 2018), as well as compensated ferrimagnetic insulators such as $Gd_3Fe_5O_{12}$ (Ganzhorn et al., 2016) or spiral ferrimagnets such as $CuOSeO_2$ (Aqeel et al., 2016). Furthermore, potential candidates can be a low dimensional ferromagnets (Vélez et al., 2019b) or, paramagnetic insulators (Aqeel et al., 2015; Lammel et al., 2019; Schlitz et al., 2018; Oyanagi et al., 2020). However, so far there are still no reports in SMR characterizing purely ferromagnetic insulators (FMI). In 2006, Brataas, Bauer, and Kelly, 2006b suggested that, at the interface of a FMI, such as europium chalcogenides, G_i might dominate over G_r.

We know from chapter 2 and the original SMR theory of Chen et al., 2013 that there exist an AHE-like SMR amplitude, $\Delta\rho_2/\rho$, which is governed by G_i. This AHE-like contribution has been poorly studied so far, mainly because of the minority of FMIs with large enough Curie temperature (T_C). As a potential candidate for FMI,

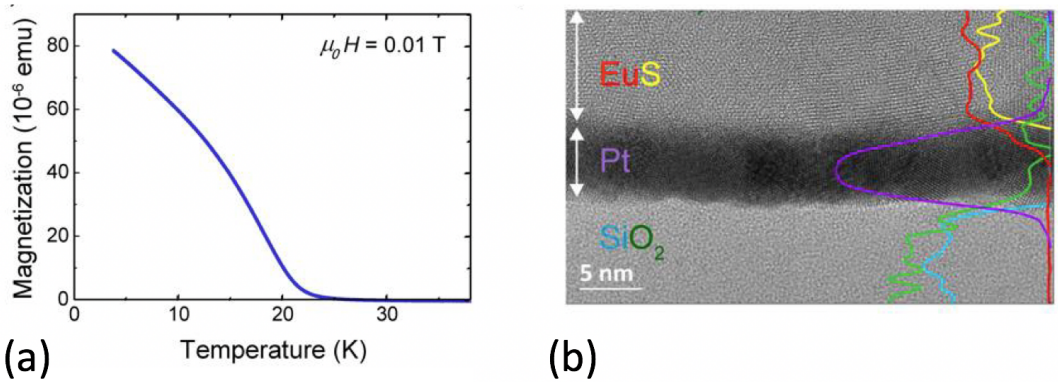

FIGURE 4.1: **Magnetization of EuS and transmission electron microscopy image of the EuS/Pt heterostructure** (a) Temperature dependence of the EuS magnetization measured at $\mu_0 H = 0.01$ T. (b) TEM image of the SiO_2/Pt/EuS heterostructure. The solid lines on the right side represent the composition profile along the sample thickness. The colors correspond to Si (blue), O (green), Pt (purple), Eu (red), and S (yellow).

Europium sulfide (EuS) has a sizable T_C typically around 16.5 K (Müller and Nolting, 2002). This FMI, in combination with conventional superconductors, such as Al, has been studied for decades in the context of the magnetic proximity effect by Meyer et al., 2014; Li et al., 2013; Strambini et al., 2017; Rouco et al., 2019. The exchange interaction between the conduction electrons of the superconductor and the localized magnetic moments of the EuS leads to a spin-splitting field in Al, even in the absence of an external magnetic field. Such spin-split in superconductors are subjected to intense research (Bergeret et al., 2018; Heikkilä et al., 2019) because of their possible applications in cryogenic memories (De Simoni et al., 2018), thermoelectric detectors (Heikkilä et al., 2018), superconducting spintronics and caloritronics (Linder and Robinson, 2015; Giazotto, Heikkilä, and Bergeret, 2015), and in the field of the topological superconductivity induced in the superconducting hybrid structures (Virtanen et al., 2018; Liu et al., 2019a). All these applications require a spin-splitting field induced in the superconductor adjacent to a FMI. Such field is proportional to the G_i, which quantifies the interfacial exchange field and, therefore, knowledge of the latter is crucial.

In this chapter, we report the SMR in a HM such as Pt on top of EuS. The temperature dependence of the SMR amplitudes can be fitted by using either random phase approximation (RPA) or Weiss field theory (WFT) model in the microscopic theory for SMR introduced in Chapter 2. From the fittings, we can quantify the exchange interaction between the conduction electrons of Pt and the localized moments of Eu ($\sim$18 meV), as well as the values of G_s, G_r and G_i as a function of temperature. In a FMI where there is no compensation of magnetic moments at the interface, we demonstrated that G_i is larger than G_r. The precise quantification of the interfacial exchange field from G_i is relevant in many fields where this quantity plays a crucial role.

4.2 Experimental details

In this section, we briefly introduce the SMR experiment's details in HM/FMI heterostructure, such as the thermal and magnetic properties of FMI and the device parameters.

Here, the FMI is chosen as EuS. It has a lattice constant $a_{EuS} = 6.0$ A, a gap $E_g = 1.6$ eV and a sizable Curie temperature $T_C = 16.5$ K (Müller and Nolting, 2002), which dramatically increases into about 160 K in proximity to Co (Fumagalli, Schirmeisen, and Gambino, 1998). A respectable Curie temperature is necessary to a large sensitive regime, in which the field and temperature dependence of SMR measurements are obvious. Consequently, EuS is a potential candidate to study the SMR effect. First of all, we evaluate the Pt/EuS interface quality by transmission electron microscopy and scanning transmission electron microscopy. FIGURE 4.1(b) sketches the stack of Pt/EuS grown on top of SiO_2 substrate. In principle, we grew a 14-nm-thick layer of EuS. However, from the transmission electron microscope image and the energy dispersive X-ray analysis, we find that the upper-4-nm zone of the EuS is oxidized, and there exists an amorphous structure. Fortunately, close to the Pt, the EuS has the right composition and crystalline structure, which means that the interface between the Pt and EuS, which participates in the spin-dependent scattering of SMR, is of good quality. Have this structural characterization in mind, and we next study the magnetization of the EuS film, which can be measured by a superconducting quantum interference device. FIGURE 4.1(a) plots the temperature dependence of M at small enough field H = 10 mT. Apparently, EuS exhibits a ferromagnetic behavior with Courier temperature $T_C = 25$ K. Below this temperature, EuS behaves like a ferromagnetic compound and exhibits simple paramagnetic properties above it. The growth of T_C with respect to the text-book one of 16.5 K (Müller and Nolting, 2002) is due to the adulteration of little EuO in EuS layer, in agreement with previous reports of Mauger and Godart, 1986; Hao, Moodera, and Meservey, 1990. On the other hand, we observed no saturation behavior down to 4 K, which can be related to the two magnetic layers present in the stack. A similar $M(T)$ behavior has been reported in an evaporated 10-nm-thick EuS film by Muduli et al., 2018.

EuS/Pt samples were prepared by patterning a Pt Hall bar (width W = 500 μm, length L = 900 μm, and thickness d_N = 5 nm) on top of SiO_2(150 nm)/Si by photolithography process and magnetron-sputtering deposition. EuS was evaporated by our collaborators from the Material Physics Center. EuS layer was *ex-situ* evaporated on top of the Pt film: the sample was inserted in a UHV preparation chamber (base pressure 10^{-9} mbar) and left for twelve hours at room temperature. EuS was grown employing sublimation of a stoichiometric EuS powder (99.9% purity) in a commercial e-beam evaporator. The growth rate calibrated with a quartz microbalance was 0.5 nm/min (total thickness of 14 nm). During preparation, the substrate was kept at room temperature. Unlike the PMI situation in chapter 3, where the Pt layer was deposited on top of the GGG, in the case of FMI, we had to change the order of the stack in order to not damage the EuS during the Pt deposition.

4.3 Results and discussion

4.3.1 Angular dependence of magnetoresistance

In this subsection, we present some typical behavior of SMR, which is the oscillation of longitudinal and transverse resistivity with the change of the relative orientation of the magnetization of FMI and the spin of itinerant electron generated by SHE.

The longitudinal ($\Delta\rho_L/\rho$) and transverse ($\Delta\rho_T/\rho$) resistivity are measured using the standard Hall bar devices sketched on the right-side insets of FIGURE 4.2, where the rotations along three main planes are parameterized by three angles α, β and γ, respectively. First of all, let us consider the low-field and low-temperature case. FIGURE 4.2 (a) plots the angular dependence of MR at field $\mu_0 H = 0.1$ T and

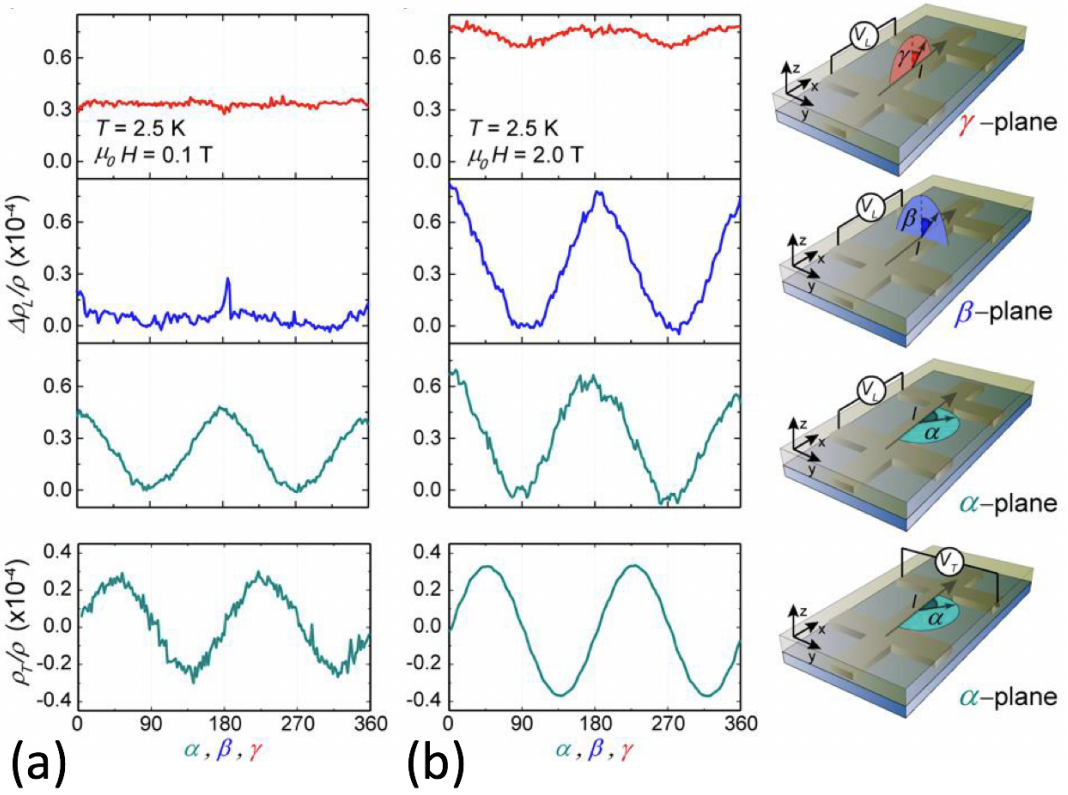

FIGURE 4.2: **Relative longitudinal resistivity and sketch of the devices** (a) Normalized longitudinal ($\Delta\rho_L/\rho$) and transverse (ρ_T/ρ) ADMR at 2.5 K along the three relevant $H-$rotation planes (α,β,γ), see sketches on the right side, for different applied magnetic fields: (a) $\mu_0 H$ = 0.1 T and (b) $\mu_0 H$ = 2 T.

T = 2.5 K. We can clearly see that the out-of-plane magnetization as shown by the blue curve in FIGURE 4.2 (a) is not well built, and only in-plane magnetization is well built and saturates. The latter confirms the soft magnetic behavior in α plane. Hence, the angular dependence of longitudinal (transverse) MR shows the typical $cos^2\alpha$ ($cos\alpha \cdot sin\alpha$) modulation related to the SMR geometry (Isasa et al., 2016; Isasa et al., 2014; Althammer et al., 2013; Vélez et al., 2019b). To build or even saturate the out-of-plane magnetization, we are required to apply a larger field $\mu_0 H$ = 2 T. In this case, the $\cos^2\beta$ modulation, as described by FIGURE 4.2 (b), is clear with the same SMR amplitude $\Delta\rho_1/\rho$ as the angular dependence of both longitudinal and transverse MR in $\alpha-$plane. The physical picture is explained as follows. When spins polarization of itinerant electrons and the magnetic moments are parallel, the spins are fully reflected at the interface and converted back into a charge current by the inverse spin Hall effect, decreasing the overall Pt resistance. However, when the spin polarization of itinerant electrons and the magnetic moments of MI are perpendicular, the spin polarization of itinerant electrons exerts a torque to the magnetic moments of MI, and part of the spin angular momentum is absorbed by the MI, resulting in an increase of the Pt resistance.

In the case of $\gamma-$plane, the rotation along the direction of spin polarization of itinerant electrons, no modulation is expected, as shown by the red curve in FIGURE 4.2 (a). This is because the Hanle precession of the spin of itinerant electrons at Pt/EuS interface keeps the same spin y component, which determines the longitudinal resistivity as shown in Eq. (1.4.5). Nonetheless, there is a small modulation not related to SMR neither to AMR (Pippard, 1989; Zou et al., 2016) due to MPE in Pt

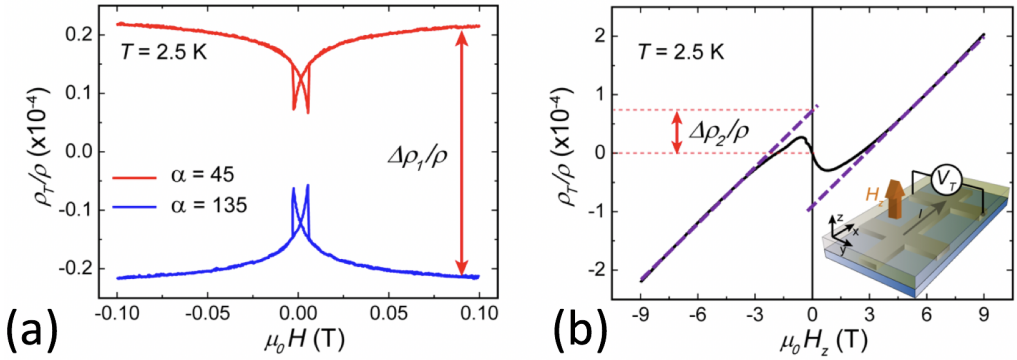

FIGURE 4.3: **Field dependence of magnetoresistance** (a) Normalized field dependence of transverse MR performed in $\alpha-$plane in $\alpha = 45^o$ and $\alpha = 135^o$. The red arrow shows the amplitude corresponding to $\Delta\rho_1/\rho$. (b) Hall configuration measurements. Dash purple lines correspond to the linear fit performed at large magnetic fields and extrapolated to zero. The red arrow shows the amplitude corresponding to $\Delta\rho_2/\rho$.

(Hauser, 1969; Antel et al., 1999; Weiler et al., 2012; Huang et al., 2012; Lu et al., 2013; Miao et al., 2014). This modulation is likely relative to the weak anti-localization that appears in Pt at low T, and large H applied out-of-plane (Shiomi et al., 2014). To exclude the influence of the weak anti-localization, the quantification of SMR amplitudes, $\Delta\rho_1/\rho$, and $\Delta\rho_2/\rho$, are performed in the transverse direction.

4.3.2 Field dependence of transverse magnetoresistance

Following the same procedure of Chapter 3, we can first quantify the SMR amplitudes $\Delta\rho_1/\rho$ and $\Delta\rho_2/\rho$ from transverse resistivity without weak anti-localization. FIGURE 4.3 (a) plots the field dependence of transverse MR in α plane, where the soft magnetic behavior demonstrates the correct modulation in the low-field regime. The red and blue curves, respectively, correspond to the magnetic field applied in $\alpha = 45^o$ and $\alpha = 135^o$, which correspond to the maximum and minimum values, respectively, as shown in FIGURE 4.2. One can also confirm that the magnetization reversal occurs around ~ 5 mT. While, for the magnetic field in z direction H_z, this magnetization reversal occurs at larger H (~ 1.5 T) as shown in FIGURE 4.3 (b), because the out-of-plane z axis happens to be the hard axis of the EuS film. On the other hand, in the high-field region, we can clearly observe a perfect linear dependence of transverse resistivity to the magnetic field that corresponds to the CHE of Pt. In comparison, there is a clear non-linearity in the low-field regime. Therefore, we can measure the AHE-like term from the H_z-field dependence of transverse resistivity, which gives us the $\Delta\rho_2/\rho$ amplitude from the intercept of the linear fittings at large (positive and negative) magnetic fields, as shown in FIGURE 4.3 (b).

4.3.3 Temperature dependence of the spin-dependent conductance

We have already discussed, in last chapter, that $\Delta\rho_1/\rho$ and $\Delta\rho_2/\rho$ are the SMR amplitudes and depended on spin-mixing conductance $G_{\uparrow\downarrow} = (G_r + iG_i)$, where the real and imaginary parts correspond to STT and FLT at Pt/EuS interface. In the case of a ferrimagnetic insulator, with compensated magnetic moments, G_i is at least one order of magnitude smaller compared to G_r, giving rise to a minimal AHE-like effect in this kind of materials, such as YIG (Althammer et al., 2013; Vlietstra et al., 2013b; Jia et al., 2011). Therefore, it is usually difficult to measure in the Hall configuration

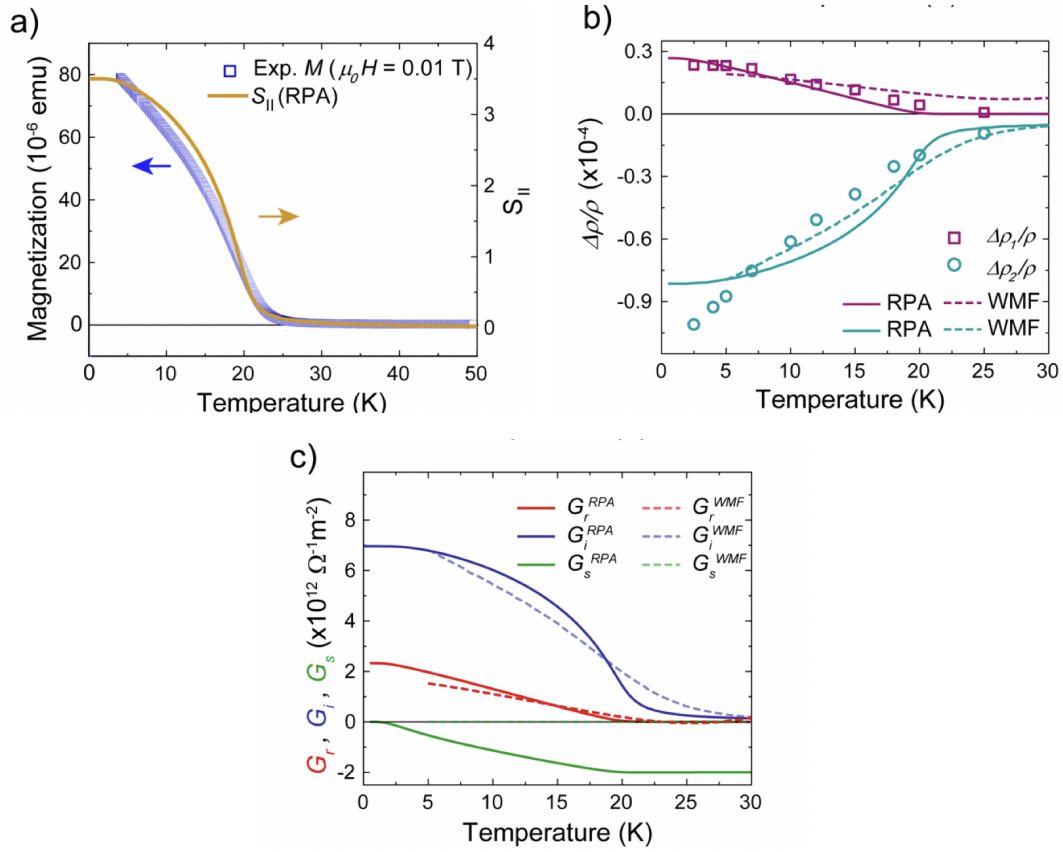

FIGURE 4.4: **Temperature dependence of the spin Hall magnetoresistance amplitudes and the spin conductances.** (a) Temperature dependence of the normalized SMR amplitudes $\Delta\rho_1/\rho$ (extracted from the ADMR in $\alpha-$plane at $H = 0.1$ T) and $\Delta\rho_2/\rho$ (extracted from from the AHE-like contribution in the Hall configuration measurement. The open dots represent the experimental data and the solid (dashed) lines are the best fits obtained with the RPA (WFT) model and the microscopic theory Zhang, Bergeret, and Golovach, 2019. (b) Temperature dependence of the real part (G_r), imaginary part (G_i) of the spin-mixing conductance and the SSC (G_s). The solid (dashed) lines are calculated values from the best fits obtained with the RPA (WFT) model.

due to the huge Hall effect background compared to the contribution of the AHE-like amplitude, $\Delta\rho_2/\rho$. Nonetheless, in the EuS/Pt sample, we can see a clear $\Delta\rho_2/\rho$ signals as shown in FIGURE 4.3(b). By changing the temperature from 0 to 30 K, we can quantify SMR amplitudes $\Delta\rho_1/\rho$ and $\Delta\rho_2/\rho$ by means of the method presented in FIGURE 4.3. FIGURE 4.4 (b) plots the temperature dependence of $\Delta\rho_1/\rho$ and $\Delta\rho_2/\rho$. We find that $\Delta\rho_2/\rho$ is larger than $\Delta\rho_1/\rho$ at all temperatures. In addition, both amplitudes disappears close to the T_c of our EuS film.

Next, we investigate the evolution of the different spin conductance terms with the temperature. For that purpose, we make use of the microscopic theory of SMR in chapter 2. We perform two kinds of fittings to our experimental data by using two different models for the ferromagnetism of EuS. They are random phase approximation (RPA) and Weiss field theory (WFT). In RPA method, we first fits the EuS magnetization in order to extract both spin-spin correlation function $\langle\widehat{S}^2_{\parallel}\rangle$ and spin expectation $\langle\widehat{S}_{\parallel}\rangle$. The latter is plotted by the yellow curve in FIGURE 4.4 (a). While, in WFT method, we uses the experimental magnetization as a input of $\langle\widehat{S}_{\parallel}\rangle$ as indicated by the blue boxes in FIGURE 4.4 (a) and, from which the $\langle\widehat{S}^2_{\parallel}\rangle$ can be

calculated from Zhang, Bergeret, and Golovach, 2019. For the fitting of the temperature dependence of the two SMR amplitudes as shown in FIGURE 4.4(b), we are required to provide with the values of λ_s ($\sim$ 1.3 nm) and θ_{SH} ($\sim$ 0.19), which can be extracted from the Pt resistivity at each temperature by Sagasta et al., 2016. FIGURE 4.4 (b) shows the fitting curves for the SMR amplitudes $\Delta\rho_1/\rho$ (purple line) and $\Delta\rho_2/\rho$ (blue line) as a function of T, with J_{sf}, n_{imp}^{2D}, J_1 and J_2 being the fitting parameters for RPA model, whereas in WFT the free parameters are J_{sf} and n_{imp}^{2D} only, because we use the experimental magnetization as an input of the model and, thus, J_1 and J_2 are not needed. Here, J_{sf} describes the hybridization of between 1s electrons in Pt and 4f electrons in Eu^{2+} localized at Pt/EuS interface, while, J_1 and J_2 are the exchange couplings in the EuS for first neighbors (12 first neighbors) and second neighbors (6 second neighbors), respectively. With quite an accuracy, the simulation reproduces the obtained experimental data for both RPA and WFT models. The fitting parameters used for the simulations are n_{imp}^{2D}(RPA) = $0.12/a^2$ with a = 5.94 Åthe EuS lattice parameter (n_{imp}^{2D}(WFT) =$0.14/a^2$) and J_{sf}(RPA) = 4 meV (J_{sf}(WFT) = 3 meV). EuS exchange constants extracted from the fitting $J_1 = 0.2k_B$ (ferromagnetic exchange interaction of $4f$ electrons in EuS) and $J_2 = -0.1k_B$ (antiferromagnetic exchange interaction with the second neighbors) are in very good agreement with previous theoretical reports of Meyer et al., 2014 and experimental values extracted by neutron scattering by Bohn et al., 1980; Bohn, Kollmar, and Zinn, 1984. FIGURE 4.4(b) shows that both models reproduce quite accurately the experimental data and that the best fitting parameters are similar for both models, which strengthen the reliability of the obtained values. The obtained J_{sf} here is much smaller than other experimental accessible values, for instance, 350 meV for Co/Cu, but it is similar to the one extracted for Pt/GGG in the previous chapter. n_{imp}^{2D} values are $12-14\%$ of the ideal value, but n_{imp}^{2D} values depend on the slicing of the lattice surface and the quality of HM/FMI surface.

Utilizing the same fitting parameters obtained from FIGURE 4.4 (b), we can calculate the temperature dependence of spin-dependent conductance, G_r, G_i, and G_s with the aid of Eqs. (2.2.15)-(2.2.17). They are plotted in FIGURE 4.4 (c). At low enough temperature so that the magnetization of EuS saturates, G_r and G_i are maximum, whereas G_s becomes zero due to the reduction of the spin-flip scattering. At higher temperatures and close to T_c, with the absence of net magnetization due to the randomized spins ($\langle \widehat{S}_{\parallel} \rangle \to 0$), G_r and G_i vanish to zero, because of the isotropic relaxation time as shown in Eqs. (2.2.16)-(2.2.15). Whereas, G_s becomes maximum. This observed behavior is equivalent (or similar) to the field dependence of the spin conductance in Pt/GGG described in chapter 3. The key point of the temperature dependence of the spin conductivity is that we experimentally demonstrate for the first time that in a FMI such as EuS, G_i is larger than G_r, up to 4 times larger at the lowest temperatures (T = 2.5 K), as predicted by Brataas, Bauer, and Kelly, 2006b for europium chalcogenides. The small differences between the model used and the experimental data can arise from the small defects at the interface and the higher T_c (for the case of RPA fits), as shown in FIGURE 4.1 (a). According to our results, we can confirm that the FLT plays an important role in Pt/EuS, not negligible than in other MIs (Althammer et al., 2013; Vlietstra et al., 2013b; Jia et al., 2011), where there is a compensation of the magnetic moments.

From the value obtained for G_i from the SMR measurements, we can calculate the effective interfacial exchange h_{ex} that is related to G_i using the following expression (Zhang, Bergeret, and Golovach, 2019): $h_{ex} = G_i/\pi G_0 \nu_F b$, where G_0 is the quantum of conductance, ν_F is the density of states of the HM at the Fermi level and b is

a length of the order of the mean free path (l). By assuming $\nu_F \approx 3-4\times10^{28}$ $\mathrm{m}^{-3}\mathrm{eV}^{-1}$ and $l \approx 10^{-9}$ m and taking the value of G_i from SMR measurements, $G_i \approx 7.65\times10^{12}\ \Omega^{-1}\mathrm{m}^{-2}$, we obtain $h_{ex} = 0.7$ meV. If we assume this value of h_{ex} for an EuS/Al bilayer, then the effective spin-splitting field induced in Al is given by $h_{eff} = h_{ex}b/d_{Al}$, where d_{Al} is the thickness of the Al layer. For $d_{Al} \approx 2-10$ nm (Strambini et al., 2017; Liu et al., 2019a), we calculate $h_{eff} \approx 0.1-0.35$ meV, whereas the superconducting gap for Al at low temperatures is approximately $\Delta \approx 0.2$ meV. In order to observe coexistance between superconductivity and the spin-splitting field, $h_{eff} < 0.7\Delta$ and hence for the observation of a clear spin-split BCS density of states, special care should be taken in the fabrication of EuS/Al bilayers.

4.4 Conclusions

In summary, the SMR in a Pt/EuS bilayer has been observed and explained within our model. EuS is a ferromagnetic insulator below 25 K. The SMR is observed by ADMR and FDMR measurements, in which the magnetization reversal of EuS is observed. Furthermore, from the measured AHE-like contribution to the SMR, we can extract microscopic parameters such as the exchange interaction between the $1s$ electrons of Pt and the $4f$ electrons of Eu ($J_{sf} \sim 17-19$ meV). We study the temperature dependence of the Pt/EuS interface's spin conductances, showing for the first time experimentally a field-like torque (G_i) larger than the spin-transfer torque (G_r) at the HM/MI interface. The effective exchange field associated with G_i is expected to be ~ 1 meV. SMR measurements, combined with our theory, offer a simple way to quantify effective interfacial fields, which are of interest in different applications.

Chapter 5

Phase-Controllable Nonlocal Spin Polarization in Proximitized Nanowires

5.1 Introduction

Semiconducting NWs in proximity with SCs are central to the creation of a topologically non-trivial superconducting state, which manifests itself through the MZMs at the edges of the NWs (Lutchyn, Sau, and Sarma, 2010; Oreg, Refael, and Oppen, 2010; Mourik et al., 2012; Rokhinson, Liu, and Furdyna, 2012; Das et al., 2012; Finck et al., 2013; Albrecht et al., 2016; Deng et al., 2016; Suominen et al., 2017; Nichele et al., 2017; Takei et al., 2013; Chang et al., 2015; Lutchyn, Stanescu, and Sarma, 2011). The basic ingredients needed for the topological phase are the SOC, superconducting correlations, and Zeeman splitting (Qi and Zhang, 2011; Elliott and Franz, 2015; Beenakker, 2013; Alicea, 2012; Lutchyn et al., 2018; Sarma, Freedman, and Nayak, 2015; Stanescu and Tewari, 2013). Whereas SOC and superconductivity are intrinsic properties of the materials, the Zeeman splitting is usually generated by applying a rather large magnetic field (Lutchyn, Sau, and Sarma, 2010; Oreg, Refael, and Oppen, 2010), which introduces technical limitations on the use of superconducting elements.

Additionally, such a spin splitting can be generated by the magnetic proximity effect from a MI, rather than an external field (Bergeret et al., 2018; Giazotto and Taddei, 2008; Yang et al., 2013; Eremeev et al., 2013; Virtanen et al., 2018; Wei et al., 2016; Katmis et al., 2016). Indeed, a zero-field spin split has been observed in superconducting Al layers in contact with the ferromagnetic insulator (FI) EuS (Hao, Moodera, and Meservey, 1991; Meservey, Tedrow, and Fulde, 1970; Hao, Moodera, and Meservey, 1990; Strambini et al., 2017; Moodera et al., 1988; Rouco et al., 2019). Furthermore, Liu et al., 2019b have reported the first hybrid epitaxial growth of InAs NWs in proximity with EuS and Al. Even though the experiment is inconclusive with regard to Majorana physics, the NWs show clear signs of the coexistence of the minigap and the spin split from the superconducting and magnetic proximity effects, respectively. Recently, Vaitiekėnas et al., 2020 have reported the experimental measurement of zero-field topological superconductivity in ferromagnetic hybrid NWs. These proximitized NWs are pivotal in the study of the topological superconductivity (Sau et al., 2010; Lee, Alicea, and Refael, 2012; Livanas, Sigrist, and Varelogiannis, 2019).

In this Chapter, motivated by the recent experiment by Liu et al., 2019b, we study theoretically a multiband NW in the diffusive regime proximitized by FIs and SCs, see the sketch in FIGURE 5.1(a). We show that, apart from the local spin polarization

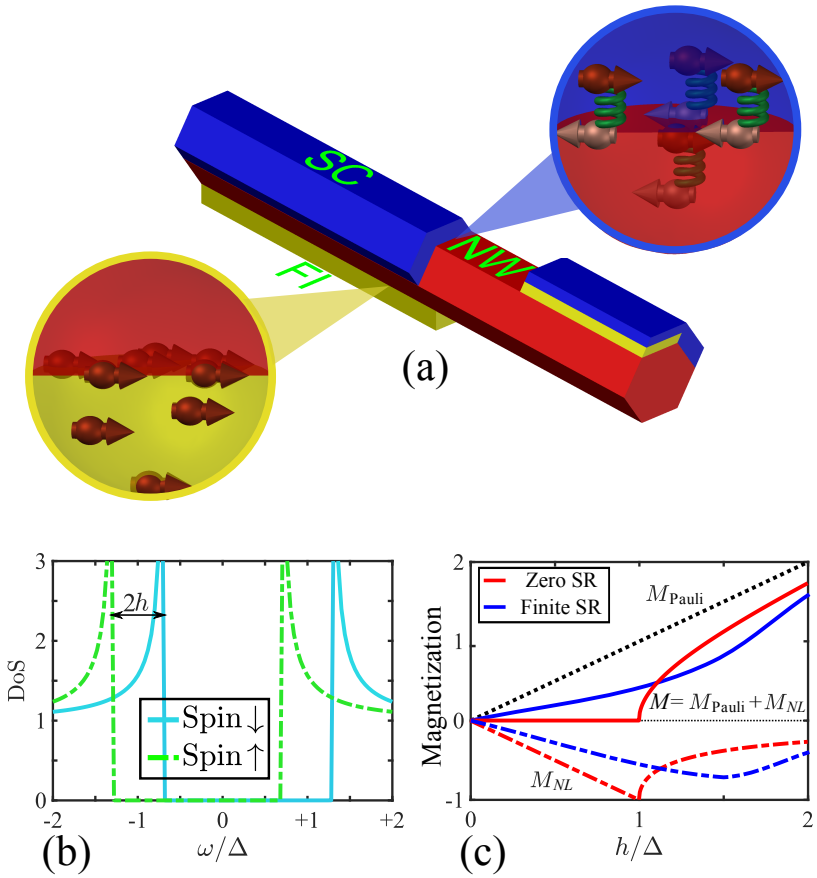

FIGURE 5.1: (Color online.) (a) Sketch of a nanowire (NW) in proximity with superconductors (SCs) and ferromagnetic insulators (FIs). (b) Spin-resolved density of state (DoS) of a spin-split SC. (c) Magnetizations induced in a SC in an homogeneous Zeeman field h. The dot black line describes Pauli magnetization, M_{Pauli} and the solid lines plot the total magnetization, M for zero (red) and finite (blue) spin relaxation (SR). The dashed lines show the nonlocal magnetization, M_{NL} given by the difference between M and M_{Pauli}, displayed for zero (red) and finite (blue) SR.

induced by the FI, a nonlocal electronic spin polarization emerges in the NW as a result of an interplay between the magnetic and superconducting proximity effects. The magnetic proximity effect occurs at the FI/NW interface, where the conduction electrons in the NW interact with the FI's local moments via the spin-exchange coupling. This interaction leads to a Pauli paramagnetic response of the conduction electrons, which is manifested as a locally induced magnetization in the NW at the FI. In addition, the superconducting proximity effect at the NW/SC interface allows for leakage of Cooper-pair correlations into the NW. The Cooper pairs become polarized by the FI exchange field, admixing the usual singlet pairing a triplet component of the superconducting correlations. As a result, the Pauli paramagnetic response at the NW/FI interface becomes screened by a spin polarization, which spreads in the NW over large distances, on the order of the superconducting coherence length. This long-ranged component of magnetization is opposite in sign to the Pauli magnetization, and its strength is proportional to the condensate density in the NW. In this letter, we calculate this nonlocal magnetization as a function of the system parameters, demonstrate its control by the phase difference in a loop geometry, and propose

a way of measuring it via spin-dependent spectroscopy.

It is illustrative to review the response of a conventional SC to a Zeeman or exchange field $h(\vec{r})$ (Abrikosov and Gor'kov, 1962; Larkin and Varlamov, 2005; Fulde and Ferrell, 1964). In normal state, the response is local and leads to a Pauli magnetization $M_{\text{Pauli}}(\vec{r}) = g\mu_B\nu_F h(\vec{r})$, dot-black curve in FIGURE 5.1(c). Here, g is g-factor, μ_B is Bohr magneton, and ν_F is the normal density of states (DoS) at the Fermi level for each spin. When the temperature, T is below the critical superconducting temperature, there exists an additional nonlocal contribution to magnetization, $M_{NL}(\vec{r})$ (dashed-red curve in FIGURE 5.1c), from the superconducting condensate. In a homogeneous SC at zero temperature, this contribution exactly compensates the Pauli one, $M_{NL} = -M_{\text{Pauli}}$, for fields h smaller than the superconducting gap, Δ . This explains the zero magnetic susceptibility of a SC (Yosida, 1958). In the presence of a spin relaxation (SR), the full magnetization cancellation fails, according to Abrikosov and Gorkov's theory of the Knight shift in SCs (Abrikosov and Gor'kov, 1962). In FIGURE 5.1(c), we include the SR due to the SOI and static disorder (blue curves). For $h > \Delta$, the compensation is incomplete and the total magnetization reads $M = M_{\text{Pauli}}\sqrt{h^2 - \Delta^2}/h$ (Bergeret, Volkov, and Efetov, 2005; Karchev et al., 2001; Shen et al., 2003). One can draw a connection between the nonlocal magnetization and the modified spectrum of the SC (FIGURE 5.1b). The exchange field h leads to both a splitting of the quasi-particle DoS and a reduction of the superconducting gap. As far as the latter is finite, the total magnetization is zero. For $h > \Delta$, the gap closes and a finite magnetization appears as a consequence of an incomplete compensation $|M_{NL}| < M_{\text{Pauli}}$ (see more discussions in Appendix 5.5.1). The previous discussion has been introduced for pedagogical purposes, as it is useful when presenting our main results. Strictly speaking, for a large enough field h, the superconducting gap has to be determined self-consistently, and an inhomogeneous superconducting phase may appear (Larkin and Varlamov, 2005; Fulde and Ferrell, 1964). The situation is simpler when superconductivity is induced in a non-superconducting material via the proximity effect. In this case, the self-consistency is not needed, and the exchange field can be arbitrarily large. This is the case considered in the rest of the manuscript.

5.2 Model and Theory

We now focus on an inhomogeneous system, as shown in FIGURE 5.1(a). It consists of a NW in contact with SCs and FIs. To describe the superconducting proximity effect, we use the quasiclassical equations and assume the diffusive regime in the NW. The characteristic length over which the Cooper-pair correlations decay in the NW is denoted as ξ_N. To describe the magnetic proximity effect in the FI/NW interface, we follow the approach of Zhang, Bergeret, and Golovach, 2019 and assume a region of thickness b where the local magnetic moments of FI and the itinerant electrons of NW interact via a spin-exchange coupling. This interaction leads to an interfacial exchange field h_{ex} acting on the itinerant electrons. Because $b \ll \xi_N$, the exchange field can be described in the quasiclassical equations by $h_b(y) = h_{ex}b\delta(y)$, where we denote with y the coordinate axis perpendicular to the FI/NW interface (Bergeret, Efetov, and Larkin, 2000). At this stage, we can already anticipate the appearance of a nonlocal magnetization in the opposite direction to the one localized at the FI/NW interface. The Cooper pairs in the NW consist of electrons with opposite spins (singlet state).

Energetically it is favorable that one electron of the pair with spin parallel to the local exchange localizes at the interface, while the other with opposite spin remains in the NW. Thus, a nonlocal magnetization opposite to the interfacial one is induced in the NW and extends over the characteristic Cooper size, ξ_N. This physical picture resembles the inverse proximity effect in metallic superconductor-ferromagnetic junctions predicted by Bergeret, Volkov, and Efetov, 2004b; Bergeret, Volkov, and Efetov, 2004a; Dahir, Volkov, and Eremin, 2019 and experimentally verified by Xia et al., 2009; Salikhov et al., 2009a; Salikhov et al., 2009b.

To quantify this effect we calculate the nonlocal electronic equilibrium spin polarization, M_{NL}, induced in the NW. This is given by

$$\frac{M_{NL}(X)}{g\mu_B\nu_F} = \frac{1}{2}\int_{-\infty}^{+\infty} d\omega f(\omega)[N^{\uparrow}(\omega, X) - N^{\downarrow}(\omega, X)], \tag{5.2.1}$$

where $f(\omega) = 1/(e^{\omega/T}+1)$ is equilibrium Fermi distribution function, and $N^{\uparrow/\downarrow}(\omega, X)$, are the local DoS for spin-up and -down electrons. The exchange field at the FI/NW leads to $N^{\uparrow} \neq N^{\downarrow}$ and hence to a finite M_{NL}. In addition to the nonlocal term there is the Pauli magnetization localized at the FI/NW interface $M_{\text{Pauli}} = g\mu_B\nu_F h_{ex} b\delta(y)$. Thus, the total magnetization equals $M_{\text{Pauli}} + M_{NL}$.

We consider the SC/NW-FI/SC setup sketched in the inset of FIGURE 5.2(c). The NW is in contact with a FI and sandwiched between two SCs. The phase difference between the SCs, ϕ, can be tuned by a magnetic flux when the junction is part of a superconducting loop. We assume a diffusive NW in order to use the well-established Usadel equation (Usadel, 1970). In this respect, our results apply straightforwardly to metallic NW like Cu. In semiconducting NWs, the degree of the disorder depends on doping. For example, the InAs wires studied in the experiments of Giazotto et al., 2011; Tiira et al., 2017; Iorio et al., 2018; Strambini et al., 2020 are in a metallic regime and are good candidates for the verification of our predictions. We denote with x the axis of the NW of length L_N. The NW-FI interface is orthogonal to the y-axis, and the NW width in this direction is W_N. In this first example, we assume that $W_N, L_N \ll \xi_N$, and integrate the quasiclassical equations over the volume of the NW. The integration in y direction results in an effective exchange field $h_F = h_{ex}b/W_N$, whereas the integration over x can be performed with the help of the Kupriyanov-Lukichev boundary conditions (Kuprianov and Lukichev, 1988) and accounts for the superconducting proximity effect. In this way, we obtain a compact expression for the DoS (see detailed derivations in Appendix 5.5.2):

$$N^s(\omega) = \left|\text{Re}\left\{\frac{\omega_r + sh_F}{\sqrt{(\omega_r + sh_F)^2 - (\Delta_r)^2}}\right\}\right|, \tag{5.2.2}$$

where $s = \pm 1$ for spin $\uparrow/\downarrow$. This expression has the same structure as the BCS DoS of a spin-split superconductor with renormalized frequency, $\omega_r = \omega + 2i\epsilon_b\mathcal{G}_S$ and order parameter $\Delta_r = 2\epsilon_b\cos(\phi/2)\mathcal{F}_S$, where $\mathcal{G}_S = -i\omega/\sqrt{\Delta^2-\omega^2}$, $\mathcal{F}_S = \Delta/\sqrt{\Delta^2-\omega^2}$. $\epsilon_b = D/(L_N\sigma_N R_\square)$ is an energy proportional to the tunneling rate across the NW/SC interface, where $R_\square$ is the interface resistance per area, D is the diffusion coefficient, and σ_N is the conductivity of the NW. Equation (5.2.2) is the generalization of the short-junction limit expression for the DoS (Seviour and Volkov, 2000; Börlin, Belzig, and Bruder, 2002; Bezuglyi, Bratus, and Shumeiko, 2011) in the presence of a FI. With its help we provide below a clear physical picture of the main effect by making a connection between the spectrum of the junction

and the spectral properties of the bulk system.

5.3 Result and Discussion

From Eq. (5.2.2), one can calculate the gap induced in the NW by the superconducting proximity effect. In the limit of transparent contact, $\epsilon_b \gg \Delta$, this gap is of the same order as the SC gap, and the spin splitting is negligibly small. In the case of a finite NW/SC barrier, when $\epsilon_b \ll \Delta$, Eq. (5.2.2) describes a NW with an induced mini gap, $\Delta_N = \Delta_N^0 \cos(\phi/2)$, with $\Delta_N^0 = 2\epsilon_b$, and a spin splitting in the DoS due to the effective exchange field, h_F. In all cases the minigap induced in the NW is maximum when $\phi = 0$ and vanishes at $\phi = \pi$. By substituting Eq. (5.2.2) into Eq. (5.2.1), we obtain the nonlocal magnetization, M_{NL} plotted in FIGURE 5.2. As far as $h_F < \Delta_N$, nonlocal magnetic moments, $M_{NL}W_N A$ compensates the Pauli ones, $\int_b M_{\text{Pauli}} = g\mu_B \nu_F h_{ex} b A$ localized at the FI/NW interface, with A being the area of FI/NW interface. At $h_F = \Delta_N$, M_{NL} reaches a maximum value, $g\mu_B\nu_F\Delta_N$ and decays as $h_F - \sqrt{h_F^2 - \Delta_N^2}$ for $h_F > \Delta_N$ (Bergeret, Volkov, and Efetov, 2005; Karchev et al., 2001; Shen et al., 2003). This is the same behaviour as the bulk superconductor discussed in FIGURE 5.1(c), after identifying Δ and h with the induced minigap Δ_N and effective exchange field h_F, respectively. This analogy is clearly seen if we plot the curves of FIGURE 5.2(a) as a function h_F/Δ_N. In this case, all curves collapse into one (inset of FIGURE 5.2a), coinciding with the behavior shown in FIGURE 5.1(c). In FIGURE 5.2(b) we show the dependence of M_{NL} on the phase difference ϕ for different values of h_F. When $h_F \leq \Delta_N^0$, M_{NL} remains constant for all phases smaller than $\arccos h_F/\Delta_N^0$ (red curve in FIGURE 5.2b). In other words, as far as h_F is smaller than the induced gap $\Delta_N = \Delta_N^0 \cos(\phi/2)$, the $M_{NL}(\phi)$ curve shows a plateau at the value opposite to M_{Pauli}. Interestingly, the value of M_{NL} is proportional to the distance between the coherent peaks in the spin-splitting DOS, similar to those shown in FIGURE 5.1(b). Indeed, in the present case when $\Delta_N \ll \Delta$, according to Eq. (5.2.2), the peaks at positive energies occur at $\omega^{\uparrow,\downarrow} \approx \Delta_N(\phi) \pm h_F$ (See Appendix 5.5.2). The maximum modulation is achieved for $h_F = \Delta_N^0$ (green curve in FIGURE 5.2b) in which the full screening of M_{NL} only occurs at $\phi = 0$. For larger values of h_F, the NW is gapless and $M_{NL}(\phi)$ is overall reduced (blue curve).

In the presence of SOI, electron spin channels are mixed. In this case the DoS of the NW is described by Eq. (5.2.2), after replacing ω_r and Δ_r by $\omega_r^s = \omega + i\Delta_N^0 \mathcal{G}_S + 2i\epsilon_{so} G_N^{-s}$ and $\Delta_r^s = \Delta_N \mathcal{F}_S + 2\epsilon_{so} F_N^{-s}$, respectively. Here, F_N^s and G_N^s are the normal and anomalous parts of the retarded Green's function of the NW, respectively. ϵ_{so} is the spin-relaxation rate due to SOI. The effect of a finite SR is shown in FIGURE 5.2(c-d). As expected from the analogy with the bulk SC, FIGURE 5.1(c), the main effect of the SR is the uncompensated screening of the Pauli magnetization, $-M_{NL} < M_{\text{Pauli}}$, as shown by the green and blue curves in panel 5.2(c). In addition, the SR leads to a shift of the maximum of the $M_{NL}(h_F)$ curves towards larger values of h_F, such that, for $h_F > \Delta_N$, M_{NL} is enhanced by the SR. This is due to the reduction of the effective exchange field, which results in the right shift of M_{NL} with respect to h_F in analogy with the bulk case shown by the dot-dash-blue curve of FIGURE 5.1(c).

So far, we have analyzed a short NW sandwiched between two SCs. In a more realistic setup, the NW's length, L_N can be larger than the ξ_N. Moreover, in typical lateral structures, the NW is partially covered by the SCs films of length L_S. Such a lateral setup is sketched in FIGURE 5.3(a). We assume that the NW is grown on top of a FI substrate and that its cross-section dimensions are smaller than ξ_N. In this case, one can integrate the Usadel equation over the cross-section and reduce the

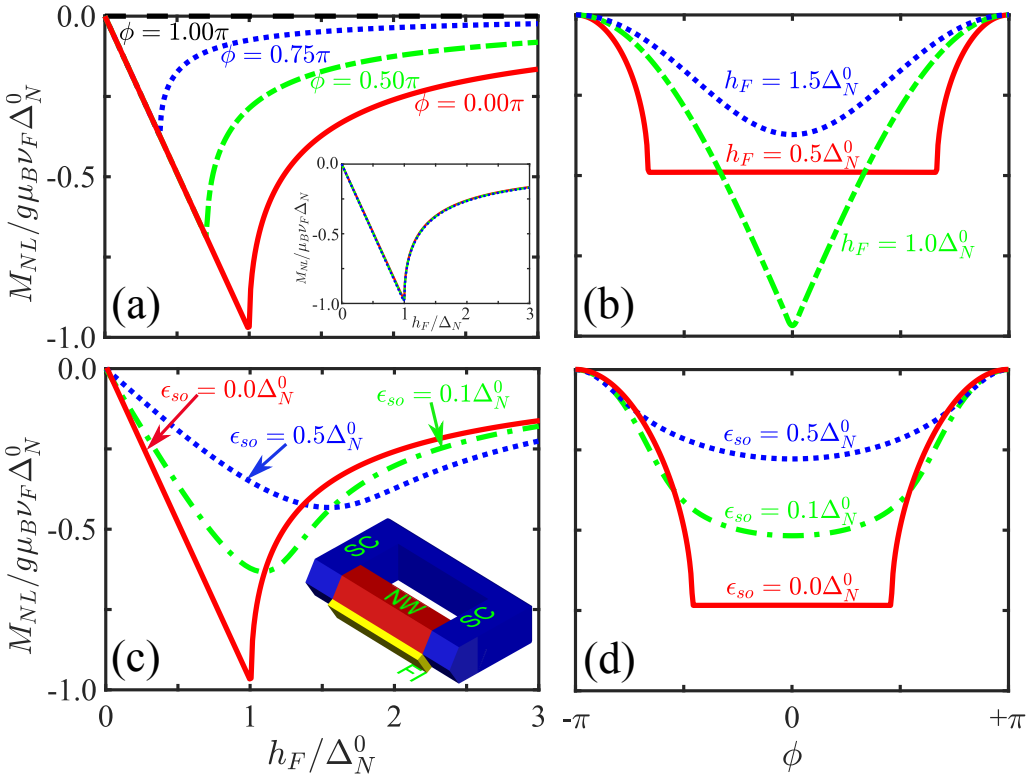

FIGURE 5.2: (Color online.) Nonlocal magnetization, M_{NL} induced in the NW in a SC/NW-FI/SC setup (see inset of panel (c)). Panels (a,b) show M_{NL} as a function of (a) h_F/Δ_N^0 and (b) ϕ, respectively, in the absence of SR. Panels (c,d) shows the same dependencies in the presence of SR caused by static disorder and SOI. We have set $\phi = 0$ in panel (c) and $h_F = 0.75\Delta_N^0$ in panel (d). Other parameters: $T = 0$ and $\Delta_N^0 = 0.02\Delta$.

problem to an effective 1D geometry (details are given in Appendix 5.5.2). Hereafter, we assume a symmetric setup with $L_S = L_N/3$ and $L_F = L_N$ (other situations are analyzed in Appendix 5.5.2), such that the distance between the SCs is $L = L_N/3$, and solve the Usadel equation numerically. We neglect the effect of SOI. This is a good approximation if the NM is a metal such as Cu, for which the SR rate is much smaller than the gap (Villamor et al., 2013). But also in InAs, the typical SR time is $\tau_s \simeq 0.02 - 1.00$ ns (Murzyn et al., 2003; Song and Kim, 2002; Murdin et al., 2005), which corresponds to $\epsilon_{so} = \hbar/\tau_s \simeq 1 - 30\mu$eV. Whereas the induced gap may reach 150 μeV or even larger (Chang et al., 2015; Kjærgaard et al., 2016), such that the ratio $\epsilon_{so}/\Delta < 1$.

Once induced, the mini gap is constant in all the NW (Le Sueur et al., 2008). Its value depends on the distance between the superconducting electrodes and the characteristic barrier energy $\epsilon_b = D/(W_N R_\square \sigma_N)$. In the short limit, $L_N \ll \xi_N$, M_{NL} is almost constant in the NW and the results are similar to those shown in FIGURES 5.2(a) and (b) (See FIGURE 5.5 (a) and (b) in Appendix 5.5.2). More interesting is the case when L_N is of the order of ξ_N. Numerical results of the spatial dependence $M_{NL}(X)$ for $L_N = 4.7\xi_0$ and different values of h_F, are shown in FIGURE 5.3(d). Remarkably, the shape of the $M_{NL}(X)$ curve depends on the strength of h_F. These different behaviours can be explained in light of Eq. (5.2.1). The integrand in this expression can be well approximated by replacing the exact DoS, $N(\omega, X)$ by a BCS-like one, $N_{BCS}(\omega, \Delta_N^*(X))$ with a position-dependent pseudogap $\Delta_N^*(X)$, defined as

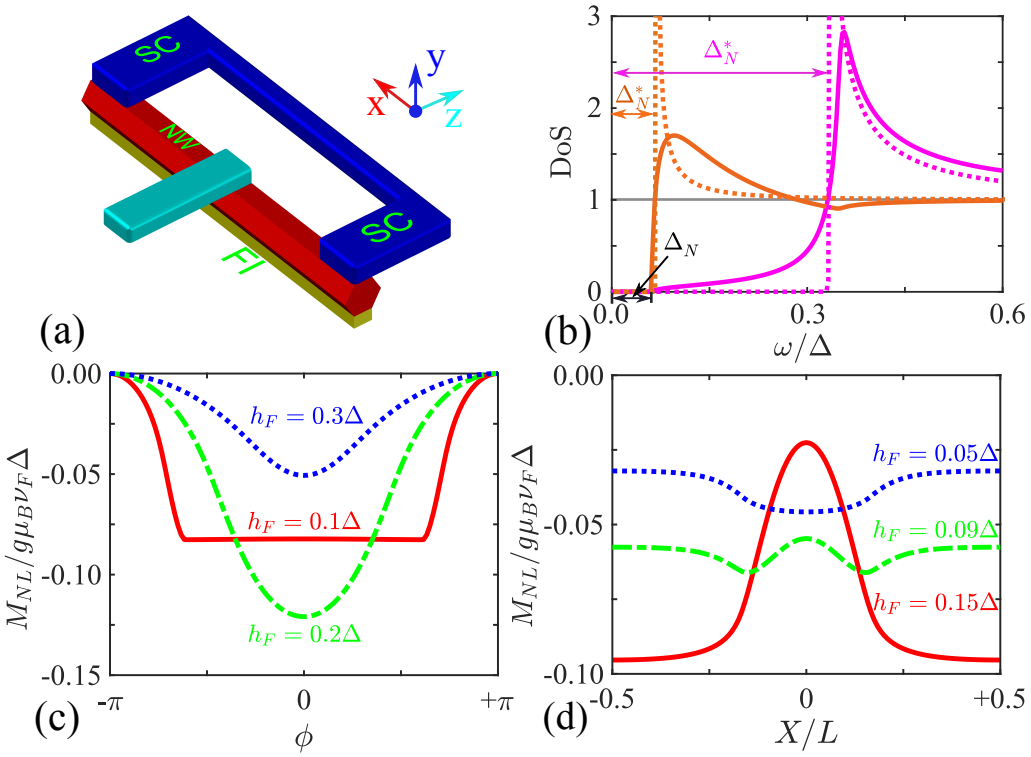

FIGURE 5.3: (Color online.) (a) Sketch of SC-FI-SC NW structure with a tunneling probe (bright-blue) (b) DoS of the NW with $L = 4.7\xi_0$. Here, the orange and magenta curves correspond to DoS at the center ($X = L_N/2$) and the end ($X = L_N/6$) of the NW, respectively. The dotted lines show the BCS-like DoS with a gap equal to $\Delta^*(X)$. The latter is defined by the intersection point between the actual DoS and the one in the normal state. (c,d) Nonlocal magnetization, M_{NL}, induced in the NW, as a function of (c) phase difference, ϕ and (d) position, X. We have set $L = 2.1\xi_0$ and $X = 0$ in panel (c), while $L = 4.7\xi_0$ and $\phi = 0$ in panels (b) and (d). In all panels, other parameters are chosen as follows: $T = 0$, $\epsilon_{so} = 0$, $\epsilon_b = \Delta/2$, $\xi_0 = \sqrt{D/\Delta}$, and $L_S/L_N = 1/3$.

the energy where $N(\omega)$ intersects with the one in the normal state $N_0(\omega) = 1$, as shown in FIGURES 5.3(b). Whereas the real mini gap, Δ_N, is position independent, Δ_N^* is not. In fact, the pseudogap is smaller in the middle of the wire, becoming larger in the regions below the SCs (see also FIGURE 2d in Appendix 5.5.2). The shape of the $M_{NL}(X)$ is determined by the ration $h_F/\Delta_N^*(X)$, in the same way as in the short junction limit h_F/Δ_N^0 determines M_N, see FIGURE 5.2 (a,c). Indeed, for a given h_F with $h_F < \Delta_N^*(X)$ for all X, the values of $|M_{NL}|$ increases towards the middle of the wire (blue curve in FIGURE 5.3(d)). In contrast, if $\Delta^*(-L/2) > h_F > \Delta^*(0)$ then a double-minima curve is obtained (green curve). Larger values of h_F leads to $|M_N(X)|$ with a minimum at $X = 0$ (red curve). The actual shape of the curve can be inferred from the X dependence of Δ^*, which is shown in FIGURE 5.3(d) in the Appendix 5.5.2. Finally, FIGURE 5.3(c) shows the phase dependence of M_{NL} calculated in the center of the wire for different values of h_F. The result at low temperatures is qualitatively similar to the one obtained for the simpler setup analyzed in FIGURE 5.2(b): for values of h_F smaller than the pseudogap Δ_N^*, $M_{NL}(\phi)$ remains almost constant up to the value of φ for which $\Delta_N^*(\phi) = h_F$ (red curve in FIGURE 5.3c).

Finally, we discuss possible ways of detecting M_{NL} via its dependence on the phase-difference in a Josephson junction geometry. As discussed above, the magnetic moment M_{NL} depends crucially on the spectral properties of the proximitized NW, which in turn can be controlled by tuning the phase difference. This has been demonstrated experimentally in spectroscopy measurements, for example, by using a superconducting quantum interference proximity transistor (SQUIPT) (Giazotto et al., 2010; Meschke et al., 2011; Giazotto and Taddei, 2011; Ronzani, Altimiras, and Giazotto, 2014), sketched in FIGURE 5.3(a), or by combining STM/AFM techniques (Le Sueur et al., 2008). In these experiments, the phase difference, hence the mini gap, is controlled by the magnetic flux through a superconducting loop (Strambini et al., 2016; Ronzani et al., 2017). In the present case, the wire is in contact with a FI, and hence the DoS in the NW is spin-split due to the exchange field at the FI/NM interface. This should manifest as a splitting of the peaks at the edge of the gap. According to our predictions, if the SR is negligibly small, the observed splitting of the peaks remains almost constant, as far as the phase-dependent pseudogap Δ_N^*, is larger than the effective exchange field (see red curves in FIGURE 5.2b and 5.3c). The splitting in the DoS of the NW can be detected by measuring the differential conductance with a tunneling probe attached to the NW, as shown in FIGURE 5.3(a). When the phase difference is larger than $\arccos(h_F/\Delta_N^0)$, then we predict a rapid suppression of the splitting as the phase difference is further increased. The results of FIGURE 3 are obtained when SOI is negligible. If it is not, all sharp features will vanish, and the red curve in FIGURE 5.3(c) will be modified similarly to those in 5.2(d) when increasing ϵ_{so}. It is also interesting to note that the tuning of a mini gap with the phase difference can lead to a phase-tuned topological superconductivity (Fornieri et al., 2019). Moreover, a comparison of experimental results with the curves in FIGURE 5.2b and 5.3c may provide useful information about the proximity-induced gap and field in the NW.

More direct measurement of M_{NL} and its phase-dependence can be achieved by using a ferromagnetic probe tunnel-coupled to NW, as shown in FIGURE 5.3(a) setup. We assume that the probe's polarization and the FI can be tuned between parallel (P) and antiparallel (AP) configurations. The measured differential conductance at low temperature is proportional to the DoS in the NW. The difference between the conductances in the P and AP configurations is proportional to the spectral magnetization induced in the NW. Namely, $G_P(V) - G_{AP}(V) = pG_0[N_\uparrow(V) - N_\downarrow(V)]$, where p is the polarization of the probe/NW tunnel junction and G_0 is normal-state tunneling conductance. The total induced magnetization can then be obtained from Eq. (5.2.1) by knowing the normal state properties of the tunneling contact. By using the SQUIPT setup of FIGURE 5.3(a), one can tune the phase difference by an external magnetic field and measure the $N_{NL}(\phi)$ curve. From a material perspective, our theoretical description is based on the diffusive approach, and therefore our findings can be best verify in metallic NM, like Cu, or highly doped semiconducting nanowires, like those used by Giazotto et al., 2011; Tiira et al., 2017; Iorio et al., 2018; Strambini et al., 2020. For the FI, EuS is the best candidate. Interfacial exchange fields of the order of tens of Tesla has been reported in system combing EuS with metals and graphene (Wei et al., 2016; Strambini et al., 2017), which would lead to effective $h_F \sim 10^{-2} - 10^{-1}$meV such that one can reach all regimes studied above. Moreover, the strength of the effective exchange field can be tuned by an external magnetic field (Xiong et al., 2011).

5.4 Conclusion

In conclusion, we predict the appearance of a nonlocal magnetization M_{NL} in a NW when proximitized to SCs and a FI. This magnetization appears as a consequence of the interplay between the long-range superconducting correlations induced in the NW and the exchange field localized at the FI/NW interface. The sign of M_{NL} is opposite to the local Pauli spin polarization right at the FI/NW interface, and its value can be controlled by the phase difference between superconducting electrodes in a Josephson junction setup.

5.5 Appendix

The fundamental equation describing diffusive systems with superconducting correlations is the Usadel equation for the quasiclassical Green's functions (GFs) $\check{g}(\vec{r})$ in the Keldysh-Nambu-spin space,

$$D\vec{\nabla}[\check{g}(\vec{r})\vec{\nabla}\check{g}(\vec{r})] + \Big[i(\omega + \vec{s}\cdot\vec{h}(\vec{r}))\hat{\kappa}^3 - \Delta(\vec{r})(\cos\phi(\vec{r})\hat{\kappa}^1 - \sin\phi(\vec{r})\hat{\kappa}^2), \check{g}(\vec{r})\Big] = \epsilon_{so}\left[\hat{\vec{s}}\check{g}(\vec{r})\hat{\vec{s}}, \check{g}(\vec{r})\right]. \tag{E.5.1}$$

$\hat{s}_k(\hat{\kappa}_k)$ with $k = 1, 2, 3$ are the Pauli matrix for spin and Nambu spaces, respectively. D is the diffusion coefficient. $\Delta(\vec{r})$ is the gap of superconductor with phase, $\phi(\vec{r})$. $\vec{h}(\vec{r})$ is an exchange or Zeeman field. In this work, the order parameter, $\Delta(\vec{r})$ phase, $\phi(\vec{r})$ and Zeeman or exchange field, $\vec{h}(\vec{r})$ can be position-dependent. The right hand side of Eq. (E.5.1) describes the effect of spin-orbit-induced spin relaxation (SR) caused by scattering off static impurities, where ϵ_{so} is the corresponding SR rate, which is measured in units of energy and introduced in Subsection 1.2.3. For the sake of simplicity, both Planck and Boltzmann constants have been set to one, *i.e.* $\hbar = 1$ and $k_B = 1$.

To described hybrid interfaces between different materials we used the Kupriyanov-Lukichev boundary conditions from Hammer et al., 2007; Kuprianov and Lukichev, 1988:

$$\sigma_L\check{g}_L(\mathbf{n}\nabla)\check{g}_L|_{int} = \sigma_R\check{g}_R(\mathbf{n}\nabla)\check{g}_R|_{int} = \frac{1}{R_\square}\left[\check{g}_L, \check{g}_R\right]|_{int}, \tag{E.5.2}$$

where $g_{L,R}$ are the Green's functions at the left and right side of the interface, $\sigma_{L,R}$ the corresponding conductivities, $R_\square$ the interface resistance per unit area, and $\mathbf{n}$ a vector normal to the interface. The first equality in Eq. (E.5.2) corresponds to the current conservation at any interface. In particular if the interface is between a metal and vacuum the right hand side equlas to zero and the boundary condition reduces to

$$\check{g}(\mathbf{n}\nabla)\check{g}|_{int} = 0. \tag{E.5.3}$$

In what follows, we solve Eq. (E.5.1) and determine the local density of states in different situations addressed in the main text. Because we are only interested in an equilibrium situation, it is enough to consider the retarded block of Eq. (E.5.1).

5.5.1 Homogeneous Superconductors

We review first some basic features of the response of SC to a Zeeman field in the presence of SOI (Abrikosov and Gor'kov, 1962; Larkin and Varlamov, 2005; Fulde and Ferrell, 1964). In spatially homogeneous situation the Usadel equation ((E.5.1))

for the retarded component reduces to

$$[-i(\omega_\delta + sh)\hat{\kappa}^3 + \Delta\hat{\kappa}^1, \check{g}_S^s] + 2\epsilon_{so}\left[\check{g}_S^{-s}, \check{g}_S^s\right] = 0. \tag{E.5.4}$$

Here $\omega_\delta = \omega + i\delta$, with *delta* being an infinitesimal small positive real number. $s = \pm 1$, correspond to the spin anti-parallel and parallel to the direction of exchange field,respectively. Thus, $\check{g}_S^s$ are matrices in the Nambu space. Hereafter, we consider only the retarded Green's function and omit δ for simplicity. The last term of the left-hand side of Eq. (E.5.4) describes the SR due to SOI and static disorder. The general solution of Eq. (E.5.4) is

$$\hat{g}_S^s = G_S^s\hat{\kappa}^3 + F_S^s\hat{\kappa}^1, \tag{E.5.5}$$

where G_S is the normal and F_S the anomalous component. They can be written in a self-consistent form:

$$G_S^s = \frac{-i(\omega_r^s + sh)}{\sqrt{(\Delta_r^s)^2 - (\omega_r^s + sh)^2}}, \tag{E.5.6}$$

$$F_S^s = \frac{\Delta_r^s}{\sqrt{(\Delta_r^s)^2 - (\omega_r^s + sh)^2}}. \tag{E.5.7}$$

Here spin flipping causes a spin-dependent renormalization of both, the frequency

$$\omega_r^s = \omega + 2i\epsilon_{so}G_S^{-s}, \tag{E.5.8}$$

and the order parameter

$$\Delta_r^s = \Delta + 2\epsilon_{so}F_S^{-s}. \tag{E.5.9}$$

Once the Greens' function is determined the DoS can be obtained from its normal part, *i.e.*, Eq. (E.5.6)

$$N^s(\omega) = \left|\mathrm{Re}\left\{\frac{\omega_r^s + sh}{\sqrt{(\omega_r^s + sh)^2 - (\Delta_r^s)^2}}\right\}\right|. \tag{E.5.10}$$

In the absence of SR, the solution can be explicitly written

$$\hat{g}_S^s = \mathcal{G}_S^s\hat{\kappa}^3 + \mathcal{F}_S^s\hat{\kappa}^1, \tag{E.5.11}$$

with

$$\mathcal{G}_S^s = \frac{-i(\omega + sh)}{\sqrt{\Delta^2 - (\omega + sh)^2}}, \tag{E.5.12}$$

$$\mathcal{F}_S^s = \frac{\Delta}{\sqrt{\Delta^2 - (\omega + sh)^2}}. \tag{E.5.13}$$

Therefore, the DoS (E.5.10) reduces to

$$N^s_{BCS}(\omega,\Delta) = \left|\mathrm{Re}\left\{\frac{\omega+sh}{\sqrt{(\omega+sh)^2-\Delta^2}}\right\}\right|, \tag{E.5.14}$$

which is nothing but the spectrum of a spin-split superconductor with coherent peaks in the DoS at:

$$\omega^s_{\pm} = \pm\Delta - sh. \tag{E.5.15}$$

The (homogenoeus) nonlocal magnetization originated from the superconducting condensate is then given by

$$\frac{M_{NL}}{g\mu_B\nu_F} = \frac{1}{2}\int_{-\infty}^{+\infty} d\omega f(\omega)[N^{\uparrow}_{BCS}(\omega,\Delta) - N^{\downarrow}_{BCS}(\omega,\Delta)], \tag{E.5.16}$$

where μ_B is Bohr magneton, ν_F is the normal DoS at the Fermi level, and the electron g-factor is set to be 2. $f(\omega) = 1/(e^{\omega/T}+1)$ is equilibrium distribution function for frequency, ω and temperature, T. $N^{\uparrow/\downarrow}(\omega)$ are the DoS for spin-up and -down electrons. By substitution of Eq. (E.5.14) in Eq. (E.5.16) we obtain

$$\frac{M_{NL}}{g\mu_B\nu_F} = \frac{1}{2}\int_{-\infty}^{+\infty} d\omega f(\omega)\mathrm{Re}\left\{\frac{|\omega+h|}{\sqrt{(\omega+h)^2-\Delta^2}} - \frac{|\omega-h|}{\sqrt{(\omega-h)^2-\Delta^2}}\right\}. \tag{E.5.17}$$

Hereafter, we consider the limit of $T \to 0$. The Fermi-Dirac distribution function reduces a step function, *i.e.*, $f(\omega) = \theta(-\omega)$. For $h < \Delta$, we obtain $M_{NL} = -g\mu_B\nu_F h = -M_{\mathrm{Pauli}}$, *i.e.* opposite to the Pauli spin response. Thus, the total magnetization becomes zero. In general we find a compact expression for magnetization:

$$\frac{M}{g\mu_B\nu_F} = \theta(h-\Delta)\sqrt{h^2-\Delta^2}. \tag{E.5.18}$$

In the presence of the SR, the spin-dependent renormalization of frequency, as shown in Eqs. (E.5.8), reveals that Zeeman field might be renormalized by normal Green function (E.5.6). For the sake of simplicity, let us consider the case of a low SR rate, $\epsilon_{so} \ll \Delta$. The first-order correction of normal Green function can be obtained by replacing the GFs, G^s_S and F^s_S on the right hand side of Eq. (E.5.6), by the GFs, $\mathcal{G}^s_S$ and $\mathcal{F}^s_S$ in Eqs. (E.5.12) and (E.5.13)

$$G^s_S \simeq \frac{-i(\omega^s_r + sh^s_r)}{\sqrt{(\Delta^s_r)^2 - (\omega^s_r + sh^s_r)^2}}. \tag{E.5.19}$$

Therefore, in this limit, the effect of SR is a further renormalization of the frequency, order parameter, and Zeeman field

$$\omega^s_r = \omega\left[1 + \frac{2\epsilon_{so}}{\Lambda(sh)}\right], \tag{E.5.20}$$

$$\Delta_r^s = \Delta\left[1 + \frac{2\epsilon_{so}}{\Lambda(sh)}\right], \tag{E.5.21}$$

$$h_r^s = h\left[1 - \frac{2\epsilon_{so}}{\Lambda(sh)}\right], \tag{E.5.22}$$

with

$$\Lambda(sh) = \sqrt{\Delta^2 - (\omega - sh)^2}. \tag{E.5.23}$$

The DoS of SC, to first order of SR rate, can be derived from Eq. (E.5.19)

$$N^s \simeq \left|\mathrm{Re}\left\{\frac{|\omega_r^s + sh_r^s|}{\sqrt{|\omega_r^s + sh_r^s|^2 - (\Delta_r^s)^2}}\right\}\right|. \tag{E.5.24}$$

Now the coherent peaks are shifted according to:

$$\omega_\pm^s = \pm\Delta - sh\left(\frac{\Lambda^\pm(sh) - 2\epsilon_{so}}{\Lambda^\pm(sh) + 2\epsilon_{so}}\right), \tag{E.5.25}$$

with

$$\Lambda^\pm(sh) = \sqrt{\Delta^2 - (\omega_\pm^s - sh)^2}. \tag{E.5.26}$$

In the present case, $\epsilon_{so} \ll \Delta$, we can approximately replace the $\omega_\pm^s$ in the right hand side of Eq. (E.5.25) by Eq. (E.5.15). Then, we obtain

$$\omega_\pm^s \simeq \pm\Delta - sh\left(\frac{\sqrt{\pm s\Delta h - h^2} - \epsilon_{so}}{\sqrt{\pm s\Delta h - h^2} + \epsilon_{so}}\right). \tag{E.5.27}$$

The peaks at negeative energy are then given by

$$\omega_-^+ \simeq -\Delta - h\left(\frac{i\sqrt{\Delta h + h^2} - \epsilon_{so}}{i\sqrt{\Delta h + h^2} + \epsilon_{so}}\right), \tag{E.5.28}$$

$$\omega_-^- \simeq -\Delta + h\left(\frac{\sqrt{\Delta h - h^2} - \epsilon_{so}}{\sqrt{\Delta h - h^2} + \epsilon_{so}}\right). \tag{E.5.29}$$

and therefore the effective Zemman field becomes

$$h_{eff} = \frac{h}{2}\mathrm{Re}\left\{\frac{i\sqrt{\Delta h + h^2} - \epsilon_{so}}{i\sqrt{\Delta h + h^2} + \epsilon_{so}} + \frac{\sqrt{\Delta h - h^2} - \epsilon_{so}}{\sqrt{\Delta h - h^2} + \epsilon_{so}}\right\}. \tag{E.5.30}$$

For $h < \Delta$, we find

$$\frac{h_{eff}}{h} \simeq 1 - \frac{\epsilon_{so}^2}{\Delta h + h^2 + \epsilon_{so}^2} - \frac{\epsilon_{so}}{\sqrt{\Delta h - h^2} + \epsilon_{so}}. \tag{E.5.31}$$

For $h > \Delta$, we reach

$$\frac{h_{eff}}{h} \simeq 1 - \frac{\epsilon_{so}^2}{\Delta h + h^2 + \epsilon_{so}^2} - \frac{\epsilon_{so}^2}{h^2 - \Delta h + \epsilon_{so}^2}. \tag{E.5.32}$$

The latter result explains the suppression of the effective Zeeman field in the presence of the SR, which manifests as a shift of the $\delta M_S(h)$ curve in the FIGURE 1(c) of the main text.

5.5.2 Hybrid Superconductor Structures

In this section, we consider hybrid structures with inhomogeneous fields. In particular, we focus on the case when the exchange field is spatially localized, originated from the interaction between localized moments in the FI and the conduction electrons of the NW, and the superconducting correlations are induced in the NW via the proximity effect. The Usadel equation, Eq. (E.5.1), determines an energy-dependent length over which the pair correlations decay in the NW. We denote this length as ξ_N.

To describe the magnetic proximity effect in the FI/NW, we follow the approach developed by Zhang, Bergeret, and Golovach, 2019 and assume a region of thickness b in which the local magnetic moments of FI and the itinerant electrons of NW coexist and interact via a sd-exchange coupling. This interaction leads to an interfacial exchange field h_{ex} acting on the latter, which is localized at the interface. Because $b \ll \xi_N$ the exchange field can be included in the quasiclassical equations as a localized field, $h_b(y) = h_{ex} b\delta(y)$, where y is the coordinate perpendicular to the FI/NW interface (Bergeret, Efetov, and Larkin, 2000).

The SC/NW-FI/SC structure

We first focus on the setup, depicted in the inset of FIGURE 2(c) of the main text. Here the FI is grown along with one of the facets of the NW. In principle, we are dealing with a 3D problem. We simplify by assuming that the NW's transverse dimensions are smaller than ξ_N, such that we can assume the GFs being independent of y and z. We can then integrate the Usadel equation, (E.5.1), first over z-direction, where the zero current BC at both Vacuum/NW interfaces applies, Eq. (E.5.3), and second over the y-direction where at $y = 0$ there is a local exchange field from the FI. After these integrations, the Usadel equation in the NW region reduces to a 1D equation:

$$\begin{aligned} &D\partial_x[\check{g}_N^s(x)\partial_x\check{g}_N^s(x)] + \left[i\left(\omega + sh_F\right)\hat{\kappa}^3, \check{g}_N^s(x)\right] \\ &\quad = 2\epsilon_{so}\left[\check{g}_N^{-s}(x), \check{g}_N^s(x)\right]. \end{aligned} \tag{E.5.33}$$

The magnetic proximity effect results in an effective exchange field $h_F = h_{ex} b/W_N$, where W_N is the width of NW in y direction.

In this example, for the sake of clarity, we also assume that the length of the wire, L_N, is smaller than ξ_N such that we also integrate the above Usadel equation over x. At the interfaces with the superconducting leads, we use the BC in Eq. (E.5.2) and assume that the superconductors are massive and are not modified by the inverse

proximity effect. This results in a matrix algebraic equation:

$$\begin{aligned} 2\epsilon_b(\mathcal{G}_S[\hat{\kappa}^3, \check{g}_N^s] + \mathcal{F}_S \cos(\phi/2)\,[\hat{\kappa}^1, \check{g}_N^s]) \\ = i(\omega + sh_F)[\hat{\kappa}^3, \check{g}_N^s] - 2\epsilon_{so}\left[\check{g}_N^{-s}, \check{g}_N^s\right]. \end{aligned} \tag{E.5.34}$$

The superconducting proximity effect is described by the barrier energy

$$\epsilon_b = D/(L_N \sigma_N R_\square). \tag{E.5.35}$$

and $\check{g}_S$ is the bulk BCS GF:

$$\check{g}_S(x)|_{x=\pm\frac{L_N}{2}} = \mathcal{G}_S\hat{\kappa}^3 + \mathcal{F}_S\left[\cos\left(\frac{\phi}{2}\right)\hat{\kappa}^1 \mp \sin\left(\frac{\phi}{2}\right)\hat{\kappa}^2\right], \tag{E.5.36}$$

with

$$\mathcal{G}_S(\omega) = \frac{-i\omega}{\sqrt{\Delta^2 - \omega^2}}, \tag{E.5.37}$$

$$\mathcal{F}_S(\omega) = \frac{\Delta}{\sqrt{\Delta^2 - \omega^2}}, \tag{E.5.38}$$

and ϕ the corresponding phase-difference between the superconductors.

The solution of Eq. (E.5.34) together with the normalization condition $g_N^2 = 1$ for each spin block $s = \pm$, can be written as

$$\hat{g}_N^s = G_N^s\hat{\tau}_3 + F_N^s\hat{\tau}_1, \tag{E.5.39}$$

with

$$G_N^s = \frac{-i(\omega_r^s + sh_F)}{\sqrt{(\Delta_r^s)^2 - (\omega_r^s + sh_F)^2}}, \tag{E.5.40}$$

$$F_N^s = \frac{\Delta_r^s}{\sqrt{(\Delta_r^s)^2 - (\omega_r^s + sh_F)^2}}. \tag{E.5.41}$$

These soluctions have the same form as the BCS GFs with a renormalized frequency

$$\omega_r^s = \omega + 2i\epsilon_b\mathcal{G}_S + 2i\epsilon_{so}G_N^{-s}, \tag{E.5.42}$$

and an induced gap

$$\Delta_r^s = 2\epsilon_b\cos(\phi/2)\mathcal{F}_S + 2\epsilon_{so}F_N^{-s}. \tag{E.5.43}$$

The DoS of NW can be obtained from the normal part of the retarded Green function, *i.e.*, Eq. (E.5.40)

$$N^s(\omega) = \left|\mathrm{Re}\left\{\frac{|\omega_r^s + sh_F|}{\sqrt{(\omega_r^s + sh_F)^2 - (\Delta_r^s)^2}}\right\}\right|. \tag{E.5.44}$$

In the absence of SR, the solutions in Eqs. (E.5.39)-(E.5.43) reduce to

$$\hat{g}_N^s = \mathcal{G}_N^s \hat{\kappa}^3 + \mathcal{F}_N^s \hat{\kappa}^1, \tag{E.5.45}$$

with

$$\mathcal{G}_N^s = \frac{-i(\omega + 2i\epsilon_b \mathcal{G}_S + sh_F)}{\sqrt{4\epsilon_b^2 \cos^2(\phi/2)\mathcal{F}_S^2 - (\omega + 2i\epsilon_b \mathcal{G}_S + sh_F)^2}}, \tag{E.5.46}$$

$$\mathcal{F}_N^s = \frac{2\epsilon_b \cos(\phi/2)\mathcal{F}_S}{\sqrt{4\epsilon_b^2 \cos^2(\phi/2)\mathcal{F}_S^2 - (\omega + 2i\epsilon_b \mathcal{G}_S + sh_F)^2}}, \tag{E.5.47}$$

and the corresponding DoS for each spin block, $s = \pm$ from Eq. (E.5.46)

$$N^s = \left| \mathrm{Re} \left\{ \frac{|\omega + 2i\epsilon_b \mathcal{G}_S + sh_F|}{\sqrt{(\omega + 2i\epsilon_b \mathcal{G}_S + sh_F)^2 - 4\epsilon_b^2 \cos^2(\frac{\phi}{2})\mathcal{F}_S^2}} \right\} \right|. \tag{E.5.48}$$

Thus, we obtain the coherent peaks in the spin-splitting DOS

$$\omega_\pm^s = \pm 2\epsilon_b \cos(\phi/2)\mathcal{F}_S(\omega_\pm^s) - sh_F - 2i\epsilon_b \mathcal{G}_S(\omega_\pm^s). \tag{E.5.49}$$

Let us study the renormalization effect of a mini gap and spin splitting from the superconducting proximity effect, in the limit of $\epsilon_b, h_F \ll \Delta$. The zero-order effect can be obtained by setting $\omega_\pm^s = 0$ on the right-hand side of Eq. (E.5.49). Thus, we obtain the coherent peaks with the spin splitting of $2h_F$:

$$\omega_\pm^s \simeq \pm\Delta_N(\phi) - sh_F. \tag{E.5.50}$$

with

$$\Delta_N(\phi) = 2\epsilon_b \cos(\phi/2), \tag{E.5.51}$$

where $\Delta_N(\phi)$ is the mini gap of NW in the absence of SR, which depends on the phase difference ϕ between the two SCs. Clearly, $\Delta_N(\phi)$ is zero at $\phi = \pi$, while reaches its maximum value, $\Delta_N^0 = 2\epsilon_b$ at $\phi = 0$. Next, we consider the first-order effect, which can be obtained by substituting Eq. (E.5.50) on the right-hand side of Eq. (E.5.49). Hence we reach

$$\omega_\pm^s = \pm\Delta_N(\phi) - sh_{eff}, \tag{E.5.52}$$

with

$$\Delta_N(\phi) \simeq 2\epsilon_b \cos(\phi/2)\left(1 - \frac{2\epsilon_b}{\Delta}\right), \tag{E.5.53}$$

$$h_{eff} \simeq h_F \left(1 - \frac{2\epsilon_b}{\Delta}\right). \tag{E.5.54}$$

We find both minigap and spin splitting decrease with increasing ϵ_b. The later corresponds to the weakening of spin screening.

FIGURE 5.4 (a) shows the field dependence of M_{NL}. The magnetization is given

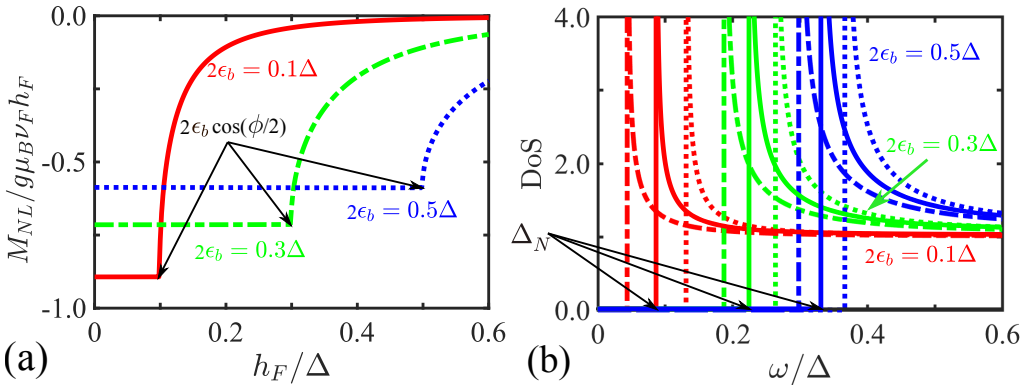

FIGURE 5.4: (Color online.) Nonlocal magnetization, M_{NL} of SC/NW-FI/SC structure. Panel (a) plots the field, h_F dependence of M_{NL}, in the unit of $g\mu_B\nu_F h_F$, and hence the full spin screening means value of -1. The corresponding DoS are plotted in panel (b), where $h_F = 0.05\Delta$. Other parameters: $T = 0$, $\epsilon_{so} = 0$ and $\phi = 0$.

in units of $g\mu_B\nu_F h_F$, and hence the full spin screening corresponds to the value -1 in the curves. Here, different curves correspond to different choices of the barrier energies, ϵ_b. The maximum effect occurs for $h_F^{max} = 2\epsilon_b\cos(\phi/2)$. In the limit $\epsilon_b \ll \Delta$, $h_F^{max} \simeq \Delta_N$ (Eq. E.5.51, red curves in FIGURE 5.4). On the other hand, we find the weakening of spin screening with increasing the barrier energy, ϵ_b or mini gap, Δ_N^0. This can be understood from the spin resolved DoS in FIGURE 5.4(b). Here, $N^{\uparrow}(\omega)$ and $N^{\downarrow}(\omega)$, are related to each other by a BCS-like DoS, $N_{BCS}(\omega, \Delta_N)$ with a renormalized minigap, Δ_N (Eq. E.5.53). Thus, $N^{\uparrow}(\omega) = N_{BCS}(\omega - \alpha_r h_F, \Delta_N)$ and $N^{\downarrow}(\omega) = N_{BCS}(\omega + \alpha_r h_F, \Delta_N)$, where $\alpha_r = (1 - 2\epsilon_b/\Delta) < 1$ in the limit of $\epsilon_b \ll \Delta$ (Eq. E.5.54). The full spin screening corresponds to $\alpha_r = 1$ (FIGURE 1b of main text). However, the failure of full screen is a result of the reduction of the spin-splitting due to the superconducting proximity effect. It becomes more obvious for larger Δ_N (ϵ_b), (Eq. E.5.54 and blue curves in FIGURE 5.4).

In the presence of the SR, we find a spin-dependent renormalization of the frequency (see Eq. (E.5.42)). This implies a renormalization of the effective exchange field. For the sake of simplicity, let us consider the case of a small SR rate, $\epsilon_{so}, \epsilon_b \ll \Delta_N$, and hence $\Delta_N^0 \simeq 2\epsilon_b$. The first-order correction to the normal Green function can be included by replacing the GFs, G_N^s and F_N^s on the right-hand side of Eq. (E.5.40), by the GFs, $\mathcal{G}_N^s$ and $\mathcal{F}_N^s$ in Eqs. (E.5.46) and (E.5.47). Then, we reach

$$G_N^s = \frac{-i(\omega_r^s + sh_r^s)}{\sqrt{(\Delta_r^s)^2 - (\omega_r^s + sh_r^s)^2}}. \tag{E.5.55}$$

In the present limit, $\epsilon_{so} \ll \Delta_N$, the SR then leads to the following renormalization of frequency, mini gap, and effective exchange field:

$$\omega + i\Delta_N^0\mathcal{G}_S \to \omega_r^s \simeq (\omega + i\Delta_N^0\mathcal{G}_S)\left(1 + \frac{2\epsilon_{so}}{\Lambda(sh_F)}\right), \tag{E.5.56}$$

$$\Delta_N\mathcal{F}_S \to \Delta_r^s \simeq \Delta_N\mathcal{F}_S\left(1 + \frac{2\epsilon_{so}}{\Lambda(sh_F)}\right), \tag{E.5.57}$$

$$h_F \to h_r^s \simeq h_F \left(1 - \frac{2\epsilon_{so}}{\Lambda(sh_F)}\right), \tag{E.5.58}$$

with

$$\Lambda(sh_F) = \sqrt{(\Delta_N \mathcal{F}_S)^2 - \left(\omega + i\Delta_N^0 \mathcal{G}_S - sh_F\right)^2}. \tag{E.5.59}$$

Thus, the DoS of NW in the first order of SR reads

$$N^s \simeq \left| \mathrm{Re}\left\{ \frac{|\omega_r^s + sh_r^s|}{\sqrt{|\omega_r^s + sh_r^s|^2 - (\Delta_r^s)^2}} \right\} \right|, \tag{E.5.60}$$

For spin block s, the coherent peaks in the spin-splitting DOS are given by

$$\begin{aligned} \omega_\pm^s = &\pm \Delta_N \mathcal{F}_S(\omega_\pm^s) - i\Delta_N^0 \mathcal{G}_S(\omega_\pm^s) \\ &- sh\left(\frac{\Lambda^\pm(sh_F) - 2\epsilon_{so}}{\Lambda^\pm(sh_F) + 2\epsilon_{so}}\right), \end{aligned} \tag{E.5.61}$$

with

$$\Lambda^\pm(sh_F) = \sqrt{(\Delta_N \mathcal{F}_\pm^s)^2 - \left(\omega_\pm^s + i\Delta_N^0 \mathcal{G}_\pm^s - sh_F\right)^2}. \tag{E.5.62}$$

In the limit of $\Delta_N \ll \Delta$, we have $\mathcal{G}_S(\omega_\pm^s) \simeq 0$ and $\mathcal{F}_S(\omega_\pm^s) \simeq 1$. Hence, Eq. (E.5.61) reduces into

$$\omega_\pm^s = \pm\Delta_N - sh\left(\frac{\Lambda^\pm(sh_F) - 2\epsilon_{so}}{\Lambda^\pm(sh_F) + 2\epsilon_{so}}\right). \tag{E.5.63}$$

with

$$\Lambda^\pm(sh_F) \simeq \sqrt{(\Delta_N)^2 - (\omega_\pm^s - sh_F)^2}. \tag{E.5.64}$$

For a small SR rate, $\epsilon_{so} \ll \Delta_N$, we can approximately replace the $\omega_\pm^s$ in the right hand side of Eq. (E.5.63) by Eq. (E.5.50). Thus, we arrive at

$$\omega_\pm^s \simeq \pm\Delta_N - sh_F\left(\frac{\sqrt{\pm\Delta_N sh_F - h_F^2} - \epsilon_{so}}{\sqrt{\pm\Delta_N sh_F - h_F^2} + \epsilon_{so}}\right). \tag{E.5.65}$$

For zero temperature, we are only interested in the spin splitting of negative frequency

$$\omega_-^+ \simeq -\Delta_N - h_F\left(\frac{i\sqrt{\Delta_N h_F + h_F^2} - \epsilon_{so}}{i\sqrt{\Delta_N h_F + h_F^2} + \epsilon_{so}}\right), \tag{E.5.66}$$

$$\omega_-^- \simeq -\Delta_N + h_F\left(\frac{\sqrt{\Delta_N h_F - h_F^2} - \epsilon_{so}}{\sqrt{\Delta_N h_F - h_F^2} + \epsilon_{so}}\right). \tag{E.5.67}$$

Thus the effective exchange field reads

$$h_{eff} = \frac{h_F}{2}\mathrm{Re}\left\{\frac{i\sqrt{\Delta_N h_F + h_F^2} - \epsilon_{so}}{i\sqrt{\Delta_N h_F + h_F^2} + \epsilon_{so}} + \frac{\sqrt{\Delta_N h_F - h_F^2} - \epsilon_{so}}{\sqrt{\Delta_N h_F - h_F^2} + \epsilon_{so}}\right\}. \tag{E.5.68}$$

For $h_F < \Delta_N$, we reach

$$\frac{h_{eff}}{h_F} \simeq 1 - \frac{\epsilon_{so}^2}{\Delta_N h_F + h_F^2 + \epsilon_{so}^2} - \frac{\epsilon_{so}}{\sqrt{\Delta_N h_F - h_F^2} + \epsilon_{so}}. \tag{E.5.69}$$

For $h_F > \Delta_N$, we reach

$$\frac{h_{eff}}{h_F} = 1 - \frac{\epsilon_{so}^2}{\Delta_N h_F + h_F^2 + \epsilon_{so}^2} - \frac{\epsilon_{so}^2}{h_F^2 - \Delta_N h_F + \epsilon_{so}^2}. \tag{E.5.70}$$

Clearly, we find that the effective exchange field decreases in the presence of the SR. This causes a shift to the right of the nonlocal magnetization curve as a function of the exchange field (see the blue dashed curve in FIGURE 2(c) of the main text).

The SC-FI-SC NW structure

In this section, we consider a more realistic setup, the lateral SC-FI-SC NW structure depicted in FIGURE 3(a) of the main text. Here, an arbitrary long normal wire (NW) is grown on the top of FI. Two superconductors (SCs) with phase difference, ϕ cover partially the NW. The starting point is again the Usadel equation for the retarded quasiclassical Green's function in the NW:

$$D\vec{\nabla}[\check{g}_N^s(\vec{r})\vec{\nabla}\check{g}_N^s(\vec{r})] + i\left[(\omega + sh_b(\vec{r}))\,\hat{\kappa}^3, \check{g}_N^s(\vec{r})\right] = 0, \tag{E.5.71}$$

where we have neglected the SR. The magnetic proximity effect of FI can be described by a localized exchange field at FI/NW interface, $h_b(\vec{r}) = bh_{ex}\theta_F(x)\delta(y)$, with

$$\theta_F(x) = \begin{cases} 1, & \frac{L_N}{2} - \frac{L_F}{2} < x < \frac{L_N}{2} + \frac{L_F}{2}; \\ 0, & otherwise, \end{cases} \tag{E.5.72}$$

where L_F is the length of FI. On the other hand, the proximity effect of SCs is captured by the Kupriyanov-Lukichev boundary conditions (E.5.2) at two NW/SC interfaces, which can be written in a compact form

$$\sigma_N[\check{g}_N(\vec{r})\ \partial_y\check{g}_N(\vec{r})]\big|_{y=W_N} = \frac{1}{R_\square}[\theta_L(x) + \theta_R(x)] \times [\check{g}_N(\vec{r}), \check{g}_S(\vec{r})]\big|_{y=W_N}. \tag{E.5.73}$$

The positions of the left and right superconducting electrodes, in x direction, are respectively described by two step-like functions

$$\theta_L(x) = \begin{cases} 1, & 0 < x < L_S; \\ 0, & otherwise, \end{cases} \tag{E.5.74}$$

$$\theta_R(x) = \begin{cases} 1, & L_N - L_S < x < L_N; \\ 0, & otherwise, \end{cases} \tag{E.5.75}$$

with L_S being the length of both SCs. We do not consider the inverse proximity effect of FI on SCs and hence their GFs are the BCS ones

$$\begin{aligned} \check{g}_S(\vec{r})|_{y=W_N} = \theta_R(x) \left\{ \mathcal{G}_S \hat{\kappa}^3 + \mathcal{F}_S[\cos(\frac{\phi}{2})\hat{\kappa}^1 - \sin(\frac{\phi}{2})\hat{\kappa}^2] \right\} \\ + \theta_L(x) \left\{ \mathcal{G}_S \hat{\kappa}^3 + \mathcal{F}_S[\cos(\frac{\phi}{2})\hat{\kappa}^1 + \sin(\frac{\phi}{2})\hat{\kappa}^2] \right\}, \end{aligned} \tag{E.5.76}$$

where we introduce phase difference, ϕ between SCs.

Because the transverse dimensions of the NW are smaller than the characteristic length ξ_N, we can assume that the GFs do not depend on y and z. We can then integrate the Usadel equation, (E.5.71), first over z-direction, where the zero current BC at both vacuum/NW interfaces applies, Eq. (E.5.3), and second over the y-direction. In the second integration, the local exchange field at the NW/FI at $y = 0$ results in an effective spin-splitting field h_F, whereas at the SC/NW interface, $y = W_N$, the boundary condition, Eq. (E.5.73) introduces a term in the Usadel equation describing the induced superconducting condensate. The final 1D equation after these integrations reads:

$$\begin{aligned} D\partial_x[\check{g}_N^s(x)\partial_x\check{g}_N^s(x)] + i\left[(\omega + \theta_F(x)sh_F)\,\hat{\kappa}^3, \check{g}_N^s(x)\right] \\ = \epsilon_b[\theta_L(x) + \theta_R(x)]\,[\check{g}_S(\vec{r}), \check{g}_N^s(x)]|_{y=W_N}. \end{aligned} \tag{E.5.77}$$

The strength of the superconducting proximity effect is parametrized by the energy:

$$\epsilon_b = D/(W_N \sigma_N R_\square). \tag{E.5.78}$$

Eq. (E.5.77) is complemented by the normalization condition, $\check{g}_N^2(x) = 1$. In order to solve numerically these two matrix equations it is convenient to use the Riccati parameterization to express the GFs in terms of two coherent functions γ and $\tilde{\gamma}$ as follows:

$$\check{g} = \check{N} \begin{bmatrix} 1 - \gamma\tilde{\gamma} & 2\gamma \\ 2\tilde{\gamma} & \tilde{\gamma}\gamma - 1 \end{bmatrix} = \begin{bmatrix} \mathcal{G} & \mathcal{F} \\ \tilde{\mathcal{F}} & \tilde{\mathcal{G}} \end{bmatrix}, \tag{E.5.79}$$

with

$$\check{N} = \begin{bmatrix} (1 + \gamma\tilde{\gamma})^{-1} & 0 \\ 0 & (1 + \tilde{\gamma}\gamma)^{-1} \end{bmatrix}. \tag{E.5.80}$$

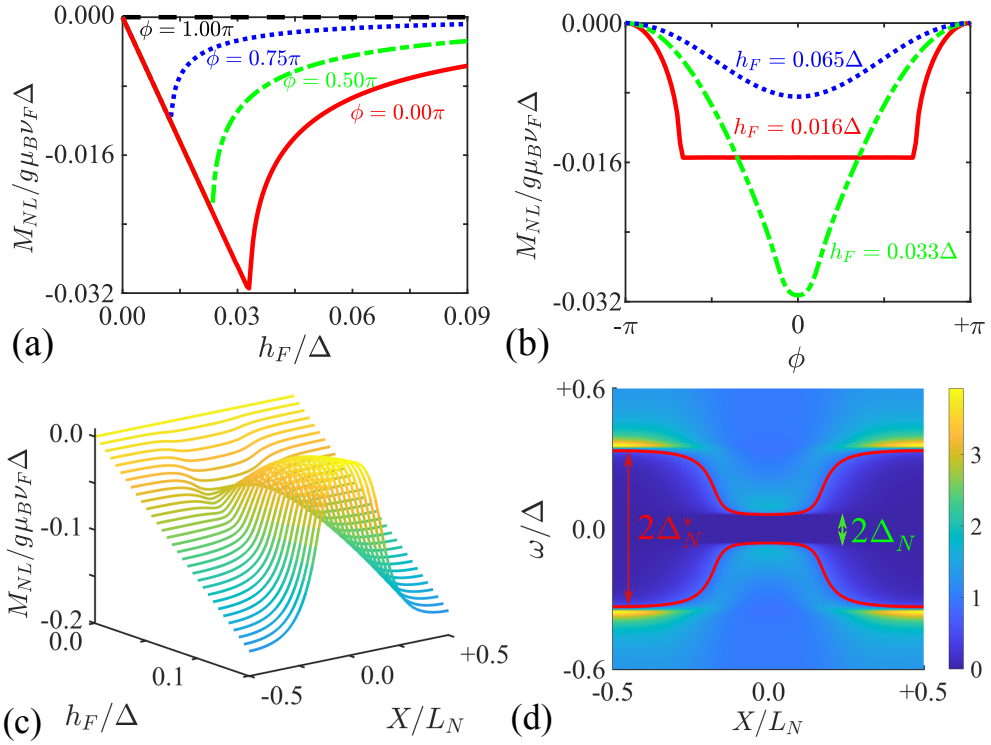

FIGURE 5.5: (Color online.) Nonlocal magnetization, M_{NL} of SC-FI-SC NW structure. Panels (a,b) plot the M_{NL} of as a function of (a) h_F/Δ and (c) ϕ, respectively, where $X = 0$, $\epsilon_b = 0.05\Delta$ and $L = \xi_0/3$. Panel (c) shows M_{NL} as a function of h_F/Δ and X/L_N, where $\phi = 0$, $\epsilon_b = 0.5\Delta$ and $L = 4.7\xi_0$. While panel (d) shows the corresponding local DoS, $N(\omega, X)$. The red curve represents the pseudogap, $\Delta_N^*(X)$. Other parameters: $T = 0$, $\epsilon_{so} = 0$, $\epsilon_b = 0.5\Delta$, $\phi = 0$, $\xi_0 = \sqrt{D/\Delta}$, $L_F = L_N$ and $L_S = L_N/3$.

where $\mathcal{F}$ and $\tilde{\mathcal{F}}$ describe the Cooper pairs penetrating from both S regions. In Riccati parameterization, Usadel equation (E.5.77), for each spin block $s = \pm$, reads

$$\gamma_s'' = \gamma_s'\tilde{\mathcal{F}}_s\gamma_s' - 2i[\omega_r(l) + sh_F\theta_F(l)]\gamma_s - \alpha_N\mathcal{F}_S(l) + \alpha_N\tilde{\mathcal{F}}_S(l)\gamma_s^2, \tag{E.5.81}$$

$$\tilde{\gamma}_s'' = \tilde{\gamma}_s'\mathcal{F}_s\tilde{\gamma}_s' - 2i[\omega_r(l) + sh_F\theta_F(l)]\gamma_s - \alpha_N\tilde{\mathcal{F}}_S(l) + \alpha_N\mathcal{F}_S(l)\tilde{\gamma}_s^2, \tag{E.5.82}$$

with

$$\omega_r^s(l) = \omega + i\alpha_N\mathcal{G}_S[\theta_L(l) + \theta_R(l)], \tag{E.5.83}$$

$$\mathcal{F}_S(l) = \mathcal{F}_S[\theta_L(l)e^{-i\phi/2} + \theta_R(l)e^{+i\phi/2}], \tag{E.5.84}$$

$$\tilde{\mathcal{F}}_S(l) = \mathcal{F}_S[\theta_L(l)e^{+i\phi/2} + \theta_R(l)e^{-i\phi/2}], \tag{E.5.85}$$

where $\alpha_N = L_N^2/(W_N\sigma_N R_\square)$, and we have made the position coordinate dimensionless by introducing $l = x/L_N$ and energy is in the unit of $\epsilon_{th} = D/L_N^2$.

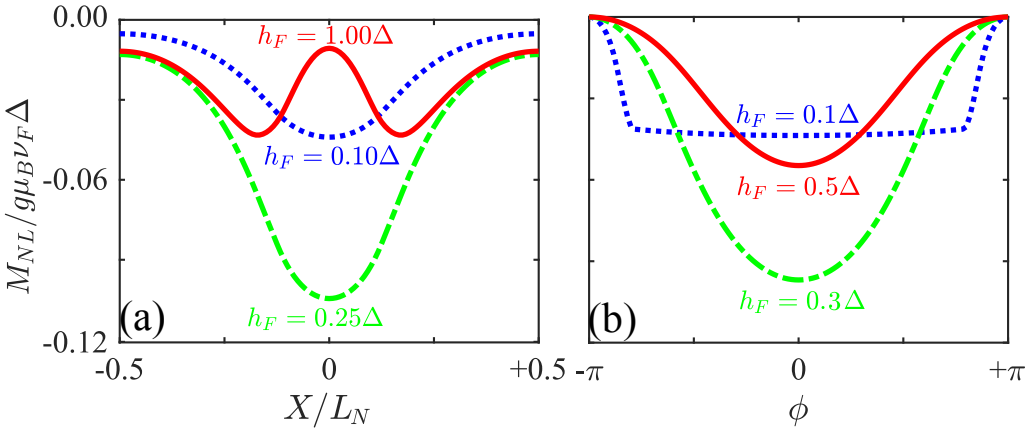

FIGURE 5.6: (Color online.) Nonlocal magnetization of the long NW partially covered by FI. Panels (a,b) show M_{NL} as a function of (a) X/L and (b) ϕ. We set $\phi = 0$ in panel (a) and $X = 0$ in panel (b). Other parameters: $T = 0$, $\epsilon_{so} = 0$, $\epsilon_b = 0.5\Delta$, $\xi_0 = \sqrt{D/\Delta}$, $L = 2.4\xi_0$, $L_F = L_N/4$ and $L_S = L_N/3$.

In a more realistic setup, the length of the NW, L_N can be larger than the characteristic length ξ_N. Moreover, the NW can be partially covered by the SCs films of length, L_S. We assume that the NW is grown on top of a FI substrate with length, L_F. Hereafter, we assume a symmetric setup with $L_S = L_N/3$, and hence the distance between the SC leads is $L = L_N/3$. The mini gap induced in the NW, Δ_N depends on this distance, and the NW/SC barrier resistance.

Let us begin with the case of weak superconducting proximity, $\epsilon_b = 0.05\Delta$ and short NW, $L = \xi_0/3$, where $\xi_0 = \sqrt{D/\Delta}$. FIGURE 5.5(a) shows the h_F dependence of M_{NL} at the center of NW for different values of the phase difference, ϕ. As far as $h_F < \Delta_N$, $M_{NL}W_N A$ compensates the Pauli magnetic moment $\int_b M_{\text{Pauli}} = g\mu_B\nu_F h_{ex} bA$ localized at the FI/NM interface, with A being the area of FI/NW interface. At $h_F = \Delta_N$, M_{NL} reaches a maximum value, $g\mu_B\nu_F\Delta_N$ and decays as $h_F - \sqrt{h_F^2 - \Delta_N^2}$ for $h_F > \Delta_N$ (Bergeret, Volkov, and Efetov, 2005; Karchev et al., 2001; Shen et al., 2003). In FIGURE 5.4(b), we show the phase difference, ϕ dependence of M_{NL} at the center of NW for different values of h_F. The maximum minigap is about $\Delta_N^0 \simeq 0.032\Delta$. When $h_F \leq \Delta_N^0$, M_{NL} remains constant for all phases smaller than $\arccos h_F/\Delta_N^0$ (red curve in FIGURE 5.4b). In other words, as far as h_F is smaller than the induced gap $\Delta_N = \Delta_N^0 \cos(\phi/2)$, the $M_{NL}(\phi)$ curve shows a plateau at the value opposite to M_{Pauli}. The maximum modulation is achieved for $h_F = \Delta_N^0$ (green curve in FIGURE 5.4 b). For larger values of h_F, M_{NL} the NW is gapless and $M_{NL}(\phi)$ is overall reduced (blue curve).

Let us now go beyond the limits of weak superconducting proximity and short NW. The results are plotted in FIGURE 5.5 , where $\epsilon_b = 0.5\Delta$ and $L = 4.7\xi_0$. In this case, the local DoS, $N(\omega, X)$ strongly depends on X (FIGURE 5.5d here and FIGURE 3b of main text). The induced mini gap, Δ_N, though, is spatially constant, as shown by the green line in FIGURE 5.5(d). The local pseudogap, $\Delta_N^*(X)$ defined by the energy in which the exact DoS, $N(\omega, X)$ coincide with the DOS in the normal state, $N_0(\omega, X) = 1$, is position-dependent, as shown by the red curves in FIGURE 5.5(d). It is smallest at the center, $\Delta_N^*(0) \simeq \Delta_N$, and becomes bigger closer to both ends. At zero temperature, the calculation of the local $M_{NL}(X)$, Eq. (1) of the main text, can be well approximated by replacing the exact DoS, $N(\omega, X)$ by a BCS-like one, $N_{BCS}(\omega, \Delta_N^*(X))$ with the position-dependent gap, $\Delta_N^*(X)$.

Panel 5.5(c) depicts M_{NL} as a function of h_F/Δ and X/L_N. We find an interesting transition from a maximum to a minimum at $X = 0$ in the $M_{NL}(X)$ dependence. For small h_F, the shape with a minimum is due to the weakening of spin screening with increasing pseudogap, $\Delta_N^*(X)$ from the center to both ends.

In FIGURE 5.6 we show the nonlocal magnetization in a setup when the FI is in contact only to a certain portion of the NW, for example, if $L_F/L_N = 1/4$. In FIGURE 5.6 (a), we show the spatial dependence of M_{NL} for different values of h_F and in panel (b) the phase-dependence at $x = 0$.

Part II

Spin and valley transports in two-dimensional materials

Chapter 6

Valley Hall effect and nonlocal transport in strained graphene

6.1 Introduction

The manipulation of the valley degree of freedom, i.e. the field of *valleytronics*, is currently under intensive research, not only concerning graphene (Jiang et al., 2013; Gorbachev et al., 2014; Gradinar et al., 2013; Cosma et al., 2014; Beconcini, Taddei, and Polini, 2016) but also other two dimensional (2D) materials (Xiao, Chang, and Niu, 2010; Shimazaki, Yamamoto, and Borzenets, 2015; Sie and McIver, 2015; Lee, Mak, and Shan, 2016). Indeed, the generation of valley currents has been recently demonstrated (Gorbachev et al., 2014) in graphene devices deposited on a hexagonal Boron Nitride (hBN) substrate, as discussed in subsection 1.3.1. This phenomenon, known as the valley Hall effect (VHE), which was introduced in subsection 1.3.2, can be detected as a large enhancement of the nonlocal resistance in a Hall bar device (Gorbachev et al., 2014; Abanin et al., 2009; Beconcini, Taddei, and Polini, 2016).

Here, we report a different approach to generate valley-polarized currents in graphene, which relies on the nonuniform strain, as presented in subsection 1.3.1. Since strain can be controlled more easily than the magnitude of the hBN-induced gap, it will allow for a larger tunability of the effect, thus providing a novel link between valleytronics and *straintronics* (Guinea, Katsnelson, and Geim, 2010; Vozmediano, Katsnelson, and Guinea, 2010; Amorim et al., 2016; Gradinar et al., 2013; Cosma et al., 2014; Mikkel Settnes, 2016). Furthermore, the strain also provides a "dual counterpart" to the VHE emerging from Berry curvature in momentum space (Xiao, Chang, and Niu, 2010; Gorbachev et al., 2014). This is because in graphene and other 2D materials, the strain can be described as a (pseudo) gauge field, which induces a (Aharonov-Bohm-like) phase in real space (Cazalilla, Ochoa, and Guinea, 2014; Pearce, Mariani, and Burkard, 2016).

A direct consequence of the strain-induced gauge fields is the emergence of pseudo-Landau levels, whose experimental observation has been reported in both real (Levy et al., 2010; Shioya et al., 2015; Li et al., 2015) and artificial graphene systems (Gomes et al., 2012; Rechtsman et al., 2013). Nevertheless, the observation of quantized valley edge currents (i.e., the quantum VHE), which was predicted by Guinea, Katsnelson, and Geim, 2010, has not yet been reported. Indeed, the requirements for the latter are rather stringent, involving devices under relatively high shear strain, low temperatures, and high mobility graphene, which is free of atomic-size defects and armchair-like edges (Cosma et al., 2014). On the other hand, bulk valley Hall currents can be generated in graphene nanoresonators by applying the pulsed strain, as predicted by Jiang et al., 2013.

In this chapter, an alternative for creating valley currents is discussed. It does not require either pulsed strain or highly strained, neither high-mobility devices. The

strain-induced VHE that we predict should be observable with fairly modest strain levels in Hall bar devices. By "modest strain", we mean strain levels lower than those required for the observation of pseudo-Landau levels. In a Hall (H-shaped) device, such strain can be achieved by applying, for instance, uniaxial strain in the direction perpendicular to the channel direction, i.e., by stretching one edge while clamping the other. Furthermore, unlike recent works along similar lines (Milovanovic and Peeters, 2016; Carrillo-Bastos et al., 2016; Jiang et al., 2013; Gradinar et al., 2013; Cosma et al., 2014), which focuses on nanometer-size devices and ballistic transport, our results apply to much larger and disordered devices in the micrometer scale, where conduction occurs in the diffusive regime, and hence it is potentially more interesting from the application point of view.

The hallmark of the strain-induced VHE is the emergence of a large nonlocal resistance in Hall bar devices (Gorbachev et al., 2014; Beconcini, Taddei, and Polini, 2016). The nonlocal resistance can be computed from the diffusion equations for the valley polarization. Extending previous treatments of the VHE (Gorbachev et al., 2014; Abanin et al., 2009; Beconcini, Taddei, and Polini, 2016), which have relied on a phenomenological treatment of the diffusion equations, here we provide a microscopic derivation of the diffusion equations starting from the linearized quantum Boltzmann equation derived by Huang et al., 2016. The latter allows us to account for the full quantum coherence of the valley (pseudo-spin) degree of freedom. We are thus able to show that, upon averaging over all the possible equilibrium impurity configurations, the diffusion equations depend on only two scattering rates: the inverse of the mean scattering time and the inter-valley scattering rate. For the latter, we provide expressions that can be used to extract the scattering rates from first-principle calculations of a single impurity potential.

Finally, it is worth mentioning that the strain-induced valley Hall currents predicted here are neutral currents that do not couple to external magnetic fields. Therefore, unlike spin currents (Abanin et al., 2009; Balakrishnan et al., 2014), valley currents will not display Hanle precession (i.e., modulation of the nonlocal resistance as a function of the strength of the in-plane magnetic field). Thus, our findings are relevant for the interpretation of some of the nonlocal transport measurements in graphene decorated with hydrogen (Kaverzin and Wees, 2015) and gold adatoms (Wang, Cai, and Reutt-Robey, 2015), for which Hanle precession was not observed. Indeed, the nonuniform strain may have been introduced unintentionally during device preparation in the studies reported by Kaverzin and Wees, 2015; Wang, Cai, and Reutt-Robey, 2015 . The application of the present theory to such experiments and the study of the interplay with other neutral currents will be explored in Chapter 7. (Zhang, Huang, and Cazalilla, 2019).

This chapter is organized as follows. In the next section, we describe the model's details and discuss the range of validity. In Sec. 6.3, we compute the linear response of strained graphene and, in particular, the doping and temperature dependence of the valley Hall conductivity. The derivation of the diffusion equation for the valley polarization is provided in Sec. 6.4. In Sec. 6.5, we compute the nonlocal resistance of a Hall bar device, which provides a convenient way to detect the VHE. In Sec. 6.6, we provide a summary of our results.

6.2 Model

Semiclassically, the electron motion in non-uniformly strained graphene is described using the following set of equations:

$$\dot{\vec{r}} = \vec{u}_k, \quad \dot{\vec{k}} = \left(e\vec{E} + \tau_z \dot{\vec{r}} \times \vec{\mathcal{B}}_s \right), \tag{6.2.1}$$

where $\vec{r}$ and $\vec{k}$ are the average position and momentum of a narrow wave packet of Bloch states, $\epsilon_k = \lambda v_F |\vec{k}|$ the electron dispersion ($\lambda = +1$ for the conduction and $\lambda = -1$ for the valence band, respectively), and $\vec{u}_k = \vec{\nabla}_k \epsilon_k = \lambda v_F \vec{k}/|\vec{k}|$ the carrier group velocity (henceforth we set $\hbar = 1$). In addition, $\vec{E}$ is the applied electric field, $e < 0$ the electron charge, and $\tau_z \vec{\mathcal{B}}_s$ is the strain-induced pseudo-magnetic field (Guinea, Katsnelson, and Geim, 2010; Vozmediano, Katsnelson, and Guinea, 2010; Amorim et al., 2016; Katsnelson, 2012). Note that, because strain does not break time-reversal invariance (unlike a real magnetic field), the sign of the magnetic field is opposite at opposite valleys. In terms of the strain tensor $u_{\alpha\beta}$ (Vozmediano, Katsnelson, and Guinea, 2010; Amorim et al., 2016; Katsnelson, 2012), $\vec{\mathcal{B}}_s = \nabla \times \vec{\mathcal{A}}_s$ where $\vec{\mathcal{A}}_s = \frac{\beta}{a}\left(u_{xx} - u_{yy}, -2u_{xy}\right)$ is the pseudo gauge field. Here $a = 1.42$ Å is the carbon-carbon distance and $\beta \simeq 2$ (Guinea, Katsnelson, and Geim, 2010). In the absence of an electric field (i.e. $\vec{E} = 0$), Eq. (6.2.1) predicts that a wave packet of mean momentum $\vec{k}_0 \neq 0$ moves in a circular orbit and in opposite directions depending on whether $\vec{k}_0$ lies closer to the K or K' valley. Such a valley-dependent circular motion of electron wavepackets has been obtained numerically by Costa et al., 2012

When quantized, the circular orbits lead to pseudo-Landau levels (pLLs) (Katsnelson, 2012; Guinea, Katsnelson, and Geim, 2010; Mikkel Settnes, 2016) with energy dispersion $\varepsilon_n = \pm\Omega_c\sqrt{n}$, where $\Omega_c = \sqrt{2v_F^2|\mathcal{B}_s|}$ is the cyclotron frequency of graphene. Here we explore the semiclassical regime, for which pLL are absent due to the broadening induced by disorder and/or temperature (T). This is the case when the distance between consecutive Landau levels, i.e. $\Delta_n = \varepsilon_{n+1} - \varepsilon_n$, is smaller or comparable to $\max\{k_B T, \tau_D^{-1}\}$, where τ_D^{-1} is the impurity scattering rate (see below). For large pLL filling factor, i.e. for $\mu \gg \Omega_c$, where $\mu = v_F k_F$ is the Fermi energy (at $T = 0$) and k_F the Fermi momentum, we have $\Delta_n \simeq \Omega_c n^{-1/2}$. Taking into account that $\sqrt{n} \simeq \mu/\Omega_c$, the condition $\Delta_n \tau_D \lesssim 1$ translates into $\omega_c \tau_D \lesssim 1$, where $\omega_c = \Omega_c^2/\mu = v_F |e\mathcal{B}_s|/k_F$. Below, we shall see that the modified cyclotron frequency ω_c naturally emerges when the Boltzmann kinetic equation is applied to describe doped graphene.

Besides the low pseudo-magnetic field (i.e., low strain) limit, our results are also applicable in high field limit where $\omega_c \tau_D \gg 1$ provided the temperature $T \gg \omega_c/k_B$ (where k_B is Boltzmann's constant). A rough estimate of the limits of applicability of the present semiclassical theory is displayed in FIGURE 6.1(b), in the temperature (T), and chemical potential (μ) plane. The blue curves correspond (for typical system parameters) to $k_B T = \tau_D^{-1}$, and separate the regime where the pseudo-Landau levels are dominantly broadened by disorder from the regime where thermal broadening dominates. At low temperatures, the semiclassical condition $\Delta_n \lesssim \tau_D^{-1}$ translates into $\omega_c \lesssim \tau_D^{-1}$ (i.e., $\omega_c \tau_D \lesssim 1$). Two vertical lines, determined by the condition that $\omega_c \tau_D = 1$ ($\mu \simeq -0.07$ eV and $\mu \simeq 0.13$ eV), separate the disorder-dominated regime into two additional regimes, where regime (1) corresponds to the semiclassical regime. The regions shaded regimes (in red and yellow) cannot be described by the present semiclassical approach, and our theory is not reliable there.

Under the conditions stated above, we can use the following linearized Boltzmann equation (BE) to describe a doped layer of strained graphene (Huang et al., 2016)

$$\partial_t \delta n_k + \vec{r}\cdot\nabla_r \delta n_k + \vec{k}\cdot\nabla_k \left[n_k^0 + \delta n_k\right] = \mathcal{I}[\delta n_k], \tag{6.2.2}$$

where δn_k is deviation of the electron distribution from the equilibrium distribution, i.e. $\delta n_k = n_k - n_k^0$, where $n_k^0 = n^0(\epsilon_k - \mu)$, being $n^0(\epsilon) = \left[e^{\epsilon/k_BT}+1\right]^{-1}$ the Fermi-Dirac distribution at temperature T and chemical potential μ. Note that, in order to correctly account for the quantum entanglement between the two valleys within the $\vec{k}\cdot\vec{p}$ theory, Katsnelson, 2012 $\delta n_{\vec{k}}$ must be treated as a 2×2 density matrix acting on the space of valley pseudo-spinors.

In Eq. (6.2.2), the collision integral $\mathcal{I}\left[\delta n_{\vec{k}}\right]$ describes the effect of disorder. Its form has been derived by Huang et al., 2016, extending the work of Luttinger and Kohn, 1958 in order to account for the effects of disorder on the electron internal degrees of freedom, such as the valley pseudo-spin. To leading order in the impurity density, n_{imp}, we have

$$\begin{aligned}\mathcal{I}[\delta n_{\vec{k}}] = 2\pi n_{\text{imp}} \sum_{\vec{p}} \delta(\epsilon_k - \epsilon_p) \Big[& T^+_{kp}\delta n_p T^-_{pk} \\ & -\frac{1}{2}\left\{\delta n_k T^+_{kp}T^-_{pk} + T^+_{kp}T^-_{pk}\delta n_k\right\}\Big],\end{aligned} \tag{6.2.3}$$

where $T^{\pm}_{kp}$ is the scattering matrix for a single impurity (the system area is assumed to be unity).

At low temperatures, the dominant mechanism that limits the diffusion of bulk valley currents is the inter-valley scattering caused by atomic-size impurities and defects. Here we consider a random ensemble of atomic-size impurities, which are assumed to reside on the honeycomb lattice sites (e.g., vacancies). Our considerations can be generalized to the other types of impurity potentials classified on symmetry grounds in the work of Cheianov et al., 2009. The effect of random strain fluctuations, which dominate transport in high-quality devices on substrates like hBN, has been studied elsewhere (Couto et al., 2014) and will be neglected here. Within the $\vec{k}\cdot\vec{p}$ theory, the potential for one such impurity takes the following form (Basko, 2008; Cheianov et al., 2009; Kopylov et al., 2011)

$$\begin{aligned}V(\vec{r}) = & \left[v_0\mathbb{1} + s v_z\sigma_z\right]\delta(\vec{r}) \\ & + v_{xy}\left(\mathbb{1}+s\sigma_z\right)\left(u_x\tau_x + i u_y\sigma_z\tau_y\right)\Big]\delta(\vec{r}),\end{aligned} \tag{6.2.4}$$

where the Pauli matrices σ_α and τ_α ($\alpha = x,y,z$ describe the sublattice and valley pseudo-spin, respectively. In the above expression, the terms in the first line ($\propto v_0, v_z$) conserve the valley pseudo-spin τ_z while the terms in the second line induce inter-valley scattering. The Ising variable $s = +1$ ($s=-1$) when the impurity sits on the A (B) sublattice. The vector $\vec{u} = (u_x, u_y) \in S = \{(1,0), (-\frac{1}{2}, \frac{\sqrt{3}}{2}), (-\frac{1}{2}, -\frac{\sqrt{3}}{2})\}$ parametrizes the inter-valley scattering potential (Basko, 2008; Cheianov et al., 2009; Kopylov et al., 2011). The impurities are assumed to form a completely disordered ensemble, which is the most stable configuration at high doping and temperatures of interest here (Cheianov et al., 2009; Kopylov et al., 2011. Thus, the configurational variables ($s_l = \pm 1, \vec{u}_l \in S$) can take all the six possible values allowed by symmetry with equal probability. Hence, upon solving the scattering problem, the

band-projected (on shell) T-matrix can be obtained, and it takes the general form, $T^{+}_{kp} = A_{kp}\mathbb{1} + \vec{B}_{kp}\cdot\vec{\tau}$, where $\vec{B}_{kp} = \vec{B}^{\parallel}_{kp} + \vec{z}\, B^{\perp}_{kp}$, describes the valley-dependent scattering with $\vec{z}\cdot\vec{B}^{\parallel}_{kp} = 0$, and

$$A_{kp} = \gamma_0(k)\cos\frac{\theta}{2}, \tag{6.2.5}$$

$$B^{\perp}_{kp} = is\tau_z\gamma_z(k)\sin\frac{\theta}{2}, \tag{6.2.6}$$

$$\vec{B}^{\parallel}_{kp} = \lambda\gamma_{xy}(k)\left[s\left(u_x\cos\frac{\phi}{2} + u_y\sin\frac{\phi}{2}\right)\vec{x} + \left(-u_x\sin\frac{\phi}{2} + u_y\cos\frac{\phi_{kp}}{2}\right)\vec{y}\right], \tag{6.2.7}$$

where $\theta = \varphi_k - \varphi_p$ and $\phi = \varphi_k + \varphi_p$, and $\varphi_k = \tan^{-1}(k_y/k_x)$. The functions $\gamma_0(k), \gamma_z(k)$ and $\gamma_{xy}(k)$ depend on $k = |\vec{k}|$ (where $\vec{k}$ is the momentum of the incoming electron) and the potential parameters v_0, v_z, v_{xy} (see e.g. Basko, 2008; Yang et al., 2016 for details of such scattering calculations).

Next, we average over the impurity configurations and find that the only non-vanishing scattering rates of the theory are given by the total current relaxation (i.e., Drude scattering rate, τ_D^{-1}) and the intervalley scattering rate τ_v^{-1}. Other terms in the collision integral, such as those proportional to $A_{kp}B^{\perp}_{kp}$ or $A_{kp}\vec{B}^{\parallel}_{kp}$, change sign under sublattice inversion, as dictated by the group theory that determines the structure of the scattering potential, Eq. (6.2.4), and the corresponding T-matrix (Basko, 2008). Thus, their contribution to the collision integral vanishes when impurities occupy both sublattices with equal probability, as we have assumed. This can be most easily understood if we neglect intervalley scattering (which corresponds to the terms in the second line of Eq. 6.2.4). The term proportional to $s\sigma_z$ gives rise to valley current perpendicular to the incident electron current, whose sign is determined by the Ising variable $s = \pm 1$. Upon taking impurity average, the valley current generated by impurities in sublattice A ($s = +1$) and B ($s = -1$) cancel each other. A similar (albeit slightly more complicated) cancellation occurs for other scattering rates resulting from the quantum interference of intervalley scattering potential. The intravalley scattering amplitude, $B^{\perp}_{kp}$ depends linearly on the Ising variable s, while the intervalley scattering potential, $\vec{B}^{\parallel}_{kp}$ depends both on s and u_x, u_y. Therefore, the $B^{\perp}_{kp}\vec{B}^{\parallel}_{kp}$ contributions are $\vec{u}$-dependence, which will also vanish after impurity average of equal probability of each configuration $(s, \vec{u})$. Physically, this means that a random impurity ensemble cannot lead to phenomena like anisotropic spin precession (ASP) scattering discussed in the context of spin transport in the work of Huang et al., 2016. It was shown that ASP leads to a *direct* coupling between (non-equilibrium) spin polarization and charge current.

6.3 Linear Response

In order to obtain the response of the system, we parametrize $\delta n_k = \rho_k\mathbb{1} + \vec{\mathcal{P}}_k\cdot\vec{\tau}$, where ρ_k describes the charge fluctuations and $\vec{\mathcal{P}}_k = \vec{\mathcal{P}}^{\parallel}_k + \vec{z}\,\mathcal{P}_k$ (with $\vec{z}\cdot\vec{\mathcal{P}}^{\parallel}_k = 0$) the valley pseudo-spin fluctuations of the electron distribution, δn_k. Summing over the impurity configurations, the kinetic equations for $\rho_k, \mathcal{P}_v$ on one side, and $\vec{\mathcal{P}}^{\perp}_v$, on the other side, decouple. Thus, in what follows, we focus on the equations for ρ_k, $\mathcal{P}_v$,

which describe the valley Hall effect of interest here. In addition, as described above, the collision integral for the latter is found to be parametrized by two scattering rates: the Drude scattering rate $\tau_D^{-1} = \frac{n_{\text{imp}}k}{4v_F}(|\gamma_0|^2 + 3|\gamma_z|^2 + 4|\gamma_{xy}|^2)$, and the intervalley scattering rate $\tau_v = \frac{n_{\text{imp}}k}{4v_F}(8|\gamma_{xy}|^2)$.

In the steady state, we employ the ansatz proposed by Huang et al., 2016

$$\rho_k = \left(\delta\mu + \vec{u}_c \cdot \vec{k}\right)\left[-\partial_\mu n_k^0\right], \tag{6.3.8}$$

$$\vec{\mathcal{P}}_k = \left[h_v\vec{n}_0 + \vec{n}_1\left(\vec{u}_v \cdot \vec{k}\right)\right]\left[-\partial_\mu n_k^0\right], \tag{6.3.9}$$

which allows us to obtain the constitutive relations by multiplying Eq. (6.2.2) by $\vec{u}_k(\mathbb{1}, \tau_z)$, and tracing over $\vec{k}, \lambda$ and valley pseudo-spin. Thus,

$$\vec{J} = -\mathcal{D}\vec{\nabla}_r\delta n(\vec{r}) + \omega_c\tau_D\left(\vec{\hat{z}} \times \vec{\mathcal{J}}\right) + \sigma_D\vec{E}(\vec{r}), \tag{6.3.10}$$

$$\vec{\mathcal{J}} = -\mathcal{D}\vec{\nabla}_r\mathcal{P}(\vec{r}) + \omega_c\tau_D\left(\vec{\hat{z}} \times \vec{J}\right), \tag{6.3.11}$$

where $\delta n = g_s e\text{Tr}\sum_k \delta n_k$ and $\vec{J} = eg_s\text{Tr}\sum_k[\vec{u}_k\delta n_k]$ are the particle density and charge current, respectively. $\mathcal{P} = g_s e\text{Tr}\sum_k[\tau_z\delta n_k]$ and $\vec{\mathcal{J}} = eg_s\text{Tr}[\vec{u}_k\tau_z\delta n_k]$ are the valley polarization and current, respectively (g_s is the spin degeneracy). In the above expression $\sigma_D = ne^2\tau_D/(m_F)$ ($m_F = k_F/v_F$ and n is the carrier density) is the Drude conductivity and $\mathcal{D} = v_F^2\tau_D/2$ the diffusion coefficient. The last equation describes the classical VHE, while the second term on the right-hand side of Eq. (6.3.10) describes the inverse VHE.

We can solve Eq. (6.3.10) and (6.3.11) for the charge $\vec{J}$ and valley current $\vec{\mathcal{J}}$:

$$\vec{J} = -\mathcal{D}_\parallel\vec{\nabla}_r\delta n(\vec{r}) + \mathcal{D}_\perp\vec{\hat{z}} \times \vec{\nabla}_r\mathcal{P}(\vec{r}) + \sigma_\parallel\vec{E}(\vec{r}), \tag{6.3.12}$$

$$\vec{\mathcal{J}} = -\mathcal{D}_\parallel\vec{\nabla}_r\mathcal{P}(\vec{r}) + \mathcal{D}_\perp\vec{\hat{z}} \times \vec{\nabla}_r\delta n(\vec{r}) + \sigma_\perp\hat{z} \times \vec{E}(\vec{r}), \tag{6.3.13}$$

where the longitudinal (transverse) diffusion constant $\mathcal{D}_\parallel$ ($\mathcal{D}_\perp$) and longitudinal (transverse) conductivity $\sigma_\parallel$ ($\sigma_\perp$) are given by the following expressions (at $T = 0$)

$$\mathcal{D}_\parallel = \frac{\mathcal{D}}{1 + \omega_c^2\tau_D^2}, \qquad \mathcal{D}_\perp = \frac{\omega_c\tau_D\mathcal{D}}{1 + \omega_c^2\tau_D^2}, \tag{6.3.14}$$

$$\sigma_\parallel = \frac{\sigma_D}{1 + \omega_c^2\tau_D^2}, \qquad \sigma_\perp = \frac{\omega_c\tau_D\sigma_D}{1 + \omega_c^2\tau_D^2}. \tag{6.3.15}$$

Note that, for a uniform electric field, both $\vec{\nabla}_r\delta n(\vec{r})$ and $\vec{\nabla}_r\mathcal{P}(\vec{r})$ vanish, and one obtains the linear response relations, $\vec{J} = \sigma_\parallel\vec{E}$ and $\vec{\mathcal{J}} = \sigma_\perp\left(\vec{\hat{z}} \times \vec{E}\right)$. According to Eq. (6.3.15), the longitudinal charge conductivity $\sigma_\parallel$ is reduced by the strain pseudomagnetic field in a way similar to a real magnetic field. Similar to the conventional Hall effect, both the inverse and direct VHE can be characterized by a figure of merit, namely the valley Hall angle θ, which is defined as follows

$$\tan\theta(T) = \frac{\sigma_\perp(T)}{\sigma_\parallel(T)}. \tag{6.3.16}$$

The expressions for the charge ($\sigma_{\parallel}$) and spin Hall ($\sigma_{\perp}$) conductivities at temperature $T > 0$ read

$$\sigma_{\parallel}(T) = \frac{e^2}{2\pi}\int d\epsilon\,|\epsilon|\frac{\tau_{\mathrm{D}}\left[-\partial_\mu n^0\left(\epsilon-\mu\right)\right]}{\left(1+\omega_c^2\tau_{\mathrm{D}}^2\right)}, \tag{6.3.17}$$

$$\sigma_{\perp}(T) = \frac{e^2}{2\pi}\int d\epsilon\,|\epsilon|\frac{\omega_c\tau_{\mathrm{D}}^2\left[-\partial_\mu n^0\left(\epsilon-\mu\right)\right]}{\left(1+\omega_c^2\tau_{\mathrm{D}}^2\right)}. \tag{6.3.18}$$

where both τ_D and ω_c are energy (i.e. Fermi momentum) dependent. Eq. (6.3.16) reduces to $\tan\theta(T \simeq 0) \simeq \omega_c\tau_D$ at low enough temperature (i.e. $T \simeq 0$). The dependence of $\theta(T)$ on the chemical potential μ at different temperatures is shown in FIGURE 6.1(a). We find that the valley Hall angle can approach $\frac{\pi}{2}$ at low doping and low temperatures. This is because the pseudo cyclotron frequency ω_c is inversely proportional to μ and τ_D is resonantly enhanced in the neighborhood of the Dirac point. However, the semiclassical theory becomes less reliable close to the Dirac point where $\mu = 0$, especially for low temperatures. Indeed, $\theta \to \frac{\pi}{2}$ at low doping and low temperature, which implies that $\omega_c\tau_D \gg 1$, meaning that the semiclassical theory ceases to be valid, as discussed above. However, as explained above, at sufficiently high temperatures, the pseudo-Landau levels are broadened by thermal fluctuations, and the semiclassical theory can describe the system. Although thermal fluctuations slightly suppress the magnitude of $\theta(T)(< \theta(T=0))$, fairly sizable valley Hall angles can be reached $\theta(T) \gtrsim \pi/4$ in high-temperature semiclassical regime for $T \simeq 100K$ and $\mu \simeq 0.05$ eV, as shown in FIGURE 6.1(a).

6.4 Diffusion of the valley polarization

The above quantum Boltzmann equation also allows us to obtain the continuity equations for the charge and the valley current. After multiplying Eq. (6.2.2) by $(\mathbb{1}, \tau_z)$ and taking the trace after summing over λ and $\vec{k}$, we obtain (in the steady state) $\vec{\nabla}\cdot\vec{J} = 0$, for the charge current and $\vec{\nabla}_r\cdot\vec{\mathcal{J}} + \mathcal{P}/\tau_{\mathrm{v}} = 0$, for the valley current. By combining the last equation with Eq. (6.3.13), the diffusion equation for the valley polarization is obtained:

$$\mathcal{D}_{\parallel}\nabla_r^2\mathcal{P}\left(\vec{r}\right) - \frac{\mathcal{P}\left(\vec{r}\right)}{\tau_{\mathrm{v}}} = S\left(\vec{r}\right), \tag{6.4.19}$$

where $S\left(\vec{r}\right) = \vec{\hat{z}}\cdot\vec{\nabla}_r\times\left[\sigma_{\perp}\left(\vec{r}\right)\vec{E}\left(\vec{r}\right)\right]$ is the source of the diffusion. For uniform pseudo-magnetic field, $\mathcal{B}_s$, it is only where the strain-induced pseudo-magnetic field vanishes abruptly, i.e., at the device boundary, that the source term is not zero. Eq. (6.4.19) indicates the existence of the following length scale that controls the diffusion of valley polarization:

$$\ell_{\mathrm{v}} = \sqrt{\mathcal{D}_{\parallel}\tau_{\mathrm{v}}} = L_{\mathrm{v}}(1+\omega_c^2\tau_D^2)^{-1/2}, \tag{6.4.20}$$

where $L_{\mathrm{v}} = \sqrt{\mathcal{D}\tau_{\mathrm{v}}}$. In FIGURE 6.2(a), we have plotted the length scale ℓ_{v} against the chemical potential for different values of strength of the pseudo-magnetic field. We find that the magnitude of ℓ_{v} decreases with the magnitude of the pseudo-magnetic field, as expected from Eq. (6.4.20). For the present choice of parameters, note that the resulting valley diffusion length ℓ_{v} (i.e. about $5\,\mu$m at $\mu = 0.1$ eV) is, in most regimes, larger than the width of the device, $W = 1\,\mu$m. However, as shown in

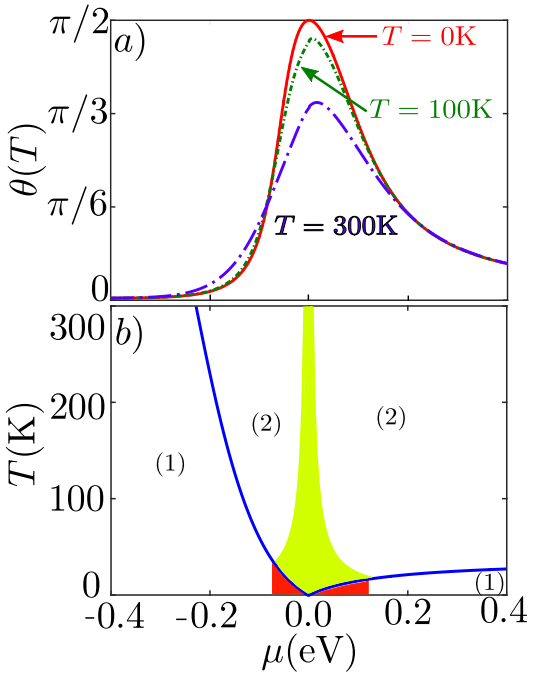

FIGURE 6.1: (color online) (a) The valley Hall angle, $\theta(T)$ is plotted against chemical potential μ for different temperatures $T = 0, 100, 300$K. (b) Limit of applicability of semiclassical theory in the plane of absolute temperature, T, and chemical potential μ as determined from the condition $\omega_c \simeq \max\{k_B T, \tau_D^{-1}\}$ (τ_D^{-1} is the elastic impurity scattering rate). The parameters used are: $\mathcal{B}_s = 0.3$ T, $n_{\text{imp}} = 1.0 \times 10^{12}$ cm^{-2}, the impurity (vacancy) potential is parametrized by $v_0 = 100$ eV, $v_z = v_{xy} = 3$ eV, impurity radius $R = 0.142$ nm, and cut-off momentum $k_c = 2/R$ (Basko, 2008).

the next section, the decay of the nonlocal resistance along the channel direction is controlled by L_v rather than ℓ_v.

6.5 Nonlocal resistance

Following Beconcini, Taddei, and Polini, 2016, we solve the diffusion equation for a Hall bar device geometry, consisting of a channel of width W, which we assume to be infinitely long. Thus, the solution of the diffusion equations can be found by imposing suitable boundary conditions (BCs): i) On the charge current: $J_y(x, y = \pm W/2) = I\delta(x)$. This BC describes the current injection (extraction) along the y direction ii) On the valley current: $\mathcal{J}_y(x, y = \pm W/2) = 0$, implying that no valley current flows across the device boundary.

The solution can be simplified by taking $\delta n(\vec{r}) \simeq 0$, which amounts to assuming complete screening of the electric field in the device (Beconcini, Taddei, and Polini, 2016). Thus, the electrostatic potential $\phi(\vec{r})$ obeys the Laplace equation, $\nabla^2\phi(\vec{r}) = 0$.

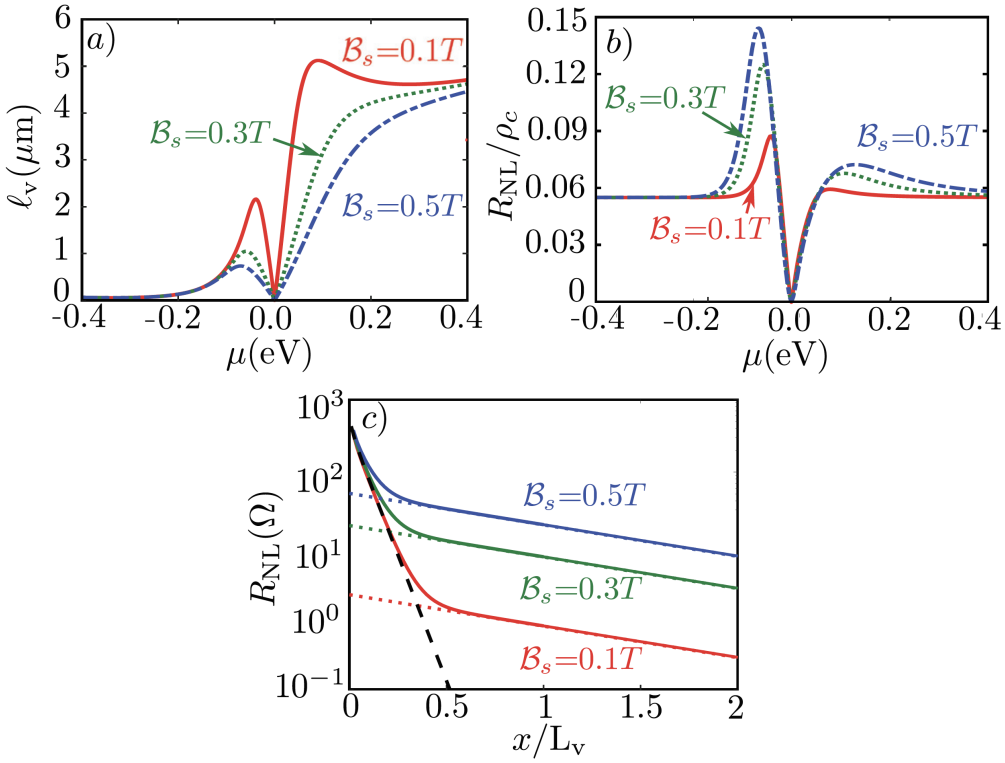

FIGURE 6.2: (color online) (a) ℓ_v, in μm, versus the chemical potential μ. (b) Nonlocal resistance R_{NL} (in units of ρ_c) evaluated at $x = 1\,\mu$m as a function of chemical potential μ. (c) Nonlocal resistance R_{NL} (in logarithmic scale) as a function of chemical potential x/L_v for fixed chemical potential $\mu = 0.15$ eV ($L_v \simeq 5\mu$ m), where the Ohmic nonlocal resistance corresponds to the black imaginary line. Note that the decay is controlled by the same length scale L_v for all values of the pseudo-magnetic field. The latter is induced by applying along the y direction an average (uniaxial) strain of 0.4%, 1.2% and 2.0%, respectively, to a ribbon of width $W = 1\,\mu$m. The parameters are the same as for FIGURE 6.1 and temperature is $T = 0$.

Using Eq. (6.3.12) and (6.3.13), the BCs can be recast as:

$$I\delta\left(x\right) = \left[-\mathcal{D}_{\perp}\partial_x\mathcal{P}\left(\vec{r}\right) - \sigma_{\parallel}\partial_y\phi\left(\vec{r}\right)\right]_{y=\pm\frac{W}{2}}, \tag{6.5.21}$$

$$0 = \left[-\mathcal{D}_{\parallel}\partial_y\mathcal{P}\left(\vec{r}\right) - \sigma_{\perp}\partial_x\phi\left(\vec{r}\right)\right]_{y=\pm\frac{W}{2}}, \tag{6.5.22}$$

where we have dropped the terms contaning $\delta n\left(\vec{r}\right)$. We see that the BCs couple the Laplace equation for $\phi(\vec{r})$ with the diffusion equation for $\mathcal{P}\left(\vec{r}\right)$. Eq. (6.4.19) together with the Laplace equation can be solved using Eq. (6.5.21) and (6.5.22) as BCs. Thus, we obtain:

$$\phi\left(\vec{r}\right) = -I\rho_c\int_{-\infty}^{+\infty}\frac{dk}{2\pi k}\frac{e^{+ikx}}{F\left(k\right)}\frac{\omega(k)\sinh\left(ky\right)}{\sinh\left(\frac{kW}{2}\right)}, \tag{6.5.23}$$

$$\mathcal{P}\left(\vec{r}\right) = \frac{I\tan\left(\theta\right)}{iD_{\parallel}}\int_{-\infty}^{+\infty}\frac{dk}{2\pi}\frac{e^{+ikx}}{F\left(k\right)}\frac{\cosh\left(\omega(k)y\right)}{\sinh\left(\frac{\omega(k)W}{2}\right)}, \tag{6.5.24}$$

with

$$F(k) = \tan^2(\theta)\, k \coth\left(\frac{\omega(k)W}{2}\right) + \omega(k) \coth\left(\frac{kW}{2}\right) \tag{6.5.25}$$

where $\rho_c = 1/\sigma_{||}$ and $\omega(k) = \sqrt{k^2 + \ell_{\mathrm{v}}^{-2}}$.

Hence, the nonlocal resistance can be obtained from

$$R_{\mathrm{NL}}(x) = [\phi(x, -W/2) - \phi(x, W/2)]/I. \tag{6.5.26}$$

Substituting Eq. (6.5.23) yields (Beconcini, Taddei, and Polini, 2016):

$$R_{\mathrm{NL}}(x) = 2\rho_{\mathrm{c}} \int_{-\infty}^{+\infty} \frac{dk}{2\pi k}\, e^{+ikx} \frac{\omega(k)}{F(k)}. \tag{6.5.27}$$

For $\theta = 0$, the nonlocal resistance reduces to the ohmic contribution:

$$R_{\mathrm{NL}}^0(x) = \frac{2\rho_c}{\pi} \ln\left|\coth\left(\frac{\pi x}{2W}\right)\right|. \tag{6.5.28}$$

FIGURE 6.2 shows the results of numerically integrating Eq. (6.5.27). At a fixed distance $x = 1\ \mu$m away from the current injection point, FIGURE 6.2(b) shows the nonlocal resistance R_{NL} versus the chemical potential, for different values of the pseudo-magnetic field strength, $\mathcal{B}_s$. The nonlocal resistance arising from the combined effect of VHE and inverse VHE is enhanced at low doping. At large doping, i.e. far from $\mu = 0$, the ratio of nonlocal resistance to the resistivity ρ_c flattens out to a constant value ($\simeq 0.055$ in FIGURE 6.2(b)). This flattening is due to the sharp decrease of the Hall angle away from $\mu = 0$ (cf. FIGURE 6.1). Taking the $\theta \to 0$ limit of Eq. (6.5.27), we retrieve the expression for Ohmic contribution, Eq. (6.5.28), which scales as $R_{NL} \propto \rho_c$ for fixed x and W (For $W = 1\ \mu$m, $\frac{2}{\pi}\ln\left|\coth\left(\frac{\pi}{2}\right)\right| \simeq 0.055$, which explains the numerical value reached by R_{NL} in FIGURE 6.2(b).

Panel (c) in FIGURE 6.2 shows the dependence of the nonlocal resistance $R_{\mathrm{NL}}(x)$ with x/L_{v} at fixed chemical potential $\mu = 0.15$ eV. Nonuniform strain enhances the nonlocal resistance relative to its ohmic value. At large $|x|$, and for $W \ll \ell_{\mathrm{v}}$, R_{NL} decays according to:

$$R_{\mathrm{NL}}(x) = \rho_c \frac{W}{2L_{\mathrm{v}}} \frac{\tan^2(\theta)}{1 + \tan^2(\theta)} e^{-|x|/L_{\mathrm{v}}}, \tag{6.5.29}$$

which agrees well with the numerical results for $|x| \gg \ell_{\mathrm{v}} \gg W$ (cf. FIGURE 6.2, showing that the ohmic contribution, cf. Eq. (6.5.28) is also much smaller in this limit). Note that, in this regime, the decay is controlled by L_{v} rather than the length scale ℓ_{v} introduced in Eq. (6.4.20). This can be understood from the fact that Eq. (6.5.27) is obtained by solving the coupled diffusion and Laplace equations, which takes into account the buildup of electrostatic potential (due to the inverse valley Hall effect) along the channel. The latter modifies the decay of $R_{\mathrm{NL}}(x)$ by effectively replacing $\ell_{\mathrm{v}} = L_{\mathrm{v}}(1 + \omega_c^2 \tau_D^2)^{1/2}$ by $L_{\mathrm{v}} = \sqrt{\mathcal{D}\tau_{\mathrm{v}}}$.

6.6 Summary and outlook

In this chapter, we have presented a theory of the strain-induced classical valley Hall effect (VHE). Specifically, using the quantum Boltzmann equation, we have provided a microscopic derivation of the equations governing valley polarization

diffusion. The latter has been solved for a Hall bar device geometry, subject to nonuniform strain leading to the uniform pseudo-magnetic field. The observable nonlocal resistance of the device has been obtained. We found that for low doping, the figure of merit of the VHE, namely the valley Hall angle, $\theta(T)$ can be of order unity, even at room temperature. The nonlocal resistance of the device decays exponentially. Moreover, the usage of the present theory to these nonlocal experiments and the study of the interplay with other neutral currents (spin and spin-valley currents) will be explored in Chapter 7.

Finally, it is interesting to consider a strain configuration's effect leading to a slowly varying (on the scale of the Fermi wavelength) pseudo-magnetic field. The equations derived here are also applicable in this case, with the caveat that in such a case, $\omega_c\tau_D$ becomes space dependent. This complicates the solution of the diffusion equation, Eq. (6.4.19), as the source term on the right-hand side $S(\vec{r})$ will not be a boundary term. In addition, the diffusion coefficient $D_{\parallel} = D_{\parallel}(\vec{r})$ is now a function of the position in the device. However, qualitative, one can still expect a nonlocal signal to exist even if the pseudo-magnetic field fluctuates in space because the nonlocal resistance depends quadratically on the valley Hall angle $\theta \sim \omega_c\tau_D$ as it arises from the combination of the direct and inverse valley Hall effects.

Chapter 7

The interplay of spin and valley Hall effects in graphene with strain and adatoms

7.1 Introduction

Spintronics (Xiao, Chang, and Niu, 2010; Sinova et al., 2015; Nagaosa et al., 2010; Sinova et al., 2004; Huertas-Hernando, Guinea, and Brataas, 2006) and valleytronics (Xu et al., 2014; Cao et al., 2012; Rycerz, Tworzydło, and Beenakker, 2007; Sie and McIver, 2015), as mentioned in Chapter 1, aim at manipulating internal degrees of freedom of Bloch electrons, which can have promising applications in low-energy consumption electronics and quantum computation. Previous theoretical studies of nonlocal transport have focused either on the VHE (Beconcini, Taddei, and Polini, 2016; Zhang, Huang, and Cazalilla, 2017; Song and Vignale, 2018) or on the SHE (Abanin et al., 2009; Huang, Chong, and Cazalilla, 2017).However, symmetry considerations imply that spin and valley are coupled in materials with broken spin-rotation and/or inversion symmetry (see more discussions about the indivisibility of spin and valley transport in subsection 1.5.2).

Being electrically neutral, direct detection of spin and valley currents is not possible, and their existence must be inferred by indirect means such as nonlocal transport measurements performed on a Hall bar device as depicted in FIGURE 7.1(a). In this setup, spin/valley currents are generated by driving an electric current between the two opposite right-hand side contacts of the device. The neutral (spin/valley) currents diffuse in the transverse direction to the applied electric current (field), leading to charge accumulation and a nonlocal voltage on the left-hand side of the device. The nonlocal resistance (NLR) is defined as the ratio of the nonlocal voltage, V_{nl} to the external current applied to the device, I. Using this setup, the VHE has been experimentally observed in devices made by depositing monolayer graphene on hexagonal boron nitride (hBN) (Gorbachev et al., 2014), bilayer graphene in a perpendicular displacement field (Shimazaki, Yamamoto, and Borzenets, 2015), as well as optically pumped TMDs (Mak et al., 2014; Lee, Mak, and Shan, 2016; Zeng et al., 2012; Lee et al., 2017). Likewise, the SHE has been experimentally observed in graphene decorated with absorbates (Balakrishnan et al., 2014; Balakrishnan et al., 2013; Weeks et al., 2011; Ma, Li, and Yang, 2012) and graphene-TMDs heterostructures (Avsar et al., 2014; Safeer et al., 2018; Benítez et al., 2018).

In connection to the observation of the SHE, the Hanle effect (HE), i.e., the modulation of the NLR as a function of an in-plane magnetic field, is considered to be the hallmark of the existence of spin currents (Balakrishnan et al., 2014; Balakrishnan et al., 2013; Huang, Chong, and Cazalilla, 2017; Abanin et al., 2009). However, the

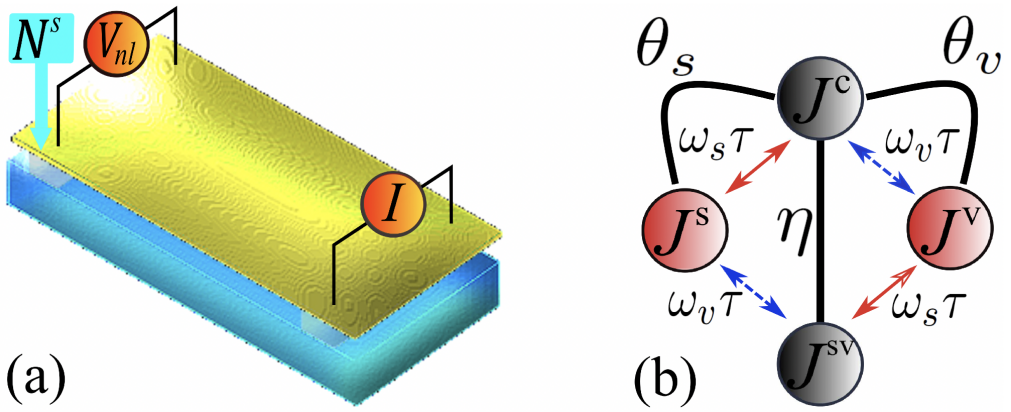

FIGURE 7.1: (a) Sketch of a Hall-bar device used for measuring the nonlocal resistance R_{nl}: A current I is injected on one side and a (non local) voltage V_{nl} is detected in the opposite side. The nonlocal resistance is defined as $R_{nl} \equiv V_{nl}/I$. In this work, we assume that the spin and valley Hall effect coexist in the device. (b) Sketch of the four types of current response described by our model. Unlike the longitudinal electric (charge) current (J^c), the transverse spin (J^s) and valley (J^v) currents and the longitudinal spin-valley (J^{sv}) current are all electrical neutral and therefore cannot be detected by all electrical means. In the absence of SHE (VHE), $\omega_v\tau$ ($\omega_s\tau$) determines the conversion rate from J^c to J^v (J^s). However, when both SHE and VHE are present, J^{sv} mediates a coupling between J^s and J^v, which has important consequences for the spin-diffusion as shown on the spin density of FIGURE 7.2(a).

absence of HE in some experiments in which a large enhancement of the NLR was observed (Völkl et al., 2018; Kaverzin and Wees, 2015; Wang, Cai, and Reutt-Robey, 2015) hints at the existence of additional contributions to the NLR that are insensitive to the magnetic field. One candidate that can contribute to the NLR is a valley current, which, as we have shown elsewhere (Zhang, Huang, and Cazalilla, 2017), can arise from a modest amount of nonuniform strain present in the Hall bar device.

This chapter studies the nonlocal transport caused by the interplay of both spin and valley Hall effects, which are induced by adatoms and strain, respectively. In connection with the experiments described above, we show that this interplay can have nontrivial consequences for spin transport in 2D materials. For instance, we find that spin density along the Hall bar can be modulated by the coupling between spin and valley currents, which can be controlled by applying a non-uniform strain to the device (Zhang, Huang, and Cazalilla, 2017). This provides an exciting link between spintronics and straintronics (Guinea, Katsnelson, and Geim, 2010; Vozmediano, Katsnelson, and Guinea, 2010; Amorim et al., 2016; Cazalilla, Ochoa, and Guinea, 2014). Besides, we find that the HE may be strongly suppressed by the interplay with the VHE and even absent under some circumstances. This finding can reconcile the apparently contradictory experimental results of various groups (Kaverzin and Wees, 2015; Avsar et al., 2015; Wang, Cai, and Reutt-Robey, 2015), some of which have observed a large enhancement of the NLR but failed to observe the HE (Kaverzin and Wees, 2015; Wang, Cai, and Reutt-Robey, 2015). Thus, the study reported here can guide future studies of nonlocal transport in graphene, TMDs, and other 2D materials.

This chapter is organized as follows. In the next section, we describe the theory's details for the coexistence of the spin and valley Hall effects in graphene with strain and adatoms. In Sec. 7.3, we demonstrate the control of spin diffusion through strain. In Sec. 7.4, we study the nonlocal resistance of a Hall bar device and prove the suppression of the Hanle effect. In Sec. 7.5, we provide a summary and outlook of our work. Detailed mathematical expressions and derivations are relegated to the Appendix.

7.2 Coexistence of spin and valley Hall effects

We shall work in the diffusive regime where $k_F\ell \gg 1$, k_F being the Fermi momentum of the electrons, and ℓ the elastic mean-free path. This is the relevant regime to the devices that are experimentally studied (e.g., Balakrishnan et al., 2014; Balakrishnan et al., 2013; Kaverzin and Wees, 2015; Avsar et al., 2015; Wang, Cai, and Reutt-Robey, 2015). In this regime, the transport of spin and valley degrees of freedom can be described by a set of diffusive equations. The latter can be derived microscopically from the Boltzmann equation (Huang, Chong, and Cazalilla, 2016; Zhang, Huang, and Cazalilla, 2017; Huang, Chong, and Cazalilla, 2017) or the Kubo formalism (Burkov, Núñez, and MacDonald, 2004; Burkov and Hawthorn, 2010). In the steady state, the diffusion equations describing the diffusion of spin and valley take the following generic structure (see detailed derivation in Appendix 7.6.1 and 7.6.2):

$$\mathcal{D}\partial_i N^\mu - \sigma_D E_i^\mu = \left[-\delta_\nu^\mu \delta_{ij} + (R_H)_\nu^\mu \epsilon_{ij}\right] J_j^\nu . \tag{7.2.1}$$

In the above set of equations, we have used the convention that repeated indices are summed over. The Latin indices correspond to the spatial component of the current, or field, i.e., $\{i,j\} \in \{x,y\}$ and ϵ_{ij} is the antisymmetric 2D Levi-Civita tensor. The Greek indices of the currents, $\vec{J}^\mu$, and densities, N^μ, take values from the set $\{c, sv, v, s\}$. The latter stands for for charge (c), spin-valley (sv), valley (v), and spin (s) current (density) respectively. Note that the spin-valley current $\vec{J}^{sv}$ and density N^{sv} must be included in the above hydrodynamic description as they can be excited when the spin splitting energy is much smaller than $\hbar/\tau$, where τ is the elastic scattering time.

The left hand side of Eq. (7.2.1) contains the driving terms that result from spatial non-uniformity of the densities $\propto \partial_i N^\mu$ and the generalized electric fields $\propto E_i^\mu$ (to describe real devices, we shall set $E_i^\mu = 0$ for all $\mu \neq c$). The Drude conductivity $\sigma_D = ne^2\tau/m$ and the diffusion constant $\mathcal{D} = v_F^2\tau/2$, which for the sake of simplicity, we shall assume to be equal for all types of currents. The right-hand side of Eq. (7.2.1) describes the effective Lorentz forces as well as current relaxation. We shall assume that all currents' relaxation rates are the same and equal to the Drude relaxation time τ (which is related to the mean-free path by $\ell = v_F\tau$ where v_F is the Fermi velocity). This, together with the assumption of equal diffusion coefficients, can be relaxed and will not alter our conclusions qualitatively. Next, we introduce the coupling between different currents via the Hall resistivity matrix R_H, which describes both SHE and VHE. The latter couples the charge (c, 1st row) and spin-valley currents (sv, 2nd row) to valley (v, 3rd row) and spin (s, 4th row) currents:

$$R_H = \begin{bmatrix} 0 & 0 & \omega_v\tau & \omega_s\tau \\ 0 & 0 & \omega_s\tau & \omega_v\tau \\ \omega_v\tau & \omega_s\tau & 0 & 0 \\ \omega_s\tau & \omega_v\tau & 0 & 0 \end{bmatrix} \begin{matrix} c \\ sv \\ v \\ s \end{matrix} \tag{7.2.2}$$

The SHE (VHE) can be regarded as emerging from an effective spin (valley) dependent Lorentz force (Shen, 2005; Huang et al., 2016; Mak et al., 2014; Zhang, Huang, and Cazalilla, 2017). In R_H, the magnitude of such forces is parameterized by the "cyclotron" frequencies ω_s and ω_v, for spin and valley, respectively. These forces can have their origin in intrinsic or extrinsic SOC for the SHE (Sinova et al., 2015), and in nonuniform strain (Zhang, Huang, and Cazalilla, 2017) or skew scattering with impurities in gapped (monolayer/bilayer) graphene (valley) (Ando, 2015; Ishizuka and Nagaosa, 2017). In the latter case, we neglect intrinsic Berry-curvature contributions to the valley current, as they are subdominant in the limit where impurities are dilute (Ishizuka and Nagaosa, 2017). Note that when the valley and spin Hall effects coexist, the effective Lorentz force driving the VHE (SHE) current will act on the spin (valley) current. This is described by the additional entries in the R_H, which are not present when only the SHE or the VHE exists in the material (see FIGURE 7.1(b)).

In order to describe spin-valley transport with the above equations, we invert the resistivity matrix R_H in the right hand side of Eq. (7.2.1) and solve for the currents J_i^μ:

$$J_i^\mu = -\left(D_{ij}\right)_\nu^\mu \partial_j N^\nu + \left(\sigma_{ij}\right)_\nu^\mu E_j^\nu. \tag{7.2.3}$$

Note that the diffusion matrix is a rank-2 tensor in the Latin indices i, j, and therefore it can be split into a symmetric ($\propto \delta_{ij}$) and antisymmetric ($\propto \epsilon_{ij}$) part according to $D_{ij} = D_0\delta_{ij} + D_H\epsilon_{ij}$, where

$$D_0 = \mathcal{D}_r \begin{bmatrix} 1 & \eta & 0 & 0 \\ \eta & 1 & 0 & 0 \\ 0 & 0 & 1 & \eta \\ 0 & 0 & \eta & 1 \end{bmatrix}, \tag{7.2.4}$$

$$D_H = \mathcal{D}_r \begin{bmatrix} 0 & 0 & \theta_v & \theta_s \\ 0 & 0 & \theta_s & \theta_v \\ \theta_v & \theta_s & 0 & 0 \\ \theta_s & \theta_v & 0 & 0 \end{bmatrix}, \tag{7.2.5}$$

$$\mathcal{D}_r = \mathcal{D}\frac{1 + (\omega_v\tau)^2 + (\omega_s\tau)^2}{[1 + (\omega_v\tau)^2 + (\omega_s\tau)^2]^2 - 4\omega_s\omega_v\tau^2}. \tag{7.2.6}$$

Similarly, a decomposition of conductivity matrix as $\sigma_{ij} = \sigma_0\delta_{ij} + \sigma_H\epsilon_{ij}$ can be obtained by replacing in the above expressions the diffusion constant $\mathcal{D}$ with the Drude conductivity σ_D. Note that the diffusion equation (7.2.3) involves an off-diagonal diffusion coefficient (cf. Eqs. 7.2.4 to 7.2.6) and conductivity, which reduces to the well known limits. Thus, it yields the spin diffusion equations for a 2D electron gas (Raimondi et al., 2012; Huang et al., 2016) when the second and third rows and columns of the diffusion matrix D vanish. However, when the entries of the second and fourth rows and columns of D vanish, Eq. (7.2.3) describes the diffusion of valley polarization.

In order to understand some of the important consequences of the coupling of spin and valley Hall effect, let us first solve Eq. (7.2.3) in the spatial uniform case where $\partial_j N^\mu = 0$. The ratios of the induced current (spin-valley $\vec{J}^{sv}$, valley $\vec{J}^v$, spin current $\vec{J}^s$) over charge current $\vec{J}^c$ are the figures of merit for the various effects and they are denoted respectively as η, θ_s, θ_v; in particular, θ_s and θ_v are the spin Hall and valley Hall angles; η describes the conversion efficiency of the electric current to the

spin-valley current, and it is given by the following expression:

$$\eta = -\frac{2\,(\omega_v\tau)\,(\omega_s\tau)}{1+(\omega_v\tau)^2+(\omega_s\tau)^2}. \tag{7.2.7}$$

Note that η is proportional to the product of $\omega_v\tau$ and $\omega_c\tau$, meaning it is not zero provided that both SHE and VHE coexist. As shown in FIGURE 7.1(b), the generation of the spin-valley current is a two-stage process requiring the generation of a spin (valley) current from driving electric current via the SHE (VHE). The resulting transverse current is then again deflected by the effective Lorentz force that causes the VHE (SHE), resulting in a *longitudinal* spin-valley current. The factor of two in Eq. (7.2.7) stems from the two possible routes by which this spin-valley conversion can take place: charge to spin to spin-valley and charge to the valley to spin-valley (see FIGURE 7.1(b)).

Furthermore, due to the spin-valley interplay, the valley (θ_v) and spin Hall (θ_s) angles are modified as follows:

$$\theta_v = \frac{1+(\omega_v\tau)^2-(\omega_s\tau)^2}{1+(\omega_v\tau)^2+(\omega_s\tau)^2}\,\omega_v\tau, \tag{7.2.8}$$

$$\theta_s = \frac{1+(\omega_s\tau)^2-(\omega_v\tau)^2}{1+(\omega_v\tau)^2+(\omega_s\tau)^2}\,\omega_s\tau. \tag{7.2.9}$$

As expected, the spin (valley) Hall angle reduces to the familiar form $\theta_s = \omega_s\tau$ ($\theta_v = \omega_v\tau$) only when $\eta \propto \omega_s\omega_v = 0$. However, in general θ_s (θ_v) deviates from their "bare" values due to the interplay of the spin and valley Hall effects. In typical spintronic materials, $\omega_s\tau \ll 1$ (Sinova et al., 2015). However, nonuniform strain in graphene (Zhang, Huang, and Cazalilla, 2017), for instance, can yield large values of the (bare) Hall angles for which $|\omega_v\tau| \sim 1$. In this case, $|\theta_s| \sim |\omega_s\tau|^3 \ll 1$ implying that the spin current will be strongly suppressed.

7.3 Control of spin diffusion by means of strain

Next, we study the consequences of the interplay between spin and valley Hall effects for the spin transport. We first derive the drift-diffusion equations by supplementing Eq. (7.2.1) with the steady-state continuity equations for the currents, i.e. $\partial_i J_i^\mu = -\delta_\nu^\mu(\tau^\nu)^{-1}N^\nu$, where the limit $\tau^\mu \to +\infty$ for $\mu = c$ must be taken since the electric current is strictly conserved. Hence,

$$\left[(D_0)_\nu^\mu\,\nabla^2 - \frac{\delta_\nu^\mu}{\tau^\nu}\right] N^\nu = S^\mu. \tag{7.3.10}$$

In the above equations, τ^ν are the relaxation times of the various currents. We have also assumed that spin-charge conversion mechanisms like the Edelstein effect or the direct magnetoelectric coupling (Raimondi et al., 2012; Huang, Chong, and Cazalilla, 2017) can be neglected in a first approximation. S^μ is a source term given by

$$S^\mu = \epsilon_{ij}\left[-\partial_i\,(D_H)_\nu^\mu\,\partial_j N^\nu + \partial_i\,(\sigma_H)_\nu^\mu\,E_j^\nu\right]. \tag{7.3.11}$$

Note that S^μ vanishes in the bulk of the Hall bar device, and it is only nonzero wherever D_H and σ_H are discontinuous, i.e., at the boundary. Thus, away from the boundaries, D_H and σ_H become homogeneous, and Eq. (7.3.10) can be written as

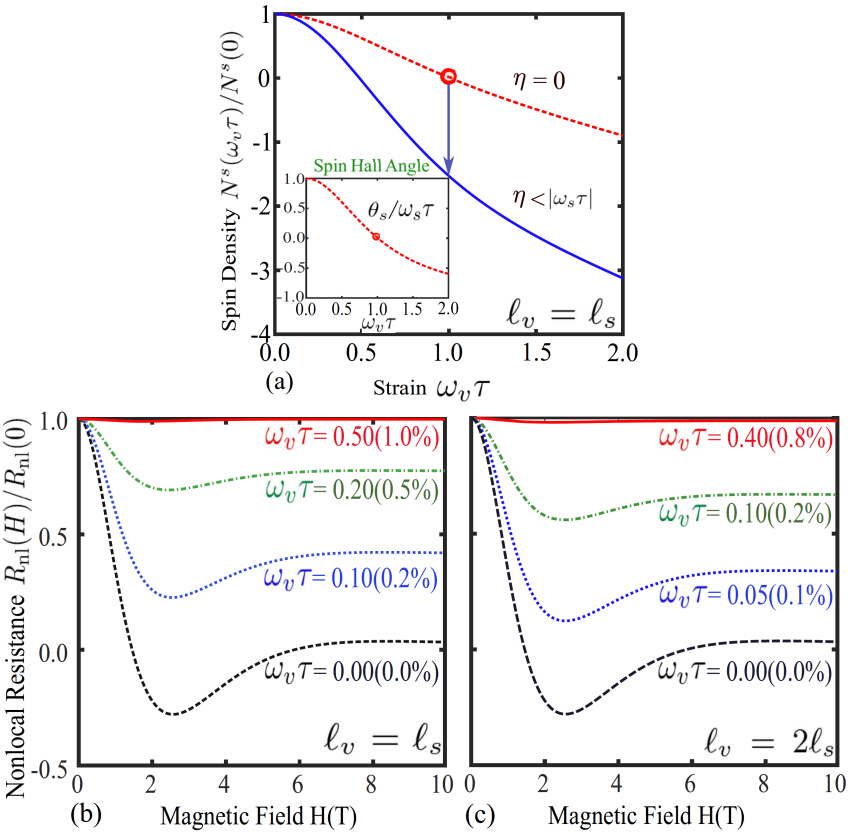

FIGURE 7.2: (Color online) (a) Spin polarization, $N^s(x)$ at $x = 2\,\mu$m for a Hall bar device of width $w = 0.5\,\mu$m versus $\omega_v\tau$, which is controlled by the non-uniform strain applied to the device (τ is mean elastic collision time). The red dotted line is plotted by artificially setting the coupling η that controls the interplay of spin and valley to zero. The inset shows the spin Hall angle θ_s from Eq. (7.2.9) normalized to $\omega_s\tau \simeq -0.12$. Panels (b) and (c) show the nonlocal resistance $R_{nl}(x, H)$ (normalized to $R_{nl}(x, H = 0)$) plotted versus the in plane magnetic field H for two different values of the ratio of the valley to spin diffusion lengths: (b) for $\ell_v = \ell_s$ and (c) for $\ell_v = 2\ell_s$. Parameters: $\ell_s = 0.53\,\mu$m, $x = 2.00\,\mu$m and $y = 0.25\,\mu$m.

follows:

$$\nabla^2 N^\mu - \mathcal{M}^\mu_\nu N^\nu = 0, \tag{7.3.12}$$

where

$$\mathcal{M}^\mu_\nu = \frac{1}{1-\eta^2}\begin{bmatrix} \ell_v^{-2} & -\eta\ell_s^{-2} \\ -\eta\ell_v^{-2} & \ell_s^{-2} \end{bmatrix} \begin{matrix} v \\ s \end{matrix}. \tag{7.3.13}$$

Only spin and valley densities are considered in the above equations because they are the only responses in the transverse direction to the applied electric field. In this expression, $\ell_v = \sqrt{\mathcal{D}_r\tau^v}$ ($\ell_s = \sqrt{\mathcal{D}_r\tau^s}$) is valley (spin) relaxation length and $\mathcal{D}_r$ is the (renormalized) diffusion constant (cf. Eq. 7.2.6). Note that the off-diagonal term η mixes the spin and valley densities. Eq. (7.3.12) are solved by diagonalizing the diffusion matrix, such that $\mathcal{M}^\mu_\nu|\vec{e}^\nu_a\rangle = \mathcal{L}_a^{-2}|\vec{e}^\mu_a\rangle$, where $\mathcal{L}_a$ ($a = 1, 2$) corresponds to the diffusion length of the eigenmode $|\vec{e}^\mu_a\rangle$.

In order to illustrate the properties of the solution to the above diffusion equations, we consider a non-uniformly strained graphene device decorated with absorbates that locally induce SOC (see details in Appendix 7.6.1). As mentioned above, this system can be relevant to the experiments reported by Wang, Cai, and Reutt-Robey, 2015; Kaverzin and Wees, 2015. In the long-wavelength limit, the effect of nonuniform strain can be described by an out-of-plane (orbital) pseudo-magnetic field, which takes opposite signs at opposite valleys (Guinea, Katsnelson, and Geim, 2010; Vozmediano, Katsnelson, and Guinea, 2010; Zhang, Huang, and Cazalilla, 2017). In earlier work, we have shown that modest amounts of nonuniform strain can lead to a sizable VHE (Zhang, Huang, and Cazalilla, 2017). Besides, skew scattering with the absorbates induces the SHE (Ferreira et al., 2014; Balakrishnan et al., 2014; Yang et al., 2016; Huang et al., 2016). Thus, in this system, both VHE and SHE coexist, and the spin and valley transport is described by Eq. (7.3.12), whose solution we shall analyze in what follows.

For the sake the simplicity, we take the Hall bar to be an infinitely long conducting channel of width w (Abanin et al., 2009; Beconcini, Taddei, and Polini, 2016). The solution of the coupled diffusion equations is simplified by setting $N^c(\vec{r}) = 0$, which results from assuming the complete screening of the electric field inside the metal. Thus, the electrostatic potential $\Phi(\vec{r})$ obeys the Laplace equation, i.e. $\nabla^2\Phi(\vec{r}) = 0$. Using the appropriate boundary conditions proposed by Beconcini, Taddei, and Polini, 2016; Zhang, Huang, and Cazalilla, 2017, the valley and spin densities, at the edge ($y = \pm w/2$), are given by the following expression (see detailed derivations in Appendix 7.6.2):

$$
\begin{aligned}
N^{\mu}(x) &= \frac{iI}{\mathcal{D}_r}\sum_{\nu,b}\vec{\tilde{e}}_b^{\mu}(\vec{\tilde{e}}^{-1})_{\nu}^{b}\theta_{\nu}\int_{-\infty}^{\infty}\frac{dk}{2\pi k}\frac{e^{ikx}\mathcal{F}_b(k)}{1+\sum_a \Theta_a^2\mathcal{F}_a(k)}, \\
\mathcal{F}_a(k) &= \frac{k\tanh(kw/2)}{\kappa_a\tanh(\kappa_a w/2)},
\end{aligned}
\tag{7.3.14}
$$

with $a, b = (1, 2)$. $\mu = v, s$ correspond to valley and spin densities, respectively. $\kappa_a = \sqrt{k^2 + \mathcal{L}_a^{-2}}$ and $\Theta_a^2 = \left[\vec{\tilde{e}}_a^{\mu}\theta_{\mu}\right][(\vec{\tilde{e}}^{-1})_a^{\nu}\theta_{\nu}]$.

In FIGURE 7.2(a), we plot the spin polarization $N^s(x, y)$ (taking $x = 2\,\mu$m and $y = 0.25\,\mu$m) as a function of the $\omega_v\tau$, which is determined by the strength of the pseudo-magnetic field induced by the nonuniform strength applied to device (Zhang, Huang, and Cazalilla, 2017). Notice that a modest nonuniform strain can lead to a large valley Hall effect (Zhang, Huang, and Cazalilla, 2017), $\omega_v\tau(\gtrsim 1)$. $\omega_v\tau = 1$ can be induced by e.g. applying a nonuniform (uniaxial) strain of 2.0% to a ribbon of width $w = 0.50\mu$m. Interestingly, the spin polarization does not vanish even when the strain is tuned to make the effective spin Hall angle (cf. Eq. (7.2.9)) $\theta_s = 0$ (see red circle in the inset of FIGURE 7.2(a)). This is a dramatic consequence of the coupling between the SHE and VHE, whose strength is measured by η (cf. Eq. (7.2.7)). Due to this coupling, the valley density accumulation induced by VHE can be converted to spin density. Note that if we solve the diffusion equations by ignoring the spin-valley coupling (i.e., by artificially setting the parameter $\eta = 0$), the behavior of the spin polarization (red line in FIGURE 7.2(a)) would be very different.

7.4 Suppression of the Hanle effect

Finally, we show that the interplay between the SHE and VHE can lead to the HE's suppression. As mentioned above, the quantity of experimental interest is the NLR of the Hall bar measured at a distance x from the current injection point. The HE results in the appearance of an oscillatory component in the NLR as a function of the external magnetic field H applied in the device's plane. The oscillation results from the precession of the electron spin in the external magnetic field H.

By solving the coupled diffusion and Laplace equations, the NLR can be obtained from:

$$R_{nl}(x,H) = \frac{1}{I}\left[\Phi\left(x,-\frac{w}{2},H\right) - \Phi\left(x,\frac{w}{2},H\right)\right], \tag{7.4.15}$$

where $\Phi(x,y,H)$ is the electrostatic potential for an in-plane magnetic field H. In the absence of both SHE and VHE, the NLR is given by the van der Paw law: $R_{nl}^0 \simeq \frac{4}{\pi\sigma^e}e^{-|x|/\mathcal{L}_0}$, for $|x| \gg \mathcal{L}_0 = w/\pi$. However, experimentally it is found that the NLR is greatly enhanced with respect to the Ohmic signal (Balakrishnan et al., 2014; Balakrishnan et al., 2013; Huang, Chong, and Cazalilla, 2017; Kaverzin and Wees, 2015). When the spin-diffusion length ℓ_s is shorter than the valley-diffusion length, ℓ_v, a suppression of the HE is expected. This is because the valley currents, which diffuse much farther and therefore will yield the dominant contribution to $R_{nl}(x,H)$, are completely insensitive to the in-plane magnetic field. Strikingly, we find that for ℓ_v and ℓ_s take comparable values, the HE can be suppressed by a moderate amount of nonuniform strain present in the device.

In order to compute $R_{nl}(x,H)$ we add to the diffusion equations (7.3.10), a Zeeman term, which induces precession. A sufficiently strong magnetic field $\vec{H} \propto \hat{\mathbf{y}}$ converts the out-of-plane spin polarization, $N^s(x)$, into an in-plane spin polarization (along the x-direction). Since the nonlocal voltage is determined by the magnitude $N^s(x)$ at the location of the voltage probes (see Appendix 7.6.3), this results in the NLR developing an oscillatory component. When the SHE and VHE coexist, describing precession requires that we account for the diffusion of the components of the spin and spin-valley densities in the plane perpendicular to $\vec{H}$. The resulting diffusion equations' solution becomes more involved, and the details are provided in Appendix 7.6.4. Here we focus on discussing the result for the NLR, which is shown in FIGURE 7.2(b,c).

In FIGURE 7.2(b), the NLR versus the applied magnetic field H has been plotted for $\ell_v = \ell_s$. Setting $\omega_v\tau = 0$, we recover the result obtained by Abanin et al., 2009, showing the characteristic oscillatory component in $R_{nl}(x,H)$ associated with the HE. By applying an increasing amount of nonuniform strain to the Hall bar (i.e., increasing $\omega_v\tau$), the amplitude of the oscillatory component in the NLR is suppressed. It almost disappears for $\omega_v\tau \sim 0.5$, which, for typical experimental parameters (Kaverzin and Wees, 2015), corresponds to a nonuniform (uniaxial) strain of $\approx 1\%$ applied to a Hall bar 0.5 μm wide. Thus, the HE's suppression happens due to the competition between the spin and valley Hall effects. As mentioned above, when $\omega_v\tau \sim 1$, the spin Hall angle θ_s (cf. Eq. 7.2.9) is strongly reduced, see Eq. (7.2.9). Since the magnitude of θ_s determines the HE, the existence of a sizable VHE resulting from strain can suppress the HE. For larger valley diffusion length ($\ell_v = 2\ell_s$), the suppression of the HE becomes even more obvious and happens for a smaller amount of strain, as shown in FIGURE 7.2(c). In Appendix 7.6.4, we show that the suppression of the HE is not affected by charging the carrier density or sign. Notice that the moderate amounts of strain considered here could be unintentionally introduced during the process of device fabrication. Thus, our findings

are relevant for the interpretation of some of the nonlocal transport measurements in graphene decorated with hydrogen (Wang, Cai, and Reutt-Robey, 2015) and gold adatoms (Kaverzin and Wees, 2015), where a large enhancement of the NLR was detected without HE.

Before concluding, it is worth commenting on other possible causes for the suppression of the HE. Indeed, suppression of the effect may also arise from a sizable spin-valley locking, such as the one present in the band structure of TMDs (Suzuki et al., 2014). Effectively, this type of spin-valley locking can be described as a Zeeman coupling to an out-of-plane magnetic field, which takes opposite signs at opposite valleys. However, in graphene devices, such type of spin-valley would require breaking the sublattice symmetry, induced by either the substrate or the absorbates decorating the device. However, such a strong sublattice symmetry breaking was not experimentally observed by Kaverzin and Wees, 2015.

7.5 Summary and outlook

This chapter explores several important consequences of the coexistence of spin and valley Hall effects in a two-dimensional material: We show the latter leads to the emergence of neutral longitudinal spin and valley polarized current. Furthermore, we have shown that spin polarization diffusing in the material can be controlled through non-uniform strain. Finally, we show the Hanle effect in response to an in-plane magnetic field can be strongly suppressed due to the competition of the two effects. We believe the suppression of the Hanle effect noticed here will shed light on experimental controversies concerning the origin of the enhancement of the nonlocal resistance in various types of graphene devices (Balakrishnan et al., 2013; Balakrishnan et al., 2014; Kaverzin and Wees, 2015; Avsar et al., 2015; Wang, Cai, and Reutt-Robey, 2015). The theory presented here can also be extended in various other directions, such as accounting for other spin-charge conversion mechanisms beyond the SHE (such as the inverse spin-galvanic effect) and a weak spin-valley (Zeeman) coupling, which is present in hybrid graphene-TMD structures. Both effects are expected to be important when spatial inversion symmetry is broken.

7.6 Appendix

7.6.1 Kinetic theory

Boltzmann equation

We first introduce the quantum Boltzmann equation (QBE) capable of describing a system in which both spin (SHE) and valley Hall (VHE) effects co-exist:

$$\dot{n}_{\vec{k}} + \vec{v}^{\vec{k}} \cdot \nabla_{\vec{r}} n_{\vec{k}} + \vec{F}_{\vec{k}} \cdot \nabla_{\vec{k}} n_{\vec{k}} + i\omega_L \left[n_{\vec{k}}, \vec{s} \cdot \vec{m} \right] = \mathcal{I}_r \left[n_{\vec{k}} \right]. \tag{G.6.16}$$

In the above expression, the function $n_{\vec{k}}$ is the density-matrix distribution function of the carriers (electrons or holes) in the Bloch state characterized by (crystal) momentum $\vec{k}$. Thus, it is a 4×4 matrix in spin-valley space. The force $\vec{F}$ driving the carrier motion can be split into three terms:

$$\vec{F}_{\vec{k}} = \vec{F}^{l}_{\vec{k}} + \vec{F}^{s}_{\vec{k}} + \vec{F}^{v}_{\vec{k}}, \tag{G.6.17}$$

where

$$\vec{F}^{l}_{\vec{k}} = \vec{F}^{E}_{\vec{k}} + \vec{F}^{B}_{\vec{k}} \equiv e\vec{E} + e\vec{v}^{\vec{k}} \times \vec{B}, \tag{G.6.18}$$

$$\vec{F}^{s}_{\vec{k}} = e\vec{v}^{\vec{k}} \times (\hat{s}_z \vec{\mathcal{B}}_s), \tag{G.6.19}$$

$$\vec{F}^{v}_{\vec{k}} = e\vec{v}^{\vec{k}} \times (\hat{\tau}_z \vec{\mathcal{B}}_v). \tag{G.6.20}$$

The $F^{l}_{\vec{k}}$ is the electromagnetic Lorentz force due to external (in-plane) electric and (out-of-plane) magnetic fields ($\vec{E} \perp \vec{z}$ and $\vec{B} \parallel \vec{z}$, respectively). While $F^{s/v}_{\vec{k}}$ are the effective (Lorentz-like) forces for effective (out-of-plane) spin/valley magnetic field ($\vec{\mathcal{B}}_s \parallel \vec{z}$ and $\vec{\mathcal{B}}_v \parallel \vec{z}$, respectively), from which the SHE and VHE originate. In Eq. (G.6.18), $e(<0)$ is the charge of the electron, $\vec{v}^{\vec{k}} = \hbar^{-1}\nabla_{\vec{k}}\epsilon_{\vec{k}}$ is the velocity of electron with (crystal) momentum $\vec{k}$, and $\epsilon_{\vec{k}}$ is the band dispersion. We assume that there is no Berry curvature in the band and therefore anomalous velocity vanishes. $\hat{s}_a$, $\hat{\tau}_a$ $(a = o, x, y, z)$ are Pauli matrices describing the spin and valley (pseudo-spin), respectively. The matrix s_o (τ_o) corresponds to the spin (valley) unit matrix.

The magnitude of the SHE (VHE) has been parameterized in the above equations by the effective spin (valley) magnetic field $\hat{s}_z\vec{\mathcal{B}}_s$ ($\hat{\tau}_z\vec{\mathcal{B}}_v$), which points in opposite directions for electrons of different spins (valleys). The last term of the left hand side of Eq. (G.6.16) describes spin precession with a Larmor frequency $\omega_L = g\mu_B H/\hbar$, which is proportional to the magnitude of the total applied (Zeeman) magnetic field $\vec{H}$ (g is the gyromagnetic factor and μ_B is the Bohr magneton). In Eq. (G.6.16), $\vec{m} = \vec{H}/H$ denotes the direction of the total magnetic field and $\vec{B}$ in Eq. (G.6.18) denotes the component of the magnetic field perpendicular to the plane of the material. In what follows, we shall assume that the external magnetic field (when present) is applied in the plane of the 2D system, which means $\vec{B} = 0$ and therefore the magnetic field part of Lorentz force $\vec{F}^{B}_{\vec{k}} = 0$.

On the right hand side of Eq. (G.6.16) $\mathcal{I}_r\left[n_{\vec{k}}\right]$ is the (dissipative) collision integral. Strictly speaking, the force terms proportional to $\vec{F}^{s/v}_{\vec{k}}$ can arise from the collision integral as a result of skew scattering (see 7.6.1 below and e.g. Huang et al., 2016; Zhang, Huang, and Cazalilla, 2017). Alternatively, a weak uniform (i.e. intrinsic) Rasbha-type SOC can also give rise to a Lorentz-like force term like $\vec{F}^{s}_{\vec{k}}$ in the QBE (Raimondi et al., 2012; Huang, Milletarì, and Cazalilla, 2017). Furthermore, nonuniform strain can give rise to a force like $\vec{F}^{v}_{\vec{k}}$ (see below, 7.6.1, and Zhang, Huang, and Cazalilla, 2017).

Linearized Boltzmann equation

For small applied electric field, $\vec{E}$, the solution to the QBE (G.6.16), can be obtained by using the following ansatz for electron density-matrix distribution function:

$$n_{\vec{k}}(\vec{r}, t) = n^0\left[\epsilon_k - \mu_F - \gamma_\nu(\mu^\nu(\vec{r}, t) + \vec{v}^\nu(\vec{r}, t)\cdot\vec{k})\right]. \tag{G.6.21}$$

In the above equation, $n^0(\epsilon)$ is Fermi-Dirac distribution at the absolute temperature T and global chemical potential μ_F. The convention of summing over repeated Greek indices like ν has been used, with matrix γ_ν belonging to the set of 4×4 matrices $\{\hat{s}_o, \hat{s}_z\}\otimes\{\hat{\tau}_o, \hat{\tau}_z\} = \{\hat{s}_o\hat{\tau}_o, \hat{s}_o\hat{\tau}_z, \hat{s}_z\hat{\tau}_o, \hat{s}_z\hat{\tau}_z\}$, which are a set of 4×4 matrices in spin-valley space. The index ν runs over the combinations for charge ($c = oo$), spin-valley ($sv = zz$), valley ($v = oz$) and spin ($s = zo$) indices. The fields

$\vec{v}^{\nu}(\vec{r},t)$ and $\mu^{\nu}(\vec{r},t)$ correspond to the drift velocity of the electron fluid and the local chemical potential, respectively. Both are proportional to applied electric field, i.e., $|\vec{v}^{\nu}(\vec{r},t)| \propto |\vec{E}|$ and $\mu^{\nu}(\vec{r},t) \propto |\vec{E}|$. To linear order in $\vec{v}^{\nu}(\vec{r},t)$ and $\mu^{\nu}(\vec{r},t)$, the deviation of distribution function from its equilibrium, $\delta n_{\vec{k}} = n_{\vec{k}} - n^0_k$ reads:

$$\delta n_{\vec{k}}(\vec{r},t) \simeq \gamma_{\nu}\left[\mu^{\nu}(\vec{r},t) + \vec{v}^{\nu}(\vec{r},t)\cdot\vec{k}\right]\left[-\partial_{\epsilon} n^0_{\epsilon}\right]_{\epsilon=\mu_F}, \tag{G.6.22}$$

with $\nu = (c, sv, v, s)$. Hence,

$$\nabla_{\vec{k}}\delta n_{\vec{k}}(\vec{r},t) \simeq \gamma_{\nu}\vec{v}^{\nu}(\vec{r},t)\left[-\partial_{\epsilon} n^0_{\epsilon}\right]_{\epsilon=\mu_F}. \tag{G.6.23}$$

Thus, to linear order in $\vec{E}$, linearization of QBE yields:

$$\begin{aligned}\delta\dot{n}_{\vec{k}} + \vec{v}^{\vec{k}}\cdot\nabla_{\vec{r}}\delta n_{\vec{k}} + e\left(\vec{E} + \vec{v}^{\vec{k}}\times\vec{B}\right)\cdot\nabla_{\vec{k}} n^0_{\vec{k}} + \vec{F}^{s}_{\vec{k}}\cdot\nabla_{\vec{k}}\delta n_{\vec{k}} + \vec{F}^{v}_{\vec{k}}\cdot\nabla_{\vec{k}}\delta n_{\vec{k}} \\ + i\omega_L\left[\delta n_{\vec{k}}, \vec{s}\cdot\vec{m}\right] = \mathcal{I}_r\left[\delta n_{\vec{k}}\right],\end{aligned} \tag{G.6.24}$$

where we have used:

$$\vec{F}^{s}_{\vec{k}}\cdot\nabla_{\vec{k}} n^0_{\vec{k}} \propto (\hat{\vec{k}}\times\hat{z})\cdot\hat{\vec{k}} = 0, \tag{G.6.25}$$

$$\vec{F}^{v}_{\vec{k}}\cdot\nabla_{\vec{k}} n^0_{\vec{k}} \propto (\hat{\vec{k}}\times\hat{z})\cdot\hat{\vec{k}} = 0, \tag{G.6.26}$$

together with the vanishing of the collision integral for the equilibrium distribution n^0_k.

Example of a microscopic model

The above linearized QBE can be obtained for various types of microscopic models. In this subsection, we study an instance of much experimental interest describing a monolayer of graphene subject to nonuniform strain and decorated with adatoms. The nonuniform strain was explained in Subsection 1.3.1, which can be charaterized by the pseudo-magnetic field that determines the valley Lorentz-like force, $\vec{F}^{v}_{\vec{k}}$ can be obtained from the standard expression:

$$\hat{\tau}_z\vec{\mathcal{B}}_v = \hat{\tau}_z\nabla\times\vec{\mathcal{A}}(\vec{r}) = \hat{\tau}_z(\partial_x\mathcal{A}_y - \partial_y\mathcal{A}_x)\,\vec{\hat{z}}. \tag{G.6.27}$$

On the other hand, the adatoms induce spin-orbit coupling (SOC) by proximity to the graphene layer. For the sake of simplicity, the spatial dependence of SOC is approximated by a Dirac delta potential, but more complicated dependence will not alter our results qualitatively (Ferreira et al., 2014). The spin-dependence corresponds to the so-called Kane-Mele SOC, which is known to lead to extrinsic SHE (Huang et al., 2016; Ferreira et al., 2014). The spin transport properties of graphene can be modified by the presence of adatom impurities (Weeks et al., 2011; Ferreira et al., 2014; Yang et al., 2016; Huang et al., 2016). In the dilute impurity limit, the dominant mechanism for the spin-charge conversion via the extrinsic SHE is skew scattering (Nagaosa et al., 2010), which effectively gives rise to a spin-dependent Lorentz-like force (Huang et al., 2016).

Within the $\vec{k}\cdot\vec{p}$ theory, the potential for a single-impurity takes the following form:

$$V(\vec{r}) = (\mathcal{V}_c\hat{s}_o\hat{\tau}_o\hat{\sigma}_o + \mathcal{V}_s\hat{s}_z\hat{\tau}_z\hat{\sigma}_z)R^2\delta(\vec{r}). \tag{G.6.28}$$

In the above expression, R is a length scale of the order of the impurity radius. We shall assume that $R \gg a$, that is, much larger than the inter-carbon separation so that inter-valley scattering can be safely neglected (Basko, 2008) but $R \lesssim 10$ nm, so that the potential can be approximated by a Dirac δ-function. This approximation should be a good description of a monolayer of graphene decorated by adatom clusters (Ferreira et al., 2014; Balakrishnan et al., 2013). Hence, upon solving the scattering problem, the on-shell T-matrix projected on the carrier band can be obtained and reads:

$$T^{+}_{\vec{k}\vec{p}} = t_c(k)\hat{s}_o \cos(\theta_{\vec{k}\vec{p}}/2) + t_s(k)\hat{s}_z \sin(\theta_{\vec{k}\vec{p}}/2). \tag{G.6.29}$$

The functions $t_c(k)$ and $t_s(k)$ depend on momentum k of the incoming electron and the impurity potential parameters, i.e. $\mathcal{V}_c, \mathcal{V}_s$, in our model. See e.g. Refs.Huang, Chong, and Cazalilla, 2016 and Zhang, Huang, and Cazalilla, 2017 for the detailed expressions of these functions.

The effect of impurities is described by the collision integral $\mathcal{I}\left[\delta n_{\vec{k}}\right]$. The complete form of the latter (which includes the dissipative $\mathcal{I}_r[\delta n_{\vec{k}}]$ introduced in Eq. (G.6.16) has been derived by Huang, Chong, and Cazalilla, 2016, extending earlier work of Kohn and Luttinger in order to account for the effects of disorder on the electron internal degrees of freedom such as spin and valley pseudo-spin. To leading order in the density of impurities, n_{i}, the collision integral reads:

$$\begin{aligned}\mathcal{I}[\delta n_{\vec{k}}] = \frac{2\pi}{\hbar} n_{\mathrm{i}} \sum_{\vec{p}} \delta(\epsilon_k - \epsilon_p) \Big[T^{+}_{\vec{k}\vec{p}} \delta n_{\vec{p}} T^{-}_{\vec{p}\vec{k}} \\ - \frac{1}{2} \left\{ \delta n_{\vec{k}} T^{+}_{\vec{k}\vec{p}} T^{-}_{\vec{p}\vec{k}} + T^{+}_{\vec{k}\vec{p}} T^{-}_{\vec{p}\vec{k}} \delta n_{\vec{k}} \right\} \Big],\end{aligned} \tag{G.6.30}$$

which is determined by the scattering data of a single scatterer. Using the above ansatz, Eq. (G.6.22), the collision integral (G.6.30) reduces to:

$$\mathcal{I}\left[\delta n_{\vec{k}}\right] = \frac{\pi}{\hbar} n_{\mathrm{i}} \sum_{\vec{p}} \delta\left(\epsilon_p - \epsilon_k\right) 2\hat{T}^{+}_{\vec{k}\vec{p}} \hat{T}^{-}_{\vec{k}\vec{p}} (\delta n_{\vec{p}} - \delta n_{\vec{k}}), \tag{G.6.31}$$

where

$$\begin{aligned}2\hat{T}^{+}_{\vec{k}\vec{p}} \hat{T}^{-}_{\vec{k}\vec{p}} = \left[|t_c|^2 (1 + \cos\theta) + |t_s|^2 (1 - \cos\theta) \right] \gamma^c \\ + 2\mathrm{Im}\left(t_c t_s^*\right) \sin\theta \gamma^s\end{aligned} \tag{G.6.32}$$

$$\delta n_{\vec{p}} - \delta n_{\vec{k}} = \left[-\partial_\epsilon n^0(\epsilon)\right]_{\epsilon=\mu_F} \sum_\nu \gamma^\nu \vec{v}^\nu(\vec{r}) \cdot \hbar(\vec{p} - \vec{k}). \tag{G.6.33}$$

Substituting Eqs. (G.6.32) and (G.6.33) into Eq. (G.6.30), the collision integral takes the following form:

$$\begin{aligned}\mathcal{I}\left[\delta n_{\vec{k}}\right] = \left[\partial_\epsilon n^0(\epsilon)\right]_{\epsilon=\mu_F} \hbar\vec{k} \cdot \Bigg\{ \frac{\gamma^c}{\tau} \sum_\nu \gamma^\nu \vec{v}^\nu(\vec{r}) \\ + \gamma^s \omega_s \sum_\nu \gamma^\nu \vec{v}^\nu(\vec{r}) \times \hat{\vec{z}} \Bigg\},\end{aligned} \tag{G.6.34}$$

where

$$\frac{1}{\tau(k)} = \frac{k n_{\mathrm{i}}}{4\hbar^2 v_F}\left[|t_c(k)|^2 + 3\,|t_s(k)|^2\right], \tag{G.6.35}$$

$$\omega_s(k) = \frac{k n_{\mathrm{i}}}{4\hbar^2 v_F}\left[-2\mathrm{Im}\{t_c(k) t_s(k)\}\right]. \tag{G.6.36}$$

The above collision integral can be rewritten as

$$\mathcal{I}\left[\delta n_{\vec{k}}\right] = -\frac{\hbar\vec{k}}{\tau}\cdot\nabla_{\vec{k}}\delta n_k - \vec{F}^s_{\vec{k}}\cdot\nabla_{\vec{k}}\delta n_k, \tag{G.6.37}$$

with

$$\vec{\mathcal{B}}_s = -\frac{\hbar k\omega_s}{e v_F}\hat{\vec{z}}. \tag{G.6.38}$$

Thus, as anticipated in 7.6.1 (cf. Eqs. (G.6.16) and (G.6.19)), an effective Lorentz-like force driving the SHE emerges from skew scattering with adatom impurities. This Lorentz-like force term needs to be factored out of the collision integral, and the remaining terms are grouped in the dissipative part of the the collision integral, $\mathcal{I}_r\left[n_{\vec{k}}\right]$, which we introduced in Eq. (G.6.16), See 7.6.1 .

7.6.2 Diffusion equations

In order to derive the diffusion equations that we have employed in the main text, let us first consider the simpler case where there is no applied magnetic field and therefore the Larmor frequency vanishes, i.e. $\omega_L = 0$ in Eq. (G.6.24).

First of all, let us the define currents and generalized polarization densities as follows:

$$J^\nu_i = \sum_{\vec{k}} e v^{\vec{k}}_i \mathrm{Tr}\left[\gamma^\nu \delta n_{\vec{k}}\right], \tag{G.6.39}$$

$$N^\nu = \sum_{\vec{k}} e\,\mathrm{Tr}\left[\gamma^\nu \delta n_{\vec{k}}\right]. \tag{G.6.40}$$

At zero temperature, J^ν_i and N^ν reduce to:

$$J^\nu_i(\vec{r}) = e\nu_F \mu_F v^\nu_i(\vec{r}), \tag{G.6.41}$$

$$N^\nu(\vec{r}) = 2e\nu_F \mu^\nu(\vec{r}), \tag{G.6.42}$$

where $\nu_F = k_F^2/(\pi\mu_F)$ is the total density of states at the Fermi energy $\mu_F = \hbar v_F k_F$ at zero temperature, where k_F is the Fermi momentum.

Continuity and constitutive equations

The constitutive and continuity equations in steady state, can be obtained by tracing the linearized QBE (G.6.24), i.e. by taking $\sum_{\vec{k}} e\vec{v}^{\vec{k}}\mathrm{Tr}\left[\gamma^\mu \mathrm{QBE}\right]$ for the constitutive equations and $\sum_{\vec{k}} e\mathrm{Tr}\left[\gamma^\mu \mathrm{QBE}\right]$) for the continuity relations, respectively. The latter procedures yield the following expressions:

$$\mathcal{D}\partial_i N^\mu - \sigma_D E^\mu_i = \left[-\delta^\mu_\nu \delta_{ij} + (R_H)^\mu_\nu \epsilon_{ij}\right] J^\nu_j, \tag{G.6.43}$$

$$\partial_i J^\mu_i = 0. \tag{G.6.44}$$

Here $\mathcal{D} = v_F^2\tau/2$ is diffusion constant and $\sigma_D = ne^2\tau/m$ (n is carrier density and m is mass) is Drude conductivity. In the above expression, repeated indices are summed and ϵ_{ij} is the antisymmetric 2D Levi-Civita tensor ($i, j = x, y$). The Greek superscripts of the currents $\vec{J}^\mu$ and the densities N^μ take values over the set $\{c, sv, v, s\}$, which stand for for charge, spin-valley, valley, and spin currents (densities), respectively. The coupling between spin and valley currents naturally leads to the existence of spin and valley polarized currents that are longitudinal, i.e. have the same direction as charge current $\vec{J}^c$(external electric field $\vec{E}^c = \vec{E}$). On the other hand, the spin and valley currents are transverse, i.e. perpendicular to $\vec{J}^c$ ($\vec{E}$).

The left hand side of Eq. (G.6.43) contains the driving forces for the currents, which are the results of spatial nonuniformity of the densities $\propto \vec{\nabla} N^\mu$ and the application of the generalized electric fields $\vec{E}^\mu$ (in order to describe real devices, we shall set $\vec{E}^\mu = 0$ for all $\mu \neq c$). The right hand side of Eq. (G.6.43) describes the effective Lorentz forces as well as current relaxation. The relaxation rates for all currents are the same and equal to the Drude relaxation time τ (which is related to the mean-free path by $\ell = v_F\tau$ where v_F is the Fermi velocity). The Hall resistivity matrix R_H describes SHE and VHE, and couples *longitudinal* charge and spin-valley currents to *transverse* spin and valley currents:

$$R_H = \begin{bmatrix} 0 & 0 & \omega_v\tau & \omega_s\tau \\ 0 & 0 & \omega_s\tau & \omega_v\tau \\ \omega_v\tau & \omega_s\tau & 0 & 0 \\ \omega_s\tau & \omega_v\tau & 0 & 0 \end{bmatrix}. \tag{G.6.45}$$

The magnitude of the SHE and VHE has been parameterized in the above equations by the effective "cyclotron" frequencies

$$\omega_s = v_F e\mathcal{B}_s/\hbar k_F \tag{G.6.46}$$
$$\omega_v = v_F e\mathcal{B}_v/\hbar k_F. \tag{G.6.47}$$

The latter arise from effective Lorentz forces that deflect the electrons (according to their spin and valley orientations, respectively).

In order to describe spin-valley transport with the above equations, we need to invert the resistivity matrix R_H and solve Eq. (G.6.43) for the currents J_i^μ, which yields the following set of equations:

$$J_i^\mu = -\left(D_{ij}\right)_\nu^\mu \partial_j N^\nu + \left(\sigma_{ij}\right)_\nu^\mu E_j^\nu. \tag{G.6.48}$$

Note that the diffusion matrix is a rank-2 tensor in the Latin indices i, j, and therefore it can be split into a symmetric ($\propto \delta_{ij}$) and antisymmetric ($\propto \epsilon_{ij}$) part according to $D_{ij} = D_0\delta_{ij} + D_H\epsilon_{ij}$, where

$$D_0 = \mathcal{D}_r \begin{bmatrix} 1 & \eta & 0 & 0 \\ \eta & 1 & 0 & 0 \\ 0 & 0 & 1 & \eta \\ 0 & 0 & \eta & 1 \end{bmatrix}, \tag{G.6.49}$$

$$D_H = \mathcal{D}_r \begin{bmatrix} 0 & 0 & \theta_v & \theta_s \\ 0 & 0 & \theta_s & \theta_v \\ \theta_v & \theta_s & 0 & 0 \\ \theta_s & \theta_v & 0 & 0 \end{bmatrix}, \tag{G.6.50}$$

$$\mathcal{D}_r = \mathcal{D}\frac{1+(\omega_v\tau)^2+(\omega_s\tau)^2}{[1+(\omega_v\tau)^2+(\omega_s\tau)^2]^2-4\omega_s\omega_v\tau^2}. \tag{G.6.51}$$

Similarly, a decomposition of conductivity matrix as $\sigma_{ij} = \sigma_0\delta_{ij} + \sigma_H\epsilon_{ij}$ can be obtained by replacing in the above expressions the diffusion constant $\mathcal{D}$ with the Drude conductivity σ_D. (See exact expressions for η, θ_v, θ_s in manuscript.)

Diffusion of spin and valley polarization

Next, we derive the drift-diffusion equations for the spin and valley polarizations. To this end, we supplement the constitutive relations in Eq. (G.6.43) with the steady state phenomenological continuity equations,

$$\partial_i J_i^\mu = -\frac{\delta_\nu^\mu}{\tau^\nu}N^\nu, \tag{G.6.52}$$

where we take $\tau^c \to +\infty$ since the charge current is strictly conserved. In the above expressions, τ^ν are phenomenological relaxation times which need to be ad hoc in the present derivation, but whose existence can be rigorously derived in a more complete treatment (Huang, Chong, and Cazalilla, 2016; Zhang, Huang, and Cazalilla, 2017). Hence, we arrive at the following set of diffusion equations:

$$\left[(D_0)_\nu^\mu\partial_i^2 - \frac{\delta_\nu^\mu}{\tau^\nu}\right]N^\nu = S^\mu, \tag{G.6.53}$$

where the source term is given by

$$S^\mu = \epsilon_{ij}\left[-\partial_i(D_H)_\nu^\mu\partial_j N^\nu + \partial_i(\sigma_H)_\nu^\mu E_j^\nu\right]. \tag{G.6.54}$$

In deriving the above diffusion equations, we used $\epsilon_{ij}\partial_i\partial_j N^\mu = 0$ and that the generalized electric field is curl and divergence-free, i.e. $\epsilon_{ij}\partial_i E_j^\mu = 0$ and $\partial_i E_i^\mu = 0$, that is, we have neglected any relativistic corrections to the electrodynamics.

Note that the source term on the right hand side of (G.6.53) takes a non-zero values only at the boundary of the device. In other words, it describes the driving force for the electron diffusion arising from the abrupt change of the Hall angle at the device boundaries (Beconcini, Taddei, and Polini, 2016). However, in the bulk the above set of differential equations (G.6.53), becomes a homogeneous one:

$$\partial_i^2 N^\mu - \mathcal{M}_\nu^\mu N^\nu = 0, \tag{G.6.55}$$

where

$$\mathcal{M}_\nu^\mu = \frac{1}{1-\eta^2}\begin{bmatrix}\ell_v^{-2} & -\eta\ell_s^{-2}\\ -\eta\ell_v^{-2} & \ell_s^{-2}\end{bmatrix}. \tag{G.6.56}$$

Here $\mu,\nu \in \{v,s\}$ denote the transverse valley (spin) response, with diffusion lengths $\ell_v = \sqrt{\mathcal{D}_r\tau^v}$ ($\ell_s = \sqrt{\mathcal{D}_r\tau^s}$). The choice where $\mu,\nu = \{c, sv\}$ corresponds to the longitudinal charge (spin-valley) response, which decouples from transverse modes and will be omitted in what follows. The parameter η, which arises from the interplay of SHE and VHE, mixes the valley and spin responses.

As described in the main text, in order to solve Eq. (G.6.55), we first need to diagonalize the matrix $\mathcal{M}$ and therefore obtain the eigenvalues and eigenvectors. Thus, in what follows we shall assume this has been carried out, so that $\mathcal{L}_a^{-2}|\vec{e}_a^\mu\rangle = \mathcal{M}_\nu^\mu|\vec{e}_a^\nu\rangle$, where $\mathcal{L}_a$ is the eigenvalue, which corresponds to the diffusion length for the eigenmode $|\vec{e}_a^\mu\rangle$.

Next, following Beconcini, Taddei, and Polini, 2016, we solve the diffusion equation for a Hall bar device geometry, assuming the latter to be an infinitely long metallic channel of width w contacted by noninvasive current and voltage probes (see FIGURE 1(a) in the manuscript). We shall assume the complete screening of the electric field in the bulk of device, which amounts to take charge density into zero, i.e., $N^c(\vec{r}) = 0$. Hence, the electrostatic potential, $\Phi(\vec{r})$ obeys the Laplace equation:

$$\nabla^2 \Phi(\vec{r}) = 0. \tag{G.6.57}$$

The Laplace equation (G.6.57) and the above system of partial differential equations (G.6.55), need to be supplemented by the following boundary conditions (BCs):

$$J_y^c(x; y = \pm w/2) = I\delta(x) \tag{G.6.58}$$

$$J_y^\nu(x; y = \pm w/2) = 0, \tag{G.6.59}$$

for $\nu = v, s$. I is charge current injected on right hand side of Hall bar device. Finally, in order to solve the problem posed by Eq. (G.6.55) and Eq. (G.6.57), we use Fourier transformation along the infinitely long channel direction, x. Thus, using (G.6.48), the BCs approximately become:

$$I \simeq \left[-\mathcal{D}_r(ik) N^\nu(k,y)\theta_\nu - \sigma^c \partial_y \Phi(k,y)\right]\Big|_{y=\pm\frac{w}{2}}, \tag{G.6.60}$$

where the sum over the repeated index ν in the expression above runs over the set $\{s, v\}$ only. σ^c is charge conductivity. In addition,

$$0 \simeq \left[-\sigma^c(ik)\Phi(k,y)\theta_\nu - \mathcal{D}_r \partial_y N^\nu(k,y)\right]\Big|_{y=\pm\frac{w}{2}}. \tag{G.6.61}$$

By "approximately", we mean that we omit the boundary contributions of the longitudinal modes N^c and N^{sv} in Eq. (G.6.48) by setting $N^c, N^{sv} = 0$ and $\eta = 0$. Including them, merely leads to a small correction to the diffusion length of the spin and valley eigenmodes.

In order to solve the above system of 2nd order differential equations, i.e. Eq. (G.6.55), we first turn it into a 1st order set of equations by defining $N'_\nu(k,y) = \partial_y N^\nu(k,y)$, rendering (G.6.55) to the form:

$$\begin{bmatrix} \partial_y N^\nu(k,y) \\ \partial_y N'_\mu(k,y) \end{bmatrix} = \begin{bmatrix} 0 & \delta^\nu_\mu \\ k^2\delta^\mu_\nu + \mathcal{M}^\mu_\nu & 0 \end{bmatrix} \begin{bmatrix} N^\nu(k,y) \\ N'_\mu(k,y) \end{bmatrix}. \tag{G.6.62}$$

Let $\mathcal{L}_a^{-2}$ and $|\vec{\hat{e}}^\mu_a\rangle$ are the eigenvalues and eigenvectors of diffusion matrix, respectively. Hence,

$$\begin{bmatrix} \vec{0} & \mathbb{1} \\ k^2\mathbb{1} + \mathcal{M} & \vec{0} \end{bmatrix} \begin{bmatrix} |\vec{\hat{e}}_a\rangle \\ \pm\kappa_a |\vec{\hat{e}}_a\rangle \end{bmatrix} = \pm\kappa_a \begin{bmatrix} |\vec{\hat{e}}_a\rangle \\ \pm\kappa_a |\vec{\hat{e}}_a\rangle \end{bmatrix}, \tag{G.6.63}$$

with $\kappa_a = \sqrt{k^2 + \mathcal{L}_a^{-2}}$. Therefore, $\pm\kappa_a$ is the eigenvalue of the matrix of (G.6.62) with eigenvector

$$|\pm\kappa_a\rangle = \frac{1}{(1 + |\kappa_a|^2)^{1/2}} \begin{bmatrix} |e_a\rangle \\ \pm\kappa_a |e_a\rangle \end{bmatrix}. \tag{G.6.64}$$

Considering the symmetry of BCs in (G.6.60) and (G.6.61), the solution of the above system of differential can be solved by the following ansatz:

$$N^{\nu} = \sum_{a=1,2} A_a \vec{\tilde{e}}_a^{\nu} \left(e^{+\kappa_a y} + e^{-\kappa_a y} \right), \tag{G.6.65}$$

$$\Phi = A_o \left(e^{+ky} - e^{-ky} \right). \tag{G.6.66}$$

Substitution of these ansatz into the BCs, Eq. (G.6.60) and (G.6.61) yields:

$$I = -\sigma^c \left[A_o k \left(e^{+kw/2} + e^{-kw/2} \right) \right] - \mathcal{D}_r \sum_{\nu,a} \theta_{\nu} (ik) \left[A_a \vec{\tilde{e}}_a^{\nu} \left(e^{+\kappa_a w/2} + e^{-\kappa_a w/2} \right) \right], \tag{G.6.67}$$

$$0 \simeq -\sigma^c \theta_{\nu} (ik) A_o \left(e^{+kw/2} - e^{-kw/2} \right) - \mathcal{D}_r \sum_{a} A_a \vec{\tilde{e}}_a^{\nu} \kappa_a \left(e^{+\kappa_a w/2} - e^{-\kappa_a w/2} \right). \tag{G.6.68}$$

From Eq. (G.6.68), it is found that

$$\frac{A_a}{A_o} \simeq (-i) \frac{\sigma^c}{\mathcal{D}_r} \sum_{\mu} \frac{k \sinh (kw/2)}{\kappa_a \sinh (\kappa_a w/2)} (\vec{\tilde{e}}^{-1})_a^{\mu} \theta_{\mu}, \tag{G.6.69}$$

Hence, upon substitution of this result into Eq. (G.6.67), we obtain:

$$\frac{I}{A_o} = -2k \cosh \left(k \frac{W}{2} \right) \left[1 + \sum_a \Theta_a^2 \mathcal{F}_a (k) \right] \sigma^c, \tag{G.6.70}$$

where

$$\Theta_a^2 = [\theta_{\mu} \vec{\tilde{e}}_a^{\mu}] [(\vec{\tilde{e}}^{-1})_{\nu}^{a} \theta_{\nu}], \tag{G.6.71}$$

$$\mathcal{F}_a (k) = \frac{k \tanh (kw/2)}{\kappa_a \tanh (\kappa_a w/2)}. \tag{G.6.72}$$

Hence,

$$N^{\nu} (\vec{r}) = \frac{iI}{\mathcal{D}_r} \sum_{a,\mu} \vec{\tilde{e}}_a^{\nu} (\vec{\tilde{e}}^{-1})_{\mu}^{a} \theta_{\mu} \int dk \frac{e^{ikx}}{2\pi} \frac{\tanh (kw/2)}{\kappa_a \sinh (\kappa_a w/2)} \frac{\cosh (\kappa_a y)}{\left[1 + \sum_b \Theta_b^2 \mathcal{F}_b (k) \right]}, \tag{G.6.73}$$

for the generalized polarization densities and

$$\Phi (\vec{r}) = -\frac{I}{\sigma^c} \int dk \frac{e^{ikx}}{2\pi k} \frac{\sinh (ky)}{\cosh (kW/2) \left[1 + \sum_b \Theta_b^2 \mathcal{F}_b (k) \right]}. \tag{G.6.74}$$

for the electrostatic potential.

7.6.3 Nonlocal Resistance

In this section, we compute the nonlocal resistance (NLR) in the absence of magnetic field, which is defined as

$$R_{nl} (x) = \frac{1}{I} [\Phi (x, -w/2) - \Phi (x, +w/2)]. \tag{G.6.75}$$

Substituting the electrostatic potential (G.6.74) into (G.6.75), we obtain the following integral form for the NLR:

$$\frac{R_{nl}(x)}{R_{xx}} = \frac{1}{\pi}\int_{-\infty}^{\infty} dk \frac{e^{ikx}}{k}\frac{\tanh(kw/2)}{1+\sum_b \Theta_b^2 \mathcal{F}_b(k)}, \tag{G.6.76}$$

with $R_{xx} = 1/\sigma^c$. The above result for the NLR can be expanded as follows

$$\frac{R_{nl}(x)}{R_{xx}} = \sum_{n=0}^{\infty} \mathcal{R}^n(x), \tag{G.6.77}$$

$$\mathcal{R}^n(x) = \sum_{\vec{a}^n} \mathcal{R}_{\vec{a}^n}(x), \tag{G.6.78}$$

with $\vec{a}^n = (a_1, a_2, \cdots, a_n)$. The expression for $\mathcal{R}_{\vec{a}^n}(x)$ is given by:

$$\mathcal{R}_{\vec{a}^n}(x) = \frac{1}{\pi}(-1)^n \int_{-\infty}^{+\infty} \frac{dk\, e^{ikx}}{k\coth(kw/2)} \prod_{\iota=1}^{n} \Theta_{a_\iota}^2 \mathcal{F}_{a_\iota}(k). \tag{G.6.79}$$

Next, we obtain asymptotic expressions for the various terms in the above expansion. For $n = 0$, $\mathcal{R}^0(x)$ reduces to the Ohmic NLR:

$$\mathcal{R}^0(x) = \frac{2}{\pi}\ln\left|\coth\left(\frac{\pi x}{2w}\right)\right|. \tag{G.6.80}$$

Explicitly, it is van der Paw resistance, which behaves as $\mathcal{R}_{\mathrm{vdP}} \simeq \frac{4}{\pi}e^{-|x|/\mathcal{L}_0}$ for $|x| \gg w$ where $\mathcal{L}_0 = w/\pi$. At large $|x|$, and for $w \ll \ell_\nu$, the $n = 1$ term is $\mathcal{R}^1 = \sum_a \mathcal{R}^1_a$, where

$$\mathcal{R}^1_a(x) \simeq \Theta_a^2 \frac{w}{2\mathcal{L}_a} e^{-|x|/\mathcal{L}_a}. \tag{G.6.81}$$

In earlier work of Zhang, Huang, and Cazalilla, 2017, we showed that a modest nonuniform strain can result in rather large valley Hall angles $\theta_v \sim 1$. Thus, in order to accurately describe the NLR we need to consider high order terms in the expansion, i.e. those with $n > 1$. But we here just pick out terms $\mathcal{R}_{\vec{a}^n}$ with same eigenmode $a_\iota = a$ i.e., $R_{nl}/R_{xx} \simeq \mathcal{R}^0 + \sum_a \mathcal{R}^a$, being

$$\begin{aligned}\mathcal{R}^a(x) &= \int_{-\infty}^{+\infty} \frac{dk}{\pi k}\frac{e^{ikx}}{\coth(kw/2)} \sum_{n=1}^{\infty}(-1)^n \left[\Theta_a^2 \mathcal{F}_a(k)\right]^n \\ &= \frac{\Theta_a^2}{1+\Theta_a^2}\frac{W}{2\mathcal{L}_a^r} e^{-|x|/\mathcal{L}_a^r},\end{aligned} \tag{G.6.82}$$

where $\mathcal{L}_a^r = \sqrt{1+\Theta_a^2}\mathcal{L}_a$ is renormalized decay lengths of each eigenmode (Zhang, Huang, and Cazalilla, 2017). Finally, we obtain total NLR $R_{nl}/R_{xx} = \mathcal{R}^0 + \delta\mathcal{R}_{nl}$

$$\frac{R_{nl}(x)}{R_{xx}} \simeq \overbrace{\frac{4}{\pi}e^{-|x|/\mathcal{L}_0}}^{\mathcal{R}^0} + \overbrace{\sum_a \underbrace{\frac{\Theta_a^2}{1+\Theta_a^2}\frac{w}{2\mathcal{L}_a^r}e^{-|X|/\mathcal{L}_a^r}}_{\mathcal{R}^a}}^{\delta\mathcal{R}_{nl}}, \tag{G.6.83}$$

The first term is the Ohmic contribution, $\mathcal{R}^0$, and the second term contains the sum of the exponentially decaying contributions for each eigenmode, $\mathcal{R}^a$. Near the current injection point ($|x| \lesssim \mathcal{L}_0$), R_{nl} is dominated by the ohmic contribution, $\mathcal{R}^0$, which will become negligible at sufficiently large distances (i.e. for $|x| \gg \mathcal{L}_0$).

Here we focus on the behavior of R_{nl}, when contribution of the eigenmodes of the diffusion equation dominate over the Ohmic contribution, i.e. when $\delta\mathcal{R}_{nl} \gg \mathcal{R}^0$.

7.6.4 Suppression of the Hanle effect

In this appendix, we provide the details of the derivation and solution of the diffusion equations in the presence of an in-plane magnetic field. Note that the Larmor frequency $\omega_L \ll \mu_F$, where μ_F is the Fermi level. The in-plane magnetic field, which we shall take parallel to the direction of the electric field applied to the device, induces precession of the spin-degree of freedom, whilst the valley is not affected. This mixes the out-of-plane spin component along z with the spin in-plane components along the x and y axes. Thus, our ansatz for the density-matrix distribution function in the QBE must be now expanded in terms of γ_v matrices taken from the larger set $\{\hat{s}_o\hat{\tau}_o, \hat{s}_o\hat{\tau}_z, \hat{s}_x\hat{\tau}_o, \hat{s}_y\hat{\tau}_o, \hat{s}_z\hat{\tau}_o, \hat{s}_x\hat{\tau}_z, \hat{s}_y\hat{\tau}_z, \hat{s}_z\hat{\tau}_z\}$.

In order to simplify the calculations described below, the deviation of the distribution function from equilibrium, i.e. $\delta n_{\vec{k}} = n_{\vec{k}} - n^0_{\vec{k}}$, will be slit into two parts, $\delta n_{\vec{k}} = \delta n^+_{\vec{k}} + \delta n^-_{\vec{k}}$, with

$$\delta n^+_{\vec{k}} \simeq \sum_{\mathrm{i}} \gamma_{\mathrm{i}} \left[\mu^{\mathrm{i}}(\vec{r}) + \vec{v}^{\mathrm{i}}(\vec{r}) \cdot \hbar\vec{k}\right] \left[-\partial_\epsilon n^0(\epsilon)\right]_{\epsilon=\mu_F}, \tag{G.6.84}$$

$$\delta n^-_{\vec{k}} \simeq \sum_{\mathrm{j}} \gamma_{\mathrm{j}} \left[\mu^{\mathrm{j}}(\vec{r}) + \vec{v}^{\mathrm{j}}(\vec{r}) \cdot \hbar\vec{k}\right] \left[-\partial_\epsilon n^0(\epsilon)\right]_{\epsilon=\mu_F}, \tag{G.6.85}$$

where $\mathrm{i} \in \{c, sv, v, s\}$ and $\mathrm{j} \in \{xo, yo, xz, yz\}$.

The form of the collision integral (G.6.30) is determined by the ansatz for density matrix $\delta n_{\vec{k}}$, which in turn follows from the forms of the T-matrix ($\propto \{\hat{s}_o, \hat{s}_z\}$), the pseudo-magnetic field arising from nonuniform strain ($\propto \{\hat{\tau}_o, \hat{\tau}_z\}$), and the (Zeeman) magnetic field ($\{\hat{s}_o, \hat{s}_y\}$). To compute the collision integral, it is convenient to also split the T-matrix into two parts, i.e., $T_{\vec{k}\vec{p}} = T^o_{\vec{k}\vec{p}} + T^z_{\vec{k}\vec{p}}$, with

$$T^o_{\vec{k}\vec{p}} = t_c \mathbb{1} \cos\left(\frac{\theta}{2}\right), \tag{G.6.86}$$

$$T^z_{\vec{k}\vec{p}} = i t_s \hat{s}_z \sin\left(\frac{\theta}{2}\right), \tag{G.6.87}$$

which obey:

$$\left[\delta n^-_{\vec{k}}, T^z_{\vec{k}\vec{p}}\right]_+ = 0, \tag{G.6.88}$$

$$\left[\delta n^-_{\vec{k}}, T^o_{\vec{k}\vec{p}}\right]_- = 0, \tag{G.6.89}$$

$$\left[\delta n^+_{\vec{k}}, T_{\vec{k}\vec{p}}\right]_- = 0, \tag{G.6.90}$$

where $[A,B]_{\pm} = AB \pm BA$. Next, using the above ansatz, the collision integral (G.6.30) reduces to:

$$\begin{aligned}\mathcal{I}\left[\delta n_{\vec{k}}\right] = &\frac{\pi}{\hbar} n_{\mathrm{i}} \sum_{\vec{p}} \delta\left[\epsilon\left(p\right) - \epsilon\left(q\right)\right] 2\hat{T}_{\vec{k}\vec{p}}\hat{T}^{*}_{\vec{k}\vec{p}}(\delta n^{+}_{\vec{p}} - \delta n^{+}_{\vec{k}}) \\ &+ \frac{\pi}{\hbar} n_{\mathrm{i}} \sum_{\vec{p}} \delta\left[\epsilon\left(p\right) - \epsilon\left(q\right)\right] 2\hat{T}_{\vec{k}\vec{p}}\hat{T}^{o*}_{\vec{k}\vec{p}}(\delta n^{-}_{\vec{p}} - \delta n^{-}_{\vec{k}}) \\ &- \frac{\pi}{\hbar} n_{\mathrm{i}} \sum_{\vec{p}} \delta\left[\epsilon\left(p\right) - \epsilon\left(q\right)\right] 2\hat{T}_{\vec{k}\vec{p}}\hat{T}^{z*}_{\vec{k}\vec{p}}(\delta n^{-}_{\vec{p}} + \delta n^{-}_{\vec{k}}).\end{aligned} \tag{G.6.91}$$

Hence,

$$\begin{aligned}2\hat{T}^{+}_{\vec{k}\vec{p}}\hat{T}^{*}_{\vec{k}\vec{p}} = &\left[\left|t_c\right|^2\left(1+\cos\theta\right) + \left|t_s\right|^2\left(1-\cos\theta\right)\right]\gamma^{c} \\ &+ 2\mathrm{Im}\left(t_c t_s^{*}\right)\sin\theta\gamma^{s}\end{aligned} \tag{G.6.92}$$

$$2\hat{T}_{\vec{k}\vec{p}}\hat{T}^{o*}_{\vec{k}\vec{p}} = \left|t_c\right|^2\left(1+\cos\theta\right)\gamma^{c} + it_s t_c^{*}\sin\theta\gamma^{s}, \tag{G.6.93}$$

$$2\hat{T}_{\vec{k}\vec{p}}\hat{T}^{z*}_{\vec{k}\vec{p}} = \left|t_s\right|^2\left(1-\cos\theta\right)\gamma^{c} - it_c t_s^{*}\sin\theta\gamma^{s}, \tag{G.6.94}$$

In addition, we need to compute the differences and sums:

$$\delta n^{-}_{\vec{p}} - \delta n^{-}_{\vec{k}} = \left[-\partial_{\epsilon} n^{0}\left(\epsilon\right)\right]_{\epsilon=\mu_F} \sum_{\mathrm{j}} \gamma_{\mathrm{j}}\vec{v}_{\mathrm{j}}\left(\vec{r}\right)\cdot\hbar(\vec{p}-\vec{k}), \tag{G.6.95}$$

$$\delta n^{+}_{\vec{p}} - \delta n^{+}_{\vec{k}} = \left[-\partial_{\epsilon} n^{0}\left(\epsilon\right)\right]_{\epsilon=\mu_F} \sum_{\mathrm{i}} \gamma_{\mathrm{i}}\vec{v}_{\mathrm{i}}\left(\vec{r}\right)\cdot\hbar(\vec{p}-\vec{k}), \tag{G.6.96}$$

$$\begin{aligned}\delta n^{-}_{\vec{p}} + \delta n^{-}_{\vec{k}} = &\left[-\partial_{\epsilon} n^{0}\left(\epsilon\right)\right]_{\epsilon=\mu_F} \sum_{\mathrm{j}} \gamma_{\mathrm{j}}\vec{v}_{\mathrm{j}}\left(\vec{r}\right)\cdot\hbar(\vec{p}+\vec{k}) \\ &+ \left[-\partial_{\epsilon} n^{0}\left(\epsilon\right)\right]_{\epsilon=\mu_F} \sum_{\mathrm{j}} 2\gamma_{\mathrm{j}}\mu_{\mathrm{j}}\left(\vec{r}\right).\end{aligned} \tag{G.6.97}$$

Substituting Eqs. (G.6.92)-(G.6.97) into the collision integral (G.6.91), the explicit form of the collision integral is split into three contributions: $\mathcal{I}\left[\delta n_{\vec{k}}\right] = \mathcal{I}^{+}\left[\delta n_{\vec{k}}\right] + \mathcal{I}^{0}\left[\delta n_{\vec{k}}\right] + \mathcal{I}^{-}\left[\delta n_{\vec{k}}\right]$, with

$$\begin{aligned}\mathcal{I}^{+}\left[\delta n_{\vec{k}}\right] = &\left[\partial_{\epsilon} n^{0}\left(\epsilon\right)\right]_{\epsilon=\mu_F}\hbar\vec{k}\cdot\left\{\frac{\gamma^{c}}{\tau}\sum_{\mathrm{i}}\gamma^{\mathrm{i}}\vec{v}_{\mathrm{i}}\left(\vec{r}\right)\right. \\ &\left.+ \gamma^{s}\omega_{s}\sum_{\mathrm{i}}\gamma^{\mathrm{i}}\vec{v}_{\mathrm{i}}\left(\vec{r}\right)\times\hat{\vec{z}}\right\},\end{aligned} \tag{G.6.98}$$

$$\mathcal{I}^{0}\left[\delta n_{\vec{k}}\right] = \left[\partial_{\epsilon} n^{0}\left(\epsilon\right)\right]_{\epsilon=\mu_F}\frac{\gamma^{c}}{\tau_{s,xy}}\sum_{\mathrm{j}}\gamma^{\mathrm{j}}\mu_{\mathrm{j}}\left(\vec{r}\right), \tag{G.6.99}$$

$$\begin{aligned}\mathcal{I}^{-}\left[\delta n_{\vec{k}}\right] = &\left[\partial_{\epsilon} n^{0}\left(\epsilon\right)\right]_{\epsilon=\mu_F}\hbar\vec{k}\cdot\left\{\frac{\gamma^{c}}{\tilde{\tau}}\sum_{\mathrm{j}}\gamma^{\mathrm{j}}\vec{v}_{\mathrm{j}}\left(\vec{r}\right)\right. \\ &\left.+ i\gamma^{s}\omega_{s}\sum_{\mathrm{j}}\gamma^{\mathrm{j}}\vec{v}_{\mathrm{j}}\left(\vec{r}\right)\times\hat{\vec{z}}\right\},\end{aligned} \tag{G.6.100}$$

where $\mathrm{i} = (c, sv, v, s)$, $\mathrm{j} = (xo, yo, xz, yz)$ and we define other two kinds of relaxation times to describe the collision of electrons:

$$\frac{1}{\tau_{s,xy}(k)} = \frac{k n_{\mathrm{i}}}{4\hbar^2 v_F}\left[4\left|t_s(k)\right|^2\right], \tag{G.6.101}$$

$$\frac{1}{\tilde{\tau}(k)} = \frac{k n_{\mathrm{i}}}{4\hbar^2 v_F}\left[\left|t_c(k)\right|^2 + \left|t_s(k)\right|^2\right], \tag{G.6.102}$$

Notice that, in the presence of an in-plane magnetic field the term $\mathcal{I}^0\left[\delta n_{\vec{k}}\right]$ in the colission integral introduces an additional relaxation time, $\tau_{s,xy}(k)$.

In addition to spin (spin-valley) current, the in-plane magnetic field couples the out-of-plane and in-plane components of the spin current, $\vec{J}^{xo}$ and $\vec{J}^{yo}$ (spin-valley currents, $\vec{J}^{xz}$ and $\vec{J}^{yz}$). Here we take the magnetic field to be parallel to the applied electric field, i.e. $\vec{H} \parallel \hat{y}$, and thus the following generalized density N and current $\vec{J}$ appear in our diffusion equations:

$$\vec{J} = \begin{bmatrix}\vec{J}_{\parallel}\\ \vec{J}_{\perp}\end{bmatrix}, \vec{J}_{\parallel} = \begin{bmatrix}\vec{J}^{c}\\ \vec{J}^{sv}\\ \vec{J}^{xz}\\ \vec{J}^{yo}\end{bmatrix}, \vec{J}_{\perp} = \begin{bmatrix}\vec{J}^{v}\\ \vec{J}^{s}\\ \vec{J}^{xo}\\ \vec{J}^{yz}\end{bmatrix}, \tag{G.6.103}$$

$$N = \begin{bmatrix}N_{\parallel}\\ N_{\perp}\end{bmatrix}, N_{\parallel} = \begin{bmatrix}N^{c}\\ N^{sv}\\ N^{xz}\\ N^{yo}\end{bmatrix}, N_{\perp} = \begin{bmatrix}N^{v}\\ N^{s}\\ N^{xo}\\ N^{yz}\end{bmatrix}, \tag{G.6.104}$$

where we have divided the longitudinal and transverse modes. Let us first focus on the continuity equations. In the steady state, they read:

$$\partial_i J_i^{\mu} = -(\tau_{sr}^{-1})_{\nu}^{\mu} N^{\nu} + \omega_{\nu}^{\mu} N^{\nu}, \tag{G.6.105}$$

which is obtained by tracing the linearized QBE, i.e. taking $\frac{g_s g_v}{4}\sum_{\vec{k}} e\mathrm{Tr}\left[\gamma^{\mu}\left(\mathrm{QBE}\right)\right]$. In the above expression

$$\tau_{sr}^{-1} = \begin{bmatrix}\tau_0^{-1} & 0\\ 0 & \tau_0^{-1}\end{bmatrix}, \tau_0^{-1} = \begin{bmatrix}0 & 0 & 0 & 0\\ 0 & 0 & 0 & 0\\ 0 & 0 & \tau_{s,xy}^{-1} & 0\\ 0 & 0 & 0 & \tau_{s,xy}^{-1}\end{bmatrix}, \tag{G.6.106}$$

$$\omega = \begin{bmatrix}\omega_0 & 0\\ 0 & \omega_0\end{bmatrix}, \omega_0 = \begin{bmatrix}0 & 0 & 0 & 0\\ 0 & 0 & +\omega_L & 0\\ 0 & -\omega_L & 0 & 0\\ 0 & 0 & 0 & 0\end{bmatrix}. \tag{G.6.107}$$

The matrix τ_{sr}^{-1} describes the spin relaxation for spin polarized in the x-y plane. In our microscopic model, s_z is a good quantum number and there is no relaxation. The second term describes the spin precession induced by an in-plane magnetic field in y-axis direction. We parameterize the strength of the in-plane magnetic field H by the Larmor frequency $\omega_L = g\mu_B H/\hbar$.

The constitutive relations for the generalized currents, J_i^{μ} is given by following equations:

$$\mathcal{D}\partial_i N^{\mu} - \sigma_D E_i^{\mu} = \left[-\delta_{\nu}^{\mu}\delta_{ij} + \tau\omega_{\nu}^{\mu}\delta_{ij} + (R_H)_{\nu}^{\mu}\epsilon_{ij}\right] J_j^{\nu}, \tag{G.6.108}$$

where

$$R_H = \begin{bmatrix} 0 & R_H^0 \\ R_H^0 & 0 \end{bmatrix}, R_H^0 = \begin{bmatrix} \omega_v\tau & \omega_s\tau & 0 & 0 \\ \omega_s\tau & \omega_v\tau & 0 & 0 \\ 0 & 0 & \omega_v\tau & \omega_s\tau \\ 0 & 0 & \omega_s\tau & \omega_v\tau \end{bmatrix}. \tag{G.6.109}$$

For the sake of simplicity, we have assumed that the relaxation rates for all currents are the same and equal to Drude relaxation time ($\tilde{\tau} \simeq \tau$) (See expressions for $\tilde{\tau}$ in Eq. (G.6.102) for $i = (xo, yo, xz, yz)$ and τ in Eq. (G.6.36) for $i = (c, sv, v, s)$. Thus, we take $\mathcal{D} = v_F^2\tau/2$ ($\sigma_D = ne^2\tau/m$) to be the same for all types of currents. These assumptions can be relaxed, and will not alter our conclusions qualitatively. R_H is the coupling matrix that couples the different currents with each other due to the local impurities and the strain pseudo-magnetic field.

Solving the constitutive equations (G.6.108) for the currents J_i^μ we obtain:

$$J_i^\mu = -(D_{ij})_\nu^\mu \partial_j N^\nu + (\sigma_{ij})_\nu^\mu E_j^\nu. \tag{G.6.110}$$

As pointed out in the main text, the diffusion matrix is a rank-2 tensor in the space indices $i, j = x, y$, and therefore it can be split into a symmetric ($\propto \delta_{ij}$) and antisymmetric ($\propto \epsilon_{ij}$) parts according to $D_{ij} = D_0\delta_{ij} + D_H\epsilon_{ij}$ where

$$D_0 = \begin{bmatrix} D_0^0 & 0 \\ 0 & D_0^0 \end{bmatrix}, D_0^0 = \mathcal{D}_r \begin{bmatrix} \eta_c & \eta_{sv} & \eta_{xz} & \eta_{yo} \\ \eta_{sv} & \eta_c & \eta_{yo} & \eta_{xz} \\ \eta_{xz} & \eta_{yo} & \eta_c & \eta_{sv} \\ \eta_{yo} & \eta_{xz} & \eta_{sv} & \eta_c \end{bmatrix}, \tag{G.6.111}$$

$$D_H = \begin{bmatrix} 0 & D_H^0 \\ D_H^0 & 0 \end{bmatrix}, D_H^0 = \mathcal{D}_r \begin{bmatrix} \theta_v & \theta_s & \theta_{xo} & \theta_{yz} \\ \theta_s & \theta_v & \theta_{yz} & \theta_{xo} \\ \theta_{xo} & \theta_{yz} & \theta_v & \theta_s \\ \theta_{yz} & \theta_{xo} & \theta_s & \theta_v \end{bmatrix}. \tag{G.6.112}$$

$\mathcal{D}_r, \eta_\mu, \theta_\mu$ are rather complicated functions of $\omega_v\tau, \omega_s\tau$ and $\omega_L\tau$, and are not given here. Similarly, the conductivity matrix can be obtained by replacing the diffusion constant $\mathcal{D}$ with the Drude conductivity σ_D.

In the presence of an in-plane magnetic field, the system response consists of eight types of currents. Recall that the magnetic field acts only as a Zeeman term that induces precession, and does not introduce a Lorentz force (i.e. $\vec{F}_{\vec{k}}^B = 0$ in Eq. (G.6.24), as mentioned above). Accounting (phenomenologically) for spin relaxation, the constitutive and continuity equations in the presence of the magnetic field read:

$$J_i^\mu = -(D_{ij})_\nu^\mu \partial_j N^\nu + (\sigma_{ij})_\nu^\mu E_j^\nu, \tag{G.6.113}$$

$$\partial_i J_i^\mu = -\frac{\delta_\nu^\mu}{\tau^\nu} N^\nu + \omega_\nu^\mu N^\nu, \tag{G.6.114}$$

where

$$D_0 = \begin{bmatrix} D_0^0 & 0 \\ 0 & D_0^0 \end{bmatrix}, D_0^0 = \mathcal{D}_r \begin{bmatrix} 1 & \eta & 0 & 0 \\ \eta & 1 & 0 & 0 \\ 0 & 0 & 1 & \eta \\ 0 & 0 & \eta & 1 \end{bmatrix}, \tag{G.6.115}$$

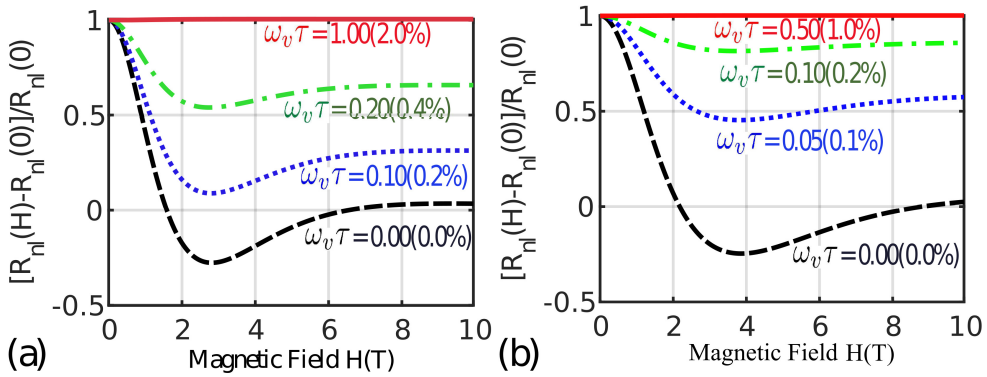

FIGURE 7.3: (Color online) Nonlocal resistance $R_{nl}(H)$, in the unit of $R_{nl}(0)$, are plotted against magnetic field H for different chemical potential (a) $\mu_F = 0.15$ eV and (b) $\mu_F = -0.10$ eV. Drude conductivity σ_D, Drude relaxation time τ and the scattering rate of spin, $\omega_s\tau$, can be obtained from the parameters of a microscopic scattering model (Huang et al., 2016): impurity density $n_{\text{imp}} = 5.0 \times 10^{10} cm^{-2}$, scalar potential $\mathcal{V}_D = 50$ meV, SOC potential $\mathcal{V}_S = 5$ meV (Balakrishnan et al., 2014), defect size $R = 20$ nm, and associated momentum cutoff $k_c = 2/R$. On the other hand, fairly modest strain can sustain a large valley Hall effect (Zhang, Huang, and Cazalilla, 2017), $\omega_v\tau(\gtrsim 1)$. $\omega_v\tau = 1$ can be induced by applying along the y direction an average (uniaxial) strain of 2%. Parameters: $\ell_s = 0.53\mu$m, $\ell_v = 0.53\mu$m, $w = 0.50\mu$m, $x = 2.00\mu$m and $y = 0.25\mu$m.

$$D_H = \begin{bmatrix} 0 & D_H^0 \\ D_H^0 & 0 \end{bmatrix}, D_H^0 = \mathcal{D}_r \begin{bmatrix} \theta_v & \theta_s & 0 & 0 \\ \theta_s & \theta_v & 0 & 0 \\ 0 & 0 & \theta_v & \theta_s \\ 0 & 0 & \theta_s & \theta_v \end{bmatrix}. \tag{G.6.116}$$

Substituting continuity equations (G.6.114) into the divergence of constitutive equations (G.6.113), the diffusion equations away from the boundaries take again a form similar to Eq. (G.6.55),

$$\partial_i^2 N^\mu - \mathcal{M}_\nu^\mu N^\nu = 0. \tag{G.6.117}$$

However, this time the diffusion matrix is 4×4 in order to accommodate the additional response modes introduced by the precession term:

$$\mathcal{M} \simeq \begin{bmatrix} \ell_v^{-2} & -\eta\ell_s^{-2} & +\eta\ell_L^{-2} & 0 \\ -\eta\ell_v^{-2} & \ell_s^{-2} & -\ell_L^{-2} & 0 \\ 0 & +\ell_L^{-2} & \ell_s^{-2} & -\eta\ell_v^{-2} \\ 0 & -\eta\ell_L^{-2} & -\eta\ell_s^{-2} & \ell_v^{-2} \end{bmatrix}. \tag{G.6.118}$$

The eigenvalues of the above diffusion matrix are

$$E_\pm^\eta = \frac{\ell_v^{-2} + \ell_s^{-2} \mp i\ell_L^{-2}}{2} + \frac{\eta}{2}\sqrt{\Delta_\pm}. \tag{G.6.119}$$

with

$$\Delta_\pm = \left(\ell_v^{-2} - \ell_s^{-2} \pm i\ell_L^{-2}\right)^2 + 4\eta_{zz}^2\ell_v^{-2}\left(\ell_s^{-2} \mp i\ell_L^{-2}\right). \tag{G.6.120}$$

Hence, following the same procedure to find the solution as in the case with $H = 0$, we arrive at the following result for the NLR:

$$\frac{R_{nl}(x,H)}{R_{xx}} = \frac{1}{\pi}\int_{-\infty}^{\infty} dk \frac{e^{ikx}}{k} \frac{\tanh(kw/2)}{1+\sum_b \Theta_b^2 \mathcal{F}_b(k)}, \tag{G.6.121}$$

where we sum over four transverse eigenmodes $\{v, s, xo, yz\}$ in the denominator of the above integral. The above equation is the basis of the analysis about the suppression of the Hanle effect described in the main text.

FIGURE 7.3 shows the NLR, $R_{nl}(x,H)$ normalized to its value at zero in-plane magnetic field, $R_{nl}(x, H=0)$ versus H, for different chemical potentials [(a) $\mu_F = 0.15$ eV and (b) $\mu_F = -0.10$ eV]. As noticed in the main text, by setting $\omega_v\tau = 0$, the result of Abanin et al., 2009 is recovered. In this case, the diffusion lengths of the (spin) eigenmodes, $\ell_{s\pm} = (\ell_s^{-2} \pm i\ell_L^{-2})^{-1/2}$ become complex (with imaginary part $\ell_L^{-2} \propto H$), which leads to the development of an oscillatory component in the NLR (Hanle effect). Upon increasing the amount of nonuniform strain, we find that the oscillating part of the NLR is suppressed and even disappears for strains of the order of $\sim 1\%$. This shows that our result concerning the suppression of the Hanle effect for nonuniform strain of the order of a few percents maximum is robust against the change of the carrier density and sign.

Chapter 8

Summary and outlook

This thesis addresses transport phenomena related to the spin- and valley-dependent transport in 2D Dirac materials and hybrid systems. Experimentalists and theorists have paid the detection of neutral currents, and the demonstration of Hall effects much attention in condensate mater physics due to their promising applications in spintronics and valleytronics. In this thesis, I investigate these effects using spin Hall magnetoresistance (SMR) and nonlocal resistance (NLR) in Part I and Part II, respectively. Besides, I have a chapter to study the nonlocal magnetization (NLM) in nanowires (NWs) and films proximity to both superconductors (SCs) and magnetic insulators (MIs).

Part I. Spin transport in normal metal/magnetic insulator heterostructures

In Part I of this thesis, I concentrate on the spin transport in normal metal/magnetic insulator (NM/MI) heterostructures. The modulation of the magnetoresistance with respect to the direction of the applied magnetic field can demonstrate the existence of the spin Hall effect (SHE). Replacing the NM by the NWs and films in proximity to SCs, I also study the NLM induced by the interplay of superconducting and magnetic proximity effects.

- In Chapter 2, I present a theory of the SMR effect from a microscopic perspective. In subsection 2.2.2, SMR relates to the microscopic processes of spin relaxation at the NM/MI interface. Our theory covers a wide range of MIs and can be used to investigate the effect of a magnetic field and temperature on MR in NM/MI Hall-bar setups and beyond. In subsection 2.3.2, we find a non-local interplay between SMR and HMR, which gives rise to a negative linear-in-magnetic-field MR. Our theory provides a useful tool for understanding transport experiments. The combination of our model with experimental data has the potential to evolve into a complete technique to reveal the interfacial magnetic properties of MIs by standard transport measurements.

- In Chapter 3, we explore the SMR in Platinum (Pt) on a paramagnetic insulator $Gd_3Ga_5O_{12}$ (GGG). The observed SMR with GGG will open a new research direction of spintronics with 4*f* electron systems in rare-earth compounds, Gd. We clarify the quantitative values of the microscopic spin parameters at the interface to GGG in section 3.3, which gives a useful piece of information for simulating spintronic functions with realistic conditions and accelerating material science.

- In Chapter 4, we investigate the SMR in a Platinum/Europium sulfide (Pt / EuS) bilayer, where EuS is a pure ferromagnetic insulator below 25 K. The SMR is observed by the measurements of angular and field dependencies of

magnetoresistance in subsection 4.3.1, in which the magnetization reversal of EuS is observed. Furthermore, we also measure the anomalous-Hall-effect-like contribution of the SMR in subsection 4.3.2, driven by a large imaginary part of the spin-mixing conductance. We can extract microscopic parameters such as the exchange interaction between the $1s$ electrons of Pt and the $4f$ electrons of Eu ($J_{sf} \sim 3-4$ meV). We study the temperature dependence of the spin conductance of the Pt / EuS interface in subsection 4.3.3, showing for the first time experimentally a larger field-like torque (G_i) than spin-transfer torque (G_r) in an HM/MI interface. The effective exchange field associated with G_i is expected to be ~ 1 meV. Therefore, SMR measurements offer a simple way to quantify effective fields, which are of interest in different areas, such as superconducting applications.

- In Chapter 5, I predict the appearance of a NLM, M_{NL} in a NW (or film) when proximitized to SCs and a ferromagnetic insulator (FI). In section 5.2, I show this magnetization appears as a consequence of the interplay between the superconducting correlations induced in the NW (or film) and the exchange field localized at the FI/NW interface. As explained in section 5.3, the sign of M_{NL} is opposite to the local Pauli spin polarization right at the FI/NW interface, and its value can be controlled by the phase difference between superconducting electrodes in a Josephson junction setup.

Part II Spin and valley Hall effects in two dimensional Dirac materials

In Part II of this thesis, we have investigated the spin- and valley-dependent transport in 2D Dirac materials with sizable spin-orbit coupling (SOC) and valley-orbit coupling (VOC). The long spin and valley diffusion lengths make it possible to indirectly detect the spin and valley Hall effects through NLR in Hall bar devices.

- In Chapter 6, I develop a theory of the strain-induced classical valley Hall effect (VHE). Specifically, using the quantum Boltzmann equation, we have provided a microscopic derivation of the equations governing the diffusion of valley polarization in section 6.4. The latter has been solved for a Hall bar device geometry, subject to nonuniform strain leading to the uniform pseudo-magnetic field. The observable NLR of the device has been obtained in section 6.5. I find that for low doping, the figure of merit of the VHE, namely the valley Hall angle, can be of order unity even at room temperature. We demonstrate that the NLR of the device decays exponentially.

- In chapter 7, I explore several important consequences of the coexistence of SHE and VHE in a two-dimensional material. I have shown the latter leads to the emergence of neutral longitudinal spin and valley polarized current in section 7.2. Furthermore, I have shown the spin polarization diffusing in the material can be controlled utilizing non-uniform strain in section 7.3. Finally, I have shown the Hanle effect in response to an in-plane magnetic field can be strongly suppressed due to the competition of the two effects in section 7.4. I believe the suppression of the Hanle effect noticed here will shed light on experimental controversies concerning the origin of enhancing the NLR in various types of graphene devices. The theory presented here can also be extended in various other directions, such as accounting for other spin-charge conversion mechanisms beyond the SHE (such as the inverse spin-galvanic

effect) and a weak spin-valley (Zeeman) coupling, which is present in hybrid graphene/transition-metal dichalcogenides structures. Both effects are expected to be important when spatial inversion symmetry is broken.

I foresee several interesting further research on the topics addressed in this thesis. For example, the SMR theory developed in Chapter 2 can be extended to other magnetic orders. Indeed, we are at the moment collaborating with experimental groups studying the SMR in Pt/MnO, which presumably has an antiferromagnetic ordering. A further perspective of this theory is extending it to study the magnetoresistance effect of magnetized metal or magnet. The magnetic and thermal properties of those can arise from the field and temperature dependence of spin diffusion length and effective Larmor frequency. One may also include new origins of interfacial spin-dependent scattering, for instance, Dzyaloshinskii-Moriya (Caretta et al., 2020; Xia et al., 2020), Elliott-Yafet (Elliott, 1954; Yafet, 1963), Dyakonov-Perel (D'yakonov and Perel, 1971; Dyakonov and Perel, 1972), and Bir-Aronov-Pikus (Bir, Aronov, and Pikus, 1975) interaction. The results in Chapter 5 on the nonlocal magnetization induced by the interplay of superconducting and magnetic proximity effects can be extended to study the superconducting phase-coherent control of the qubit frequency in proximitized quantum dot.

Regarding the topics of Part II, I foresee interesting physics from the interplay of the intrinsic and extrinsic SOC, the VOC from strain and substrate, with magnetic and superconducting proximity effects stemming from magnets and superconductors attached to the 2D material. The interplay of magnet and strain leads to the emergence of the spin-valley Hall effect. Second, we explore the coexistence of quantum SHE and VHE in graphene, arising from Berry curvature from Kane-Mele SOC and the global energy difference between A and B sublattices (σ^z), respective. We can predict the existence of quantum spin-valley Hall effect from the interplay of quantum SHE and VHE. The emergence of classical spin Hall effect induced by the local Kane-Mele SOC reveals the possibility of extrinsic ordinary and valley Hall effects from the local $\tau^z\sigma^z$ and σ^z coupling. Fourth, the SHE generated by the spatially homogeneous Rashba and Dresselhaus SOC leads to the natural guess about the VHE from the uniform strain. Finally, the quantum SHE from spatially homogeneous Kane-Mele SOC indicates the possibility of quantum spin-valley Hall effect form spatially homogeneous $s^z\sigma^z$ coupling. The interplay of spin and valley transport will be bound to integrate the spintronics and valleytronics. The methodology developed in this thesis may serve to address all these exciting problems.

Bibliography

Abanin, D. A. et al. (2009). "Nonlocal charge transport mediated by spin diffusion in the spin Hall effect regime". In: Phys. Rev. B 79 (3), p. 035304. DOI: 10.1103/PhysRevB.79.035304. URL: http://link.aps.org/doi/10.1103/PhysRevB.79.035304.

Abrikosov, A A and L P Gor'kov (1962). "Spin-orbit interaction and the Knight shift in superconductors". In: J. Exp. Theor. Phys. 15, p. 752.

Albrecht, Sven Marian et al. (2016). "Exponential protection of zero modes in Majorana islands". In: Nature 531.7593, pp. 206–209.

Alicea, Jason (2012). "New directions in the pursuit of Majorana fermions in solid state systems". In: Reports on progress in physics 75.7, p. 076501.

Althammer, Matthias et al. (2013). "Quantitative study of the spin Hall magnetoresistance in ferromagnetic insulator/normal metal hybrids". In: Phys. Rev. B 87.22, p. 224401.

Amorim, B et al. (2016). "Novel effects of strains in graphene and other two dimensional materials". In: Physics Reports 617, pp. 1–54.

Ando, Tsuneya (2015). "Theory of Valley Hall Conductivity in Graphene with Gap". In: Journal of the Physical Society of Japan 84.11, p. 114705.

Antel, W. J. et al. (1999). "Induced ferromagnetism and anisotropy of Pt layers in Fe/Pt(001) multilayers". In: Physical Review B 60.18, pp. 12933–12940. ISSN: 0163-1829. DOI: 10.1103/PhysRevB.60.12933. URL: https://link.aps.org/doi/10.1103/PhysRevB.60.12933.

Apalkov, Dmytro, Bernard Dieny, and JM Slaughter (2016). "Magnetoresistive random access memory". In: Proceedings of the IEEE 104.10, pp. 1796–1830.

Aqeel, A et al. (2016). "Electrical detection of spiral spin structures in Pt| Cu 2 OSeO 3 heterostructures". In: Physical Review B 94.13, p. 134418.

Aqeel, Aisha et al. (2015). "Spin-Hall magnetoresistance and spin Seebeck effect in spin-spiral and paramagnetic phases of multiferroic CoCr 2 O 4 films". In: Physical Review B 92.22, p. 224410.

Avci, Can Onur et al. (2015). "Unidirectional spin Hall magnetoresistance in ferromagnet/normal metal bilayers". In: Nat. Phys. 11.7, p. 570.

Avci, Can Onur et al. (2017). "Current-induced switching in a magnetic insulator". In: Nature materials 16.3, pp. 309–314.

Averkiev, NS and MI Dyakonov (1983). "Current due to inhomogeneity of the spin orientation of electrons in a semiconductor". In: SOVIET PHYSICS SEMICONDUCTORS-USSR 17.4, pp. 393–395.

Avsar, Ahmet et al. (2014). "Spin-orbit proximity effect in graphene". In: Nature communications 5.

Avsar, Ahmet et al. (2015). "Enhanced spin–orbit coupling in dilute fluorinated graphene". In: 2D Materials 2.4, p. 044009.

Baibich, Mario Norberto et al. (1988). "Giant magnetoresistance of (001) Fe/(001) Cr magnetic superlattices". In: Physical review letters 61.21, p. 2472.

Bakun, AA et al. (1984). "Observation of a surface photocurrent caused by optical orientation of electrons in a semiconductor". In: JETP Lett 40.11.

Balakrishnan, Jayakumar et al. (2013). "Colossal enhancement of spin-orbit coupling in weakly hydrogenated graphene". In: Nature Physics 9, p. 284.

Balakrishnan, Jayakumar et al. (2014). "Giant spin Hall effect in graphene grown by chemical vapour deposition". In: Nature Communications 5, p. 4748.

Baldrati, Lorenzo et al. (2018). "Full angular dependence of the spin Hall and ordinary magnetoresistance in epitaxial antiferromagnetic NiO (001)/Pt thin films". In: Physical Review B 98.2, p. 024422.

Band, Yehuda B and Yshai Avishai (2013). Quantum mechanics with applications to nanotechnology a Academic Press.

Basko, Denis M (2008). "Resonant low-energy electron scattering on short-range impurities in graphene". In: Physical Review B 78.11, p. 115432.

Beconcini, Michael, Fabio Taddei, and Marco Polini (2016). "Nonlocal topological valley transport at large valley Hall angles". In: Physical Review B 94.12, p. 121408.

Beenakker, CWJ (2013). "Search for Majorana fermions in superconductors". In: Annu. Rev. Condens. M 4.1, pp. 113–136.

Benítez, L Antonio et al. (2018). "Strongly anisotropic spin relaxation in graphene–transition metal dichalcogenide heterostructures at room temperature". In: Nature Physics 14.3, p. 303.

Berche, B et al. (2009). "Gauge field theory approach to spin transport in a 2D electron gas". In: arXiv preprint arXiv:0910.0486.

Berg, HAM Van den et al. (2013). Magnetic multilayers and giant magnetoresistance: fundamentals an Vol. 37. Springer Science & Business Media.

Bergeret, F. S, A. F Volkov, and K. B Efetov (2004a). "Spin screening of magnetic moments in superconductors". In: Europhysics Letters (EPL) 66.1, pp. 111–117. DOI: 10.1209/epl/i2004-10003-3. URL: https://doi.org/10.1209%2Fepl%2Fi2004-10003-3.

Bergeret, F Sebastian et al. (2018). "Colloquium: Nonequilibrium effects in superconductors with a spin-splitting field". In: Reviews of Modern Physics 90.4, p. 041001.

Bergeret, FS, KB Efetov, and AI Larkin (2000). "Nonhomogeneous magnetic order in superconductor-ferromagnet multilayers". In: Physical Review B 62.17, p. 11872.

Bergeret, FS, AF Volkov, and KB Efetov (2004b). "Induced ferromagnetism due to superconductivity in superconductor-ferromagnet structures". In: Physical Review B 69.17, p. 174504.

Bergeret, FS, Anatoly F Volkov, and Konstantin B Efetov (2005). "Odd triplet superconductivity and related phenomena in superconductor-ferromagnet structures". In: Reviews of modern physics 77.4, p. 1321.

Bernevig, B Andrei and Shou-Cheng Zhang (2006). "Quantum spin Hall effect". In: Physical review letters 96.10, p. 106802.

Bezuglyi, EV, EN Bratus, and VS Shumeiko (2011). "Dissipative charge transport in diffusive superconducting double-barrier junctions". In: Physical Review B 83.18, p. 184517.

Bhatti, Sabpreet et al. (2017). "Spintronics based random access memory: a review". In: Materials Today 20.9, pp. 530–548.

Binasch, Grünberg et al. (1989). "Enhanced magnetoresistance in layered magnetic structures with antiferromagnetic interlayer exchange". In: Physical review B 39.7, p. 4828.

Bir, GL, AG Aronov, and GE Pikus (1975). "Spin relaxation of electrons due to scattering by holes". In: Zh. Eksp. Teor. Fiz 69.4, p. 1382.

Bloss, WL, LJ Sham, and V Vinter (1979). "Interaction-induced transition at low densities in silicon inversion layer". In: Physical Review Letters 43.20, p. 1529.

Bohn, HG, A Kollmar, and W Zinn (1984). "Spin dynamics in the cubic Heisenberg ferromagnet EuS". In: Physical Review B 30.11, p. 6504.

Bohn, HG et al. (1980). "Neutron scattering study of spin waves and exchange interactions in ferromagnetic EuS". In: Physical Review B 22.11, p. 5447.

Börlin, Johannes, Wolfgang Belzig, and Christoph Bruder (2002). "Full counting statistics of a superconducting beam splitter". In: Physical review letters 88.19, p. 197001.

Brataas, Arne, Gerrit EW Bauer, and Paul J Kelly (2006a). "Non-collinear magnetoelectronics". In: Physics Reports 427.4, pp. 157–255.

Brataas, Arne, Gerrit E.W. Bauer, and Paul J. Kelly (2006b). "Non-collinear magnetoelectronics". In: Physics Reports 427.4, pp. 157–255. ISSN: 03701573. DOI: 10.1016/j.physrep.2006.01.001.

Brataas, Arne, Andrew D Kent, and Hideo Ohno (2012). "Current-induced torques in magnetic materials". In: Nature materials 11.5, pp. 372–381.

Brataas, Arne, Yu V Nazarov, and Gerrit EW Bauer (2001). "Spin-transport in multiterminal normal metal-ferromagnet systems with non-collinear magnetizations". In: Eur. Phys. J. B 22.1, pp. 99–110.

Bulaevskii, L. N. and S. V. Panyukov (1986). "RKKY interaction in metals with impurities". In: JETP Lett. 43 (4), pp. 240–243. URL: http://www.jetpletters.ac.ru/ps/1402/article_21282.shtml.

Burkov, A. A. and D. G. Hawthorn (2010). "Spin and Charge Transport on the Surface of a Topological Insulator". In: Phys. Rev. Lett. 105 (6), p. 066802. DOI: 10.1103/PhysRevLett.105.066802. URL: https://link.aps.org/doi/10.1103/PhysRevLett.105.066802.

Burkov, A. A., Alvaro S. Núñez, and A. H. MacDonald (2004). "Theory of spin-charge-coupled transport in a two-dimensional electron gas with Rashba spin-orbit interactions". In: Phys. Rev. B 70 (15), p. 155308. DOI: 10.1103/PhysRevB.70.155308. URL: https://link.aps.org/doi/10.1103/PhysRevB.70.155308.

Burrowes, C et al. (2012). "Enhanced spin pumping at yttrium iron garnet/Au interfaces". In: Applied Physics Letters 100.9, p. 092403.

Bychkov, Yu A and É I Rashba (1984). "Properties of a 2D electron gas with lifted spectral degeneracy". In: JETP lett 39.2, p. 78.

Cao, Ting et al. (2012). "Valley-selective circular dichroism of monolayer molybdenum disulphide". In: Nature communications 3, p. 887.

Caretta, Lucas et al. (2020). "Interfacial Dzyaloshinskii-Moriya interaction arising from rare-earth orbital magnetism in insulating magnetic oxides". In: Nature communications 11.1, pp. 1–9.

Carrillo-Bastos, R. et al. (2016). "Strained fold-assisted transport in graphene systems". In: Phys. Rev. B 94 (12), p. 125422. DOI: 10.1103/PhysRevB.94.125422. URL: http://link.aps.org/doi/10.1103/PhysRevB.94.125422.

Carva, K and I Turek (2007). "Spin-mixing conductances of thin magnetic films from first principles". In: Phys. Rev. B 76.10, p. 104409.

Casanova, Fèlix et al. (2009). "Control of spin injection by direct current in lateral spin valves". In: Physical Review B 79.18, p. 184415.

Castro Neto, A H et al. (2009). "The electronic properties of graphene". In: Rev. Mod. Phys. 81.1, p. 109.

Cazalilla, M. A., H. Ochoa, and F. Guinea (2014). "Quantum Spin Hall Effect in Two-Dimensional Crystals of Transition-Metal Dichalcogenides". In: Phys. Rev. Lett. 113 (7), p. 077201. DOI: 10.1103/PhysRevLett.113.077201. URL: https://link.aps.org/doi/10.1103/PhysRevLett.113.077201.

Chang, Cui-Zu and Mingda Li (2016). "Quantum anomalous Hall effect in time-reversal-symmetry breaking topological insulators". In: Journal of Physics: Condensed Matter 28.12, p. 123002.

Chang, W et al. (2015). "Hard gap in epitaxial semiconductor–superconductor nanowires". In: Nature nanotechnology 10.3, p. 232.

Chaves, Andrey et al. (2010). "Wave-packet dynamics and valley filter in strained graphene". In: Physical Review B 82.20, p. 205430.

Cheianov, Vadim V. et al. (2009). "Ordered states of adatoms on graphene". In: Phys. Rev. B 80 (23), p. 233409. DOI: 10.1103/PhysRevB.80.233409. URL: http://link.aps.org/doi/10.1103/PhysRevB.80.233409.

Chen, Yan-Ting et al. (2013). "Theory of spin Hall magnetoresistance". In: Phys. Rev. B 87.14, p. 144411.

Cornelissen, L. J. et al. (2017). "Nonlocal magnon-polaron transport in yttrium iron garnet". In: Physical Review B 96.10, p. 104441. ISSN: 2469-9950. DOI: 10.1103/PhysRevB.96.104441. URL: https://link.aps.org/doi/10.1103/PhysRevB.96.104441.

Cornelissen, Ludo J et al. (2016). "Magnon spin transport driven by the magnon chemical potential in a magnetic insulator". In: Physical Review B 94.1, p. 014412.

Cosma, Diana A. et al. (2014). "Strain-induced modifications of transport in gated graphene nanoribbons". In: Phys. Rev. B 90 (24), p. 245409. DOI: 10.1103/PhysRevB.90.245409. URL: http://link.aps.org/doi/10.1103/PhysRevB.90.245409.

Costa, D. R. da et al. (2012). "Wave-packet scattering on graphene edges in the presence of a pseudomagnetic field". In: Phys. Rev. B 86 (11), p. 115434. DOI: 10.1103/PhysRevB.86.115434. URL: http://link.aps.org/doi/10.1103/PhysRevB.86.115434.

Couto, Nuno J. G. et al. (2014). "Random Strain Fluctuations as Dominant Disorder Source for High-Quality On-Substrate Graphene Devices". In: Phys. Rev. X 4 (4), p. 041019. DOI: 10.1103/PhysRevX.4.041019. URL: http://link.aps.org/doi/10.1103/PhysRevX.4.041019.

Dahir, Samme M, Anatoly F Volkov, and Ilya M Eremin (2019). "Phase-dependent spin polarization of Cooper pairs in magnetic Josephson junctions". In: Physical Review B 100.13, p. 134513.

Das, Anindya et al. (2012). "Zero-bias peaks and splitting in an Al–InAs nanowire topological superconductor as a signature of Majorana fermions". In: Nature Physics 8.12, pp. 887–895.

Das, KS et al. (2019). "Temperature dependence of the effective spin-mixing conductance probed with lateral non-local spin valves". In: Appl. Phys. Lett. 114.7, p. 072405.

Datta, Supriyo and Biswajit Das (1990). "Electronic analog of the electro-optic modulator". In: Applied Physics Letters 56.7, pp. 665–667.

De Gennes, P.G. (1962). "Polarisation de charge (ou de spin) au voisinage d'une impureté dans un alliage". In: J. Phys. Radium 23.10, pp. 630–636. DOI: 10.1051/jphysrad:019620023010063000. URL: https://hal.archives-ouvertes.fr/jpa-00236651.

De Simoni, Giorgio et al. (2018). "Toward the absolute spin-valve effect in superconducting tunnel junctions". In: Nano letters 18.10, pp. 6369–6374.

Dejene, FK et al. (2015). "Control of spin current by a magnetic YIG substrate in NiFe/Al nonlocal spin valves". In: Phys. Rev. B 91.10, p. 100404.

Deng, MT et al. (2016). "Majorana bound state in a coupled quantum-dot hybrid-nanowire system". In: Science 354.6319, pp. 1557–1562.

Dolui, Kapildeb, Utkarsh Bajpai, and Branislav K Nikolic (2019). "Spin-mixing conductance of ferromagnet/topological-insulator and ferromagnet/heavy-metal heterostructure: A first-principles Floquet-nonequilibrium Green function approach". In: arXiv:1905.01299.

Dresselhaus, Gene (1955). "Spin-orbit coupling effects in zinc blende structures". In: Physical Review 100.2, p. 580.

Drude, Paul (1900). "Zur elektronentheorie der metalle". In: Annalen der physik 306.3, pp. 566–613.

Dyakonov, M. I. and V. I. Perel (1971). "Current-induced spin orientation of electrons in semiconductors". In: Phys. Lett. A 35.6, pp. 459–460. DOI: 10.1016/0375-9601(71)90196-4. URL: https://doi.org/10.1016/0375-9601(71)90196-4.

Dyakonov, MI (2007). "Magnetoresistance due to edge spin accumulation". In: Phys. Rev. Lett. 99.12, p. 126601.

D'yakonov, MI and VI Perel (1971). "Spin orientation of electrons associated with the interband absorption of light in semiconductors". In: JETP 33, p. 1053.

Dyakonov, MI and VI Perel (1972). "Spin relaxation of conduction electrons in noncentrosymmetric semiconductors". In: Soviet Physics Solid State, Ussr 13.12, pp. 3023–3026.

Dyakonov, Michel I (2017). Spin physics in semiconductors. Vol. 1. Springer.

Dyakonov, Mikhail I and VI Perel (1971). "Current-induced spin orientation of electrons in semiconductors". In: Physics Letters A 35.6, pp. 459–460.

D'Yakonov, Mikhail I and VI Perel (1971). "Possibility of orienting electron spins with current". In: JETPL 13, p. 467.

Elliott, R _ J (1954). "Theory of the effect of spin-orbit coupling on magnetic resonance in some semiconductors". In: Physical Review 96.2, p. 266.

Elliott, Steven R and Marcel Franz (2015). "Colloquium: Majorana fermions in nuclear, particle, and solid-state physics". In: Reviews of Modern Physics 87.1, p. 137.

Eremeev, SV et al. (2013). "Magnetic proximity effect at the three-dimensional topological insulator/magnetic insulator interface". In: Physical Review B 88.14, p. 144430.

Feng, Wanxiang et al. (2012). "Intrinsic spin Hall effect in monolayers of group-VI dichalcogenides: A first-principles study". In: Physical Review B 86.16, p. 165108.

Ferreira, Aires et al. (2014). "Extrinsic Spin Hall Effect Induced by Resonant Skew Scattering in Graphene". In: Phys. Rev. Lett. 112.6, p. 066601.

Fert, Albert (2008). "Nobel Lecture: Origin, development, and future of spintronics". In: Reviews of modern physics 80.4, p. 1517.

Finck, ADK et al. (2013). "Anomalous modulation of a zero-bias peak in a hybrid nanowire-superconductor device". In: Physical review letters 110.12, p. 126406.

Fischer, Johanna et al. (2018). "Spin Hall magnetoresistance in antiferromagnet/heavy-metal heterostructures". In: Physical Review B 97.1, p. 014417.

Flipse, J et al. (2014). "Observation of the spin Peltier effect for magnetic insulators". In: Physical review letters 113.2, p. 027601.

Foner, Simon (1959). "Versatile and sensitive vibrating-sample magnetometer". In: Review of Scientific Instruments 30.7, pp. 548–557.

Fontcuberta, Josep et al. (2019). "On the Role of Interfaces on Spin Transport in Magnetic Insulator/Normal Metal Heterostructures". In: Adv. Mater. Interfaces, p. 1900475.

Fornieri, Antonio et al. (2019). "Evidence of topological superconductivity in planar Josephson junctions". In: Nature 569.7754, pp. 89–92.

Fulde, Peter and Richard A Ferrell (1964). "Superconductivity in a strong spin-exchange field". In: Physical Review 135.3A, A550.

Fullerton, Eric E and Ivan K Schuller (2007). The 2007 Nobel Prize in physics: magnetism and transport at t

Fumagalli, P, A Schirmeisen, and RJ Gambino (1998). "Exchange-induced enhancement of T C in Co 1- x (EuS) x macroscopic ferrimagnets". In: Physical Review B 57.22, p. 14294.

Ganzhorn, Kathrin et al. (2016). "Spin Hall magnetoresistance in a canted ferrimagnet". In: Physical Review B 94.9, p. 094401.

Garcia, Jose H et al. (2018). "Spin transport in graphene/transition metal dichalcogenide heterostructures". In: Chemical Society Reviews 47.9, pp. 3359–3379.

Geprägs, Stephan et al. (2016). "Origin of the spin Seebeck effect in compensated ferrimagnets". In: Nature Communications 7, p. 10452. ISSN: 2041-1723. DOI: 10.1038/ncomms10452. URL: http://www.nature.com/doifinder/10.1038/ncomms10452.

Ghimire, Kiran et al. (2015). "Optical properties of single-crystal Gd3Ga5O12 from the infrared to ultraviolet". In: Physica Status Solidi (b) 252.10, pp. 2191–2198.

Giazotto, F, TT Heikkilä, and FS Bergeret (2015). "Very large thermophase in ferromagnetic Josephson junctions". In: Physical review letters 114.6, p. 067001.

Giazotto, F and F Taddei (2008). "Superconductors as spin sources for spintronics". In: Physical Review B 77.13, p. 132501.

Giazotto, F. and F. Taddei (2011). "Hybrid superconducting quantum magnetometer". In: Phys. Rev. B 84 (21), p. 214502. DOI: 10.1103/PhysRevB.84.214502. URL: https://link.aps.org/doi/10.1103/PhysRevB.84.214502.

Giazotto, Francesco et al. (2010). "Superconducting quantum interference proximity transistor". In: Nature Physics 6.4, pp. 254–259.

Giazotto, Francesco et al. (2011). "A Josephson quantum electron pump". In: Nature Physics 7.11, pp. 857–861.

Giuliani, Gabriele and Giovanni Vignale (2005). Quantum theory of the electron liquid. Cambridge university press.

Gomes, Kenjiro K. et al. (2012). "Designer Dirac fermions and topological phases in molecular graphene". In: Nature 483.7389, pp. 306–310. URL: http://dx.doi.org/10.1038/nature10941.

Gomez-Perez, Juan M. et al. (2020). "Strong Interfacial Exchange Field in a Heavy Metal/Ferromagnetic Insulator System Determined by Spin Hall Magnetoresistance". In: Nano Letters 20.9. PMID: 32786952, pp. 6815–6823. DOI: 10.1021/acs.nanolett.0c02834. eprint: https://doi.org/10.1021/acs.nanolett.0c02834. URL: https://doi.org/10.1021/acs.nanolett.0c02834.

Gorbachev, RV et al. (2014). "Detecting topological currents in graphene superlattices". In: Science 346.6208, pp. 448–451.

Gorini, Cosimo et al. (2010). "Non-Abelian gauge fields in the gradient expansion: Generalized Boltzmann and Eilenberger equations". In: Physical Review B 82.19, p. 195316.

Gradinar, Diana A. et al. (2013). "Transport Signatures of Pseudomagnetic Landau Levels in Strained Graphene Ribbons". In: Phys. Rev. Lett. 110 (26), p. 266801. DOI: 10.1103/PhysRevLett.110.266801. URL: http://link.aps.org/doi/10.1103/PhysRevLett.110.266801.

Guinea, F, MI Katsnelson, and AK Geim (2010). "Energy gaps and a zero-field quantum Hall effect in graphene by strain engineering". In: Nature Physics 6.1, pp. 30–33.

Hahn, Christian et al. (2013). "Comparative measurements of inverse spin Hall effects and magnetoresistance in YIG/Pt and YIG/Ta". In: Phys. Rev. B 87.17, p. 174417.

Haldane, F. D. M. (2004). "Berry Curvature on the Fermi Surface: Anomalous Hall Effect as a Topological Fermi-Liquid Property". In: Phys. Rev. Lett. 93 (20), p. 206602.

DOI: 10.1103/PhysRevLett.93.206602. URL: http://link.aps.org/doi/10.1103/PhysRevLett.93.206602.

Hall, Edwin H et al. (1879). "On a new action of the magnet on electric currents". In: American Journal of Mathematics 2.3, pp. 287–292.

Hammer, JC et al. (2007). "Density of states and supercurrent in diffusive SNS junctions: Roles of nonideal interfaces and spin-flip scattering". In: Physical Review B 76.6, p. 064514.

Hao, X., J. S. Moodera, and R. Meservey (1991). "Thin-film superconductor in an exchange field". In: Phys. Rev. Lett. 67 (10), pp. 1342–1345. DOI: 10.1103/PhysRevLett.67.1342. URL: https://link.aps.org/doi/10.1103/PhysRevLett.67.1342.

Hao, X, JS Moodera, and R Meservey (1990). "Spin-filter effect of ferromagnetic europium sulfide tunnel barriers". In: Physical Review B 42.13, p. 8235.

Hauser, J. J. (1969). "Magnetic Proximity Effect". In: Physical Review 187.2, pp. 580–583. ISSN: 0031-899X. DOI: 10.1103/PhysRev.187.580. URL: https://link.aps.org/doi/10.1103/PhysRev.187.580.

Heikkilä, Tero T et al. (2019). "Thermal, electric and spin transport in superconductor/ferromagnetic-insulator structures". In: Progress in Surface Science 94.3, p. 100540.

Heikkilä, TT et al. (2018). "Thermoelectric Radiation Detector Based on Superconductor-Ferromagnet Systems". In: Physical Review Applied 10.3, p. 034053.

Heinrich, B et al. (2011). "Spin pumping at the magnetic insulator (YIG)/normal metal (Au) interfaces". In: Physical review letters 107.6, p. 066604.

Hirsch, JE (1999). "Spin hall effect". In: Phys. Rev. Lett. 83.9, p. 1834.

Hoogeboom, Geert R et al. (2017). "Negative spin Hall magnetoresistance of Pt on the bulk easy-plane antiferromagnet NiO". In: Applied Physics Letters 111.5, p. 052409.

Hou, Dazhi et al. (2017). "Tunable sign change of spin Hall magnetoresistance in Pt/NiO/YIG structures". In: Physical review letters 118.14, p. 147202.

Huang, Chunli, Y. D. Chong, and Miguel A. Cazalilla (2016). "Direct coupling between charge current and spin polarization by extrinsic mechanisms in graphene". In: Phys. Rev. B 94 (8), p. 085414. DOI: 10.1103/PhysRevB.94.085414. URL: http://link.aps.org/doi/10.1103/PhysRevB.94.085414.

Huang, Chunli, YD Chong, and Miguel A Cazalilla (2017). "Anomalous Nonlocal Resistance and Spin-Charge Conversion Mechanisms in Two-Dimensional Metals". In: Physical review letters 119.13, p. 136804.

Huang, Chunli, Mirco Milletarì, and Miguel A Cazalilla (2017). "Spin-charge conversion in disordered two-dimensional electron gases lacking inversion symmetry". In: Physical Review B 96.20, p. 205305.

Huang, Chunli et al. (2016). "Graphene electrodynamics in the presence of the extrinsic spin Hall effect". In: Phys. Rev. B 93 (16), p. 165429. DOI: 10.1103/PhysRevB.93.165429. URL: http://link.aps.org/doi/10.1103/PhysRevB.93.165429.

Huang, Ssu-Yen et al. (2012). "Transport magnetic proximity effects in platinum". In: Phys. Rev. Lett. 109.10, p. 107204.

Huertas-Hernando, Daniel, F Guinea, and Arne Brataas (2006). "Spin-orbit coupling in curved graphene, fullerenes, nanotubes, and nanotube caps". In: Phys. Rev. B 74.15, p. 155426.

Iorio, Andrea et al. (2018). "Vectorial Control of the Spin–Orbit Interaction in Suspended InAs Nanowires". In: Nano letters 19.2, pp. 652–657.

Isasa, Miren et al. (2014). "Spin Hall magnetoresistance at Pt/CoFe2O4 interfaces and texture effects". In: Appl. Phys. Lett. 105.14, p. 142402.

Isasa, Miren et al. (2016). "Spin Hall Magnetoresistance as a Probe for Surface Magnetization in Pt/Co Fe 2 O 4 Bilayers". In: Phys. Rev. Appl. 6.3, p. 034007.

Isberg, Jan et al. (2013). "Generation, transport and detection of valley-polarized electrons in diamond". In: Nature materials 12.8, pp. 760–764.

Ishizuka, Hiroaki and Naoto Nagaosa (2017). "Noncommutative quantum mechanics and skew scattering in ferromagnetic metals". In: Phys. Rev. B 96 (16), p. 165202. DOI: 10.1103/PhysRevB.96.165202. URL: https://link.aps.org/doi/10.1103/PhysRevB.96.165202.

Ji, Y et al. (2017). "Spin Hall magnetoresistance in an antiferromagnetic magnetoelectric Cr2O3/heavy-metal W heterostructure". In: Applied Physics Letters 110.26, p. 262401.

Jia, Xingtao et al. (2011). "Spin transfer torque on magnetic insulators". In: Europhys. Lett. 96.1, p. 17005.

Jiang, Yongjin et al. (2013). "Generation of Pure Bulk Valley Current in Graphene". In: Phys. Rev. Lett. 110 (4), p. 046601. DOI: 10.1103/PhysRevLett.110.046601. URL: http://link.aps.org/doi/10.1103/PhysRevLett.110.046601.

Kajiwara, Y. et al. (2010). "Transmission of electrical signals by spin-wave interconversion in a magnetic insulator". In: Nature 464.7286, pp. 262–266. ISSN: 0028-0836. URL: http://www.nature.com/articles/nature08876http://dx.doi.org/10.1038/nature08876.

Kane, Charles L and Eugene J Mele (2005). "Quantum spin Hall effect in graphene". In: Physical review letters 95.22, p. 226801.

Karchev, NI et al. (2001). "Coexistence of superconductivity and ferromagnetism in ferromagnetic metals". In: Physical review letters 86.5, p. 846.

Katmis, Ferhat et al. (2016). "A high-temperature ferromagnetic topological insulating phase by proximity coupling". In: Nature 533.7604, p. 513.

Kato, Yuichiro K et al. (2004). "Observation of the spin Hall effect in semiconductors". In: Science 306.5703, pp. 1910–1913.

Katsnelson, Mikhail I (2012). Graphene: carbon in two dimensions. Cambridge University Press.

Kaverzin, A. A. In: private communication.

Kaverzin, A. A. and B. J. van Wees (2015). "Electron transport nonlocality in monolayer graphene modified with hydrogen silsesquioxane polymerization". In: Phys. Rev. B 91 (16), p. 165412. DOI: 10.1103/PhysRevB.91.165412. URL: http://link.aps.org/doi/10.1103/PhysRevB.91.165412.

Kawahara, Takayuki et al. (2012). "Spin-transfer torque RAM technology: Review and prospect". In: Microelectronics Reliability 52.4, pp. 613–627.

Kimura, T et al. (2007). "Room-temperature reversible spin Hall effect". In: Phys. Rev. Lett. 98.15, p. 156601.

Kinney, WI and WP Wolf (1979). "Magnetic interactions and short range order in gadolinium gallium garnet". In: Journal of Applied Physics 50.B3, pp. 2115–2117.

Kjærgaard, Morten et al. (2016). "Quantized conductance doubling and hard gap in a two-dimensional semiconductor–superconductor heterostructure". In: Nature communications 7.1, pp. 1–6.

Kopylov, Sergey et al. (2011). "Transport anomaly at the ordering transition for adatoms on graphene". In: Phys. Rev. B 83 (20), p. 201401. DOI: 10.1103/PhysRevB.83.201401. URL: http://link.aps.org/doi/10.1103/PhysRevB.83.201401.

Kosub, Tobias et al. (2018). "Anomalous Hall-like transverse magnetoresistance in Au thin films on Y3Fe5O12". In: Applied Physics Letters 113.22, p. 222409.

Kuprianov, M Yu and V F Lukichev (1988). "Influence of boundary transparency on the critical current of dirty SS'S structures". In: J. Exp. Theor. Phys. 67, p. 1163.

Lammel, Michaela et al. (2019). "Spin Hall magnetoresistance in heterostructures consisting of noncrystalline paramagnetic YIG and Pt". In: arXiv:1901.09986.

Larkin, Anatoli and Andrei Varlamov (2005). Theory of fluctuations in superconductors. Clarendon Press.

Le Sueur, Hélène et al. (2008). "Phase controlled superconducting proximity effect probed by tunneling spectroscopy". In: Physical review letters 100.19, p. 197002.

Lee, Jieun, Kin Fai Mak, and Jie Shan (2016). "Electrical control of the valley Hall effect in bilayer MoS2 transistors". In: Nature Nanotechnology.

Lee, Jieun et al. (2017). "Valley magnetoelectricity in single-layer MoS 2". In: Nature materials 16.9, p. 887.

Lee, Shu-Ping, Jason Alicea, and Gil Refael (2012). "Electrical manipulation of majorana fermions in an interdigitated superconductor-ferromagnet device". In: Physical review letters 109.12, p. 126403.

Leutenantsmeyer, Johannes Christian et al. (2016). "Proximity induced room temperature ferromagnetism in graphene probed with spin currents". In: 2D Materials 4.1, p. 014001.

Levy, N. et al. (2010). "Strain-Induced Pseudo–Magnetic Fields Greater Than 300 Tesla in Graphene Nanobubbles". In: Science 329.5991, pp. 544–547. DOI: 10.1126/science.1191700.

Li, Bin et al. (2013). "Superconducting spin switch with infinite magnetoresistance induced by an internal exchange field". In: Physical review letters 110.9, p. 097001.

Li, Si-Yu et al. (2015). "Observation of unconventional splitting of Landau levels in strained graphene". In: Phys. Rev. B 92 (24), p. 245302. DOI: 10.1103/PhysRevB.92.245302. URL: http://link.aps.org/doi/10.1103/PhysRevB.92.245302.

Linder, Jacob and Jason WA Robinson (2015). "Superconducting spintronics". In: Nature Physics 11.4, pp. 307–315.

Liu, Yizhou and Guoqiang Yu (2019). "MRAM gets closer to the core". In: Nature Electronics 2.12, pp. 555–556.

Liu, Yu et al. (2019a). "Coherent Epitaxial Semiconductor-Ferromagnetic Insulator InAs/EuS Interfaces: Band Alignment and Magnetic Structure". In: arXiv preprint arXiv:1908.07096.

Liu, Yu et al. (2019b). "Semiconductor–Ferromagnetic Insulator–Superconductor Nanowires: Stray Field and Exchange Field". In: Nano letters 20.1, pp. 456–462.

Livanas, G, Manfred Sigrist, and Georgios Varelogiannis (2019). "Alternative paths to realize Majorana Fermions in superconductor-Ferromagnet Heterostructures". In: Scientific reports 9.1, pp. 1–7.

Lu, Y. M. et al. (2013). "Hybrid magnetoresistance in the proximity of a ferromagnet". In: Physical Review B 87.22, p. 220409. ISSN: 1098-0121. DOI: 10.1103/PhysRevB.87.220409. URL: https://link.aps.org/doi/10.1103/PhysRevB.87.220409.

Lutchyn, RM t et al. (2018). "Majorana zero modes in superconductor–semiconductor heterostructures". In: Nature Reviews Materials 3.5, pp. 52–68.

Lutchyn, Roman M, Jay D Sau, and S Das Sarma (2010). "Majorana fermions and a topological phase transition in semiconductor-superconductor heterostructures". In: Physical review letters 105.7, p. 077001.

Lutchyn, Roman M, Tudor D Stanescu, and S Das Sarma (2011). "Search for Majorana fermions in multiband semiconducting nanowires". In: Physical review letters 106.12, p. 127001.

Luttinger, J. M. and W. Kohn (1958). "Quantum Theory of Electrical Transport Phenomena. II". In: Phys. Rev. 109 (6), pp. 1892–1909. DOI: 10.1103/PhysRev.109.1892. URL: http://link.aps.org/doi/10.1103/PhysRev.109.1892.

Ma, Dongwei, Zhongyao Li, and Zhongqin Yang (2012). "Strong spin–orbit splitting in graphene with adsorbed Au atoms". In: Carbon 50.1, pp. 297–305.

Maekawa, Sadamichi and Takashi Kimura (2017). Spin Current. Vol. 22. Oxford University Press.

Majlis, N. (2007). The Quantum Theory of Magnetism. World Scientific. ISBN: 9789812567925. URL: https://books.google.es/books?id=EKT4YaovXuYC.

Mak, Kin Fai et al. (2014). "The valley Hall effect in MoS2 transistors". In: Science 344.6191, pp. 1489–1492.

Marmion, SR et al. (2014). "Temperature dependence of spin Hall magnetoresistance in thin YIG/Pt films". In: Physical Review B 89.22, p. 220404.

Mauger, A and C Godart (1986). "The magnetic, optical, and transport properties of representatives of a class of magnetic semiconductors: The europium chalcogenides". In: Physics Reports 141.2-3, pp. 51–176.

Mermin, N. D. and H. Wagner (1966). "Absence of Ferromagnetism or Antiferromagnetism in One- or Two-Dimensional Isotropic Heisenberg Models". In: Phys. Rev. Lett. 17 (22), pp. 1133–1136. DOI: 10.1103/PhysRevLett.17.1133. URL: https://link.aps.org/doi/10.1103/PhysRevLett.17.1133.

Meschke, Matthias et al. (2011). "Tunnel spectroscopy of a proximity Josephson junction". In: Physical Review B 84.21, p. 214514.

Meservey, R, PM Tedrow, and Peter Fulde (1970). "Magnetic field splitting of the quasiparticle states in superconducting aluminum films". In: Physical Review Letters 25.18, p. 1270.

Meyer, Sibylle et al. (2014). "Temperature dependent spin transport properties of platinum inferred from spin Hall magnetoresistance measurements". In: Appl. Phys. Lett. 104.24, p. 242411.

Meyer, Sibylle et al. (2015). "Anomalous Hall effect in YIG | Pt bilayers". In: Applied Physics Letters 106.13, p. 132402.

Miao, B.âF. et al. (2014). "Physical Origins of the New Magnetoresistance in Pt / YIG". In: Physical Review Letters 112.23, p. 236601. ISSN: 0031-9007. DOI: 10.1103/PhysRevLett.112.236601. URL: https://link.aps.org/doi/10.1103/PhysRevLett.112.236601.

Mikkel Settnes Nicolas Leconte, et. al. (2016). "Quantum Transport in Graphene in Presence of Strain-Induced Pseudo-Landau Levels". In: arXiv:1607.07300.

Milovanovic, S. P. and F. Peeters (2016). "Strain controlled valley filtering in multi-terminal graphene structures". In: arxiv:1610.09916.

Moodera, JS et al. (1988). "Electron-spin polarization in tunnel junctions in zero applied field with ferromagnetic EuS barriers". In: Physical review letters 61.5, p. 637.

Mosendz, O et al. (2009). "Magnetization dynamics in the presence of pure spin currents in magnetic single and double layers in spin ballistic and diffusive regimes". In: Physical Review B 79.22, p. 224412.

Mourik, Vincent et al. (2012). "Signatures of Majorana fermions in hybrid superconductor-semiconductor nanowire devices". In: Science 336.6084, pp. 1003–1007.

Muduli, PK et al. (2018). "Detection of the interfacial exchange field at a ferromagnetic insulator-nonmagnetic metal interface with pure spin currents". In: Physical Review B 98.2, p. 024416.

Müller, Martina, Guo-Xing Miao, and Jagadeesh S Moodera (2009). "Thickness dependence of ferromagnetic-and metal-insulator transition in thin EuO films". In: J. Appl. Phys. 105.7, p. 07C917.

Müller, W and W Nolting (2002). "Temperature-dependent quasiparticle band structure of the ferromagnetic semiconductor EuS". In: Physical Review B 66.8, p. 085205.

Murdin, BN et al. (2005). "Temperature and doping dependence of spin relaxation in n-InAs". In: Physical Review B 72.8, p. 085346.

Murzyn, P et al. (2003). "Suppression of D'yakonov–Perel spin relaxation in InAs and InSb by n-type doping at 300 K". In: Applied Physics Letters 83.25, pp. 5220–5222.

Myers, RC et al. (2005). "Antiferromagnetic s-d exchange coupling in GaMnAs". In: Phys. Rev. Lett. 95.1, p. 017204.

Nagaosa, Naoto et al. (2010). "Anomalous Hall effect". In: Rev. Mod. Phys. 82 (2), pp. 1539–1592. DOI: 10.1103/RevModPhys.82.1539. URL: http://link.aps.org/doi/10.1103/RevModPhys.82.1539.

Nakayama, H. et al. (2013). "Spin Hall Magnetoresistance Induced by a Nonequilibrium Proximity Effect". In: Phys. Rev. Lett. 110 (20), p. 206601. DOI: 10.1103/PhysRevLett.110.206601. URL: https://link.aps.org/doi/10.1103/PhysRevLett.110.206601.

Nakayama, Hiroyasu et al. (2016). "Rashba-Edelstein Magnetoresistance in Metallic Heterostructures". In: Phys. Rev. Lett. 117.11, p. 116602.

Nichele, Fabrizio et al. (2017). "Scaling of Majorana zero-bias conductance peaks". In: Physical review letters 119.13, p. 136803.

Oreg, Yuval, Gil Refael, and Felix von Oppen (2010). "Helical liquids and Majorana bound states in quantum wires". In: Physical review letters 105.17, p. 177002.

Otani, YoshiChika et al. (2017). "Spin conversion on the nanoscale". In: Nature Physics 13.9, pp. 829–832.

Overmeyer, J et al. (1963). Paramagnetic Resonance. Academic, New York.

Oyanagi, Koichi et al. (2020). "Paramagnetic Spin Hall Magnetoresistance". In: Unpublished.

Pearce, Alexander J., Eros Mariani, and Guido Burkard (2016). "Tight-binding approach to strain and curvature in monolayer transition-metal dichalcogenides". In: Phys. Rev. B 94 (15), p. 155416. DOI: 10.1103/PhysRevB.94.155416. URL: http://link.aps.org/doi/10.1103/PhysRevB.94.155416.

Pippard, A. B. (1989). Magnetoresistance in metals. Cambridge New York: Cambridge University Press, p. 253. ISBN: 9780521326605. URL: https://www.worldcat.org/title/magnetoresistance-in-metals/oclc/17413703.

Qi, Xiao-Liang and Shou-Cheng Zhang (2011). "Topological insulators and superconductors". In: Reviews of Modern Physics 83.4, p. 1057.

Qian, Xiaofeng et al. (2014). "Quantum spin Hall effect in two-dimensional transition metal dichalcogenides". In: Science 346.6215, pp. 1344–1347.

Raimondi, R. et al. (2012). "Spin-orbit interaction in a two-dimensional electron gas: A SU(2) formulation". In: Annalen der Physik 524.3-4, n/a–n/a. ISSN: 1521-3889. DOI: 10.1002/andp.201100253. URL: http://dx.doi.org/10.1002/andp.201100253.

Rashba, Emmanuel and V Sheka (2015). "Symmetry of energy bands in crystals of wurtzite type II. Symmetry of bands with spin-orbit interaction included". In:

Rechtsman, Mikael C. et al. (2013). "Strain-induced pseudomagnetic field and photonic Landau levels in dielectric structures". In: Nat Photon 7.2, pp. 153–158. URL: http://dx.doi.org/10.1038/nphoton.2012.302.

Rokhinson, Leonid P, Xinyu Liu, and Jacek K Furdyna (2012). "The fractional ac Josephson effect in a semiconductor–superconductor nanowire as a signature of Majorana particles". In: Nature Physics 8.11, p. 795.

Ronzani, Alberto, Carles Altimiras, and Francesco Giazotto (2014). "Highly sensitive superconducting quantum-interference proximity transistor". In: Physical Review Applied 2.2, p. 024005.

Ronzani, Alberto et al. (2017). "Phase-driven collapse of the Cooper condensate in a nanosized superconductor". In: Physical Review B 96.21, p. 214517.

Rouco, Mikel et al. (2019). "Charge transport through spin-polarized tunnel junction between two spin-split superconductors". In: Physical Review B 100.18, p. 184501.

Rycerz, A, J Tworzydło, and CWJ Beenakker (2007). "Valley filter and valley valve in graphene". In: Nature Physics 3.3, pp. 172–175.

Safeer, CK et al. (2018). "Room temperature spin Hall effect in graphene/MoS _2 van der Waals heterostructures". In: arXiv preprint arXiv:1810.12481.

Sagasta, Edurne et al. (2016). "Tuning the spin Hall effect of Pt from the moderately dirty to the superclean regime". In: Physical Review B 94.6, p. 060412. ISSN: 2469-9950. DOI: 10.1103/PhysRevB.94.060412. URL: https://link.aps.org/doi/10.1103/PhysRevB.94.060412.

Salikhov, RI et al. (2009a). "Experimental observation of the spin screening effect in superconductor/ferromagnet thin film heterostructures". In: Physical review letters 102.8, p. 087003.

Salikhov, RI et al. (2009b). "Spin screening effect in superconductor/ferromagnet thin film heterostructures studied using nuclear magnetic resonance". In: Physical Review B 80.21, p. 214523.

Sarma, Sankar Das, Michael Freedman, and Chetan Nayak (2015). "Majorana zero modes and topological quantum computation". In: npj Quantum Information 1, p. 15001.

Sau, Jay D et al. (2010). "Generic new platform for topological quantum computation using semiconductor heterostructures". In: Physical review letters 104.4, p. 040502.

Schaibley, John R et al. (2016). "Valleytronics in 2D materials". In: Nature Reviews Materials 1.11, pp. 1–15.

Schiffer, P et al. (1994). "Investigation of the field induced antiferromagnetic phase transition in the frustrated magnet: gadolinium gallium garnet". In: Physical Review Letters 73.18, p. 2500.

Schiffer, P et al. (1995). "Frustration induced spin freezing in a site-ordered magnet: Gadolinium gallium garnet". In: Physical Review Letters 74.12, p. 2379.

Schliemann, John and Daniel Loss (2003). "Anisotropic transport in a two-dimensional electron gas in the presence of spin-orbit coupling". In: Physical Review B 68.16, p. 165311.

Schlitz, Richard et al. (2018). "Evolution of the spin hall magnetoresistance in Cr2O3/Pt bilayers close to the Néel temperature". In: Applied Physics Letters 112.13, p. 132401.

Seviour, R and AF Volkov (2000). "Suppression and enhancement of the critical current in multiterminal superconductor–normal-metal–superconductor mesoscopic structures". In: Physical Review B 61.14, R9273.

Sham, LJ et al. (1978). "Valley-valley splitting in inversion layers on a high-index surface of silicon". In: Physical Review Letters 40.7, p. 472.

Shen, R et al. (2003). "Breakdown of the coexistence of spin-singlet superconductivity and itinerant ferromagnetism". In: Physical Review B 67.2, p. 024514.

Shen, Shun-Qing (2005). "Spin transverse force on spin current in an electric field". In: Physical review letters 95.18, p. 187203.

Shimazaki, Yuya, Michihisa Yamamoto, Ivan V Borzenets, et al. (2015). "Generation and detection of pure valley current by electrically induced Berry curvature in bilayer graphene". In: Nature Physics 11.12, pp. 1032–1036.

Shiomi, Y. et al. (2014). "Interface-dependent magnetotransport properties for thin Pt films on ferrimagnetic Y ₃ Fe ₅ O ₁₂". In: Applied Physics Letters 104.24, p. 242406. ISSN: 0003-6951. DOI: 10.1063/1.4883898. URL: http://aip.scitation.org/doi/10.1063/1.4883898.

Shioya, Hiroki et al. (2015). "Electron States of Uniaxially Strained Graphene". In: Nano Letters 15.12, pp. 7943–7948. DOI: 10.1021/acs.nanolett.5b03027. URL: http://dx.doi.org/10.1021/acs.nanolett.5b03027.

Sie, Edbert J, James W McIver, et al. (2015). "Valley-selective optical Stark effect in monolayer WS2". In: Nature Materials 14.3, pp. 290–294.

Sih, Vanessa et al. (2005). "Spatial imaging of the spin Hall effect and current-induced polarization in two-dimensional electron gases". In: Nat. Phys. 1.1, p. 31.

Sinova, Jairo et al. (2004). "Universal intrinsic spin Hall effect". In: Phys. Rev. Lett. 92.12, p. 126603.

Sinova, Jairo et al. (2015). "Spin hall effects". In: Rev. Mod. Phys. 87.4, p. 1213.

Slichter, Charles P (2013). Principles of magnetic resonance. Vol. 1. Springer Science & Business Media.

Slonczewski, John C (1996). "Current-driven excitation of magnetic multilayers". In: Journal of Magnetism and Magnetic Materials 159.1-2, pp. L1–L7.

Song, Justin CW and Giovanni Vignale (2018). "Low-dissipation edge currents without edge states". In: arXiv preprint arXiv:1805.05955.

Song, Pil Hun and KW Kim (2002). "Spin relaxation of conduction electrons in bulk III-V semiconductors". In: Physical Review B 66.3, p. 035207.

Stanescu, Tudor D and Sumanta Tewari (2013). "Majorana fermions in semiconductor nanowires: fundamentals, modeling, and experiment". In: Journal of Physics: Condensed Matter 25.23, p. 233201.

Strambini, E et al. (2016). "The ω-SQUIPT as a tool to phase-engineer Josephson topological materials". In: Nature Nanotechnology 11.12, p. 1055.

Strambini, E et al. (2017). "Revealing the magnetic proximity effect in EuS/Al bilayers through superconducting tunneling spectroscopy". In: Phys. Rev. Mater. 1.5, p. 054402.

Strambini, E et al. (2020). "A Josephson quantum phase battery". In: arXiv preprint arXiv:2001.03393.

Suominen, Henri J et al. (2017). "Zero-energy modes from coalescing andreev states in a two-dimensional semiconductor-superconductor hybrid platform". In: Physical review letters 119.17, p. 176805.

Suzuki, R et al. (2014). "Valley-dependent spin polarization in bulk MoS 2 with broken inversion symmetry". In: Nature nanotechnology 9.8, p. 611.

Takei, So et al. (2013). "Soft superconducting gap in semiconductor Majorana nanowires". In: Physical review letters 110.18, p. 186803.

Tiira, Jonna et al. (2017). "Magnetically-driven colossal supercurrent enhancement in InAs nanowire Josephson junctions". In: Nature communications 8.1, pp. 1–9.

Tokatly, IV (2008). "Equilibrium spin currents: non-abelian gauge invariance and color diamagnetism in condensed matter". In: Physical review letters 101.10, p. 106601.

Tserkovnyak, Yaroslav, Arne Brataas, and Gerrit E. W. Bauer (2002). "Spin pumping and magnetization dynamics in metallic multilayers". In: Physical Review B 66.22, p. 224403. ISSN: 0163-1829. DOI: 10.1103/PhysRevB.66.224403. URL: https://link.aps.org/doi/10.1103/PhysRevB.66.224403.

Tserkovnyak, Yaroslav et al. (2005). "Nonlocal magnetization dynamics in ferromagnetic heterostructures". In: Reviews of Modern Physics 77.4, p. 1375.

Uchida, K et al. (2014). "Longitudinal spin Seebeck effect: from fundamentals to applications". In: Journal of Physics: Condensed Matter 26.34, p. 343202.

Uchida, K-i et al. (2010a). "Spin seebeck insulator". In: Nature materials 9.11, pp. 894–897.

Uchida, Ken-ichi et al. (2010b). "Observation of longitudinal spin-Seebeck effect in magnetic insulators". In: Applied Physics Letters 97.17, p. 172505.

Umesh, Sumanth and Sparsh Mittal (2019). "A survey of spintronic architectures for processing-in-memory and neural networks". In: Journal of Systems Architecture 97, pp. 349–372.

Usadel, Klaus D (1970). "Generalized diffusion equation for superconducting alloys". In: Physical Review Letters 25.8, p. 507.

Vaitiekėnas, S et al. (2020). "Zero-field Topological Superconductivity in Ferromagnetic Hybrid Nanowires". In: arXiv preprint arXiv:2004.02226.

Valenzuela, Sergio O and M Tinkham (2006). "Direct electronic measurement of the spin Hall effect". In: Nature 442.7099, pp. 176–179.

Van Tuan, Dinh et al. (2016). "Spin Hall effect and origins of nonlocal resistance in adatom-decorated graphene". In: Physical review letters 117.17, p. 176602.

Vélez, Saül et al. (2016a). "Competing effects at Pt/YIG interfaces: Spin Hall magnetoresistance, magnon excitations, and magnetic frustration". In: Physical Review B 94.17, p. 174405.

Vélez, Saül et al. (2016b). "Hanle magnetoresistance in thin metal films with strong spin-orbit coupling". In: Phys. Rev. Lett. 116.1, p. 016603.

Vélez, Saül et al. (2016). "Hanle Magnetoresistance in Thin Metal Films with Strong Spin-Orbit Coupling". In: Physical Review Letters 116.1, p. 016603. ISSN: 10797114. DOI: 10.1103/PhysRevLett.116.016603.

Vélez, Saül et al. (2019a). "High-speed domain wall racetracks in a magnetic insulator". In: Nature communications 10.1, pp. 1–8.

Vélez, Saül et al. (2019b). "Spin Hall magnetoresistance in a low-dimensional Heisenberg ferromagnet". In: Physical Review B 100.18, p. 180401.

Villamor, Estitxu et al. (2013). "Contribution of defects to the spin relaxation in copper nanowires". In: Physical Review B 87.9, p. 094417.

Virtanen, P et al. (2018). "Majorana bound states in hybrid two-dimensional josephson junctions with ferromagnetic insulators". In: Physical Review B 98.2, p. 020501.

Vlietstra, N et al. (2013a). "Exchange magnetic field torques in YIG/Pt bilayers observed by the spin-Hall magnetoresistance". In: Appl. Phys. Lett. 103.3, p. 032401.

Vlietstra, N. et al. (2013b). "Spin-Hall magnetoresistance in platinum on yttrium iron garnet: Dependence on platinum thickness and in-plane/out-of-plane magnetization". In: Physical Review B 87.18, p. 184421. ISSN: 10980121. DOI: 10.1103/PhysRevB.87.184421.

Völkl, Tobias et al. (2018). "Absence of a giant spin Hall effect in plasma-hydrogenated graphene". In: arXiv preprint arXiv:1809.10475.

Vozmediano, María AH, MI Katsnelson, and Francisco Guinea (2010). "Gauge fields in graphene". In: Physics Reports 496.4, pp. 109–148.

Wahl, P et al. (2007). "Exchange interaction between single magnetic adatoms". In: Phys. Rev. Lett. 98.5, p. 056601.

Wang, Hua et al. (2017). "Antiferromagnetic anisotropy determination by spin Hall magnetoresistance". In: Journal of Applied Physics 122.8, p. 083907.

Wang, Yilin, Xinghan Cai, Janice Reutt-Robey, et al. (2015). "Neutral-current Hall effects in disordered graphene". In: Phys. Rev. B 92 (16), p. 161411. DOI: 10.1103/PhysRevB.92.161411. URL: http://link.aps.org/doi/10.1103/PhysRevB.92.161411.

Weeks, Conan et al. (2011). "Engineering a robust quantum spin Hall state in graphene via adatom deposition". In: Phys. Rev. X 1.2, p. 021001.

Wei, Peng et al. (2016). "Strong interfacial exchange field in the graphene/EuS heterostructure". In: Nature materials 15.7, pp. 711–716.

Weiler, Mathias et al. (2012). "Local Charge and Spin Currents in Magnetothermal Landscapes". In: Phys. Rev. Lett. 108 (10), p. 106602. DOI: 10.1103/PhysRevLett.

108.106602. URL: https://link.aps.org/doi/10.1103/PhysRevLett.108.106602.

Weiler, Mathias et al. (2013). "Experimental test of the spin mixing interface conductivity concept". In: Physical Review Letters 111.17, p. 176601. ISSN: 00319007. DOI: 10.1103/PhysRevLett.111.176601.

Winkler, Roland (2003). "Spin-orbit coupling effects in two-dimensional electron and hole systems". In: Springer Tracts in Modern Physics 191, pp. 1–8.

Wunderlich, Joerg et al. (2005). "Experimental observation of the spin-Hall effect in a two-dimensional spin-orbit coupled semiconductor system". In: Phys. Rev. Lett. 94.4, p. 047204.

Xia, Jing et al. (2009). "Inverse proximity effect in superconductor-ferromagnet bilayer structures". In: Physical review letters 102.8, p. 087004.

Xia, K et al. (2002). "Spin torques in ferromagnetic/normal-metal structures". In: Phys. Rev. B 65.22, p. 220401.

Xia, Siyu et al. (2020). "Interfacial Dzyaloshinskii-Moriya interaction between ferromagnetic insulator and heavy metal". In: Applied Physics Letters 116.5, p. 052404.

Xiao, Di, Ming-Che Chang, and Qian Niu (2010). "Berry phase effects on electronic properties". In: Reviews of modern physics 82.3, p. 1959.

Xiao, Di, Wang Yao, and Qian Niu (2007). "Valley-contrasting physics in graphene: magnetic moment and topological transport". In: Physical Review Letters 99.23, p. 236809.

Xiao, Di et al. (2012). "Coupled spin and valley physics in monolayers of MoS 2 and other group-VI dichalcogenides". In: Physical Review Letters 108.19, p. 196802.

Xiong, YM et al. (2011). "Spin-resolved tunneling studies of the exchange field in eus/al bilayers". In: Physical review letters 106.24, p. 247001.

Xu, Xiaodong et al. (2014). "Spin and pseudospins in layered transition metal dichalcogenides". In: Nature Physics 10.5, pp. 343–350.

Yafet, Y (1963). "g Factors and spin-lattice relaxation of conduction electrons". In: Solid state physics. Vol. 14. Elsevier, pp. 1–98.

Yang, H-Y et al. (2016). "Extrinsic spin Hall effect from anisotropic Rashba spin-orbit coupling in graphene". In: Physical Review B 93.8, p. 085418.

Yang, Hong-Xin et al. (2013). "Proximity effects induced in graphene by magnetic insulators: First-principles calculations on spin filtering and exchange-splitting gaps". In: Physical review letters 110.4, p. 046603.

Yao, Wang, Di Xiao, and Qian Niu (2008). "Valley-dependent optoelectronics from inversion symmetry breaking". In: Physical Review B 77.23, p. 235406.

Yosida, Kei (1958). "Paramagnetic susceptibility in superconductors". In: Physical Review 110.3, p. 769.

Zeng, Hualing et al. (2012). "Valley polarization in MoS 2 monolayers by optical pumping". In: Nature nanotechnology 7.8, pp. 490–493.

Zhang, Qinfang, Shin-ichi Hikino, and Seiji Yunoki (2011). "First-principles study of the spin-mixing conductance in Pt/Ni81Fe19 junctions". In: Appl. Phys. Lett. 99.17, p. 172105.

Zhang, Xian-Peng, F Sebastian Bergeret, and Vitaly N Golovach (2019). "Theory of Spin Hall Magnetoresistance from a Microscopic Perspective". In: Nano letters 19.9, pp. 6330–6337.

Zhang, Xian-Peng, Chunli Huang, and Miguel A Cazalilla (2017). "Valley Hall Effect and Nonlocal Transport in Strained Graphene". In: 2D Mater. 4, p. 024007.

Zhang, Xian-Peng, Chunli Huang, and Miguel A. Cazalilla (2019). "Control of spin diffusion and suppression of the Hanle oscillation by the coexistence of spin and valley Hall effects in Dirac materials". In: Phys. Rev. B 99 (24), p. 245106. DOI:

10.1103/PhysRevB.99.245106. URL: https://link.aps.org/doi/10.1103/PhysRevB.99.245106.

Zhou, Lifan et al. (2018). "Observation of spin-orbit magnetoresistance in metallic thin films on magnetic insulators". In: Sci. Adv. 4.1, eaao3318.

Zhu, Jian-Gang (2008). "Magnetoresistive random access memory: The path to competitiveness and scalability". In: Proceedings of the IEEE 96.11, pp. 1786–1798.

Zou, L. K. et al. (2016). "Tunable angular-dependent magnetoresistance correlations in magnetic films and their implications for spin Hall magnetoresistance analysis". In: Physical Review B 93.7, p. 075309. ISSN: 2469-9950. DOI: 10.1103/PhysRevB.93.075309. URL: https://link.aps.org/doi/10.1103/PhysRevB.93.075309.

Zyuzin, A. Yu. and B. Z. Spivak (1986). "Friedel oscillations and Ruderman-Kittel interaction in disordered conductors". In: JETP Lett. 43 (4), pp. 234–237. URL: http://www.jetpletters.ac.ru/ps/1402/article_21280.shtml.

List of publications

[1] Koichi Oyanag, J. M. Gomez-Perez, X.-P. Zhang, $\cdots$, and Eiji Saitoh. "Paramagnetic spin Hall magnetoresistance."arXiv:2008.02446, submitted into Phys. Rev. Lett.;

[2] J. M. Gomez-Perez, X.-P. Zhang, $\cdots$, and Felix Casanova. "Strong interfacial exchange field in a heavy metal/ferromagnetic insulator system determined by spin Hall magnetoresistance." Nano Lett., 20(9), 6815 (2020);

[3] D. Perconte, $\cdots$, X.-P. Zhang, $\cdots$, and J. Villegas. "Observation of quantum interference effects of d-wave Andreev pairs in graphene." Phys. Rev. Lett., 125, 087002 (2020);

[4] X.-P. Zhang, V. N. Golovach, F. Giazotto and F. S. Bergeret, "Phase-Controllable Nonlocal Spin Polarization in Proximitized Nanowires." Phys. Rev. B: Rap. Comm., 101, 180502 (2020);

[5] X.-P. Zhang, F. S. Bergeret and V. N. Golovach. "Theory of Spin Hall Magnetoresistance from a Microscopic Perspective." Nano Lett., 19(9), 6330 (2019);

[6] X.-P. Zhang, L.-T. Shen, Z.-Q. Yin, L. Sun, H.-Z. Wu, and Z.-B. Yang "Multi-Resonator-Assisted Multi-Qubit Resetting in a Network." arXiv:1604.08393;

[7] X.-P. Zhang, C. Huang, and M. A. Cazalilla. "Valley Hall effect and nonlocal transport in strained graphene." 2D Materials, 4.2: 024007 (2017);

[8] X.-P. Zhang, C. Huang, and M. A. Cazalilla. "Control of spin diffusion and suppression of the Hanle oscillation by the coexistence of spin and valley Hall effects in Dirac materials." Phys. Rev. B, 99, 245106 (2019);

[9] X.-P. Zhang, L.-T. Shen, Z.-Q. Yin, H.-Z. Wu, and Z.-B. Yang, "Resonator-assisted quantum bath engineering of a flux qubit." Phys. Rev. A, 91(1), 013825 (2015);

[10] X.-P. Zhang, L.-T. Shen, and Z.-B. Yang. "Multi-atom entanglement engineering and phase-covariant quantum cloning with a single resonant interaction assisted by external driving." Optics Communications, 332: 214-218 (2014).